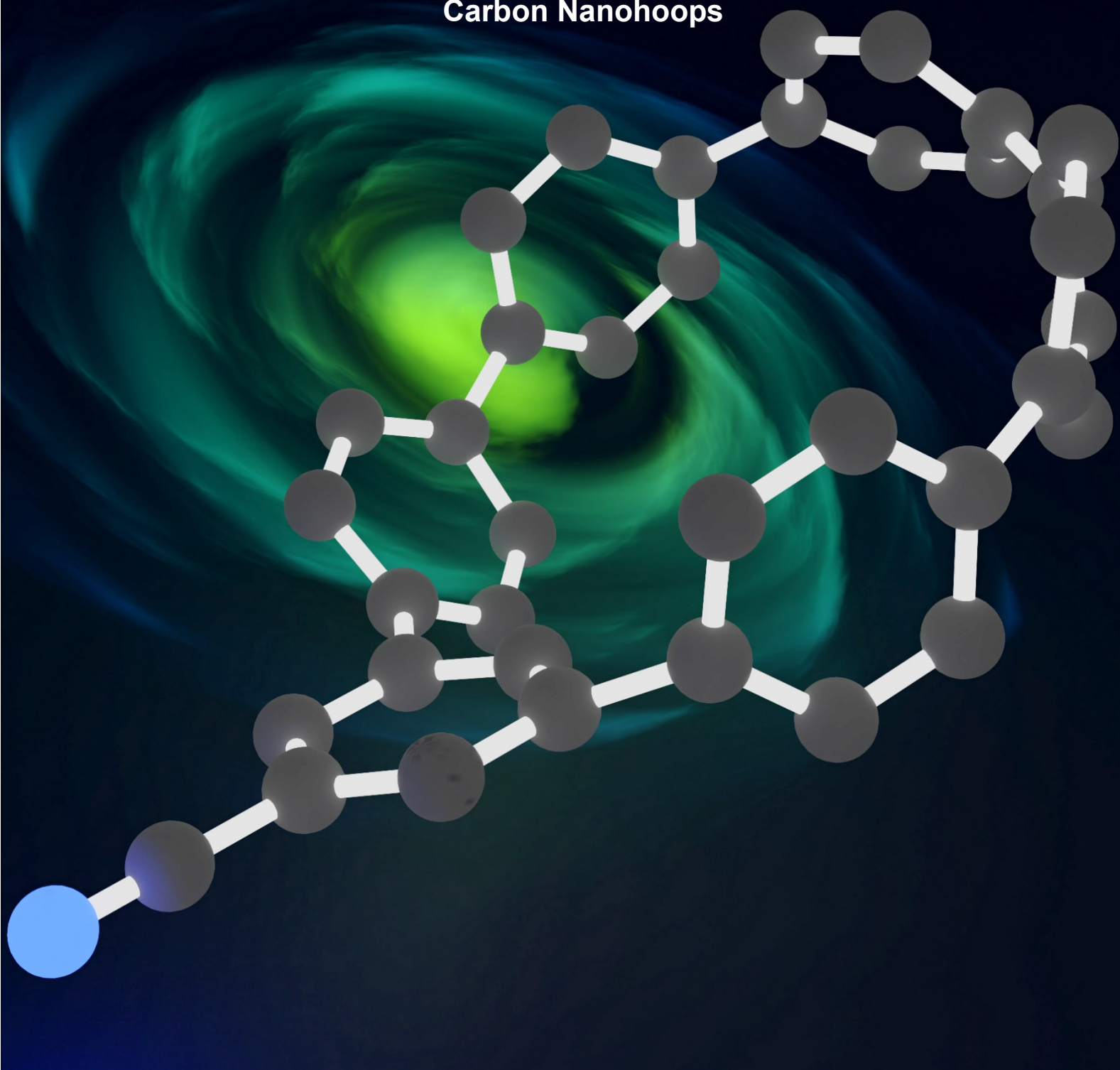


Synthesis and Investigation of (*meta*)[*n*]Cycloparaphenylenes

An Odyssey through the Realms of
Carbon Nano hoops



Synthesis and Investigation of (*meta*)[*n*]Cycloparaphenylenes

An Odyssey through the Realms of Carbon Nanohoops

INAUGURALDISSERTATION

zur Erlangung des Doktorgrades (Dr. rer. Nat.)

der Naturwissenschaftlichen Fachbereiche im Fachgebiet Chemie

der Justus-Liebig-Universität Gießen

von

Felix Bernt

geboren in

Gelnhausen

Gießen 2023

Die vorliegende Dissertation wurde in der Zeit von Juni 2021 bis Dezember 2023 am Institut für Organische Chemie der Justus-Liebig-Universität Gießen unter der Leitung von Herrn Prof. Dr. Hermann A. Wegner angefertigt.

Teile dieser Arbeit sind bereits veröffentlicht oder als Manuskript eingereicht:

1. F. Bernt, H. A. Wegner
„Substituted *meta*[*n*]Cycloparaphenylenes: Synthesis, Photophysical Properties and Host-guest Chemistry”
Chem. Eur. J. **2023**, *29*, e202301001.
2. F. Bernt, C. M. Leonhardt, D. Schatz, H. A. Wegner
„Synthesis and investigation of a *meta*[6]cycloparaphenylene gold(I) *N*-heterocyclic carbene complex”
Manuskript eingereicht, **18.12.2023**.

Dekan: Prof. Dr. Thomas Wilke
Erstgutachter: Prof. Dr. Hermann A. Wegner
Zweitgutachter: Prof. Dr. Richard Göttlich

Versicherung nach §17 der Promotionsordnung

Ich erkläre: Ich habe die vorgelegte Dissertation selbstständig und ohne unerlaubte fremde Hilfe und nur mit den Hilfen angefertigt, die ich in der Dissertation angegeben habe. Alle Textstellen, die wörtlich oder sinngemäß aus veröffentlichten Schriften entnommen sind, und alle Angaben, die auf mündlichen Auskünften beruhen, sind als solche kenntlich gemacht. Ich stimme einer evtl. Überprüfung meiner Dissertation durch eine Antiplagiat-Software zu. Bei den von mir durchgeführten und in der Dissertation erwähnten Untersuchungen habe ich die Grundsätze guter wissenschaftlicher Praxis, wie sie in der „Satzung der Justus-Liebig-Universität Gießen zur Sicherung guter wissenschaftlicher Praxis“ niedergelegt sind, enthalten.

Felix Bernt

Ort, Datum

„Be practical as well as generous in your ideals.

Keep your eyes on the stars and keep your feet on the ground.”

THEODORE ROOSEVELT

Table of Contents

<i>Abstract</i>	<i>XII</i>
<i>Zusammenfassung</i>	<i>XVI</i>
1. Introduction	1
1.1. Physical Background.....	2
1.2. Classes of Fluorophores	4
1.3. [n]Cycloparaphenylenes	5
1.4. 1,2-Aryl Shift in the Synthesis of [n]Cycloparaphenylenes	30
1.5. <i>meta</i> [n]Cycloparaphenylenes	33
1.6. N-Heterocyclic Carbenes as Ligands for Luminescent Gold-Complexes.....	39
1.7. Barrelenes.....	48
2. Objectives	51
3. Results and Discussion	54
3.1. C-H Activation towards the Post-Functionalization of [10]Cycloparaphenylene.....	54
3.2. 1,2-Aryl Shift as Synthetic Tool towards novel Macrocyclic Structures	71
3.3. Substituted- <i>meta</i> [n]Cycloparaphenylenes.....	79
3.3.1. Cyano- <i>meta</i> [n]Cycloparaphenylenes	79
3.3.2. Synthesis of a Luminescent Gold(I)-Complex.....	100
3.3.3. Towards a Barrelene-incorporated <i>meta</i> [6]CPP.....	112
4. Perspective on Future Directions	114
5. Experimental Part	116
5.1. General Information	116
5.2. Synthetic procedures.....	120
5.2.1. Syntheses of literature-known building blocks and [10]cycloparaphenylene	120
5.2.1.1. [10]Cycloparaphenylene 155	120
5.2.2. General procedure for the (LEWIS-)acid screening towards the investigation of the 1,2-aryl shift (GP 1).....	121
5.2.3. General procedure for the macrocyclization reactions (GP 2).....	121
5.2.3.1. General procedure for the homogeneous-catalyzed macrocyclization using continuous flow-chemistry (GP 2.1)	122
5.2.3.1. General procedure for the heterogeneous-catalyzed macrocyclization using continuous flow-chemistry (GP 2.2)	123
5.2.4. General procedure for the aromatization reactions using tin chloric acid (GP 3). 123	

5.2.5.	Synthetic procedures towards C-H activation of unactivated arenes	124
5.2.5.1.	DMSO-catalyzed halogenation using hydrogen halides	124
5.2.5.2.	DMSO-catalyzed chlorination using <i>N</i> -chlorosuccinimide	125
5.2.5.3.	Calcium-catalyzed arene C-H Bond activation by low-valent Al(I)	125
5.2.5.4.	Iridium-catalyzed borylation.....	126
5.2.5.5.	Pd-catalyzed C-H acetoxylation.....	127
5.2.5.6.	Pd-catalyzed C-H olefination.....	128
5.2.5.7.	Electrochemical C-H trifluoro acetoxylation	128
5.2.5.8.	Electrochemical C-H hydroxylation.....	129
5.2.6.	1,2-Aryl shift of building block 172 towards 4-bromo-4'-methoxy-[1,1':3',1'':4'',1'''-quarter-phenyl]-4'''-ol (173)	130
5.2.7.	4,4''-Dichloro-4'-methoxy-[1,1':4',1''-terphenyl]-1'(4' <i>H</i>)-yl)oxy)triethylsilane (216) 131	
5.2.8.	Reaction screening towards the 1,2-aryl shift.....	132
5.2.9.	Borylation of mixed-protected building block 219.....	133
5.2.10.	Mixed-protected macrocycle 220	134
5.2.11.	1,2-Aryl shift on mixed-protected macrocycle 220.....	135
5.2.1.	3,5-Bis(4,4,5,5-tetramethyl-1,3,2-dioxaborolan-2-yl)benzotrile (223)	136
5.2.2.	Macrocyclic precursor 226.....	137
5.2.3.	Cyano- <i>meta</i> [6]cycloparaphenylene 158.....	138
5.2.4.	Building block 229	139
5.2.5.	Macrocyclization reactions towards nitrile-substituted <i>meta</i> [<i>n</i>]cycloparaphenylenes.....	140
5.2.5.1.	Macrocyclic precursor 226.....	140
5.2.5.2.	Macrocyclic precursor 230	141
5.2.5.3.	Macrocyclic precursor 231	142
5.2.6.	Aromatization reactions towards nitrile-substituted <i>meta</i> [<i>n</i>]cycloparaphenylenes derived from methyl-ether protected macrocycles	143
5.2.6.1.	Cyano- <i>meta</i> [6]cycloparaphenylene 158	143
5.2.6.2.	Cyano- <i>meta</i> [8]cycloparaphenylene 159	144
5.2.6.3.	Cyano- <i>meta</i> [10]cycloparaphenylene 160	145
5.2.7.	Amidoxime- <i>meta</i> [6]cycloparaphenylene 233.....	146
5.2.8.	Carboxy- <i>meta</i> [6]cycloparaphenylene 234.....	147
5.2.9.	Amide- <i>meta</i> [6]cycloparaphenylene 235	148
5.2.10.	Aldehyde- <i>meta</i> [6]cycloparaphenylene 236.....	149

5.2.11.	(Amino-methylene)- <i>meta</i> [6]cycloparaphenylene 237	150
5.2.12.	1 <i>H</i> -Tetrazole-5- <i>meta</i> [6]cycloparaphenylene 238	151
5.2.13.	1-(<i>meta</i> [6]cycloparaphenylene)-2-methyl-propane-1-one 239	152
5.2.14.	4,5-Dimethylpyridinyl-2-(<i>meta</i> [6]cyclopara-phenylene) 240.....	152
5.2.15.	3-(<i>meta</i> [6]cycloparaphenylene)-1,2,4,5-tetrazine 241	153
5.2.16.	2,4,6-(<i>meta</i> [6]cycloparaphenylene)-1,3,5-triazine 242	154
5.2.17.	<i>N</i> -(Mesityl)-oxanilic acid (258).....	154
5.2.18.	[1,1':3',1''-Terphenyl]-5'-carbonitrile (252).....	156
5.2.19.	[1,1':3',1''-Terphenyl]-5'-yl-methanamine (253)	156
5.2.20.	<i>N</i> -(Mesityl)- <i>N'</i> -([1,1':3',1''-terphenyl]-5'-ylmethyl)-oxalamide (259)	157
5.2.21.	<i>N</i> -(Mesityl)- <i>N'</i> -([1,1':3',1''-terphenyl]-5'-ylmethyl)-diamine (260).....	158
5.2.22.	<i>N</i> -(Mesityl)- <i>N'</i> -{1-([1,1':3',1''-terphenyl]-5'-ylmethyl)-imidazolium chloride (261) 159	
5.2.23.	<i>N</i> -(Mesityl)- <i>N'</i> -(1-methylene- <i>meta</i> [6]cyclopara-phenylene)-oxalamide 246.....	159
5.2.24.	Bromo-methylene- <i>meta</i> [6]cycloparaphenylene 247	161
5.2.25.	<i>N</i> -(Methyl)- <i>N'</i> -(1-methylene- <i>meta</i> [6]cycloparaphenylene)-imidazolium bromide 224 162	
5.2.26.	[<i>N</i> -(Methyl)- <i>N'</i> -(1-methylene- <i>meta</i> [6]cyclopara-phenylene)-imidazolium]gold bromide 250.....	163
5.2.27.	Bromination of cyano- <i>meta</i> [6]cyclopara-phenylene 158	164
5.2.28.	Alkynylation of the allyl-bromides 264	165
6.	<i>Zusätzliche Veröffentlichungen</i>	166
7.	<i>Danksagung</i>	168
8.	<i>Abbreviations</i>	<i>a</i>
9.	<i>List of Figures</i>	<i>d</i>
10.	<i>List of Schemes</i>	<i>g</i>
11.	<i>List of Tables</i>	<i>j</i>
12.	<i>References</i>	<i>k</i>

Abstract

In this study, three distinct topics were investigated, not only focusing on the synthesis but also the functionalization and photophysical properties of (*meta*)[*n*]cycloparaphenylenes (*(m)*[*n*]CPPs).

The first section commences with the successful modification of a literature-known synthetic procedure, aimed at the most prominent and extensively investigated derivative of [*n*]CPPs, namely [10]CPP. The crucial steps involved the rapid and efficient assembly of two small building blocks into a macrocyclic precursor through the SUZUKI-MIYAUURA cross-coupling reaction. Subsequent reductive aromatization, utilizing sodium naphthalenide, yielded [10]CPP in satisfactory yields. With [10]CPP readily available, various top-down approaches based on C-H activation were explored to achieve different functionalized [10]CPPs. These approaches encompassed halogenation, borylation, acetoxylation and olefination. Additionally, electro(photo-)catalysis was applied for an acetoxylation reaction and a phenol synthesis. However, all attempts resulted in the reisolation of [10]CPP, indicating that the interplay between aromaticity, ring strain and the low-reactivity of the C-H bond remained unconquered by the chosen methods.

The second part of this study was inspired by the observations made during the synthesis of an extended building block within the synthesis of [10]CPP based on the cyclohexadiene scaffold. During deprotection of a silyl-protected alcohol using tetra-butyl ammonium fluoride, an undesired 1,2-aryl shift occurred. The design of the second project aimed to utilize this undesired side reaction in the final step of the aromatization to design different *meta*-connected macrocyclic compounds. Consequently, an extensive investigation into the influence of different (LEWIS) acids on the migration tendency was conducted. To initiate this investigation, an open-chain model substrate was selected. The use of the model substrate facilitated the examination of migration tendency in an asymmetric protected cyclohexadiene scaffold. Although all selected reagents exhibited selectivity toward the silyl-protected alcohol over the methyl ether protected one, the final treatment of the corresponding macrocyclic precursor resulted in decomposition during the aromatization process using BCl₃ as LEWIS acid.

Considering the *meta*-connectivity and the photophysical characteristics of $m[n]$ CPPs, the third part of this study focused on the synthesis and investigation of the optical properties of different substituted $m[n]$ CPPs. Specifically, three different nitrile- $m[n]$ CPPs ($n = 5, 8, 10$) were synthesized based on the building block approach using tin chloric acid as reducing agent in the final step. Investigation of their luminescent properties revealed a size-independent absorption behavior, while the emission spectra exhibited a bathochromic shift with decreasing ring-size. Additionally, the supramolecular self-assembly of CN- $m[10]$ CPP with fullerene C₆₀ was investigated. Through fluorescence titration, the association constant of this complex was determined to be $6.73 \cdot 10^4 \text{ M}^{-1}$. When compared to the association constant of [10]CPP, the association constant of CN- $m[10]$ CPP was found to be diminished by a factor of 100. This observation is rationalized by the reduced diameter of the $m[10]$ CPP ring caused by an inwards pointing proton, resulting in a slight deviation from the regular circular shape. Notably, the investigation of the CN- $m[10]$ CPP self-assembly with C₆₀ represents the first reported example using the $m[n]$ CPP scaffold for this kind of study. Moreover, the use of CN- $m[6]$ CPP demonstrated the versatility of an aryl-nitrile, enabling successful conversion into six different functional groups. These conversion reactions not only encompassed hydrolysis towards an amide or a carboxylic acid, as well as two different reductive conditions leading to an aldehyde or benzylic amine. Additionally, the successful synthesis of an amidoxime and a 1*H*-tetrazole was achieved. Unfortunately, attempts to form an alky-aryl ketone and synthesize larger heterocycles such as pyridine, tetrazine or triazine were unsuccessful. Nevertheless, UV-vis and emission spectra were measured in DMSO for a total of seven different substituted $m[6]$ CPP derivatives. These measurements revealed only a slight change in the absorption maximum compared to measurements in DCM, as well as an independence of the absorption and emission maxima from the substituent.

The successful conversion of the aryl nitrile unit was further extended to the synthesis of a *N*-heterocyclic carbene (NHC) gold(I)-complex. Initially, a synthetic strategy towards an imidazolium precursor using the (amino-methylene)- $m[6]$ CPP. Unfortunately, this approach only resulted in the successful synthesis of an $m[6]$ CPP-oxalamide, as further reduction towards a ethylene diamine derivative proved to be unfeasible due to the instability of the product. After modifying the

strategy, a successful synthesis strategy towards an imidazolium precursor was developed. Starting from the carboxy-*m*[6]CPP, reduction and bromination yielded the (bromo-methylene)-*m*[6]CPP, which was then combined with 1-methyl imidazole to form an imidazolium bromide. Utilizing a weak-base approach in the NHC synthesis, this precursor was utilized in conjunction with [AuCl(SMe₂)] to form a linear NHC gold(I)-complex, where the *m*[6]CPP acts as a fluorescent wingtip attached to the NHC ligand. Experimental and theoretical investigations have demonstrated that the optical properties of the *m*[6]CPP substituent remain unchanged upon coordination to the gold(I)-center. This can be rationalized by the distribution of the frontier orbitals solely over the fluorophore part and the electronically decoupled NHC gold(I)-core.

Furthermore, preliminary experiments were carried out to incorporate the barrelene scaffold into the CN-*m*[6]CPP. Initial experiments showed the successful bromination on the most strained bonds within the macrocyclic structure and the generation of a cyclohexadiene motif. In the subsequent step, the allyl bromides were converted into acetone protected acetylenes using a SONOGASHIRA-like reaction. Unfortunately, purification using silica column chromatography resulted in the decomposition of the intermediate.

In conclusion, the relatively new class of fluorophores, namely the (*m*)[*n*]CPPs, possess intriguing photophysical properties. A combination of these compounds with diverse types of ligands like NHCs or barrelenes may give rise to entirely unprecedented hybrid materials possessing intriguing attributes for various research areas. These research areas encompass not only synthetic organic chemistry, but also (organo-)metal chemistry, material and life sciences.

Zusammenfassung

In dieser Arbeit wurden drei verschiedene Thematiken untersucht, die sich nicht nur auf die Synthese, sondern auch auf die Funktionalisierung und photophysikalischen Eigenschaften von (*meta*)[*n*]Cycloparaphenylenen ((*m*)[*n*]CPPs) konzentrieren.

Der erste Abschnitt beginnt mit der erfolgreichen Modifizierung eines aus der Literatur bekannten Syntheseverfahrens, das auf das bekannteste und am meisten untersuchte Derivat von [*n*]CPPs, nämlich [10]CPP, abzielt. Die entscheidenden Schritte umfassten den schnellen und effizienten Aufbau von einem makrozyklischen Vorläufer durch die SUZUKI-MIYAUURA Kreuzkupplungsreaktion zweier kleineren Synthesebausteinen. Die anschließende reduktive Aromatisierung unter Verwendung von Natrium Naphthalinid ergab [10]CPP in zufriedenstellender Ausbeute. Da nun [10]CPP verfügbar war, wurden verschiedene Top-Down-Ansätze auf der Grundlage der C-H Aktivierung erforscht, um verschiedene funktionalisierte [10]CPP zu erhalten. Diese Ansätze umfassten Halogenierungsreaktionen, Borylierungen, Acetoxylierung und Olefinierung. Zusätzlich wurde die Elektro(photo-)katalyse für eine Acetoxylierungsreaktion und eine Phenolsynthese eingesetzt. Alle Versuche führten jedoch zur Reisolierung von [10]CPP, was darauf hindeutet, dass das Zusammenspiel zwischen Aromatizität, Ringspannung und der geringen Reaktivität der C-H Bindung mit den gewählten Methoden nicht überwunden werden konnte.

Der zweite Teil dieser Arbeit wurde durch die Beobachtungen inspiriert, die während der Synthese eines erweiterten Synthesebausteins im Rahmen der [10]CPP Synthese auf der Grundlage des Cyclohexadiengerüsts gemacht wurden. Bei der Entschützung eines silylgeschützten Alkohols mit Tetra-Butylammoniumfluorid kam es zu einer unerwünschten 1,2-Arylverschiebung. Das Konzept des zweiten Projekts zielte darauf ab, diese unerwünschte Nebenreaktion im letzten Schritt der Aromatisierung zu nutzen, um verschiedene *meta*-verknüpfte makrozyklische Verbindungen zu erhalten. Daher wurde eine umfassende Untersuchung des Einflusses verschiedener (LEWIS-)Säuren auf die Migrationstendenz durchgeführt. Zu Beginn dieser Untersuchung wurde ein offenkettiges Modellsubstrat ausgewählt. Die Verwendung des Modellsubstrats

erleichterte die Untersuchung der Migrationstendenz in einem asymmetrischen geschützten Cyclohexadiengerüst. Obwohl alle ausgewählten Reagenzien eine Selektivität für den silylgeschützten Alkohol gegenüber dem methylethergeschützten Alkohol aufwiesen, führte die abschließende Behandlung des entsprechenden makrozyklischen Vorläufers zu einer Zersetzung während des Aromatisierungsprozesses mit BCl_3 als LEWIS-Säure.

In Anbetracht der *meta*-Konnektivität und der photophysikalischen Eigenschaften von $m[n]$ CPPs konzentrierte sich der dritte Teil dieser Studie auf die Synthese und Untersuchung der optischen Eigenschaften verschiedener substituierter $m[n]$ CPPs. Konkret wurden drei verschiedene Nitril- $m[n]$ CPPs ($n = 5, 8, 10$) nach dem Bausteinprinzip synthetisiert, wobei im letzten Schritt Zinnchlorsäure als Reduktionsmittel eingesetzt wurde. Die Untersuchung der Lumineszenzeigenschaften der verschiedenen CN- $m[n]$ CPPs zeigte ein größenunabhängiges Absorptionsverhalten, während die Emissionsspektren eine bathochrome Verschiebung mit abnehmender Ringgröße aufwiesen. Außerdem wurde die supramolekulare Selbstanordnung von CN- $m[10]$ CPP mit Fulleren C_{60} untersucht. Durch Fluoreszenztitration wurde die Assoziationskonstante dieses Komplexes mit $6.73 \cdot 10^4 \text{ M}^{-1}$ bestimmt. Verglichen mit der Assoziationskonstante des $[10]$ CPPs wurde festgestellt, dass die Assoziationskonstante von CN- $m[10]$ CPP um den Faktor 100 niedriger ist. Diese Beobachtung lässt sich durch den verringerten Durchmesser des $m[10]$ CPP-Rings erklären, der durch ein nach innen orientiertes Proton verursacht wird und der daraus resultierenden Abweichung von der regelmäßigen Kreisform. Die Untersuchung der CN- $m[10]$ CPP Selbstanordnung mit C_{60} ist das erste berichtete Beispiel für die Verwendung des $m[n]$ CPP-Gerüsts für diese Art von Untersuchung. Darüber hinaus zeigte die Verwendung von CN- $m[6]$ CPP die Vielseitigkeit eines Arylnitrils, das erfolgreich in sechs verschiedene funktionelle Gruppen umgewandelt werden konnte. Diese Transformationen umfassten nicht nur die Hydrolyse zu einem Amid oder einer Carbonsäure, sondern auch zwei verschiedene Reduktionsreaktionen, die zu einem Aldehyd oder einem benzyliischen Amin führten. Außerdem gelang die erfolgreiche Synthese eines Amidoxims und eines 1*H*-Tetrazols. Leider waren die Versuche, ein Alkyl-Aryl Keton und größere Heterocyclen wie Pyridin, Tetrazin oder Triazin zu synthetisieren, erfolglos. Dennoch wurden für insgesamt sieben

verschiedene substituierte $m[6]$ CPP-Derivate UV/Vis und Emissionsspektren in DMSO gemessen. Diese Messungen weisen nur eine geringe Änderung des Absorptionsmaximums im Vergleich zu Messungen in DCM sowie eine Unabhängigkeit der Absorptions- und Emissionsmaxima vom Substituenten auf.

Die erfolgreiche Umsetzung der Arylnitrileinheit wurde auf die Synthese eines *N*-heterocyclischen Carben (NHC) Gold(I)-Komplexes ausgedehnt. Zunächst wurde eine Synthesestrategie für einen Imidazolium-Vorläufer unter der Verwendung von (Amino-Methylen)- $m[6]$ CPP verfolgt. Leider führte dieser Ansatz nur zur erfolgreichen Synthese eines $m[6]$ CPP-Oxalamids, da sich eine weitere Reduktion zu einem Ethylendiaminderivat aufgrund der Instabilität des Produkts als nicht durchführbar erwies. Nach Modifizierung der Strategie wurde eine erfolgreiche Synthese für einen Imidazolium-Vorläufer entwickelt. Ausgehend vom Carboxy- $m[6]$ CPP wurde durch Reduktion und Bromierung das (Bromo-Methylen)- $m[6]$ CPP erhalten, welches dann mit 1-Methylimidazol zu einem Imidazoliumbromid kombiniert wurde. Bei der NHC-Synthese wurde dieser Vorläufer in Verbindung mit $[AuCl(SMe_2)]$ verwendet, um einen linearen NHC Gold(I)-Komplex zu bilden, bei dem das $m[6]$ CPP als fluoreszierender Substituent an den NHC-Liganden gebunden ist. Experimentelle und theoretische Untersuchungen haben gezeigt, dass die optischen Eigenschaften des $m[6]$ CPP-Substituenten bei der Koordination an das Gold(I)-Zentrum unverändert bleiben. Dies lässt sich durch die Verteilung der Grenzorbitale ausschließlich über den Fluorophorteil und den elektronisch entkoppelten NHC Gold(I)-Kern erklären.

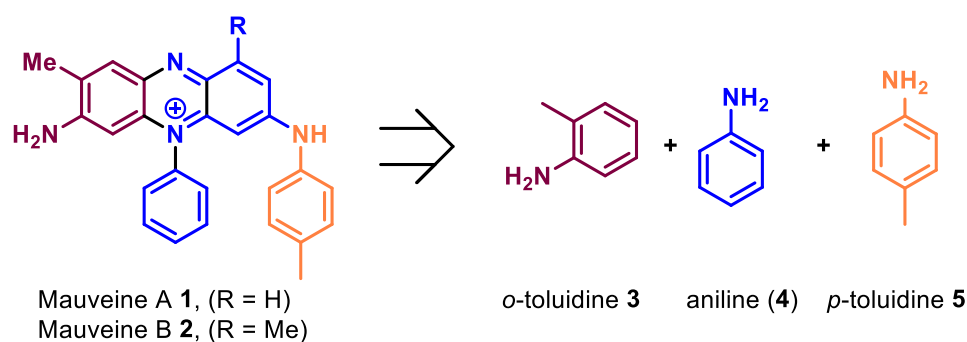
Darüber hinaus wurden erste Versuche durchgeführt, um ein Barrelengerüst in das CN- $m[6]$ CPP einzubauen. Erste Experimente zeigten die erfolgreiche Bromierung an den am stärksten gespannten Bindungen innerhalb der makrozyklischen Struktur und die Erzeugung eines Cyclohexadienmotivs. Im anschließenden Schritt wurden die erhaltenen Allylbromide durch eine SONOGASHIRA-ähnliche Reaktion in geschützte Acetylene umgewandelt. Leider führte die Aufreinigung mittels Kieselgelsäulenchromatographie zur Zersetzung des Zwischenprodukts.

Zusammenfassend lässt sich sagen, dass die relativ neue Klasse von Fluorophoren, die (*m*)[*n*]CPPs, herausragende photophysikalische Eigenschaften besitzen. Eine Kombination dieser Fluorophore mit verschiedenen Arten von

Liganden wie NHCs oder Barrelenen kann zu völlig neuartigen Hybridmaterialien führen, welche attraktive Eigenschaften für verschiedene Forschungsbereiche aufweisen. Diese Forschungsbereiche umfassen nicht nur die synthetische organische Chemie, sondern auch die (Organo-)Metallchemie, Material- und Biowissenschaften.

1. Introduction

As it is often the case in the field of chemistry, the origin of small fluorescent molecules traces back to a fortuitous event – the accidental discovery of mauveine (1 and 2) by PERKIN in 1865, who used the toluidine derivatives 3 and 5 and aniline (4) as starting material (Scheme 1).¹



Scheme 1. Chemical structure of mauveine A 1 and B 2, which consist of o-toluidine 3, aniline (4) and p-toluidine 5.

While attempting to synthesize quinine 6 (Figure 1), a natural product used in medicinal and organic chemistry, PERKIN stumbled upon mauveine 1 and 2, one of the first “aniline dyes”. Thus, his discovery is widely referred to as the birth of modern chemical industry and the subsequent development of key players in classic fluorophores.²

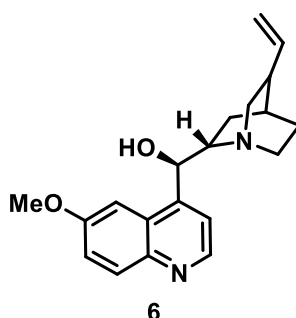


Figure 1. Chemical structure of quinine 6.

It happened that quinine 6 had given rise to the term fluorescence a few years earlier. In 1845, HERSCHEL documented the first instance of visible light being emitted from an aqueous solution of this molecule.³ STOKES explained that this phenomenon occurred as a result of absorption followed by emission. Thus, he named this process fluorescence.⁴ Moreover, quinine 6 and its inherent fluorescence played a crucial role in the development of the first fluorometer during World War II, which was later commercialized in the 1950s and is still used today.⁵

1.1. Physical Background

The most straightforward approach to understand the various mechanisms involved in how a fluorescent molecule assimilates light is to use a JABLONSKI diagram (Figure 2, left).⁶

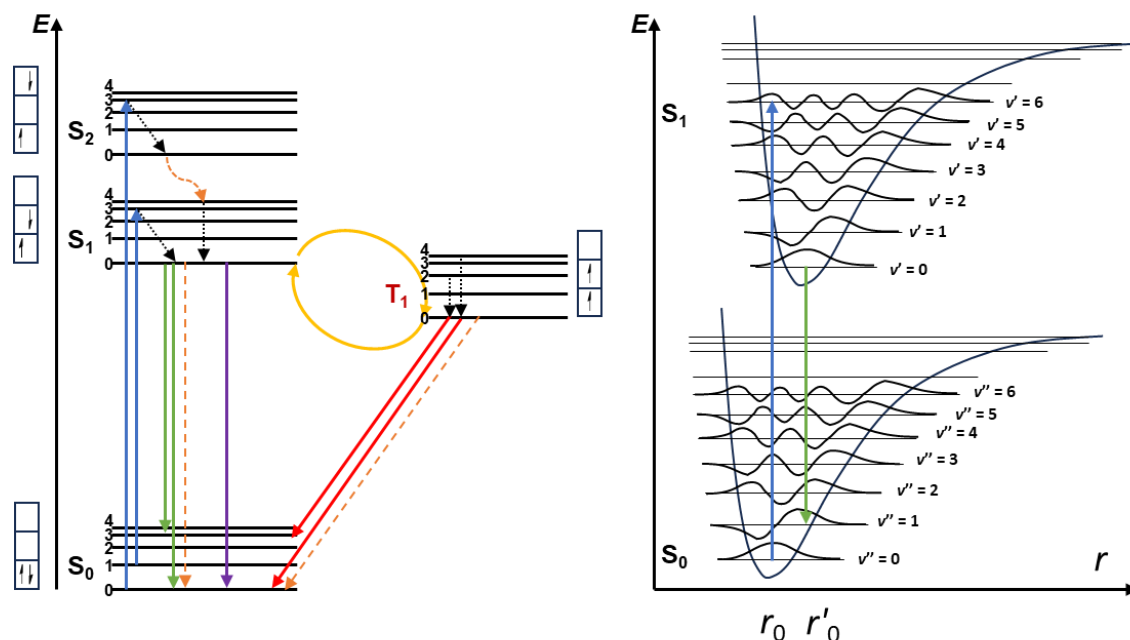


Figure 2. JABLONSKI diagram of the various comprehend mechanisms at play when a fluorescent molecule assimilates light (left). Absorption (blue arrows), fluorescence (green arrows), phosphorescence (red), internal conversion (dashed orange arrows), vibrational relaxation (dashed black arrows), (reverse) intersystem crossing (yellow arrows), quenching (purple arrow). Illustrative energy diagram of the FRANCK-CONDON principle (right).

Upon photoexcitation of an organic chromophore an electron is transferred from its electronic ground state (S_0) to higher electronic states ($S_1, S_2, S_3 \dots S_n$). Maintaining the spin orientation, an excited state with the same multiplicity is formed. According to KASHA's rule,⁷ these excited states must undergo a transition to the lowest vibrational level in S_1 through vibrational relaxation (within one spin state). If two different spin states are involved, internal conversion (IC) occurs by retaining the multiplicity. Intersystem crossing (ISC) describes the same process but while changing the multiplicity. All three processes are non-radiative and can compete with radiative processes. For the process of the S_1 to S_0 transition, various paths are possible. If an electron emits a photon while relaxing back to S_0 , fluorescence occurs. The visible color is determined by the energy of that photon. Following PLANCK's law, the wavelength of the emitted light decreases as the energy of the photon increases, resulting in a larger distance between the two states (Figure 3).⁸

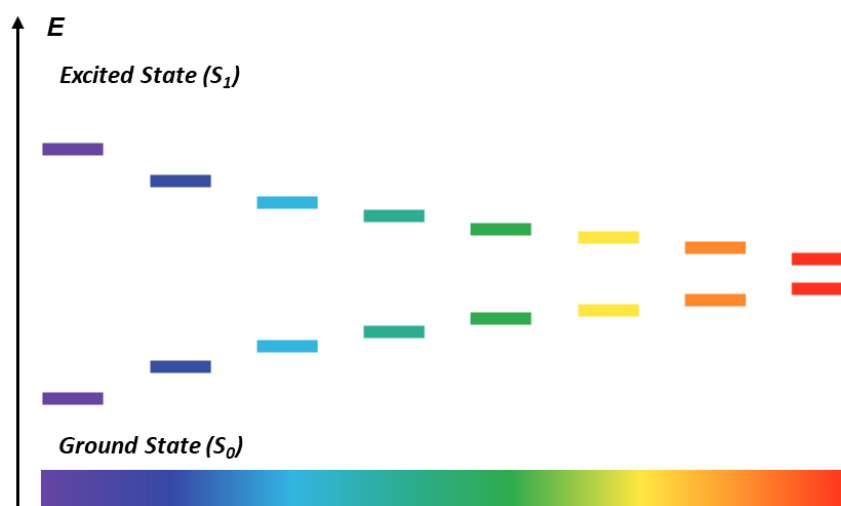


Figure 3. Corresponding emission color dependent on the energy gap between the excited state (S_1) and ground state (S_0).

In contrast to fluorescence, phosphorescence arises when an electron is transferred from S_1 to the first triplet excited state (T_1) through intersystem crossing. The lifetime of a triplet exciton can extend up to 10 s due to forbidden spin relaxation, making it approximately ten times slower than IC.⁹ However, if the energy difference between T_1 and S_1 is less than 0.1 eV, reversed intersystem crossing (rISC) and high emissive rates ($S_1 \rightarrow S_0$) of around 10^6 s^{-1} outperform non-radiative relaxation processes, leading to thermally activated delayed fluorescence (TADF) (Figure 2).¹⁰

Competing with the radiative processes are non-radiative processes such as collisional quenching or resonance energy transfer (RET).¹¹ One of the most widely utilized mechanisms in biomedical and clinical assays based on RET,¹² was quantified by FÖRSTER in 1948, and therefore was named FÖRSTER resonance energy transfer (FRET).¹³ FRET is a non-radiative energy transfer wherein an excited state donor conveys energy to an acceptor through dipole-dipole coupling.¹⁴ Hence, the emission of the acceptor is enhanced, while the luminescence of the donor is repressed. The efficiency of this process is determined by the inverse sixth power of the intramolecular separation.

While the FÖRSTER mechanism takes place when the singlet donor and the singlet acceptor are in proximity, typically within a range of 1 – 10 nm, other processes are possible involving different electronic state at distances less than 1 nm.^{11,15} Usually,

the energy transfer involving triplet states can be described by the DEXTER mechanism (Figure 4).^{16,17}

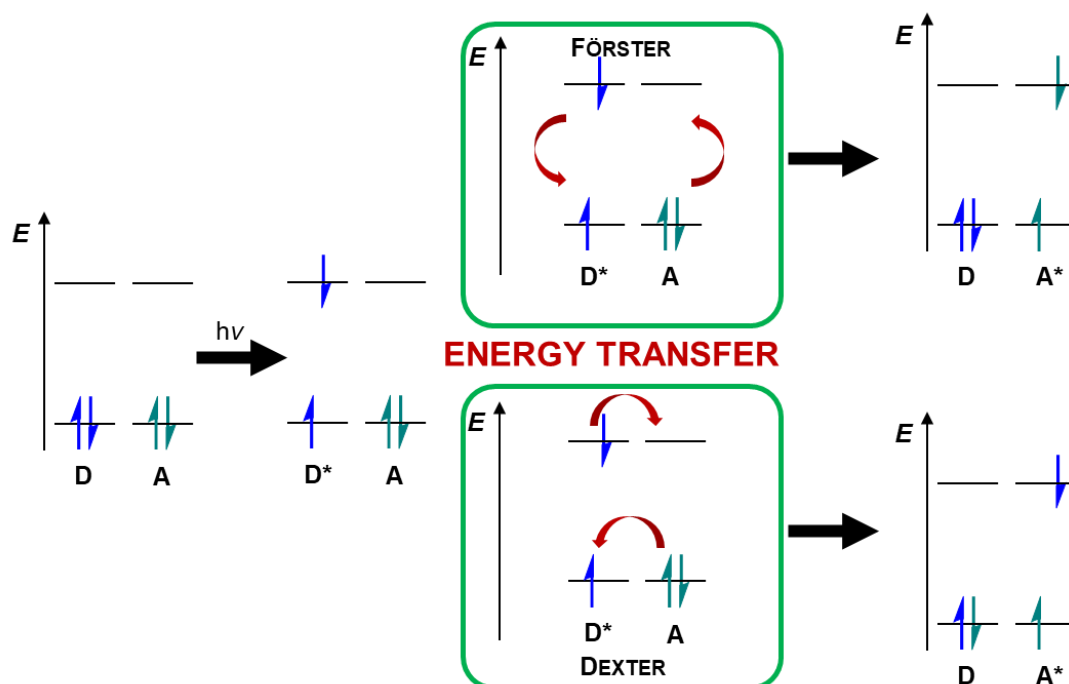


Figure 4. Schematic representation of the FÖRSTER and DEXTER energy transfer mechanisms upon photoexcitation of an electronic ground state donor.

Upon providing a brief explanation of the fundamental physical basis of fluorophores and their emissive pathways, the following part centers on various categories of fluorophores with a specific emphasis on small organic molecules.

1.2. Classes of Fluorophores

In 2022, CAVAZOS-ELIZONDO et. al conducted a meta-analysis on the existing data concerning fluorescent labels.¹⁸ These labels can be categorized into the three major groups: proteins,^{19–21} inorganic nanoparticles,^{22–25} and organic dyes, which will be discussed in the following section.

The majority of fluorescent labels are composed of fluorescent organic dyes, many of which were created as a result of PERKIN's synthesis of mauveine A **1** and B **2**.¹ The fundamental frameworks of the most frequently applied organic dye classes are presented in Figure 5.²⁶

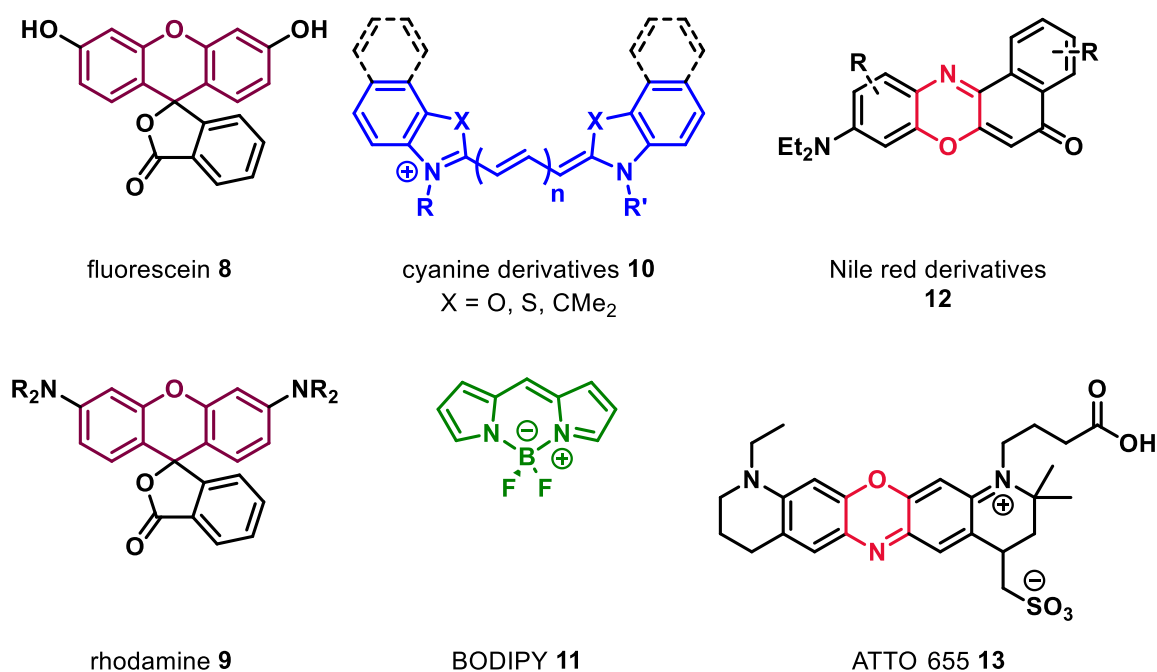


Figure 5. Core frameworks of the four organic dye classes that are most frequently utilized. (oxazole: deep red, fluorescein **8** and rhodamine **9**; cyanine **10**: blue; BODIPY **11**: green; oxazines: red, Nile red **12** and ATTO 655 **13**).

Using conventional organic synthetic techniques, a vast array of characteristics of distinct fluorophores can be synthesized,²⁷ encompassing the entire electromagnetic spectrum ranging from the ultraviolet region to the vicinity of the near-infra-red range.^{6,28}

Although, there exist numerous possibilities for adjusting the characteristics of the desired small-molecule fluorophore, challenges such as photobleaching²⁹ or specificity in biomolecules persist.³⁰ Furthermore, the necessity for extensive synthetic work for each molecule hinders the availability and distribution of chemical dyes, posing additional obstacles to overcome in the future.⁶

An attractive category of novel fluorophores, possessing size-dependent properties and showing promise for applications in both materials and life sciences, focuses on cycloparaphenylenes (CPPs).

1.3. [n]Cycloparaphenylenes

Nowadays, there is extensive research being conducted on carbon nanomaterials such as carbon nanotubes (CNTs) and their potential applications in various research areas.^{31–36} However, there are major drawbacks regarding a selective

synthesis, solubility, and biocompatibility of these carbon nanomaterials, which is why their application is still in its infancy.^{37,38} The unique properties of CNTs are directly linked to the variation in the cylindrical core structure of a graphene sheet.³⁹ Depending on how the graphene sheet is hypothetically wrapped, different types of CNTs are formed, each possessing their own distinct electronic and optical features (Figure 6).

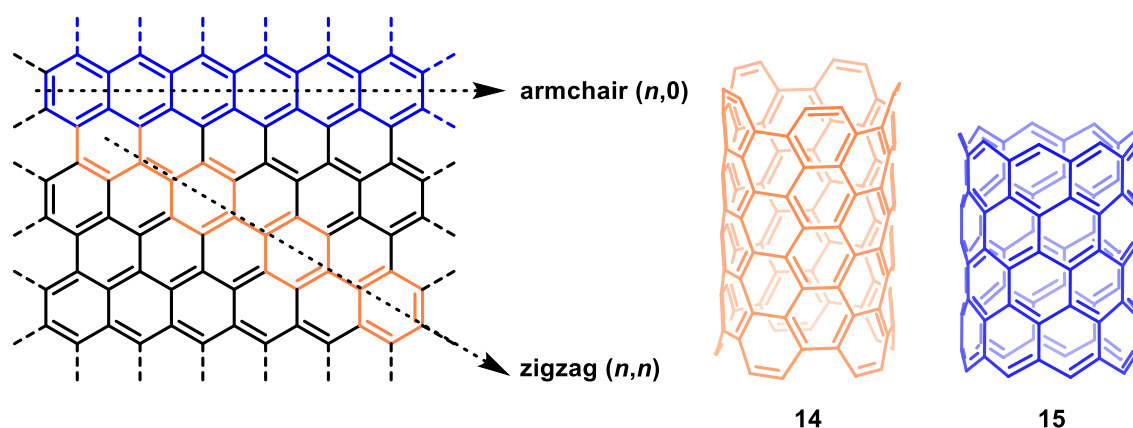
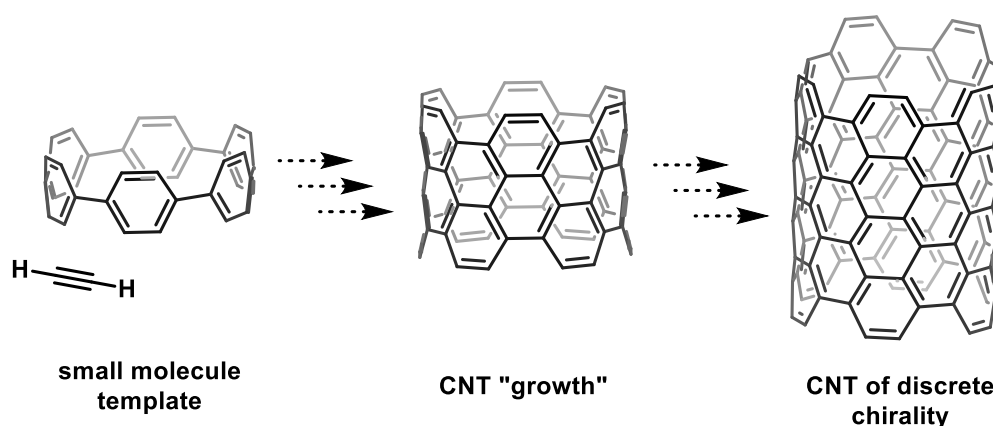


Figure 6. Structure of a graphene sheet and corresponding armchair **14** and zigzag **15** carbon nanotubes.

Therefore, the development of novel synthetic approaches for CNTs is unavoidable and has been a long-standing aspiration in the field of synthetic organic chemistry. One bottom-up approach envisions CNTs as a polymeric structure comprising of small macrocyclic fragments, which preserve the essential characteristics of chirality and diameter (Scheme 2).^{40,41}



Scheme 2. Schematic representation of the idea of a bottom-up synthesis of CNTs from a small molecule template (adapted from literature⁴⁰).

Cycloparaphenylenes ($[n]$ CPPs) are the smallest individual section of an armchair CNT. They consist of n phenylenes that are arranged in a circular manner and

connected in a 1,4-fashion. As a result, these strained macrocyclic structures possess a π -system, that is radial in nature. This system has a convex surface with a reduced electron density and a concave surface with an enriched electron density (Figure 7).⁴¹

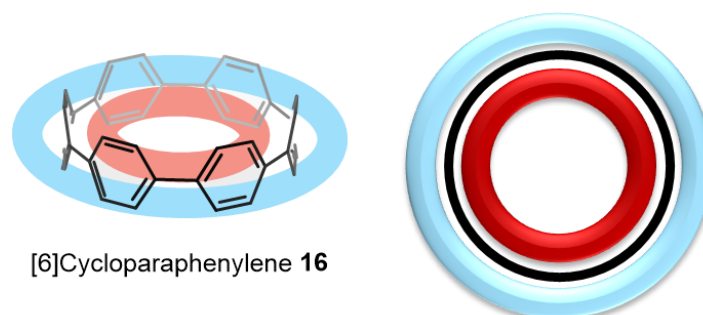
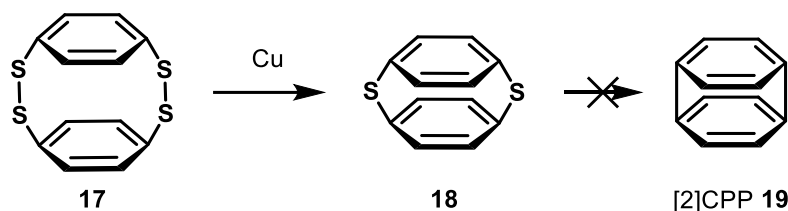


Figure 7. Schematic representation of the electron-poor (blue) and -rich (red) surfaces of [6]CPP **16**.

Initial efforts to pave the synthetic way towards CPPs addressed [2]CPP **19** and were reported in 1934 by PAREKH and GUHA, who successfully synthesized the macrocyclic disulfide **17**. However, their attempt to subsequently desulfurize this macrocycle using elemental copper, only led to a partially desulfurized compound **18** and not to the desired [2]CPP **19** (Scheme 3).⁴²

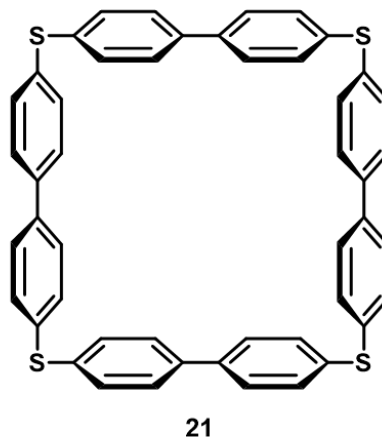
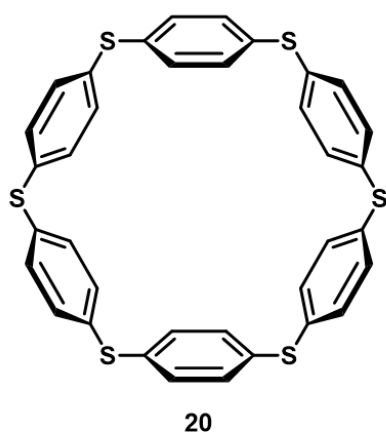


Scheme 3. Synthetic attempt towards [2]CPP by PAREKH and GUHA in 1934 through desulfurization.⁴²

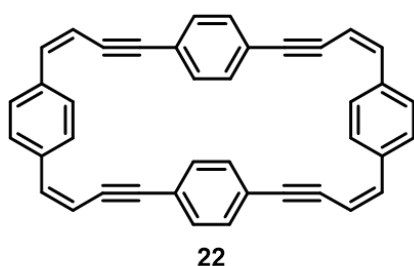
In 1993, the group of VÖGTLE resumed the utilization of their synthetic approach.⁴³ In their landmark paper, VÖGTLE's group presented various methodologies for the synthesis of macrocyclic *para*-phenylenes, commencing with the macrocyclic *oligo*-phenylsulfides **20** and **21**. Another attempt was influenced by the research of MIYAHARA et al.⁴⁴, in which a DIELS-ALDER reaction⁴⁵ was used to create 1,4-connected phenylenes starting from **22**. This approach did not yield satisfactory results; therefore, the notion arose to substitute several phenyl units with conformationally flexible cyclohexane units (as used in molecule **23**). Nevertheless, applying various synthetic approaches based on this functional building block failed to produce the desired compounds. Figure 8 emphasizes the

elucidation of compounds that were subject of investigation by the group of VÖGTLE with the aim of synthesizing CPPs.

A) Strategy via Pyrolysis



B) Strategy via DIELS-ALDER Synthesis



C) Strategy via Aromatization of Cyclohexane Building Blocks

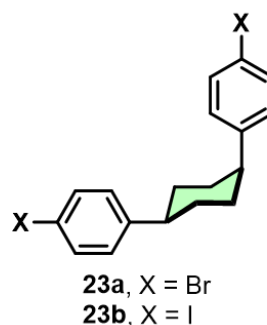
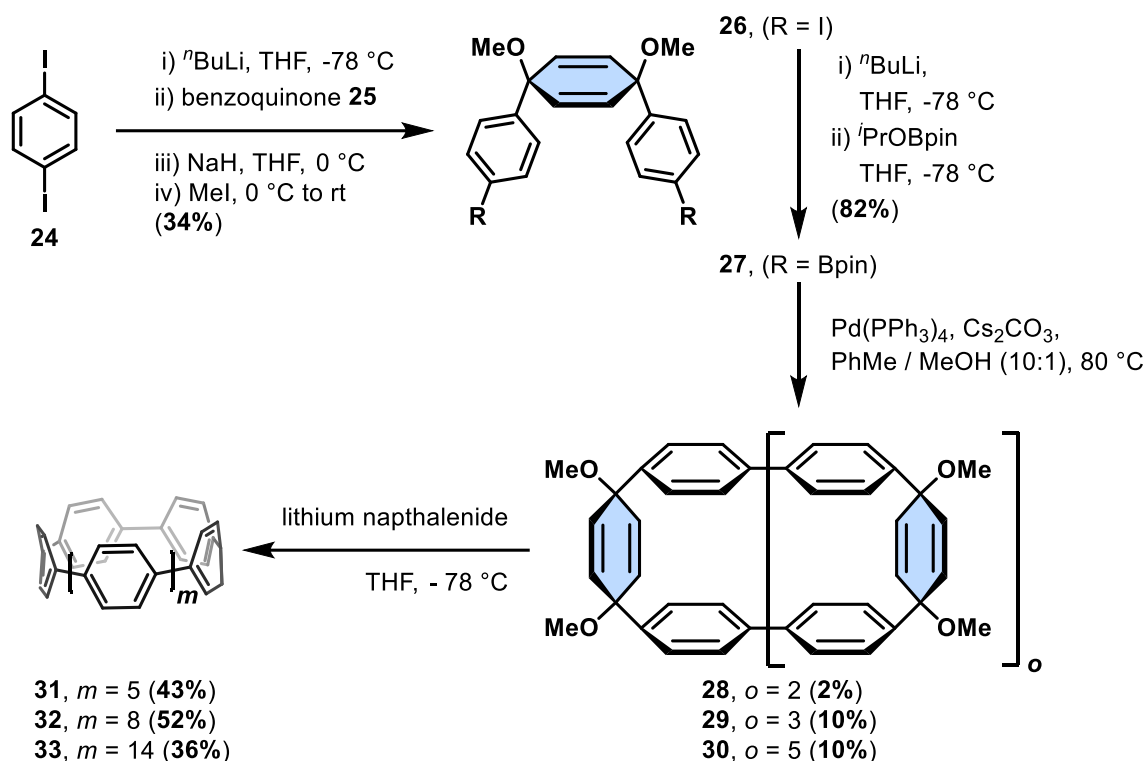


Figure 8. Different strategies by the group of VÖGTLE towards the synthesis of $[n]$ cycloparaphenylenes

Despite the lack of success in these initial studies, the overarching concept of applying strain reduced macrocyclic precursors has become a prevalent strategy in the realm of CPPs.^{46–48} After the initial contributions from the groups of PAREKH, GUHA, and VÖGTLE, it took more than 75 years to develop a successful method for synthesizing CPPs. Based on 1,4-*syn*-dimethoxy-2,5-cyclohexadiene units as masked structural motifs,⁴⁹ BERTOZZI's group accomplished the synthesis of [9], [12], and [18]CPP (**31** - **33**) in 2008 (Scheme 4).⁵⁰



Scheme 4. Synthesis approach of BERTOZZI's group in 2008 towards the first reported $[n]$ CPPs ($n = 9, 12, 18$).

To initiate their investigation, a solution of *para*-benzoquinone **25** was combined with mono-lithiated *para*-diiodobenzene (**24**) in a *syn*-selective fashion, resulting in the formation of building block **26**. Subsequently this building block underwent borylation towards compound **27** followed by a SUZUKI cross-coupling reaction with diiodide **26**, obtaining the macrocyclic precursors of varying ring sizes (**28** – **30**). Within the last step, these precursors were treated with lithium naphthalenide, leading to reductive elimination and the formation of the three distinct $[n]$ CPPs **31** – **33**. The major limitation of this synthetic approach is the non-selective formation of macrocycles during the crucial step, resulting in diminished yields. However, following this initial breakthrough in the synthesis of CPPs formed a milestone for groups focusing on the synthesis of these strained macrocyclic molecules. Following this, the groups of JASTI^{51–57}, ITAMI^{46,58,59} and YAMAGO^{60,61} have significantly shaped the realm of CPPs with their contributions. Shortly after JASTI and BERTOZZI accomplished the initial non-selective synthesis of [9], [12], and [18]CPP, ITAMI's group presented a selective approach for the synthesis of [12]CPP **32** in 2009.⁵⁹ This approach was based on VÖGTLE's suggested building block **23**, and used oxidative conditions in the final step for the aromatization. In 2010, YAMAGO's group published a third synthetic approach to synthesize CPPs.⁶⁰ At a

first glance, this strategy bears resemblance of the utilization of macrocyclic sulfides in the initial attempts made by PAREKH and GUHA. However, instead of applying sulfur-bridged macrocycles, YAMAGO and co-workers applied platinum-coordinated macrocycles, which undergo reductive elimination for aromatization. The utilization of this approach facilitated the first successful synthesis of [8]CPP. By well-chosen combination of terphenyl with biphenyl macrocyclic precursors, YAMAGO's group was also able to construct a diverse library of cycloparaphenylenes, covering ring sizes ranging from 8 to 12 phenylenes.⁶⁰ More recently, in 2020, OSAKADA's group further developed the synthesis approach pioneered by YAMAGO's group, replacing the platinum complexes with gold complexes.⁶² Although, this approach applies the same building blocks, the altered coordination geometry permits the formation of CPPs with different ring sizes when compared to the strategy of YAMAGO's group.^{62,63} A summary of the different synthetic approaches toward unsubstituted [n]CPPs is depicted in Figure 9.

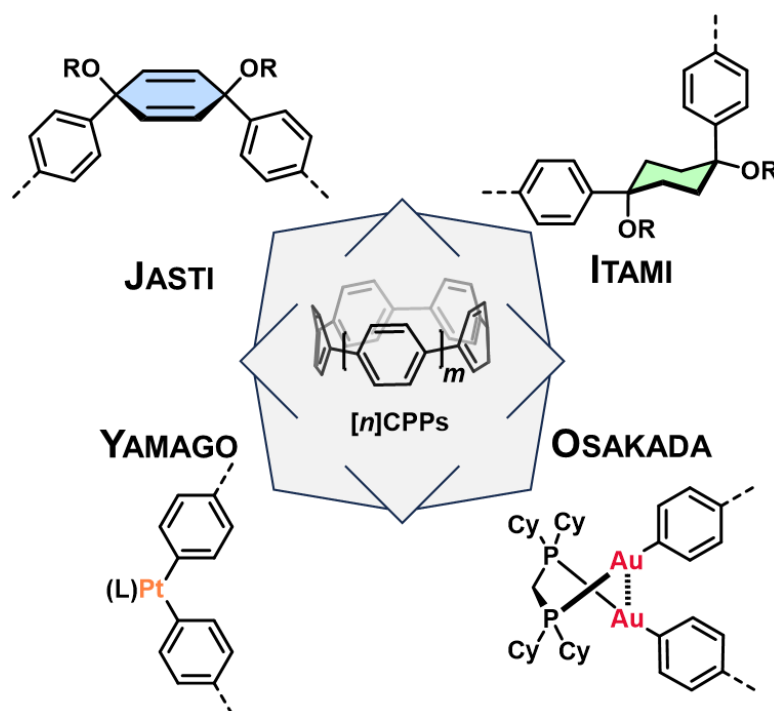


Figure 9. Schematic representation of the different synthetic strategies towards [n]CPPs reported by the groups of JASTI, ITAMI, YAMAGO, and OSAKADA.

Evaluation of the various synthetic approaches applied in the synthesis of [n]CPPs reveals their respective advantages and disadvantages, which depend on the specific target molecule. The utilization of metal complexes, while offering conciseness, suffers from the limitation of requiring a hyperstoichiometric usage of

precious metals and a restriction in the achievable ring size. On the other hand, although the other two methods are more demanding in terms of synthetic efforts, they do afford greater flexibility in determining the desired ring size of the $[n]$ CPP. When comparing the strategies applied by JASTI and ITAMI, it is observed that the utilization of a more flexible cyclohexane linker, in conjunction with oxidative aromatization, generally leads to lower yields. However, the presence of a more rigid cyclohexadiene moiety renders it more reactive, thereby increasing the likelihood of undesired side reactions.⁶⁴

The enhancement of the mentioned synthetic routes resulted in the development of a compilation of strategic syntheses, addressing the challenges of selectivity,^{51,54,56,61,65–67} efficiency,^{68–70} scalability,^{53,69–71} and the provision of milder reaction conditions for tolerance of functional groups.^{57,72–74} Particularly, the combination of three key building blocks, enables considerable adaptability and modularity in subsequent syntheses (Figure 10).^{51,56,70}

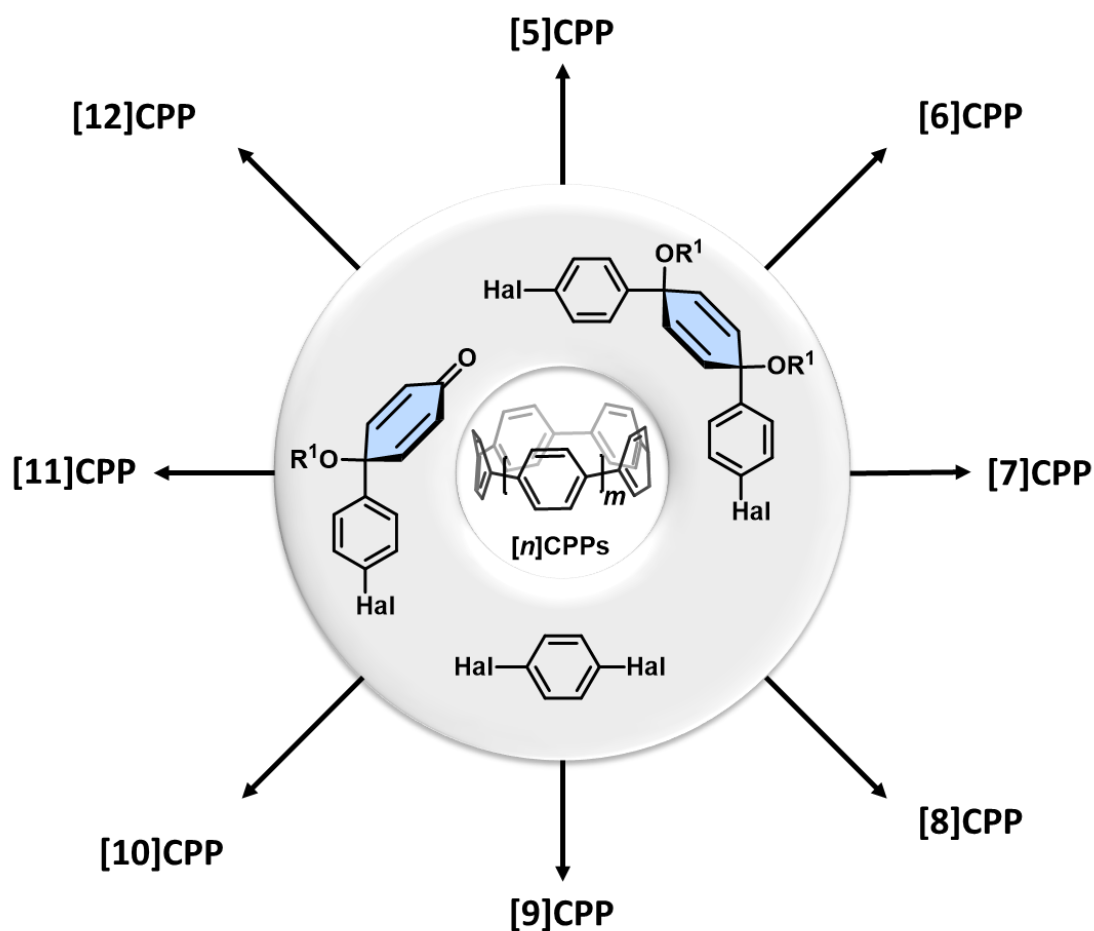


Figure 10. Modular synthesis approach towards different sized $[n]$ CPPs for $n = 5 - 12$ based on the three building blocks.

Using these building blocks allowed the selective synthesis of different $[n]$ CPPs as shown in Figure 10. Altering the protecting group at the cyclohexadiene moiety further enhanced the accessibility of a larger five-membered building block. Furthermore, the incorporation of the triethyl silyl protecting group, implemented by YAMAGO's group in the $[n]$ CPP synthesis, in general permitted the utilization of milder conditions during the reductive aromatization in the final step.^{75,76} Later, the group of STĘPIEŃ was able to apply these relatively mild conditions for the methoxy ether protected cyclohexadienes as well.⁷⁷

With the accessibility of different sized $[n]$ CPPs ($n = 5 - 12$), an analysis of their photophysical properties could be conducted, revealing a structure/property relationship regarding the optoelectronic properties.⁷⁸ It is noteworthy that $[n]$ CPPs exhibit an opposite trend in these properties compared to their linear analogues, the *oligo*-paraphenylenes ($[n]$ OPPs).⁶⁵ While the energy gap between the highest occupied molecular orbital (HOMO) and the lowest unoccupied molecular orbital (LUMO) in OPPs decreases with an increasing number of phenyl units until reaching a saturation point, $[n]$ CPPs display the opposite behavior, namely an increasing HOMO – LUMO gap (Figure 11).

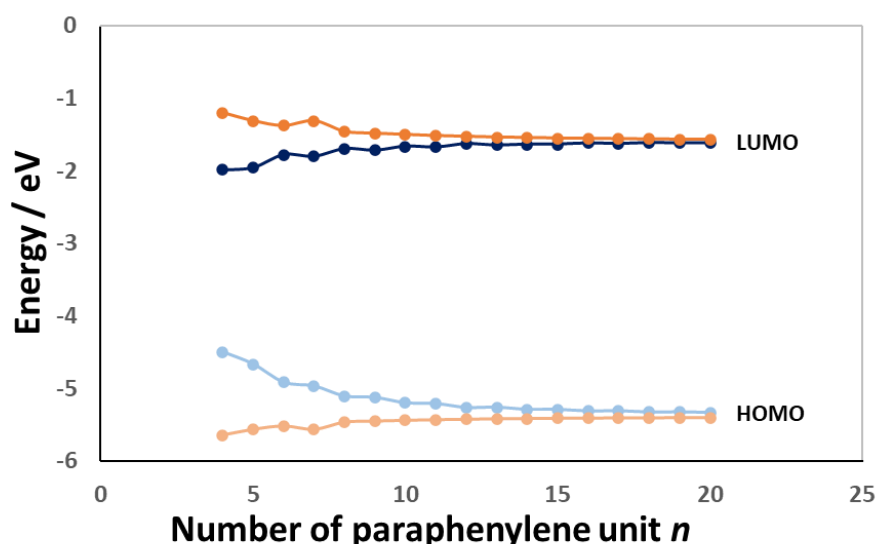


Figure 11. Schematic representation of the HOMO and LUMO energies of *oligo*-paraphenylenes (orange) and cycloparaphenylenes (blue) using the theoretically calculated values of YAMAGO's group at the B3LYP/6-31G* level of theory.⁶⁵

The resemblance between larger and thus less strained $[n]$ CPPs and their $[n]$ OPP analogues can be justified by the decreased bending and ring strain effects on the structure.⁷⁹

Considering that the emission of light by a chromophore is contingent upon the HOMO – LUMO gap, it is expected that the absorption maximum of $[n]$ CPPs will exhibit a hypsochromic shift as the number of phenyl units increases. Surprisingly, the experimental data demonstrate an independence in the absorption maximum.^{50,56,65,79,80} YAMAGO and co-workers hypothesized, applying time-dependent density functional theory (TD-DFT) at the B3LYP/6-31G(d) level of theory, that the centrosymmetry of $[n]$ CPPs provides a plausible explanation for this phenomenon.⁷⁹ Since the HOMO - LUMO transition violates LAPORTE's rule,⁸¹ the observed absorption maximum stems from the HOMO – LUMO+1/LUMO+2, or HOMO-1/HOMO-2 – LUMO transitions. These transitions have a similar energy gap, and therefore result in a size independent absorption maximum at around 340 nm.⁶⁵ In contrast to the absorption maximum, the emission of $[n]$ CPPs displays a size-dependent behavior, with a decreasing STOKES' shift for increasing ring sizes (Figure 12).^{50,56,65,79,80}

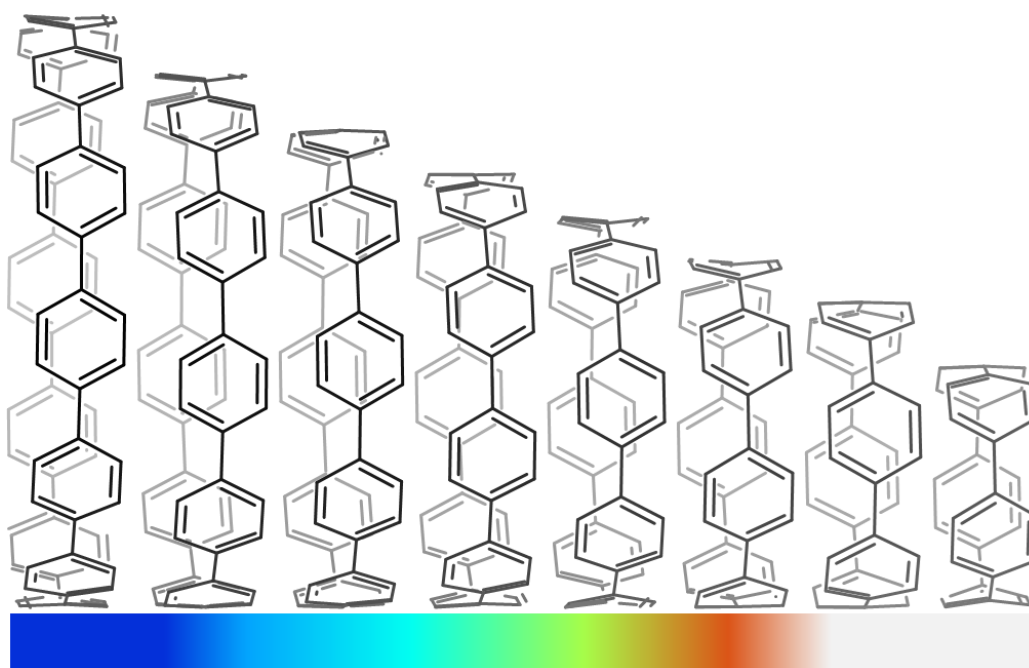


Figure 12. Schematic representation of the size-dependent emission represented by the color of the maximum wavelength of $[n]$ CPPs ($n = 5 - 12$).

The disparity in STOKES' shifts can be explained by an emission from different excited states, which partake in this process. In larger $[n]$ CPPs, the JAHN-TELLER distorted excited states S_2 and S_3 result in two visible emission maxima. In smaller $[n]$ CPPs, larger vibrational amplitudes lead to a higher probability of a non-radiative

decay to the S_1 , resulting in the symmetry forbidden transition from S_1 to S_0 and consequently, a lower intensity of emission.^{65,82}

These captivating properties of $[n]$ CPPs have ignited interest in this distinctive class of small organic fluorophores and have prompted inquiries into the possibility of further customization. Once again, $[n]$ OPPs can serve as an extensively studied model system, despite exhibiting slightly different photophysical properties. It has been demonstrated that not only the number of phenyl units impacts the electronic structure and the photophysical properties, but substitution can also serve as a useful tool.^{83–88} The substitution of $[n]$ CPPs is achieved through both top-down and bottom-up approaches (Figure 13), resulting in a vast array of novel functionalized nanocarbon-based materials.

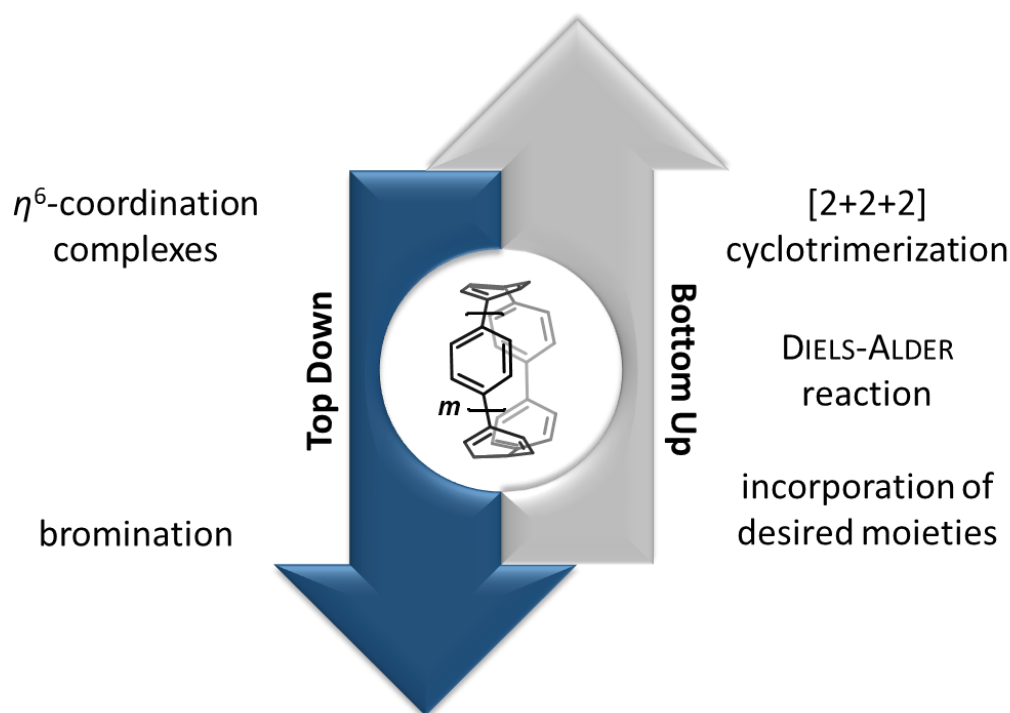
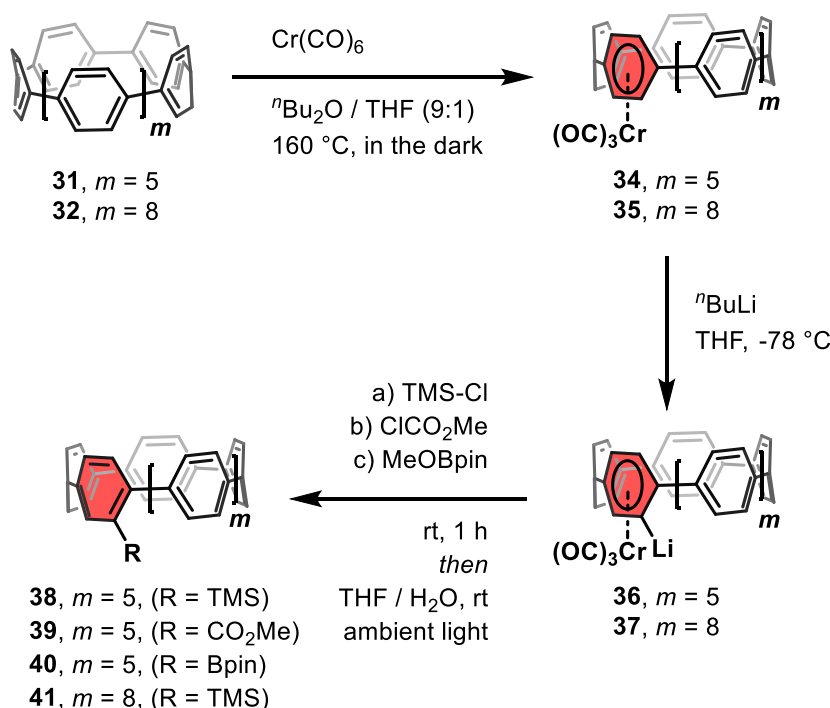


Figure 13. General representation of the top-down and bottom-up approaches towards functionalized $[n]$ CPPs.

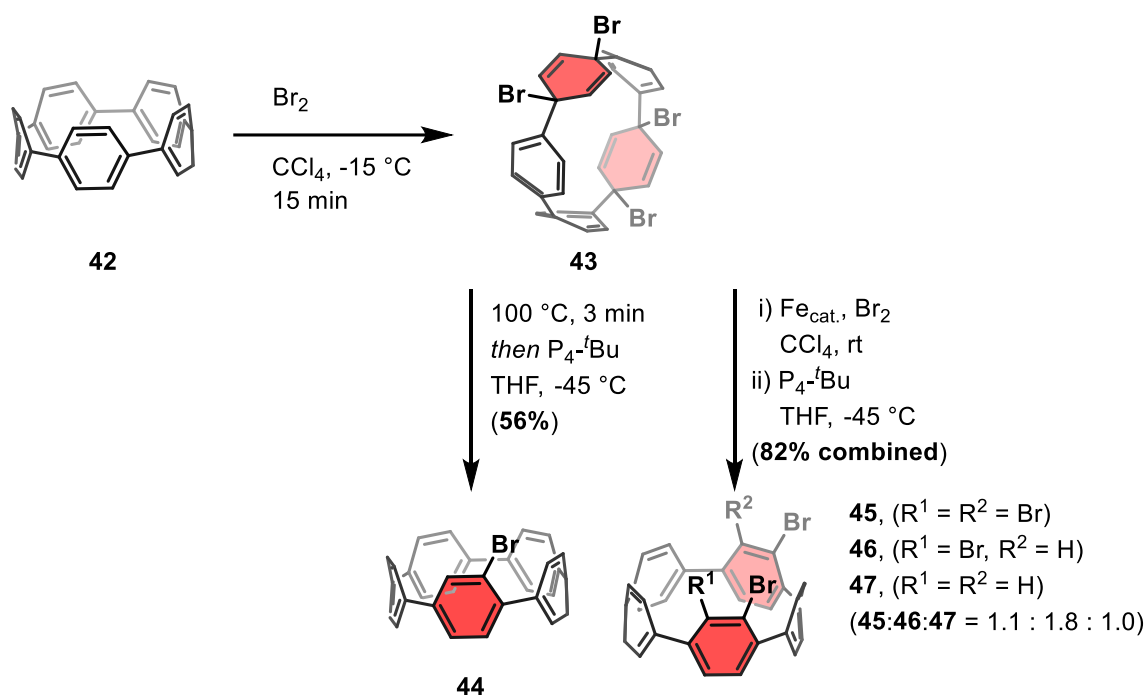
Top-down approaches do utilize the molecule of interest as starting material. This post-functionalization offers significant flexibility as it eliminates the need for developing a new synthetic approach for each derivative. However, despite its attractiveness, only a few synthetic approaches have been published in this regard. These approaches have faced challenges related to size limitations of the $[n]$ CPP and/or the selectivity of the substitution.

In 2015, ITAMI's group reported preliminary efforts in this direction. They activated [9] and [12]CPP by forming η^6 -complexes with the group VI elements chromium, molybdenum, and tungsten.⁸⁹ However, only the chromium complex remained stable under ambient conditions. Consequently, this complex proved to be efficient for subsequent functionalization by using *n*-butyl lithium (*n*BuLi) as a strong base and various electrophiles such as trimethylsilyl-chloride (TMS-Cl), oxalyl chloride, or 2-methoxy-pinacolborane (MeOBPin). By decomplexation through quenching with water and exposure to ambient conditions, selectively mono-functionalized [*n*]CPPs **38** - **41** were obtained (Scheme 5).



Scheme 5. Top-down functionalization of [9]CPP **31** and [12]CPP **32** by metal complexation.

Another attempt towards top-down functionalization of [*n*]CPPs was the bromination, which was reported first by YAMAGO's group in 2017.⁹⁰ By treating smaller [*n*]CPPs ($n = 5 - 9$) with elemental bromine, two phenyl units were brominated, resulting in a strain-relieved macrocycle. Subsequent treatment with bromine led either to tetra-brominated phenyl units (**43**) or rearrangement of one bromine atom (**44**) under the influence of heat, as demonstrated with [5]CPP. Conversion to the desired functionalized [5]CPPs **45** - **47** was only achieved by using a phosphazene superbases. However, having the bromine attached to the [5]CPP backbone further allowed the functional group conversion towards different functionalities (Scheme 6).



Scheme 6. Top-down functionalization of [5]CPP **42** through bromination. Depending on the conditions, different substitutions could be achieved.

Unfortunately, this top-down approach to obtain functionalization is only applicable to smaller [n]CPP derivatives due to the ring strain of the molecules, as mentioned earlier. YAMAGO's group calculated using DFT at a B3LYP/6-31G(d) level of theory, that the heat of formation during the first addition of bromine becomes endothermic when the [n]CPP exceeds a size of $n = 9$.⁹⁰ Additionally, they calculated the strain relief of the different sized [n]CPPs, revealing that the strain relief decreases as n becomes larger. These results conclude that the balance between endo- and exothermicity resulting from the strain relief and the resulting loss of aromaticity plays a crucial role in the reactivity of [n]CPPs. Moreover, the flexibility in substitution pattern is limited, and in the case of a higher degree of bromination, selectivity is compromised. These drawbacks have led to the conclusion that if different functionalities, substitution patterns, or sizes are required, the modification needs to be introduced at earlier stages (bottom-up approaches). Over the past several years, a range of bottom-up approaches have been developed to tackle diverse functional groups on the [n]CPPs and their prospective applications. These strategies encompass either pre-functionalized building blocks or electrocyclic reactions, as exemplified by the subsequent selected instances in the ensuing section.

As the domain of [n]CPPs rapidly emerges, it is strongly advised to consult the review articles published in 2015 by LEWIS,⁴⁷ in 2018 by Wu et al.,⁴⁸ and in 2019 by JASTI⁹¹ at this juncture.

Tuning the fluorescent characteristics of an organic chromophore often results in changes in the HOMO – LUMO energy gap. One of the most promising approaches to influence these energy levels is by incorporating electron-donor and electron-acceptor units (Figure 14).^{92–101}

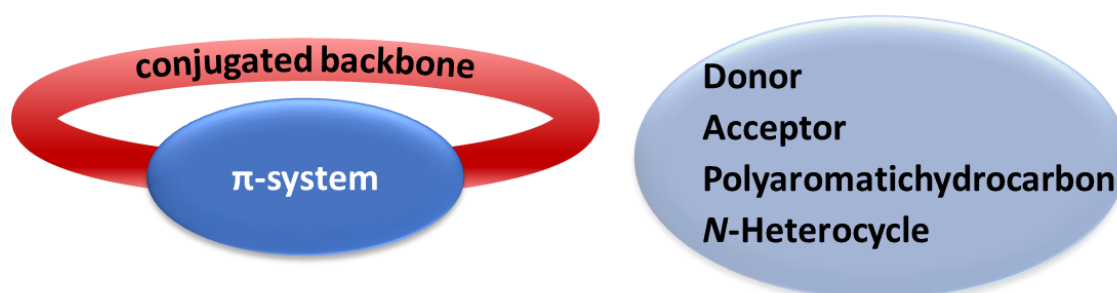
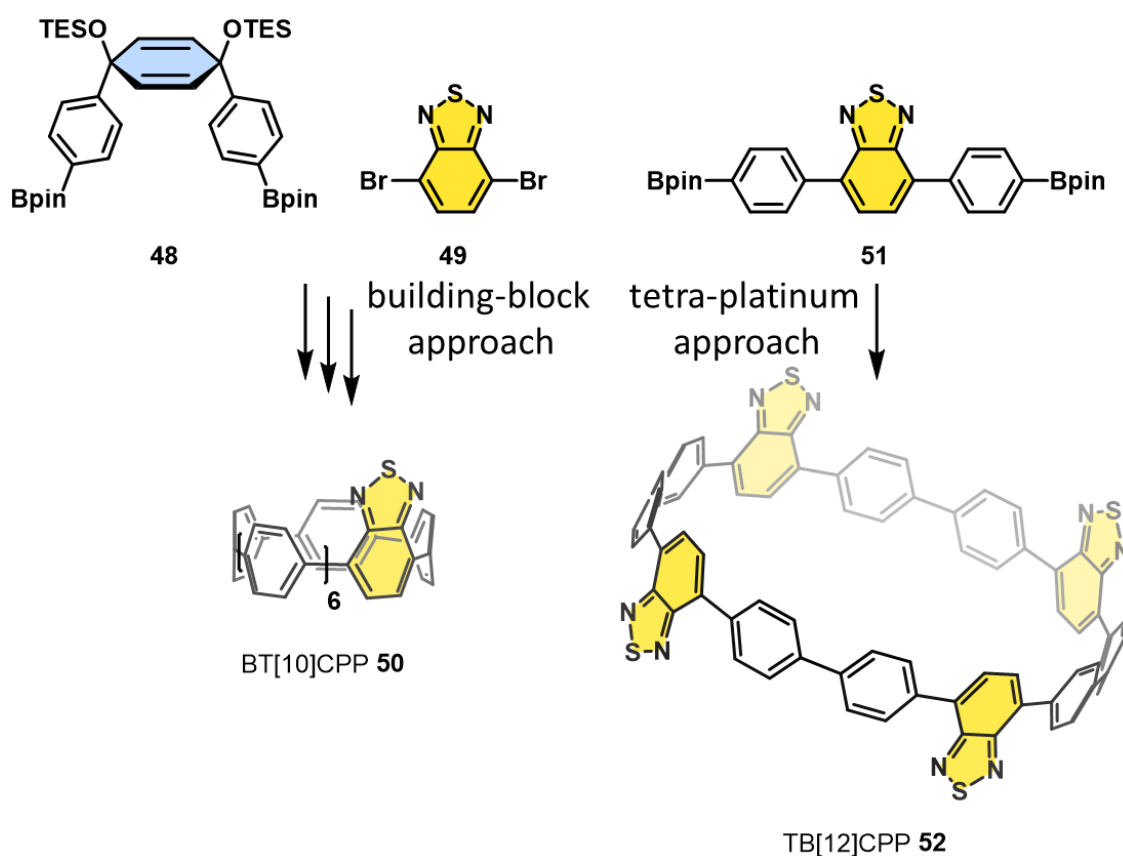


Figure 14. Design concept of donor- / acceptor-incorporated CPPs (adjusted from literature⁹²).

For example, in 2020, JASTI and co-workers reported the synthesis of the bright orange-emitting benzothiadiazole [10]CPP **50** (Scheme 7, left).⁹³ Following their bottom-up approach synthesis, the incorporation of the acceptor unit allowed a significant red-shift in emission ($\lambda_{em} = 466$ nm to $\lambda_{em} = 571$ nm) while maintaining a high fluorescence quantum yield of 0.59. These properties were further modified by QUI et al. who published TB[12]CPP **52** in 2020, which have incorporated four benzothiadiazole units (Scheme 7, right). Achieving this molecule was realized using YAMAGO's tetra-platinum complex strategy.⁹³



Scheme 7. Synthesis of benzothiadiazole [10]CPP (BT[10]CPP) **50** and tetra-benzothiadiazole [12]CPP (TB[12]CPP) **52** following different approaches

Not only does TB[12]CPP **52** display an emission wavelength exceeding 610 nm within the solid-state, but its fluorescent quantum yield could be adjusted to 0.98 in a poly-(methyl methacrylate) matrix.⁹⁴

Further, TB[12]CPP **52** was further investigated in a metallofullerene-[12]CPP self-assembly by WANG's group (Figure 15).⁹⁵ In addition to the synthesis of peapod-complex **53**, the conducted temperature-dependent electron paramagnetic resonance (EPR) spectroscopy and fluorescence analyses. The synchronous changes observed in both methods were attributed to the temperature-dependent interaction between the host and the guest. This interaction resulted in an enhanced fluorescence peak intensity of TB[12]CPP **52** with decreasing temperature. WANG's group attributed this enhancement to the fact that the thermal vibration of the molecules no longer promotes the molecular decay.¹⁰²

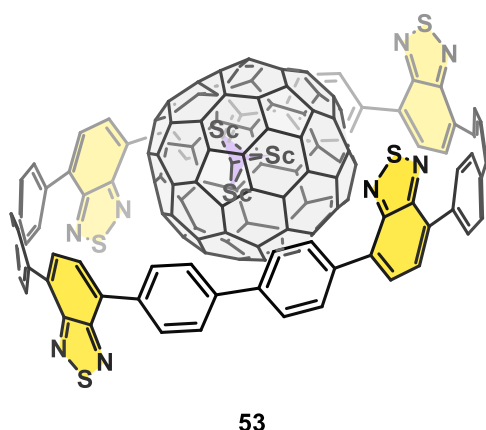


Figure 15. Schematic representation of the metallofullerene-[12]CPP complex **53**. Double bonds of fullerene C_{80} have been omitted for clarity.

Within the paramagnetic metallofullerene $Sc_3C_2@C_{80}$ the electron spin is distributed on the Sc_3C_2 cluster and can exhibit up to 22 EPR lines. Further examination of these EPR signals and the differences in intensity between complex **53** and the parent TB[12]CPP **52** revealed an enhanced host-guest interaction. This interaction in turn can modify the EPR signals of the inner guest and the fluorescence peaks of the host.

The aforementioned examples provide evidence of the precise atomic control over [n]CPPs and their structural properties. Nevertheless, to fully harness the potential of [n]CPPs radial conjugation in electronic devices, considerable efforts have been dedicated to the design of π -conjugated polymeric materials. Within these materials, the conjugated backbone of the CPP can be connected either within the main-chain^{103–107} or in the side-chain¹⁰⁸ of the polymer (Figure 16).

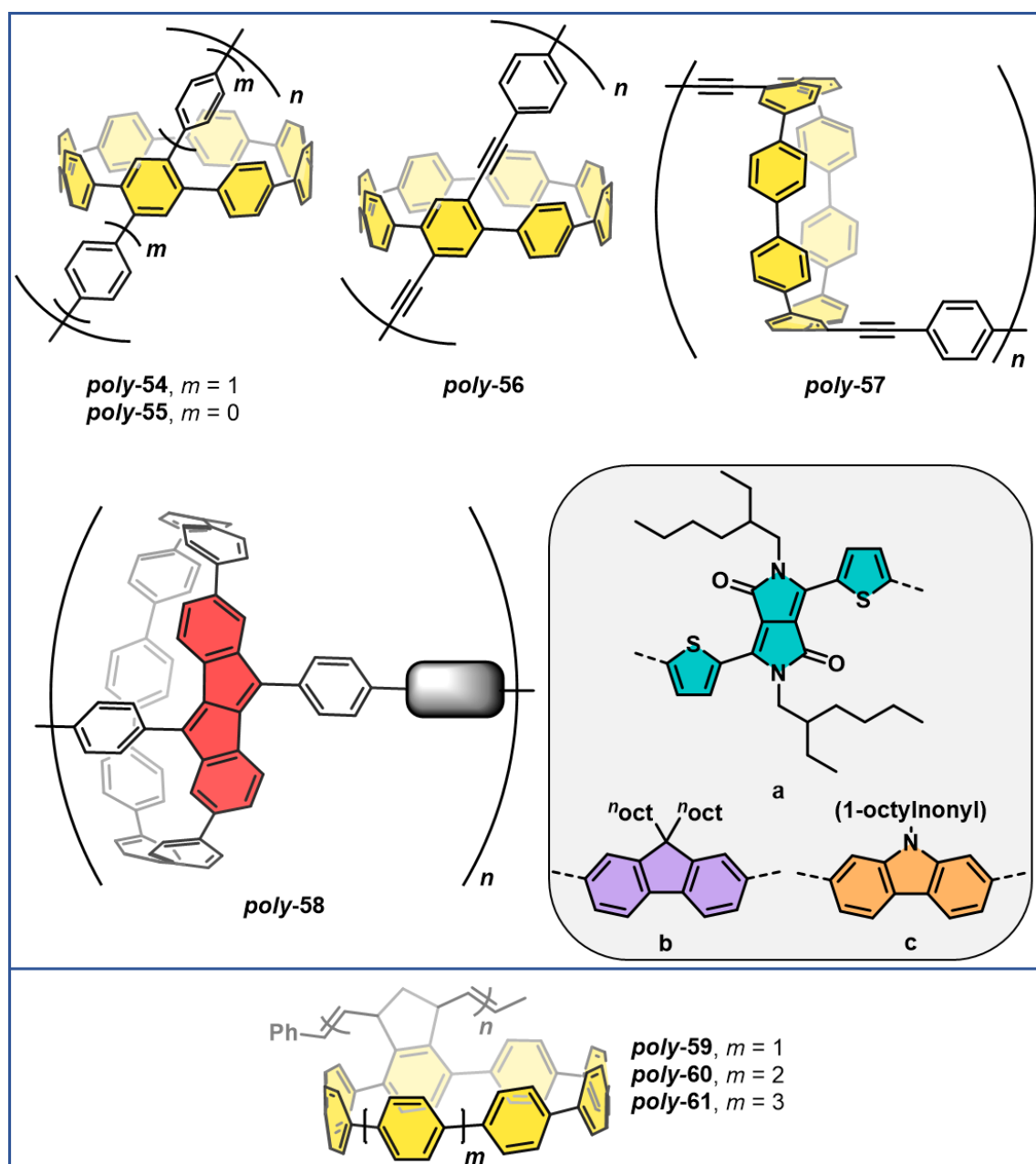
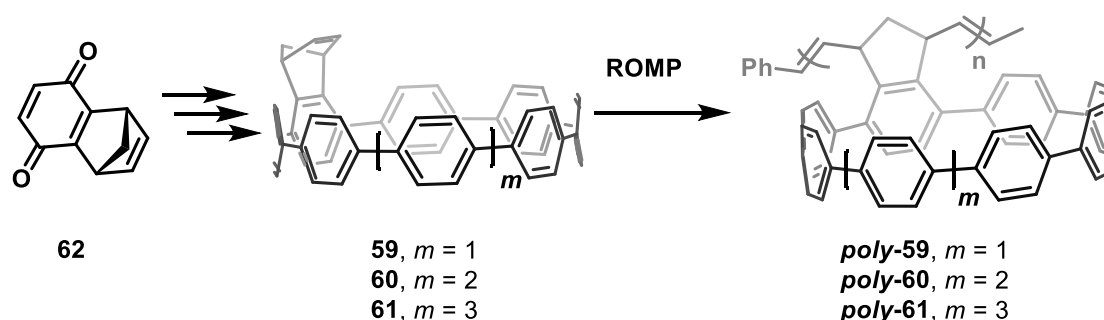


Figure 16. Examples of $[n]$ CPP-containing polymers within the main-chain and the side-chain.

Photophysical investigations of **poly-54**, published by DU et al. in 2019,¹⁰³ revealed a slight blue shift in the absorption maximum at 331 nm ($\lambda_{\text{abs,max}}([8]\text{CPP}) = 340$ nm) and an emission maximum at approximately 540 nm, which aligns closely with the maximum peak for [8]CPP. Interestingly, the fluorescence quantum yield of **poly-54** ($\phi = 0.42$) is nearly that of its monomer ($\phi = 0.22$) and roughly four times higher than that of the parent [8]CPP ($\phi = 0.10$). On the one hand, the enhanced molecular rigidity decreases the quenching rate of the excited state, while the increased conjugation length amplifies the π delocalization effect on the other hand.¹⁰³ Not only investigating the interplay of radial and linear conjugation in $[n]$ CPP co-

polymers but also the application of the material in lithium-organic half-cells was recently reported by the group of ESSER.¹⁰⁷ As depicted in Figure 16, co-monomers such as dithiophenyldiketo(pyrrolopyrrol) (**poly-58a**), fluorene **poly-58b**, and carbazole **poly-58c** have been utilized. These distinct structures exhibit varied behavior in terms of their π -conjugation. While fluorene **58b** and carbazole **58c** co-monomers only display conjugation within the $[n]$ CPP part, pyrrolopyrrol **58a** facilitates an extended π -conjugation along the polymer backbone. Similar findings have been reported in 2022 by PETERSON et al., who examined the impact of different connectivity and conjugation pathways in disjoint $[8]$ CPP-based polymers.¹⁰⁴ ESSER and co-workers were further able to demonstrate, in a proof-of-principle study, that the $[n]$ CPP-carbazole-copolymer **56c** can function as a positive electrode material in lithium-organic half cells. Although this copolymer exhibits relatively low specific capacities compared to state-of-the-art organic p-type redox polymers, it represents a significant milestone in the development of $[n]$ CPP-based polymers for future charge storage materials.¹⁰⁷

Thus far, the presented polymeric $[n]$ CPPs have been derived from cross-coupling methods. A more robust technique for polymerization is the so-called controlled polymerization, which facilitates precise control over the length of the polymer chain and enables the synthesis of block copolymers, thereby facilitating the accessibility of novel materials through a sharper molecular mass distribution. In 2021, JASTI's group successfully applied this technique by utilizing ring-opening metathesis polymerization (ROMP) to synthesize various $[n]$ CPP-based block-copolymers ($n = 8, 9, 10$; Scheme 8).¹⁰⁸



Scheme 8. Synthesis of $\text{poly}(nb[n]\text{CPP})\text{s}$ **poly-59 - poly-61** using ring-opening metathesis polymerization (ROMP).

In contrast to numerous other polymers based on fluorophores, the innovative poly- $[n]$ CPPs **poly-58** do not exhibit fluorescence quenching induced by aggregation.

This characteristic makes them highly promising candidates for fluorescence imaging applications. Additionally, the ability of the poly-block[*n*]CPPs **poly-59** – **poly-61** to form supramolecular assemblies with fullerenes allows for the preparation of materials with well-defined regions for this phenomenon.¹⁰⁸

The formation of host-guest complexes between fullerenes and [*n*]CPPs relies on the combination of multiple weak π - π interactions, which significantly contribute to their stability.¹⁰⁹ The field of supramolecular chemistry, which focuses on non-covalent interactions such as VAN DER WAALS forces, hydrogen bonds, hydrophobic forces, and metal-ligand coordination, has been instrumental in advancing this area of research.¹¹⁰ Building upon EMIL FISHER's "lock-and-key" model of supramolecular systems from 1894,¹¹¹ the field of supramolecular chemistry has grown over the years and was recognized with the NOBEL Prize in Chemistry in 1987 for the groundbreaking work of PEDERSEN, CRAM, and LEHN on crown ethers.¹¹² Since the first synthesis of [10]CPP in 2008,⁵⁰ and the initial investigation of a fullerene C₆₀@[10]CPP complex in 2011,¹¹³ extensive research has focused on the interaction between the convex π -surface of C₆₀ and the concave surface of [*n*]CPPs.^{53,93,113–117}

Recently, WEGNER's group has made contributions to the existing collection of various substituted [10]CPPs and has conducted fundamental investigations on the interactions within complexes consisting of those.^{118,119} Through the utilization of a [2+2+2] cyclotrimerization reactions, WEGNER et al. have successfully synthesized substituted [10]CPPs **62** - **64**,^{120,121} and subsequently examined their complexation behavior with different fullerenes (Figure 17).^{118,119}

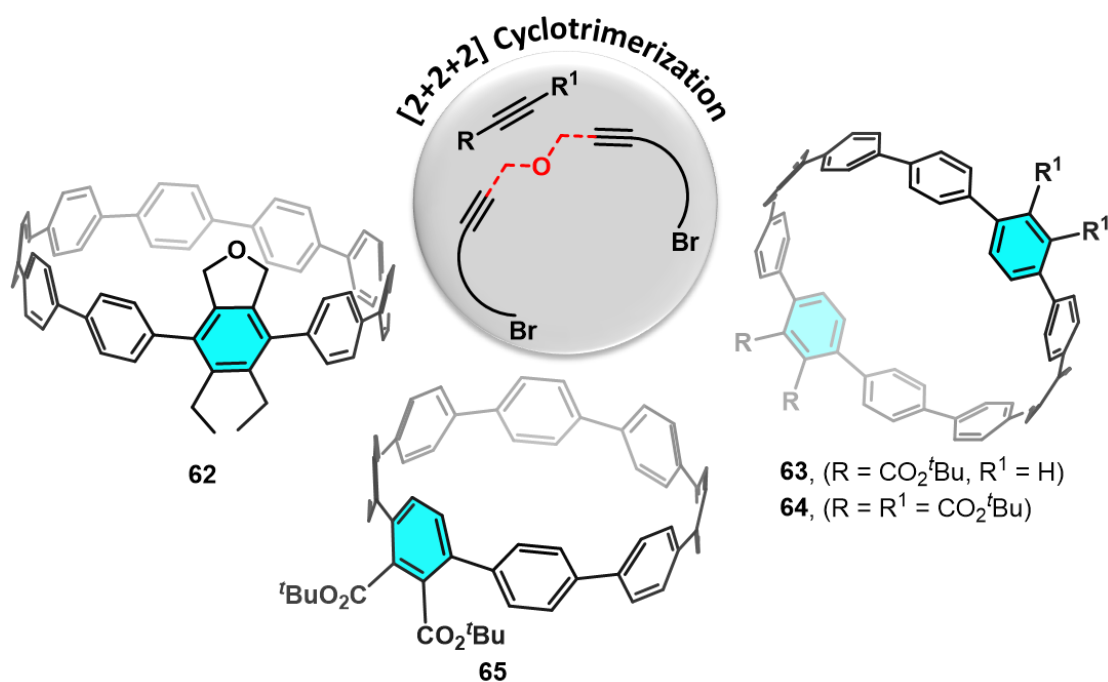


Figure 17. Representative scheme of the synthesis of substituted $[n]$ CPPs **62** - **65** through $[2+2+2]$ cyclotrimerization.

Fluorescence quenching experiments of the substituted $[10]$ CPPs **62** - **64** with fullerenes C_{60} and C_{70} have revealed that the loss of stabilization energy caused by the ellipsoid shape of C_{70} can be partially compensated by the presence of additional substituent-fullerene interactions. Furthermore, the findings suggest that the nature of the substituent does not play a crucial role in the stabilization effects; rather, it is the degree of substitution that allows for the possibility of additional interactions.¹¹⁹ In order to conduct a more comprehensive investigation, WEGNER et al. have examined the influence of fullerene BINGEL adducts that possess varying lengths of alkyl groups within a supramolecular assembly of $[10]$ CPP and substituted $[10]$ CPPs **62**- **64**.¹¹⁹ Regardless of the alkyl group, all supramolecular assemblies have exhibited an overall destabilization effect when compared to unsubstituted C_{60} . While linear alkyl substituents have not displayed a significant impact on the overall binding, the branched adamantly substituent has shown the largest effect on the stabilization, rationalized by the polarizability of the substituent. The overall outcomes of these studies can be rationalized by considering the interplay between attractive interactions such as LONDON dispersion and repulsion that arises from the steric demand of the substituent. It is worth noting that both studies conducted by WEGNER's group have the potential to lay the foundation for future design of novel carbon-based supramolecular functional systems.^{118,119}

Further common organic molecules which are used in supramolecular chemistry include calix[*n*]arenes (C[*n*]A) and pillar[*n*]arenes (P[*n*]A). Due to their shape-persistent cavities, convenient synthesis, and selective guest recognition, they have shown potential in sensing, drug delivery, and chemical separation.^{122–124}

In 2020, STĘPIEN's group successfully synthesized the “molecular squid” **67** using the structural motifs of [6]CPP **16** and C[4]A **66**, following the building block approach of JASTI (Figure 18).⁷⁷

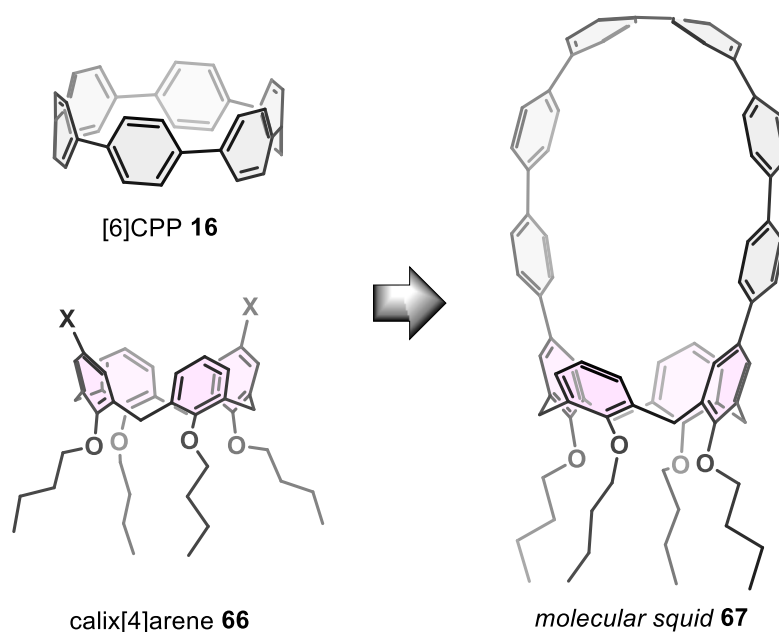


Figure 18. Design of the molecular squid **67**.

In contrast to a previous study by GAETA's group, the [6]CPP component in molecule **67** is connected to the arene moieties of the C[4]A, rather than the oxygens.¹²⁵

The electron-rich cavity of **67**, which possesses a flexible shape, allows to serve as a host for various electron-deficient guest molecules. In solution, [6]CPP-C[4]A **67** exhibits emission at a wavelength of 485 nm with a quantum yield of 0.33. However, this emission is partially quenched upon the formation of a host-guest complex. Notably, when methylacridinium and anthraquinone adducts are incorporated into a thin film of **67**, their emission spectra shift to longer wavelengths, specifically to 700 nm and 580 nm, respectively. This red-shift is attributed to the charge-transfer properties of these two complexes.⁷⁷

The utilization of pillar[n]arenes in conjunction with [n]CPP, which was reported in 2023 by Xu et al., represents a novel advancement in the field of both. Specifically, they presented the initial synthesis of two distinct [n]CPP-P[5]A-bismacrocycles ($n = 8$: **71**; $n = 10$: **72**) by applying the building block strategy for [n]CPPs (Figure 19).¹²⁶

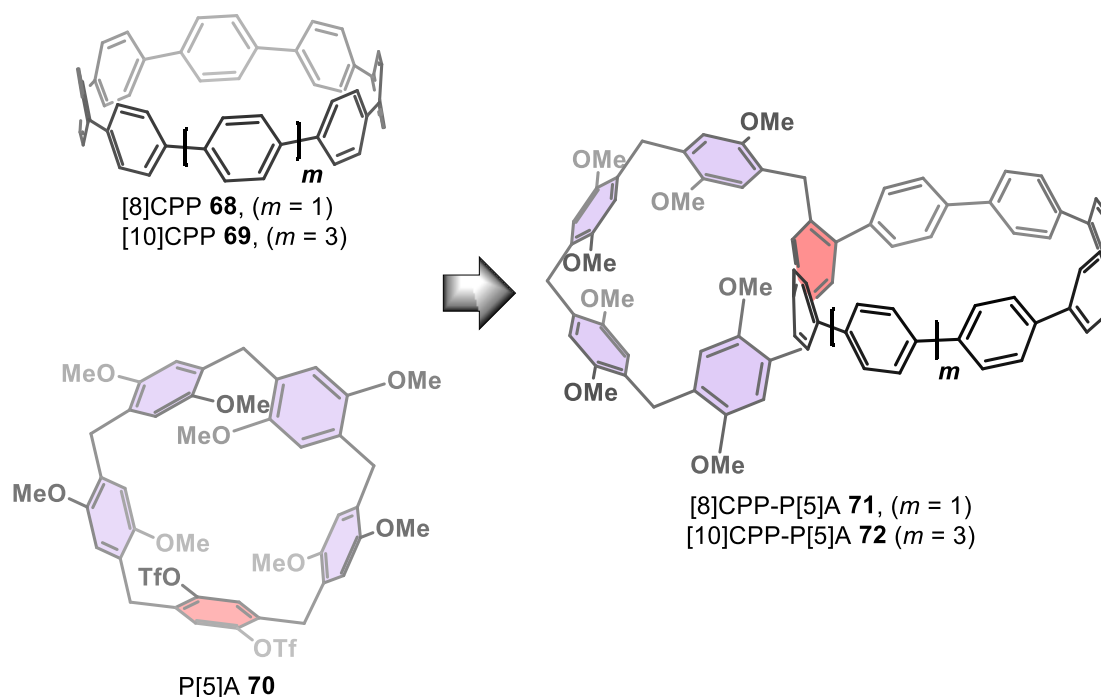


Figure 19. Design principle of [n]CPP-P[5]As **71** and **72**.

Both bismacrocycles **71** and **72** exhibit an increase in their fluorescence quantum yield in comparison to [8]CPP **65** and [10]CPP **64**. It is highly probable that the attachment of P[5]A **67** not only imparts rigidity to the structure but also imparts a charge-transfer characteristic to the emissive state. Additionally, chiral high-pressure-liquid-chromatography (HPLC) facilitated the separation of the two enantiomers (pR)/(pS)-[8]CPP-P[5]A, which possess circularly polarized luminescence (CPL) ($g_{\text{lum}} \approx 0.02$), thus making them potential CPL-active materials. Furthermore, the supramolecular properties of the bismacrocycles **71** and **72** have been demonstrated. Guest molecules such as C_{60} , pyridinium salts and 1,8-dibromooctane were capable of binding to the distinct cavities.¹²⁶ Moreover, these bismacrocycles **71** and **72** can be effectively utilized in manipulating FRET processes utilizing different rhodamine derivatives or BODIPY derivatives as a host, resulting in tunable white-light emission.¹²⁷

The supramolecular characteristics of [n]CPPs can be further enhanced through their utilization in mechanically interlocked molecules. The mechanical bond entails the entanglement of at least two molecules in space, such that they can only be separated by breaking or distorting chemical bonds.¹²⁸ Typical instances of such interlocked structures are rotaxanes¹²⁹ (wherein at least one cyclic molecule is threaded onto a dumbbell-shaped thread terminated by bulky endgroups) and catenanes¹³⁰ (consisting of at least two interlocked macrocyclic structures).¹³¹ Eminent researchers JEAN-PIERRE SAUVAGE, Sir J. FRASER STODDART and BERNARD L. FERINGA were awarded the NOBEL Prize for Chemistry in 2016 for their significant contributions in the field of small molecular machines, including the chemistry of catenanes and rotaxanes.¹³² The inclusion of [n]CPPs in these interlocked architectures has opened up various potential applications in areas such as electronics, biological sensing, or drug delivery.

The first example of a template-directed synthesis of a [10]CPP-fullerene based rotaxane was reported by the group of VON DELIUS in 2018, taking advantage of the concave-convex π - π interactions between C₆₀ and [10]CPP.¹³³ In contrast to this so-called passive template synthesis approach, active template synthesis approaches apply a metal catalyst to simultaneously preassemble the molecular components and facilitate bond formation towards an interlocked molecule. This methodology was independently introduced by the groups of SAITO¹³⁴ and LEIGH,¹³⁵ and was successfully demonstrated on a phenanthroline-incorporated [n]CPP **73** by the group of CONG in 2018.¹³⁶ After extensive efforts by ITAMI's group in 2019, the synthesis of trefoil knot **74** and *all*-benzene catenane **75** using a traceless template synthesis was achieved.^{137,138} Following this, JASTI and co-workers presented significant advancements in the active template strategy for the preparation of mechanically interlocked CPPs in 2023 (Figure 22).¹³⁹

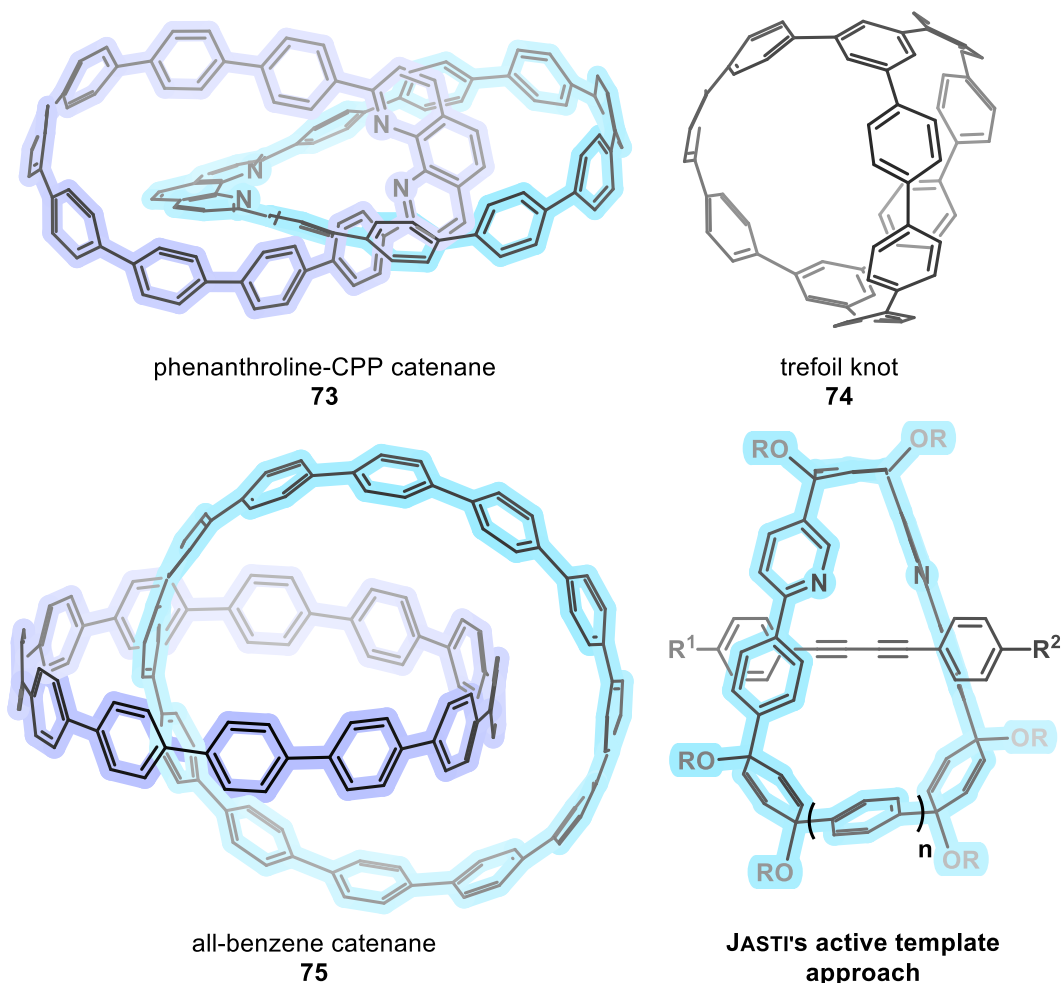
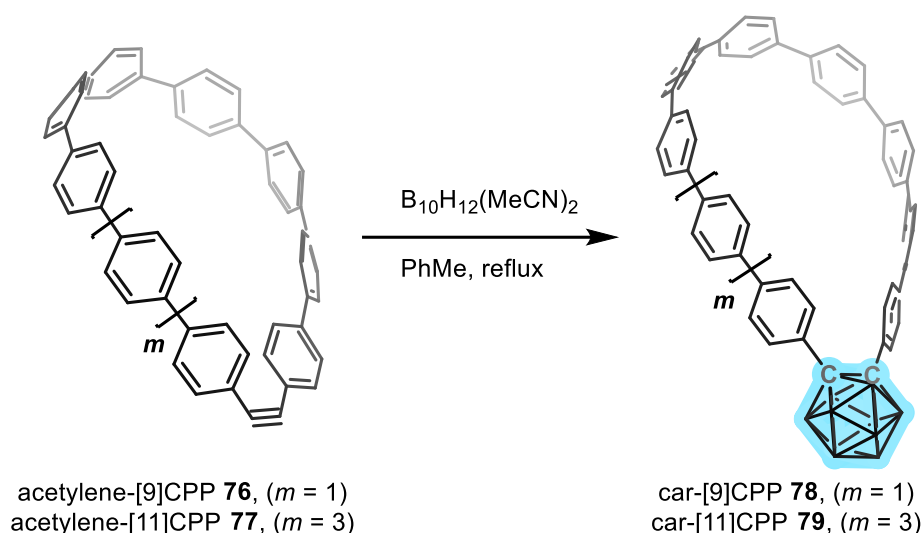


Figure 20. Structures realized through the active template synthesis approach: catenane **73**, trefoil knot **74**, and *all*-benzene catenane **75**. Additionally, JASTI's modified active template approach towards interlocked molecules is shown using the substituted alkyne and the macrocyclic precursor structure.

With the emergence of novel synthetic methodologies and chemical transformations, the accessibility of innovative materials has become viable. This phenomenon is also true for the field of inorganic-organic hybrid $[n]$ CPPs. In 2022, JIANG et al. successfully demonstrated the incorporation of $[8]$ CPP into a metal-organic framework.¹⁴⁰ This metal-organic framework was subsequently utilized to illustrate the chemical oxidation of the $[8]$ CPP units, resulting in the formation of a relatively stable radical matrix in solid state.

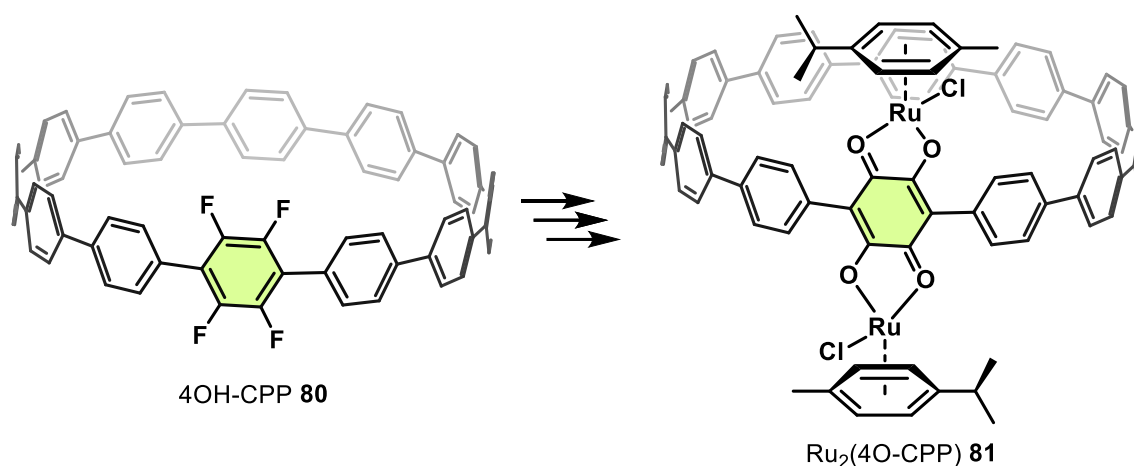
In the context of inorganic-organic hybrid $[n]$ CPPs, ZHU et al. published the pioneering “necklace-shaped” $[n]$ CPPs ($n = 9; 11$) in 2022.¹⁴¹ They modified a synthesis approach for alkyne-embedded $[n]$ CPPs, which was previously developed by JASTI's group in 2018.¹⁴² By applying a one-step alkyne insertion reaction, carborane- $[9]$ CPP (car- $[9]$ CPP) **78** and car- $[11]$ CPP **79** were successfully synthesized (Scheme 9).



Scheme 9. Synthesis towards car-[n]CPPs **78** ($n = 9$) and **79** ($n = 11$). Boron atoms within the boron cluster have been omitted for clarity and are shown as blue cage structure.

Subsequent treatment of these car-[n]CPPs with tetra-butylammonium fluoride (TBAF) led to the formation of the *nido*-car-[n]CPPs. Through the formation of a larger conjugated system, all (*nido*-)car-[n]CPPs exhibit a blue-shifted emission in solution compared to the parent [9] and [11]CPPs, with wavelengths ranging from 451 nm to 473 nm. Moreover, due to their molecular rigidity and the significant steric hinderance against cations, the *nido*-car-[n]CPPs exhibit high quantum yields in both solution and the solid state (up to 0.90).¹⁴¹

The (poly-)fluorinated [n]CPPs stand out as some of the most prominent representatives of functionalized [n]CPPs. The synthesis of these derivatives is achieved through a combination of the building block approach of JASTI's group, and the formation of platinum complexes, as introduced by YAMAGO's group.^{143–147} In the context of inorganic-organic hybrid [n]CPPs, JASTI and co-workers utilized these (poly-)fluorinated [n]CPPs to design (poly-)catechol-[n]CPPs through a nucleophilic substitution reaction (Scheme 10).¹⁴⁸



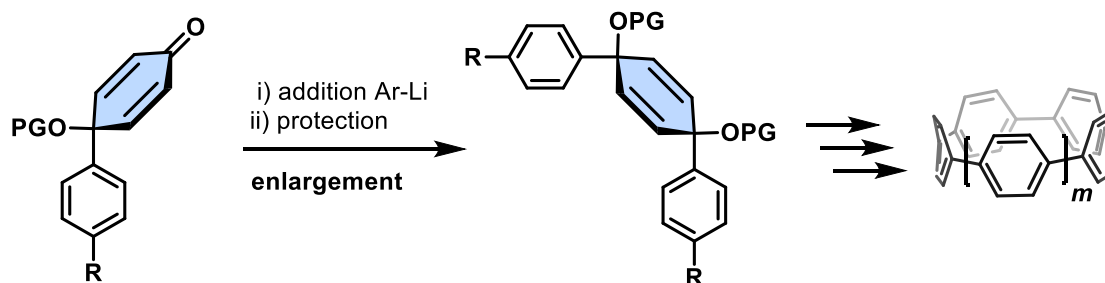
Scheme 10. Representative synthesis scheme of Ru₂(4O-COO) **81**.

The metalation of the catechol-[12]CPP subsequently resulted in the formation of well-defined multi-metallic CPP complex **80**, indicating the potential for the creation of extended structures.

Despite the limited representation in the fields of material and life sciences or other fields, $[n]$ CPPs are the subject of various efforts aimed at altering this circumstance. The aforementioned examples serve as compelling evidence of the vast potential held by (un-)substituted $[n]$ CPPs in various fields. One possible explanation for the awaited breakthrough could be attributed to the arduous multistep synthesis involved in the creation of such systems. Despite the existence of well-established synthetic strategies, there exist a multitude of challenges that must be overcome. In particular, the high reactivity exhibited by the cyclohexadiene moiety poses a significant obstacle that necessitates careful consideration to prevent the occurrence of undesired side-reactions.

1.4. 1,2-Aryl Shift in the Synthesis of $[n]$ Cycloparaphenylenes

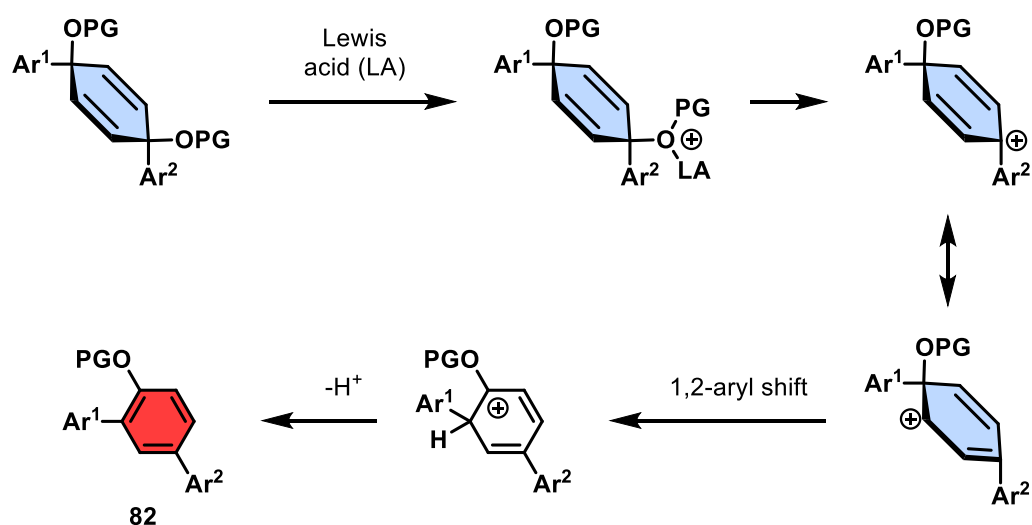
As presented in the preceding sections, the synthesis of $[n]$ CPPs primarily depends on the arrangement of pre-bent molecules and building blocks (Figure 10). Especially, building blocks relying on the cyclohexadiene scaffolds are indispensable for the synthesis of molecular nanocarbons. To achieve an efficient synthesis of the required precursors, it is crucial to protect their diol-functionality.¹⁴⁹ Moreover, this process should facilitate a *cis* conformation, enabling the macrocyclization reactions, thereby minimizing the occurrence of undesirable side reactions before aromatization (Scheme 11).



Scheme 11. General representation of the $[n]$ CPP synthesis using two different protected cyclohexadiene scaffolds.

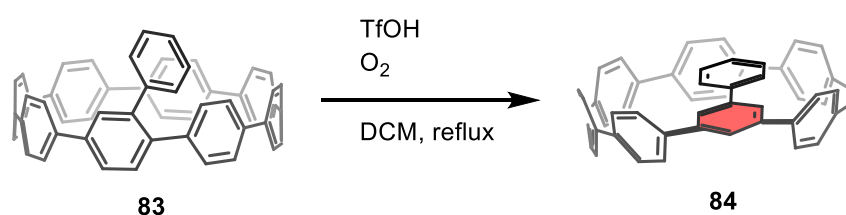
Initially, the conventional approach of applying a methyl ether group to protect the cyclohexadiene moiety of **25** resulted in poor diastereoselectivity.⁵⁰ Despite this, the diastereoselectivity of the addition of a lithiated aryl species to **32** can be manipulated by electrostatics.^{149,150} In order to further enhance the diastereoselectivity towards the *cis* conformation, YAMAGO's group introduced the bulkier triethyl-silyl (TES) protecting group for the tertiary alcohols.⁶⁶ Moreover, the TES group facilitates the use of relatively mild reaction conditions for the final aromatization step using tin-chloric acid after deprotection of the alcohols with tetra-*n*-butylammonium fluoride (TBAF).⁷³ In 2023, SOLOMEK and co-workers investigated the vulnerability of both scaffolds in **32** and **25** against acidic and alkaline reaction conditions. They also incorporated the *tert*-butyldimethylsilyl (TBS) protecting group to these building blocks, which not only increased their stability, but also preserved the high diastereoselectivity towards the *cis* conformation.⁶⁴

Although the instability of these building blocks is widely recognized in the field of molecular nanocarbon synthesis, there is limited information available regarding the specific types of side reactions that occur during the addition of arenes. Consequently, SOLOMEK and co-workers conducted a brief investigation and mechanistic discussion in their publication by subjecting their building blocks to various bases and LEWIS acids. As a result of these treatments on the cyclohexadiene scaffolds, an aromatization process involving a 1,2-aryl shift took place (exemplified shown in Scheme 12).



Scheme 12. Proposed mechanism for the 1,2-aryl shift on a protected cyclohexadiene scaffold.

This 1,2-aryl shift is not only observed in small, open-ring systems such as described previous studies, but also in more complex systems as demonstrated by JASTI and co-workers in 2016 (Scheme 13).¹⁵¹

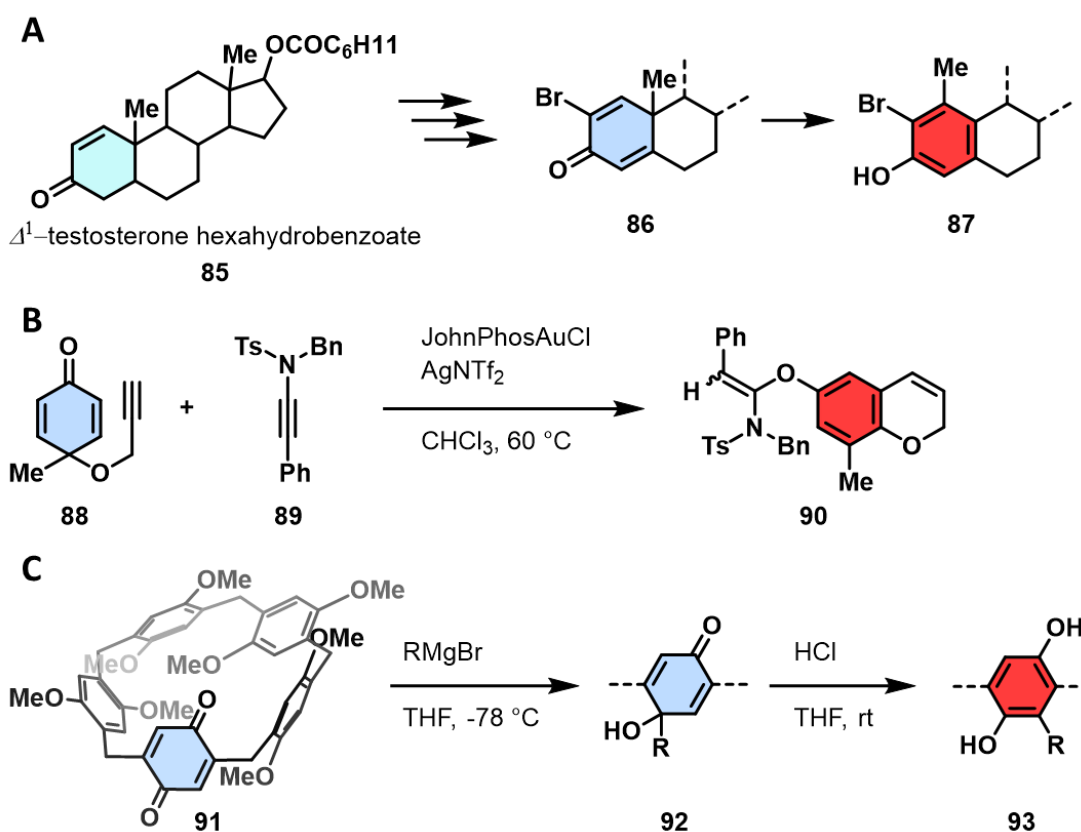


Scheme 13. 1,2-aryl shift on phenyl-substituted [8]CPP **82**.

Theoretical mechanistic investigations using DFT calculations at the B3LYP/6-31+(d,p) and B3LYP/6-31(d,p) level of theory, were conducted on their model system **82** to expose an activation barrier of 21 – 24 kcal mol⁻¹ for this cationic rearrangement. Moreover, it was found that the rearranged product **83** is approximately 20 kcal mol⁻¹ lower in energy compared to the starting material.

These findings hold true even in an *all*-phenyl substituted [8]CPP.¹⁵¹ Additionally, this mechanistic study revealed that commonly used synthetic methods for arene functionalization (e.g. nitration and halogenation) are not suitable for such cyclic systems.

Although, this 1,2-aryl shift has been an undesired reaction in the molecular nanocarbon field, the *dienone-phenol rearrangement* has numerous applications in synthetic organic chemistry and has been extensively studied in recent years.^{152–155} Interestingly, the migration tendency for two different groups can be selectively triggered at either the 4,4 position or 2,2 position, depending on the stability of the intermediate carbocation.^{156–158} Under acid-promoted conditions, there is a higher tendency for an alkoxy group to migrate compared to a phenyl group. In general, the 1,2-aryl shift has already found utility in the synthesis of steroids¹⁵⁹, poly-fused carbo- and heterocycles^{160,161}, and the functionalization of pillar[5]arenes (Scheme 14).¹⁶²



Scheme 14. Application of the 1,2-aryl shift in the synthesis of natural products (A), carbo- and heterocycles (B) and functionalization of pillar[5]arenes (C).

While the 1,2-aryl shift can be highly effective in certain situations, it frequently requires the restart of the synthesis of 1,4-connected building blocks. However, the following chapter will demonstrate that the resulting *meta*-connectivity inherent in macrocyclic nanomaterials, such as cycloparaphenylenes, can yield enhanced properties, thereby unveiling an entirely novel category of compounds.

1.5. *meta*[*n*]Cycloparaphenylenes

In 2019, JASTI's group published a set of macrocyclic *poly*-phenylenes that possess a radial π -symmetry disruption due to the incorporation of a *meta*-linked phenylene unit into the macrocyclic backbone (Figure 21).¹⁶³

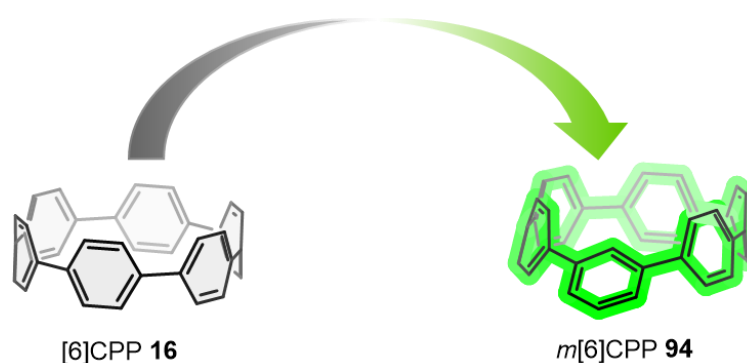
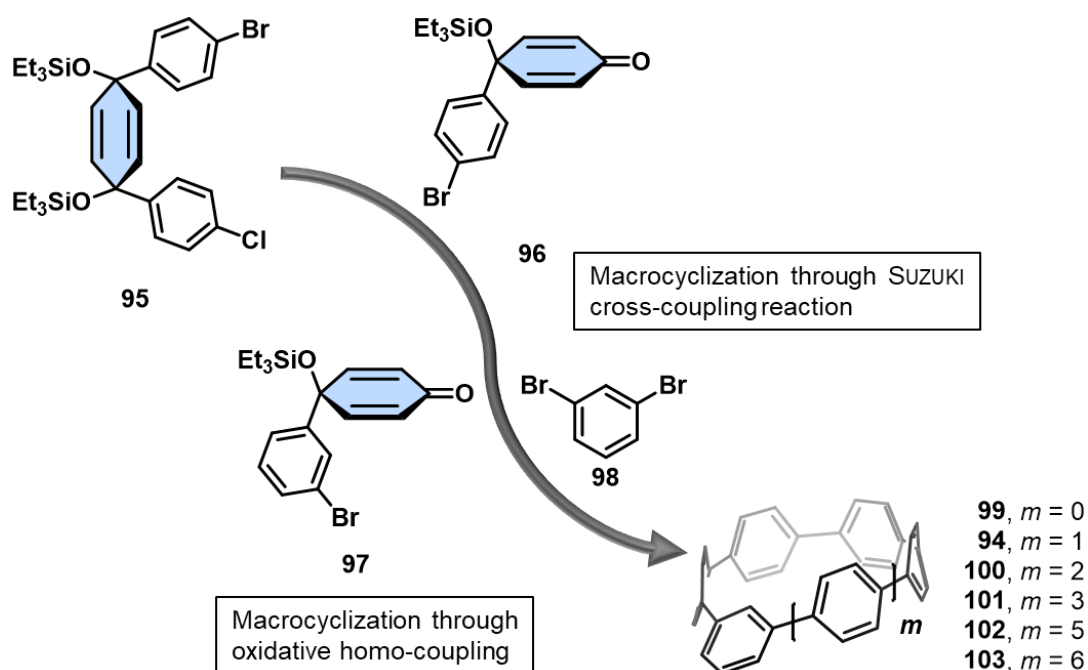


Figure 21. Turn-on of the fluorescence in smaller CPP derivatives through the incorporation of a *meta*-linkage.

This structural modification not only resulted in a reduction in strain energy when compared to their *para*-connected counterparts,¹⁶³ but it also enhanced the fluorescence properties of the smaller [*n*]CPPs. Conversely, these *meta*[*n*]CPPs (*m*[*n*]CPPs) exhibit a broken centrosymmetry, enabling the HOMO – LUMO transition. The now LAPORTE allowed transition is responsible for the appearance of a second UV-vis band. While this second band is only faintly visible in the larger *m*[*n*]CPP derivatives (*n* = 12, 10), it is clearly prominent in the smaller ones (*n* = 8, 7, 6, 5). Like their *para*-connected counterparts, the ring-size of the *m*[*n*]CPPs influences their fluorescence characteristics, with emission wavelengths ranging from 429 – 534 nm. Noteworthy, the quantum yield decreases as the ring-size decreases, which can be attributed to the greater strain effects experienced by the smaller derivatives.⁸⁰

The synthetic approach towards *m*[*n*]CPPs is once more based on JASTI's bottom-up strategy using TES-protected cyclohexadien-1,4-diols. The

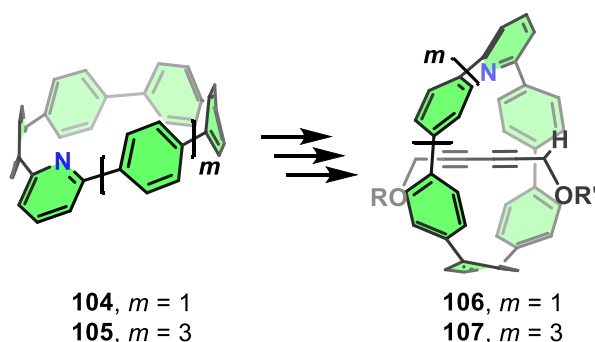
incorporation of the *meta*-connected phenyl ring occurs either at one of the initial steps (for $n = 5$) or during the macrocyclization reaction ($n = 6, 7, 8, 10, 12$) (Scheme 15).¹⁶³



Scheme 15. Schematic representation of the synthesis towards different sized $m[n]$ CPPs **94**, **99** - **103** and the corresponding key building blocks.

Since their initial appearance in literature, $m[n]$ CPPs have been sparsely encountered. Notably contributions in this field originated from JASTI's group, who have focused on interlocked molecules^{164–167} and explored potential biological applications.¹⁶⁸

In 2019, the utilization of pyridinyl- $m[n]$ CPP ($n = 6$: **104**, $n = 8$: **105**), has led to the synthesis and investigation of different rotaxanes of scaffolds **106** and **107** (Scheme 16).¹⁶⁴



Scheme 16. Schematic representation of the rotaxane synthesis based on pyridinyl- $m[n]$ CPPs **104** – **105**.

The different [2]rotaxanes were synthesized through Cu(I)-catalyzed active-metal template reactions. The luminescent properties of the *m*[6]CPP moiety are quenched during the formation of the rotaxanes, but there is a significant increase in emission intensity upon disassembling the [2]rotaxane.

Structural modifications on **106**, led to the development of a turn-on fluorescent probe for HS⁻ by JASTI's group in 2021.¹⁶⁶ The reaction between HS⁻ and rotaxane **106** leads to the formation of a MEISENHEIMER complex and the disassembly of the rotaxane.

Based on the structural scaffold of pyridinyl-*m*[6]CPP **104**, JASTI and co-workers were able to synthesize the [c2]daisy chain rotaxane **108** (Figure 22) utilizing the active-metal template synthesis approach.¹⁶⁵

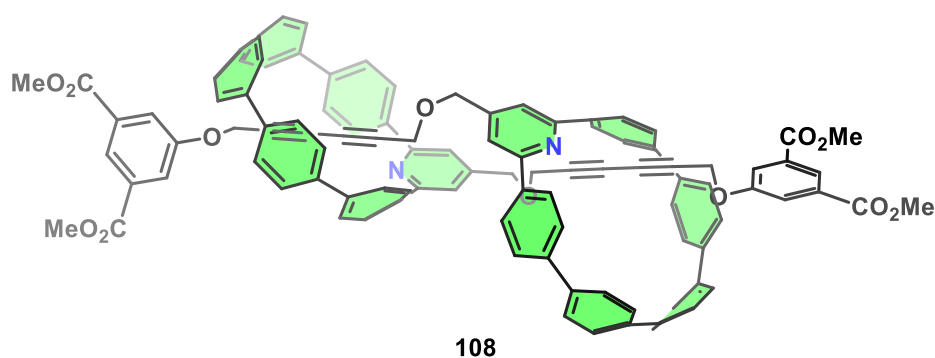


Figure 22. Chemical structure of [c2]daisy chain rotaxane **108** based on pyridinyl-*m*[6]CPP **104**.

Investigations using temperature-dependent nuclear magnetic resonance (NMR) spectroscopy, enabled the observation of the contraction and expansion of this molecule.

Moreover, the active-metal template synthesis approach was used within the synthesis of different polyynes[3]rotaxanes in 2022 by the groups of ANDERSON and JASTI (Figure 23).¹⁶⁷ Remarkably, [3]rotaxane **108** exhibits a 4.5-fold increase in stability compared to the free polyynes structures.

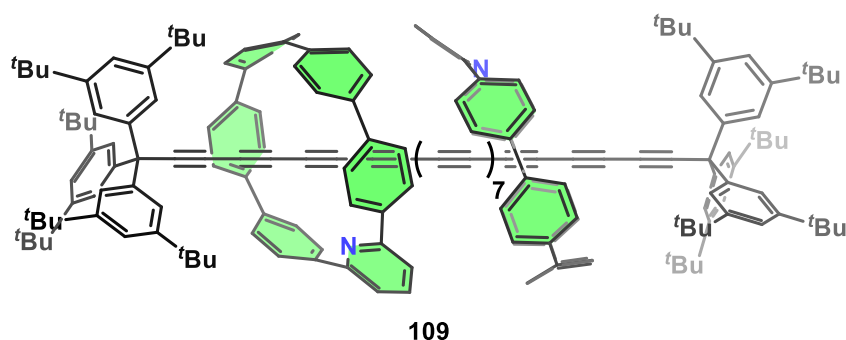
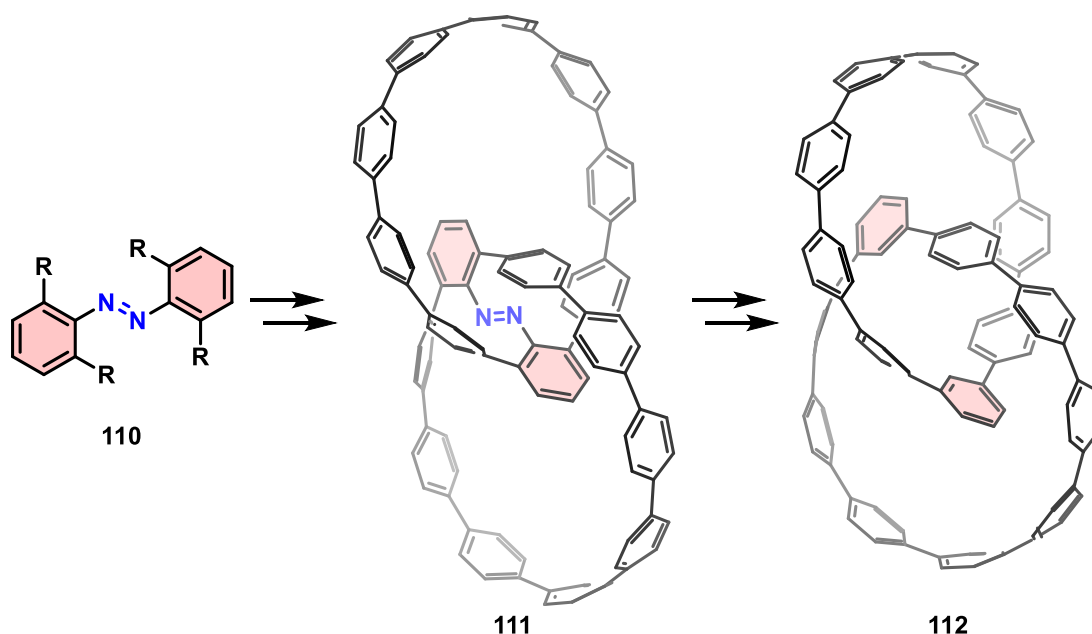


Figure 23. Chemical structure of polyynes[3]rotaxane **109** based on pyridinyl-*m*[6]CPP **104**.

In the context of interlocked molecules, CONG's group also utilized *m*[*n*]CPPs. Utilizing the tetra-substituted azobenzene **102**, they devised a conjugated covalent template strategy towards the *all*-benzene catenane **104** in 2022 (Scheme 17).

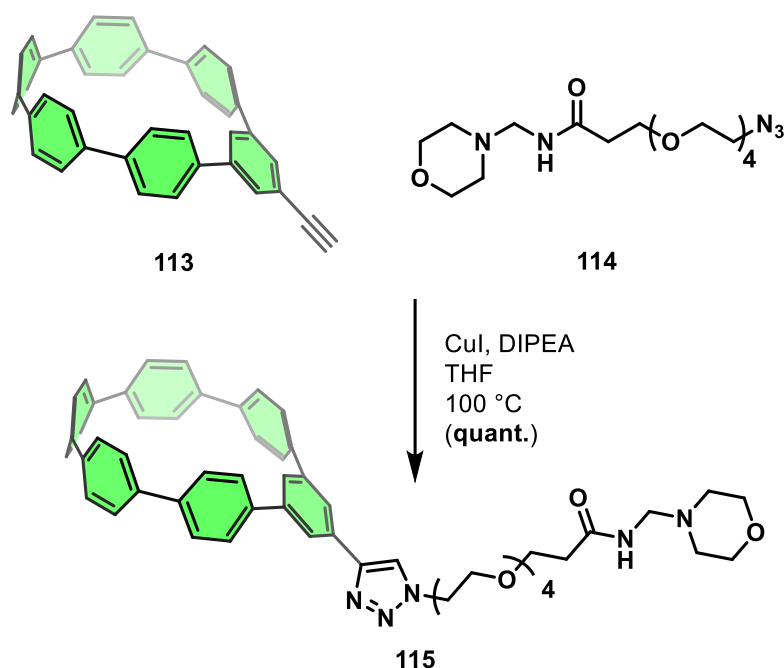


Scheme 17. Schematic representation of the synthesis of the *all*-benzene catenane **112**, deriving from the tetra-substituted azobenzene **110**.

In terms of its photophysical properties, catenane **112** exhibited no significant disparities when compared to its parent *m*[9]CPP. However, it should be noted that the fluorescence quantum yield of catenane **111** ($\phi_F = 0.56$) was found to be diminished in comparison to that of the *m*[9]CPP ($\phi_F = 0.85$).¹⁶⁹

In addition to their utilization in interlocked molecules, *m*[*n*]CPPs have been used in biological contexts by JASTI's group.¹⁶⁸ Due to its facile synthesis and relatively bright emission, *m*[6]CPP presents an advanced platform for biological applications, when compared to the previous reported functionalized [8]CPP¹⁷⁰. To

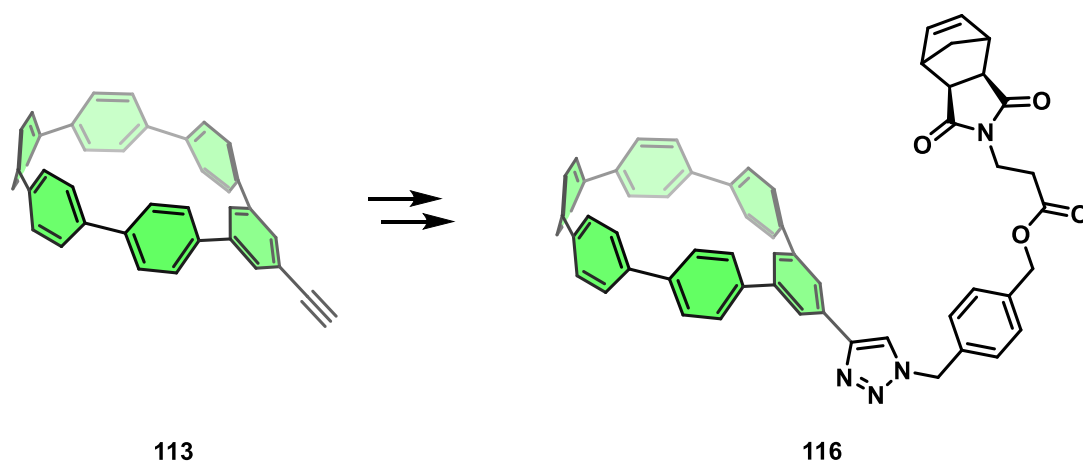
achieve lysosome targeting, alkynyl-*m*[6]CPP **113** must undergo an azide-alkyne click-reaction with morpholine-functionalized azide **114** (Scheme 18).



Scheme 18. Synthesis of lysosome targeted *m*[6]CPP **115** derived from alkynyl-*m*[6]CPP **113** under azide-alkyne click-reaction conditions.

The application of the functionalized *m*[6]CPP **115** in vivo has revealed its potential in two-photon live cell imaging. Furthermore, this type of fluorophore demonstrates noncytotoxic up to 50 μ M and displays photostability akin to commercially available fluorescent probes, enabling continuous imaging for a duration exceeding 200 s.¹⁶⁸

Following the approach used previously for parent [*n*]CPPs, the recent integration of the *m*[6]CPP scaffold into a polymer matrix has been studied to enhance their properties and evaluate their complete potential in materials. Thus, in 2023, ZHANG et al. utilized alkynyl-*m*[6]CPP **113** in an azide-alkyne click-reaction to introduce a norbornene scaffold into the side chain.¹⁷¹ Following the use of ROMP conditions on monomer **116**, subsequently resulted in **poly-116** (Scheme 19).



Scheme 19. Schematic representation of the synthesis towards monomer **116** derived from alkynyl-*m*[6]CPP **113**.

Investigation of the photophysical characteristics of **poly-116** demonstrated that the inherent properties of *m*[6]CPP are preserved after the polymerization process. This highlights the achievement of incorporating *m*[6]CPP scaffold as a fluorophore into materials without compromising its valuable properties.

However, as previously demonstrated, there has been a recent surge of interest in the field of inorganic-organic hybrid materials, which involve the incorporation of the cycloparaphenylene framework. These hybrid materials possess the capability to enhance the properties of the organic compound and act as a gateway to unexplored areas of research. Among a variety of possibilities, *N*-heterocyclic carbenes emerge as an interesting alternative as a category of ligands that can open up new avenues for cycloparaphenylenes.

1.6. *N*-Heterocyclic Carbenes as Ligands for Luminescent Gold-Complexes

In recent years, there has been a significant amount of attention devoted to the design of luminescent (transition-)metal complexes containing *N*-heterocyclic carbenes (NHCs).^{172–175} This kind of carbenes are carbon-based compounds that are neutrally charged in nature. They consist of a divalent carbon atom with a valence shell that contains six electrons. A generic carbene possesses a pair of spin states, which lead to distinct reactivity and structure. In SCHROCK-type carbenes, there are two unpaired electrons in a sp^2 -hybridized and a p -orbital, leading to an electronic configuration in the triplet state (SCHROCK-type carbene). Conversely, in the singlet configuration, these two now paired electrons are situated within a sp^2 -hybridized carbene carbon, while the p -orbital remains unoccupied (FISCHER-type carbene) (Figure 24).¹⁷⁶

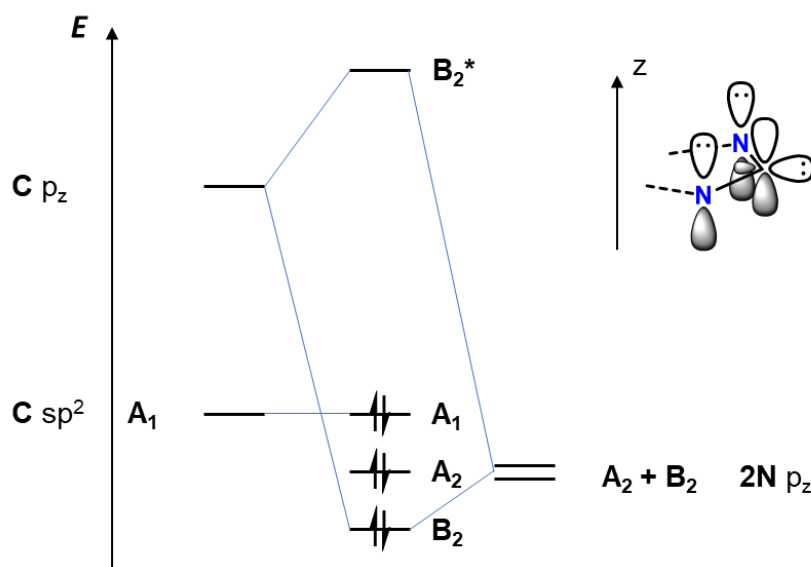


Figure 24. Molecular orbital diagram of a FISCHER-type *N*-heterocyclic carbene.

However, due to their incomplete electron octet and coordinative unsaturation, free carbenes are considered to be inherently unstable and highly reactive intermediates.¹⁷⁷ Initial attempts to synthesize, isolate, and characterize a free and uncoordinated carbene were made by J. B. DUMAS in 1835.¹⁷⁸ His approach involved the dehydration of methanol, using strong reagents like phosphorous pentoxide or sulfuric acid, which resulted in the production of methylene as the carbene species. Following these early attempts, there was a significant advancement in the studies on NHCs during the late 1980s and early 1990s. In

1988, BERTRAND and his colleagues successfully isolated the first carbene that was stabilized through phosphorous and silicon substituents (Figure 25, left).^{179,180} Three years later, in 1991, ARDUENGO et. al. reported the first stable and isolable carbene incorporated into a nitrogen heterocycle (Figure 25, right).¹⁸¹

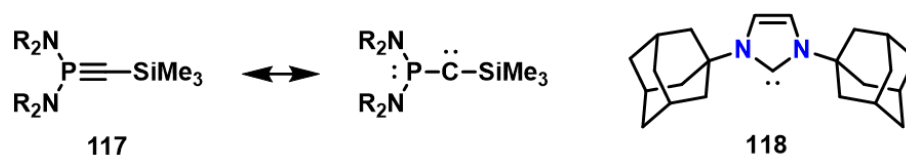


Figure 25. BERTRAND's carbene **116** stabilized through P- and Si substituents (left). ARDUENGO's carbene **117** stabilized through the nitrogen heterocycle (right).

Since then, NHCs have become one of the most powerful ligands in the field of organic chemistry, with numerous applications of industrial significance.^{182–189} Although NHCs are inherently reactive species, their cyclic structure, and the presence of heteroatoms aid in increasing their stability. The key structural parameters that contribute to stabilization and the electronic ground-state are depicted in Figure 26.^{190,191}

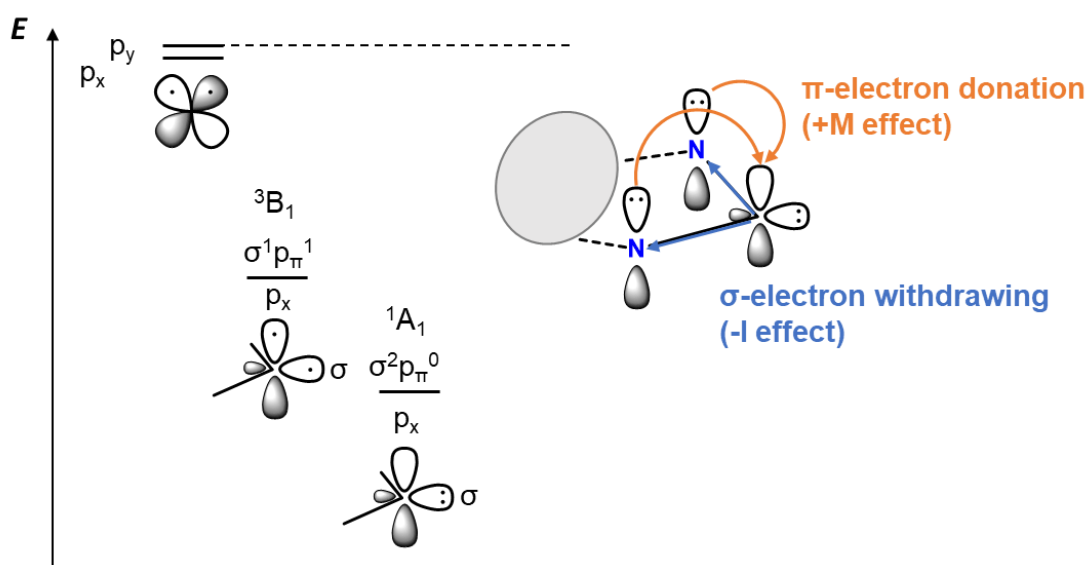


Figure 26. Relative energies of the normally degenerated p-orbitals and possible ground state electron configuration of carbenes.

In general, the presence of nitrogen atoms can greatly enhance the stability of the carbene. Due to their high electronegativity, they withdraw electron density at the carbenic carbon (HOMO; σ -electron withdrawing), while the lone pairs of the nitrogen atoms can overlap with the empty p-orbital of the carbenic carbon (LUMO; π -electron donating). In combination, both effects can be described as a push-pull

effect, which increases the energy gap between HOMO and LUMO, thereby stabilizing the singlet ground state. As seen in the first example of ARDUENGO, sterically demanding groups on the *N*-substituents can protect the reactive center from potential dimerization or decomposition, while their identity can influence the electronics of the ring system.¹⁸¹ Following the same design principle, further examples show, that NHCs can stabilize transition metals in both higher and lower oxidation states.^{192–194} The thermodynamic stability of NHCs is usually discussed in terms of the backbone structure. The presence of an unsaturated backbone contributes to the aromatic character of the heterocyclic system and thus enhances the thermodynamic stability. For example, the effect of stabilization has been calculated to be approximately 25 kcal mol⁻¹ for imidazole-2-ylidenes compared to corresponding imidazoline-2-ylidenes.¹⁹⁵ Lastly, the electronics of the system can be altered by different substitution patterns or ring sizes. The latter affects the preference for bent singlet ground states and has an impact on both steric electronic features, which are crucial in the fields of materials science and catalysis.

Among the various NHC transition-metal complexes, those containing gold as the metal center have attracted substantial attention in recent years.^{196–198} These complexes have proven not only to be highly valuable catalysts^{199–202} but found additional applications in the areas of gold nanomaterial design^{203–209} as well as life sciences (Figure 27).^{210–212}

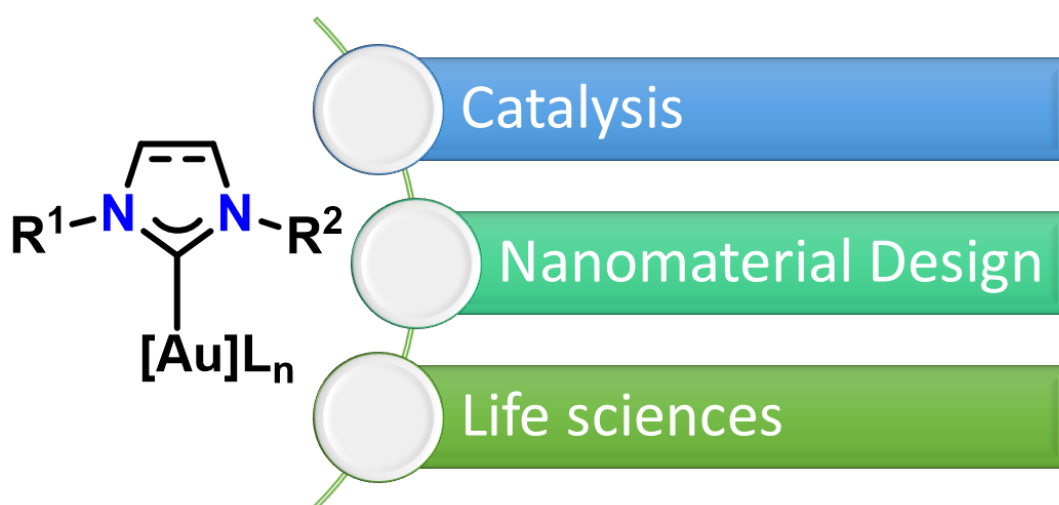


Figure 27. Applicational fields of NHC gold-complexes.

However, NHC ligands with an extended π -system have received significant attention in recent years not only due to their potential applications in catalysis but also in optoelectronics. The utilization of several (first and foremost Ir and Pt) containing these NHCs as chromophores has proven to be effective in organic light-emitting diodes (OLEDs) as efficient triplet emitters. This is attributed to their high stability and favorable emission properties.²¹³ It is known that Au(I) complexes exhibit aurophilic interactions and give rise to emissive excited states.^{214,215} Those complexes that possess ligands with large π -systems and energetically low-lying excited π - π^* states display intense intraligand emissions.^{216,217} On the other hand, Au(III), with its low-lying d-d-states, effectively quenches the excited state, leading to a decrease or even complete inhibition of luminescence.²¹⁸ Therefore, Au(III) complexes only exhibit luminescence if strong ligands destabilize these d-d-states and hinder radiationless deactivation.²¹⁹ For this reason, several groups designed novel NHC-gold complexes with chromophores attached and tuning their luminescent properties. In 2012, KRIECHBAUM et al. synthesized NHC ligand **119**, mimicking 1,10-phenanthroline and studied its coordination properties within Au(I) and Au(III) complexes.²²⁰ This study was further expanded in 2013 including the investigation of NHC ligands based on the imidazol[1,5- α]quinolinol scaffold **120**.^{220,221} Both imidazolium precursors are displayed in Figure 28.

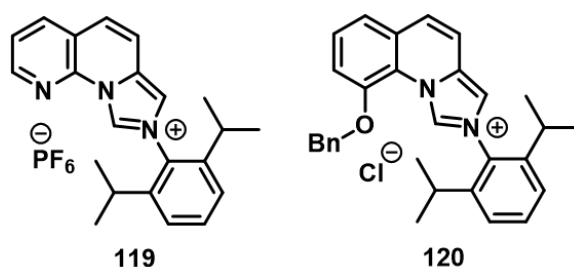
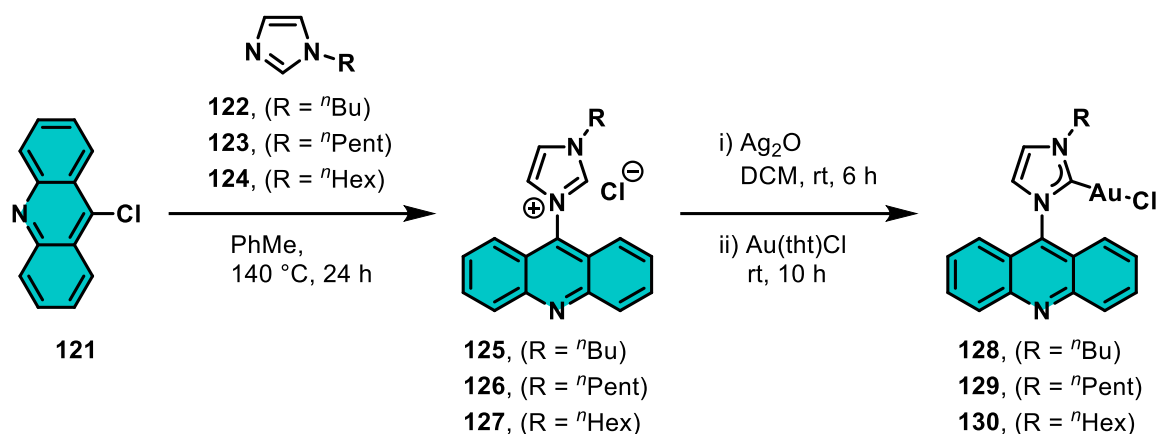


Figure 28. 1,10-Phenanthroline mimicking NHC **119** and 10-hydroxybenzo[h]quinolone mimicking NHC **120**.

Both scaffolds show luminescent behavior with a maximum wavelength at approximately 380 nm (**119**) and 350 nm (**120**), respectively, which derives from intraligand excited states.^{220,221}

In 2021, VADDAMANU et al. conducted a comprehensive study on the influence of the alkyl chain length on the optical properties of an acridine-substituted NHC gold complex (Scheme 20).²²²



Scheme 20. Synthesis of acridine-NHC-Au complexes **126** - **128** for the investigation of their luminescent properties depending on the alkyl-chain lengths on the second wingtip.

They were able to shift the solid-state fluorescence from yellow ($\lambda_{em} = 542$ nm) to deep blue ($\lambda_{em} = 420$ nm) by elongating the alkyl chain length from *n*-butyl (**128**) to *n*-hexyl (**130**). In solution, these molecules exhibited blue emission ($\lambda_{em} = 405$ nm – 415 nm). This shift in color can be explained by the folding effects of the alkyl chains, as well as intra- and intermolecular interactions, as evidenced by the X-ray solid-state structures.²²²

A versatile organic fluorophore used in NHC transition-metal complexes is naphthalimide. This compound has found utility in DNA targeting as well as in the development of anticancer and cellular imaging agents.^{223,224}

In 2021, JAMALI and coworkers synthesized a series of tetra-naphthalimide-substituted NHC coinage-metal complexes **131** - **134** to study their structure-emission relationship (Figure 29).²²⁵

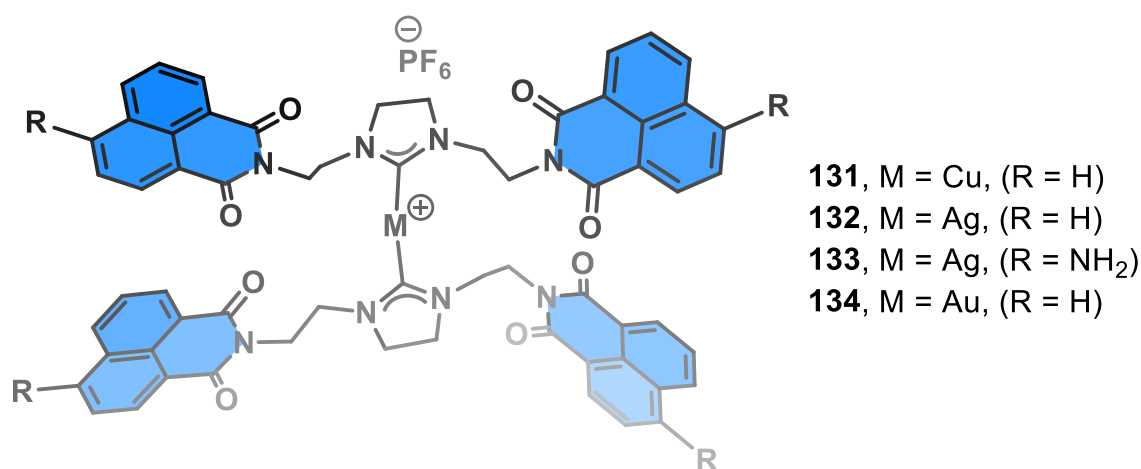


Figure 29. Tetra-naphthalimide substituted NHC coinage-metal complexes **131** - **134**.

Depending on the transition metal and the state of the material (solid-state or solution), significant differences in quantum yield efficiency were observed. In solution, the alignment of fluorophore units facilitated intramolecular interchromophoric interactions, leading to enhanced quantum yield efficiency. In the solid-state, $n \rightarrow \pi^*$ and inter- and intramolecular π -interactions replace the strong intramolecular π - and solute-solvent interactions, resulting in decreased efficiency. Furthermore, an increased quantum yield efficiency was achieved by introducing larger dihedral angles between two overlapping fluorophore units, which was facilitated by a larger metal ionic radius.²²⁵

Besides in the aforementioned research areas, NHC transition metal complexes can be utilized as sensor materials. For this reason, PLENIO's research group synthesized various BODIPY-substituted NHC-transition-metal complexes based on scaffold **135** as CO sensors in 2014, as depicted in Figure 30.²²⁶

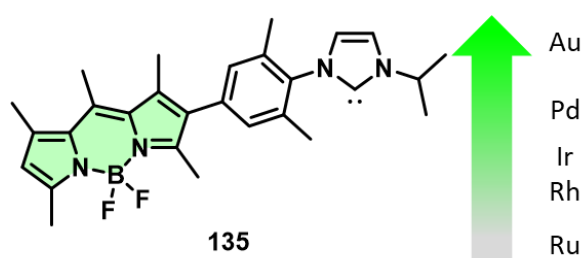


Figure 30. BODIPY NHC-transition-metal complexes **135** with Ru, Rh, Ir, Pd, and Au.

The brightness of these transition-metal complexes relied on both the substitution of the ligand and the transition-metal center. Notably, an increased brightness was observed from Ru (strongly quenched) to Rh, Ir, Pd, and finally Au (strongly fluorescent). By manipulating the electron density at the transition metal through ligand-substitution reactions, the efficiency of the PET quenching could be modulated. Specifically, electron-rich transition metals resulted in decreased fluorescence, whereas electron-deficient metal centers enhance the fluorescence emission.²²⁶

In a different study in 2022, the PLENIO's synthesized a similar BODIPY-substituted NHC ligand **136** for diverse transition-metal complexes for the conversion of $^3\text{O}_2$ to $^1\text{O}_2$. In contrast to the previously described work, the BODIPY is now directly attached to the NHC core (Figure 31).²²⁷

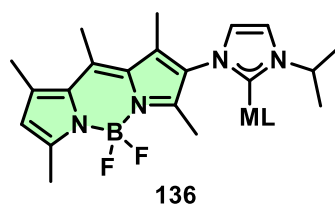


Figure 31. Modified structure of BODIPY NHC-transition-metal complexes tested as photosensitizers for the generation of ^1O .

These complexes were further utilized to investigate their photosensitizing properties for the generation of ^1O . Through ligand exchange from cyclooctadiene to carbon monoxide on the iridium complex **136-Ir**, the singlet oxygen quantum yield could be increased from 0.09 to 0.63.²²⁷

In addition to the BODIPY-substituted NHC-transition-metal complexes, PLENIO and coworkers explored coumarin-substituted NHC-transition-metal complexes, either attached to the NHC-moiety or with a short ethylene linker in between.²²⁸ Unfortunately, the complexes where the coumarin was directly attached to the NHC decomposed in most cases, rendering further studies impossible. Only the gold complex **137-Au** remained stable enough for comparison to its bridged derivative **138-Au**, which exhibited significant fluorescence quenching when reacted with *para*-substituted aryl thiols. This led to the conclusion that (very) short distances between the fluorophore and the transition-metal are highly favorable for such probes (Figure 32).²²⁸

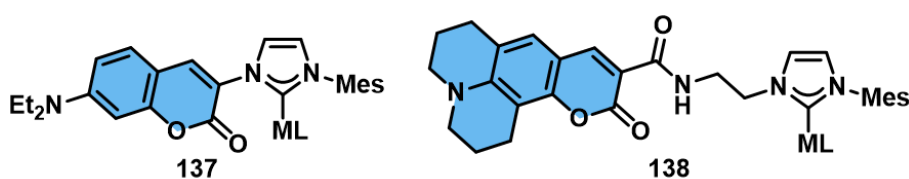
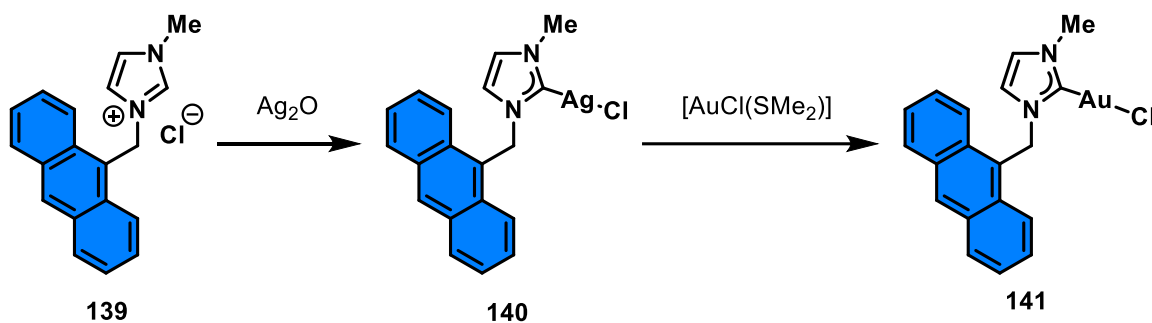


Figure 32. Coumarin NHC-transition-metal complexes **137** and **138**, which can be used as CO sensor.

Furthermore, the bridged coumarin-NHC-transition-metal complexes underwent efficient ligand-substitution reactions with carbon monoxide, resulting in the activation of their blue fluorescence. In terms of ensemble measurements in solution, the coumarin derivatives performed similarly to the BODIPY-derivatives. However, they lacked the efficient brightness required for single-molecule studies, making the BODIPY-derivatives more crucial in this regard.²²⁸

Moreover, [AuX(NHC)] complexes have emerged as intriguing compounds owing to their biological and luminescent properties.¹⁹⁷ Therefore, selected examples of fluorophore-NHC-Au complexes are presented within the next section.

In 2013, CITTA et al. reported the synthesis and characterization of a new Au(I)-NHC complex **141** (Scheme 21), bearing an anthracenyl unit anchored to the N1 position of the NHC scaffold.²²⁹



Scheme 21. Synthesis of anthracene-NHC-transition-metal complexes **138** and **139** with cytotoxic properties.

Both complexes showed cytotoxic effects in human ovarian cancer cell lines, including *cis*-platin-resistant cells. The silver complex **140** was particularly selective for cancer cells. Fluorescence microscopy experiments showed that both compounds **140** and **141** can enter cells and efficiently penetrate tumor cells, reaching the nuclear compartment.²²⁹

In 2014, CASINI et al. synthesized the coumarin-NHC gold(I) complex **142**, bearing a thio-glucose as the second ligand and investigated their cytotoxic effects in normal and cancer cells in vitro (Figure 34, left).²³⁰ Fluorescence microscopy was used for cellular uptake studies and showed a moderate antiproliferative effect of their compounds. A similar compound was synthesized by GIMENO's group in 2016, bearing an acridine moiety as fluorophore (Figure 33, right).²³¹

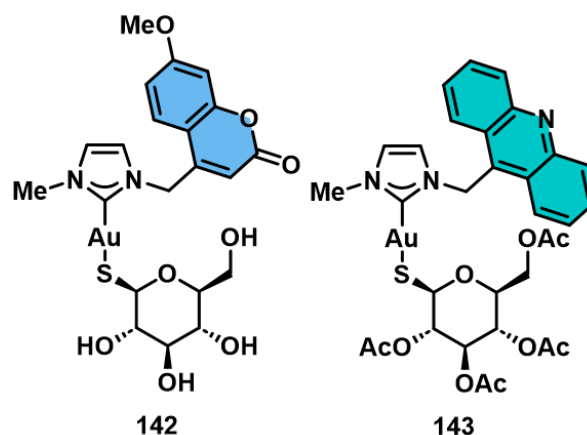


Figure 33. Fluorophore-NHC-Au complexes **142** and **143** for cytotoxicity studies.

The lung and pancreatic cells tested in the study showed the highest sensitivity to complex **143** compared to its Ag(I) analog. Moreover, **143** reached the highest cytotoxic activity within these cells. Fluorescence microscopy helped to reveal the lysosomes as targeted localization.²³¹

As the aforementioned examples demonstrate, NHCs are an intriguing class of ligands. Due to their strong σ -donor characteristics, they have emerged as an important class of compounds in various research areas including material sciences and life sciences. Another different type of ligands is based on the bicyclo[2.2.2]octa-2,5,7-triene motif. Due to its geometric structural properties, it can serve as a diene ligand for the preparation of transition-metal complexes as well as a monomer for ring-opening metathesis polymerization.

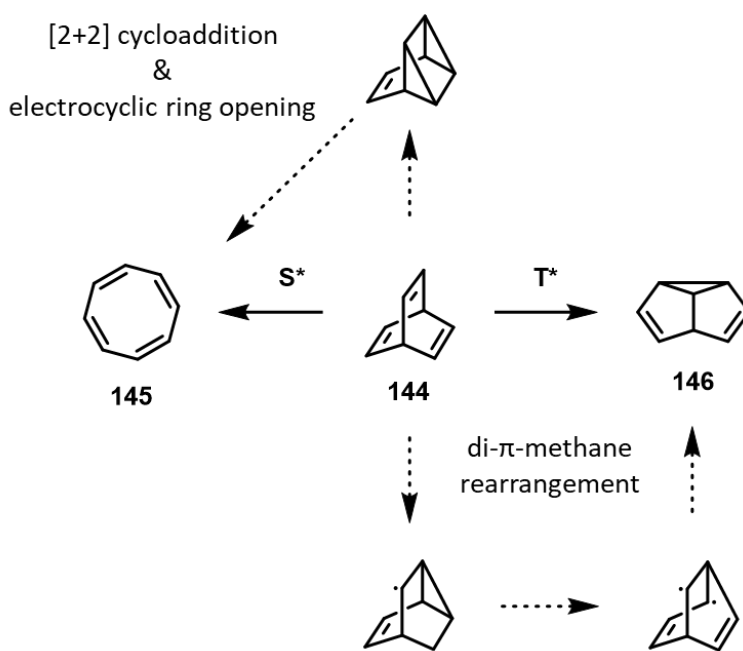
1.7. Barrelenes

Barrelene (bicyclo[2.2.2]octa-2,5,7-triene, **144**) was initially discovered and named *klovosene* by HINE in 1955.²³² Following its first synthesis in 1960, ZIMMERMAN and PAUFLER renamed this kind of molecule as *barrelene* due to its resemblance to the molecular orbitals in the shape of a wooden barrel (Figure 34)²³³



Figure 34. Bicyclo[2.2.2]octa-2,5,7-triene (**144**) and its arrangement of p-orbitals.

Barrelene and its derivatives, including (di-)benzobarrelenes and triptycenes, are well-known for their structure-controlled definite photophysical and -chemical properties. Notably, the singlet- and triplet- mediated photo transformations leading to the formation of cyclooctatetraenes (**145**) or semibullvalenes (**146**) have been extensively investigated after their initial examination by ZIMMERMANN and GRUNEWALD in 1966.²³⁴ Both mechanisms are depicted in Scheme 22.

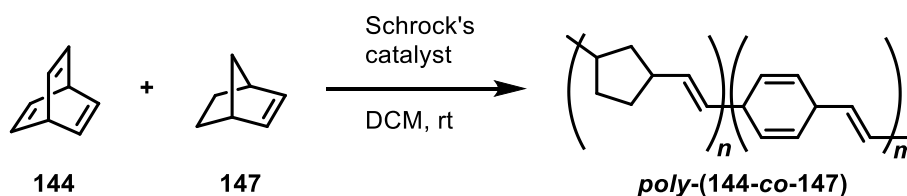


Scheme 22. Singlet- and triplet-mediated photo transformations of barrelene **144** towards cyclooctatetraene (**145**) and semibullvalene (**146**).

While the formation of cyclooctatetraene (**145**) is formed through a [2+2] cycloaddition and subsequent electrocyclic ring opening of the cycloadduct, following a singlet mediated pathway. The semibullvalene (**146**) is formed through

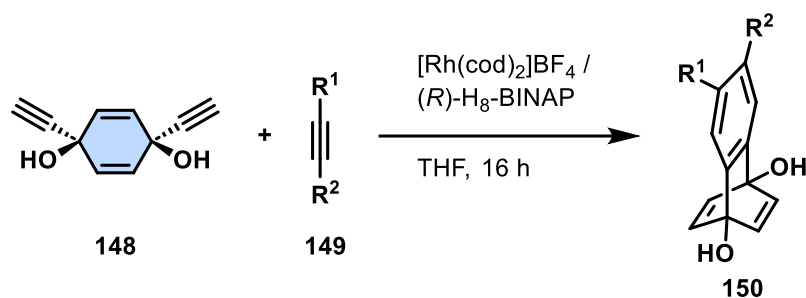
a triplet mediated pathway, involving a di- π -methane rearrangement²³⁵ that results in the formation of a biradical species.

Due to their MÖBIUS aromatic π -system²³⁶, (benzo-)barrelenes have not only been explored in photochemical reactions²³⁷ but have also been utilized as diene ligands for transition-metal complexes^{238–241} and monomers for ROMP²⁴². Recently, barrelene was characterized for the first time through X-ray diffraction analysis of a [Rh(barrelene)Cl]₂ complex and further utilized in ROMP by BIELAWSKI and co-workers.²⁴³ In their study, they also synthesized a block-co-polymer consisting of barrelene **144** and norbornene **147**, which could be utilized in direct laser writing and visualized through the fluorescence of the corresponding conjugated polymer after irradiation (Scheme 23).



Scheme 23. Co-polymerization of barrelene **144** and norbornene **147** for direct laser writing.

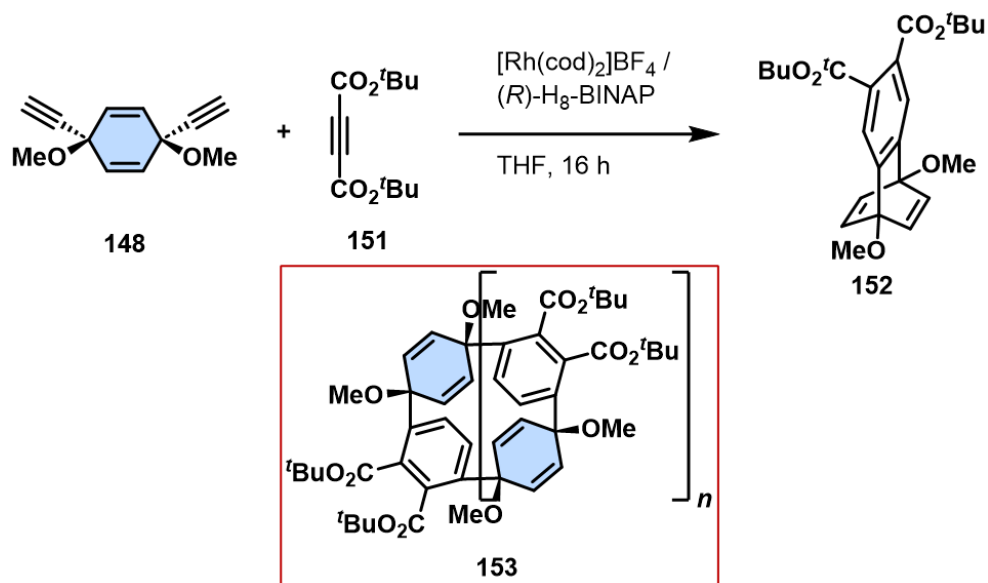
Thus far, only a limited number of functionalized benzobarrelenes have been synthesized through conventional [4+2] cycloaddition of alkynes with naphthalenes^{244,245} or arynes with benzenes^{246,247}. Another synthetic approach was presented by TANAKA's group in 2016, using the transition-metal-catalyzed [2+2+2] cyclotrimerization of cyclohexadiene-linked 1,7-diyenes **148** with monoynes **149** (Scheme 24).²⁴⁸



Scheme 24. Synthesis of substituted **157** through Rh-catalyzed [2+2+2] cyclotrimerization.

Interestingly, the same synthetic approach used by TANAKA's group for their benzobarrelenes was also used to approach the relatively unstrained macrocyclic precursors for differently sized substituted cycloparaphenylenes. However, this

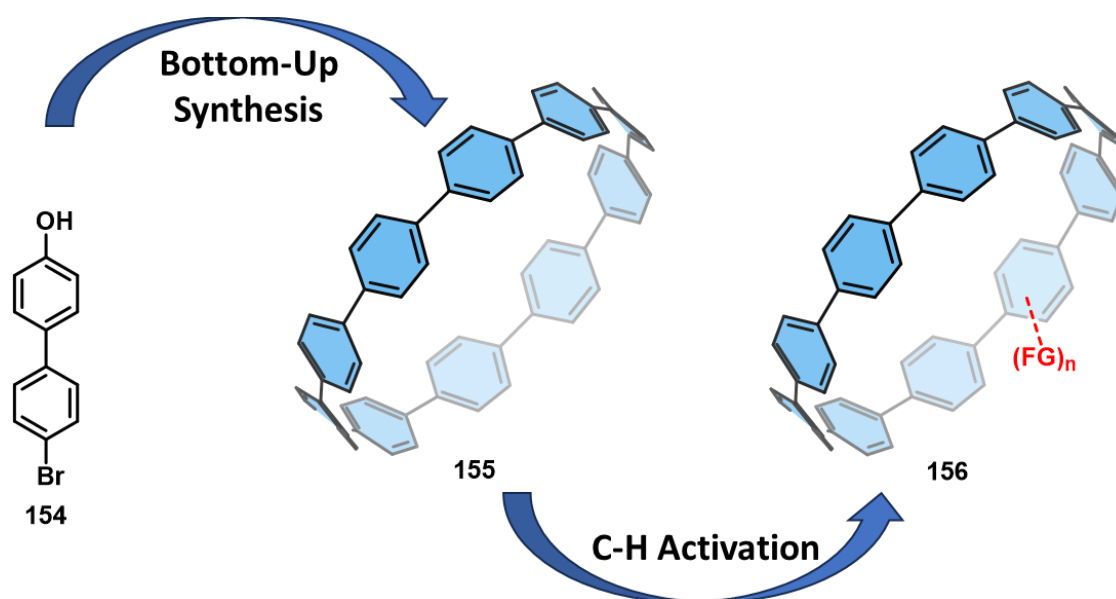
synthetic approach did not lead to the desired functionalized $[n]$ CPP precursor **153** but instead to the formation of the substituted benzobarrelene **152** (Scheme 25).²⁴⁹



Scheme 25. Rh-catalyzed cyclotrimerization towards barrelene **152**.

2. Objectives

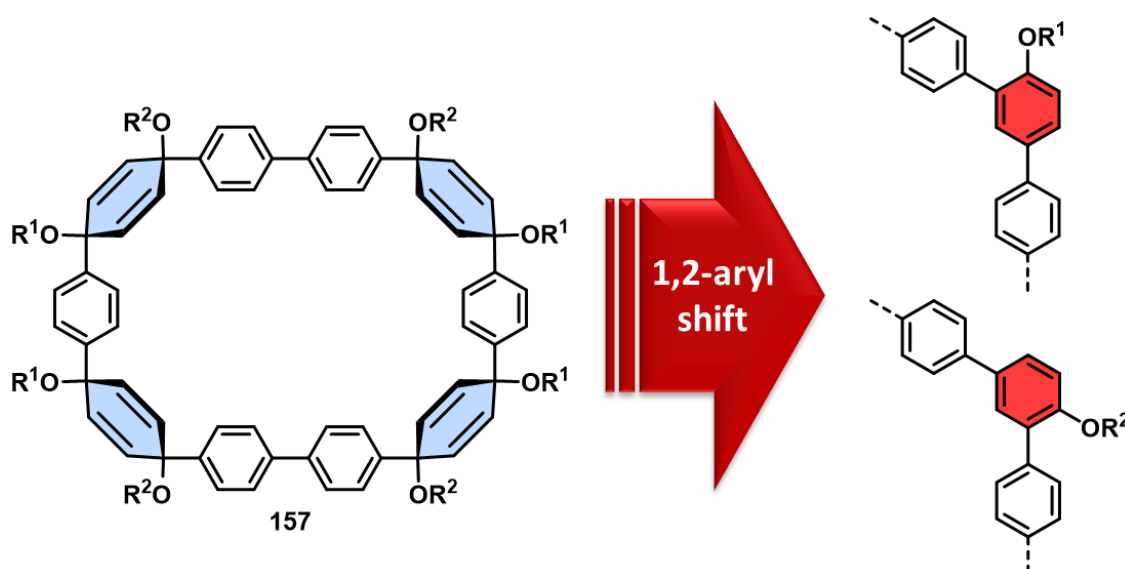
A topic that began as a concept for a synthetic method to prepare single-walled armchair carbon-nanotubes, gained significant attention after the first successful synthesis of cycloparaphenylenes in 2008. This development led to the emergence of a new category of small-molecule fluorophores with diverse applications. Cycloparaphenylenes, characterized by their cyclic structure and distinctive photophysical and chemical properties, find utility in various fields, ranging from studying fundamental interactions to the fields of material and life sciences. Unfortunately, the functionalization of these systems in a convenient manner remains a formidable challenge. Consequently, it is necessary to assess different strategies for the synthesis of unsubstituted $[n]$ cycloparaphenylenes ($[n]$ CPPs) and to establish a straightforward approach for the synthesis of [10]CPP **155** within our research group. Once a suitable synthetic approach is integrated into the group's workflow, the selective functionalization of [10]CPP **155** needs to be achieved by using C-H activation as the preferred method (Scheme 26).



Scheme 26. Synthesis of [10]CPP **155** and its top-down functionalization through C-H activation.

Another aspect of this research focuses on the typically undesirable 1,2-aryl shift that can occur during the synthesis of cycloparaphenylenes at various stages. *Meta* $[n]$ cycloparaphenylenes, as described by JASTI and colleagues in 2019, exhibit similar exceptional properties compared to the parent $[n]$ CPPs. Therefore, the concept of inducing the 1,2-aryl shift for the synthesis of *meta* $[n]$ CPPs was

conceived. Consequently, the investigation by the group of SOLOMEK had to be extended to examine selectivity and applicability to pre-strained macrocyclic structures. Theoretically, this shift can occur on any cyclohexadiene moiety incorporated into the molecule. Thus, different ring sizes should allow for varying numbers of *meta*-connectivity, providing new anchor points for further functionalization of the molecule (Scheme 27).



Scheme 27. Investigation of a 1,2-aryl shift on the macrocyclic precursor **157**.

Another aspect explored in this study involves the synthesis of nitrile-substituted $m[n]$ CPPs of various ring sizes, building on the concept of functionalized derivatives. This investigation aims to demonstrate the efficacy of this functional group as a convenient handle in regards of chemical transformations. In addition, the supramolecular properties of CN- $m[10]$ CPP **160** will be investigated, as these properties have not yet been reported for the unsubstituted molecule (Figure 35).

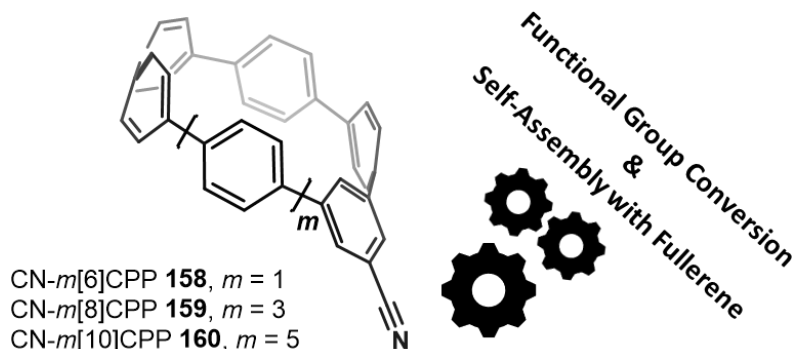


Figure 35. Project aim for the investigation of $m[n]$ CPPs **158** - **160**.

The final section of this research focuses on the potential applications of *m*[6]CPP as chromophore unit within a gold(I)-complex. To this end, a strategy has been devised to attach *m*[6]CPP as a fluorescent wingtip to a *N*-heterocyclic carbene (NHC). Given the bulkiness of the wingtip, the whole system should be stabilized, and different energy transfer processes may become observable. Furthermore, this work addresses the use of a benzobarrelene-type CPP as either a bidentate ligand or a building block for ring-opening polymerization (Figure 36).

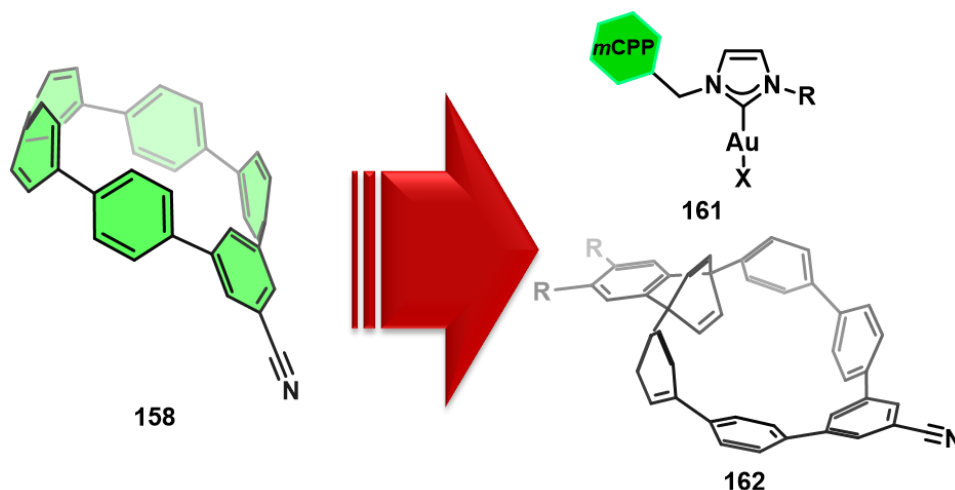


Figure 36. *Meta*[6]CPP **158** serving as platform for different transition-metal ligands.

More general, this research is concerned with (un-)substituted (*meta*)[*n*]CPPs, seeking to promote this distinctive category of fluorophores and their various applications. The primary aim of this study is to establish a range of synthetic methods for synthesizing these compounds and to carry out a thorough investigation of their photophysical properties (Figure 37).

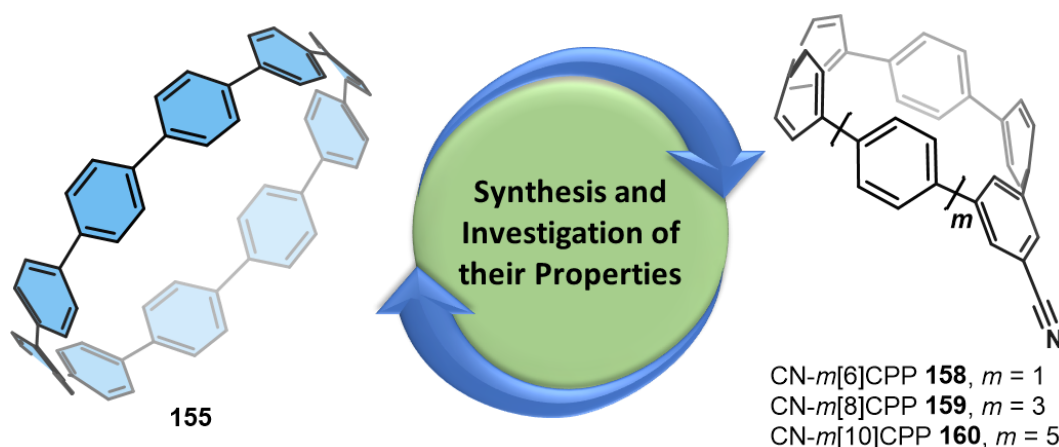


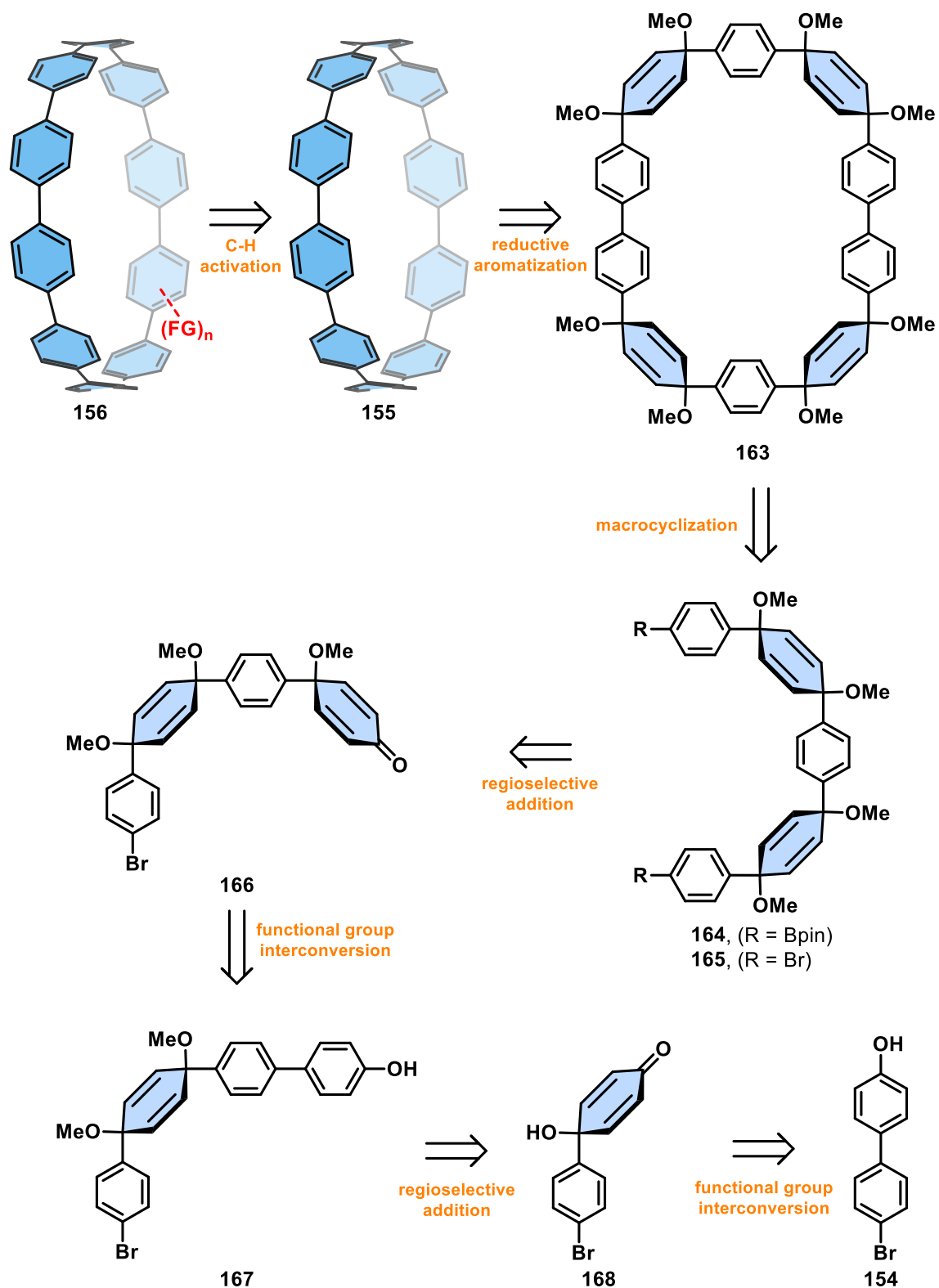
Figure 37. General research purpose of this work.

3. Results and Discussion

The following presented results will be discussed in three parts. The first part describes the efforts towards the post-functionalization of [10]CPP **155**. Consequently, different synthetic routes towards this molecule will be discussed. The second part represents the efforts towards *meta*-connected macrocyclic structures triggering the 1,2-aryl shift, which can occur as an unwanted side reaction in the synthesis of [n]CPPs. The last part of the results discusses the relatively new class of *meta*[n]CPPs (*m*[n]CPPs) and the efforts to advance them in different research areas.

3.1. C-H Activation towards the Post-Functionalization of [10]Cycloparaphenylene

[10]CPP **155** takes a prominent role in the field of [n]CPPs because its diameter of 1.38 nm¹¹³ makes it an excellent host for fullerene C₆₀. Additionally, it exhibits a low amount of strain energy, rendering bromination ineffective for successful post-functionalization. Therefore, an alternative approach is necessary, and we hypothesized that C-H activation of the molecule could be a promising approach. Consequently, the following synthetic strategy towards the C-H activation of [10]CPP **155** and its synthesis was developed (Scheme 28).

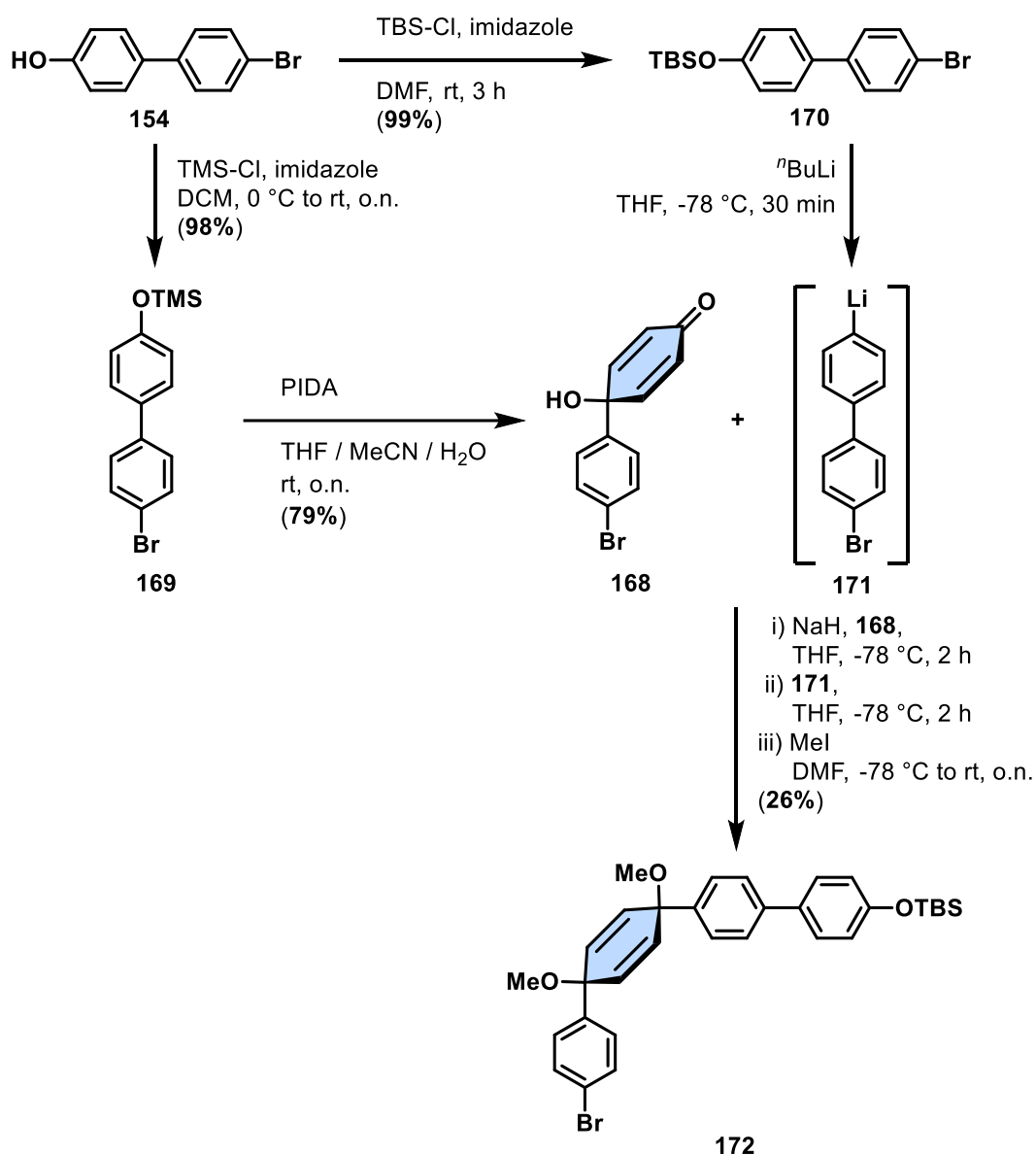


Scheme 28. Retrosynthetic analysis of the C-H functionalization and the synthesis of [10]CPP **155** starting from biphenyl **154**.

The goal was to selectively functionalize the molecule through C-H activation of one of the phenyl units. It was planned to distinguish between mono-functionalization and the maximal possible number of functional groups being

aware that functional group directing effects will occur upon successful mono-functionalization. Naturally, the realization of this idea required the synthesis of [10]CPP **155** itself. To achieve this, the gram-scale bottom-up synthesis of [10]CPP **155**, as published by the JASTI group in 2012,⁵³ was used as a starting point. The utilization of the cyclohexadiene motif in the macrocyclic precursor **163**, which is compared to **155** relatively unstrained, has proven to be advantageous compared to the use of cyclohexane units or platinum complexes. The macrocyclic precursor can be synthesized through a SUZUKI cross-coupling reaction under high dilutions, utilizing building block **165** and its borylated analog **164**. Building block **165** is sequentially synthesized through the combination smaller building blocks derived from the 1-bromo-1'-hydroxy-biphenyl (**154**).

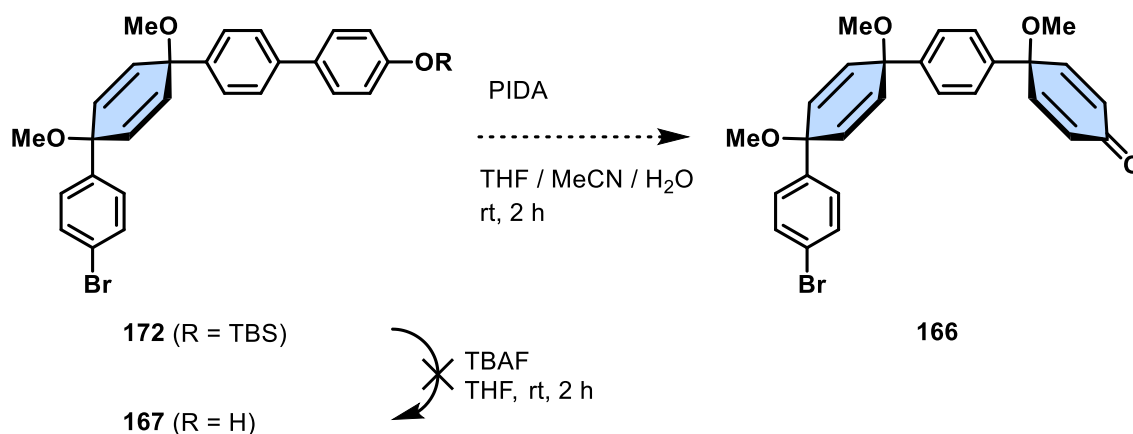
Starting with 1-bromo-1'-hydroxy-biphenyl (**154**), the two different silylated species **169** and **170** were synthesized. The introduction of these different protecting groups is necessary as they function in different contexts. On the one hand, the trimethyl silyl (TMS) protecting group is susceptible to acidic conditions, which is crucial for the incorporation of the cyclohexadiene motif in the subsequent step. On the other hand, the *tert*-butyl dimethyl silyl (TBS) protecting group is more stable than the TMS group, allowing for the regioselective combination of the two building blocks to form building block **172** (Scheme 29).



Scheme 29. Synthesis of building block **172** through the combination of the silylated building blocks **169** and **170**.

The addition of either TMS-chloride (TMS-Cl) or TBS-chloride (TBS-Cl) in dichloromethane (DCM) or dimethyl formamide (DMF), respectively, along with imidazole as a base and activation reagent, facilitated the introduction of the protecting groups on **154**. Both protection reactions yielded nearly quantitative results. Subsequent oxidation of building block **169** using phenyliodo diacetate (PIDA) successfully introduced the cyclohexadiene motif with a good yield of 79% after recrystallization. The next step presents a convenient method to combine smaller [*n*]CPP building blocks for the rapid construction of larger building blocks. The TBS-protected building block **170** is lithiated and subsequently undergoes a nucleophilic attack on the deprotonated cyclohexadienone **168**. The negative

charge at the oxygen, resulting from the deprotonation utilizing NaH, along with the sodium ion, shields one side of the cyclohexadienone and leads to the desired regioselective attack, resulting in the formation of building block **172** with a yield of 26%.⁵³ During the synthesis, several parameters were identified that could explain the lower yield compared to the literature. Each step must be carefully controlled in terms of temperature and homogeneity, as local temperatures within the flask above -60 °C led to the decomposition of intermediates. Particularly, on a large scale, these parameters can pose a challenge in terms of control. In addition, the purification of this building block is achieved through column chromatography. Due to the susceptibility of the cyclohexadiene moiety to acidic conditions, there is a possibility of material decomposition or a 1,2-aryl shift. The concern regarding a 1,2-aryl shift becomes even more relevant when discussing the subsequent step of the silyl-ether cleavage. However, with the building block **172** in hand, the synthesis towards building block **166** by removing the silyl-ether and subsequently oxidation of **167** (Scheme 30) was addressed.



Scheme 30. Synthesis attempt towards building block **166** after cleavage of the silyl-ether group on **172**.

Upon the addition of tetra-butyl ammonium fluoride to a solution of **172** in THF at room temperature, the anticipated product was not detected in the ¹H-NMR spectrum. Further investigation revealed that it is more probable that a 1,2-aryl shift has occurred on scaffold **166**, resulting in a quantitative conversion to the functionalized *meta*-quarterphenyl **173** (Figure 38).

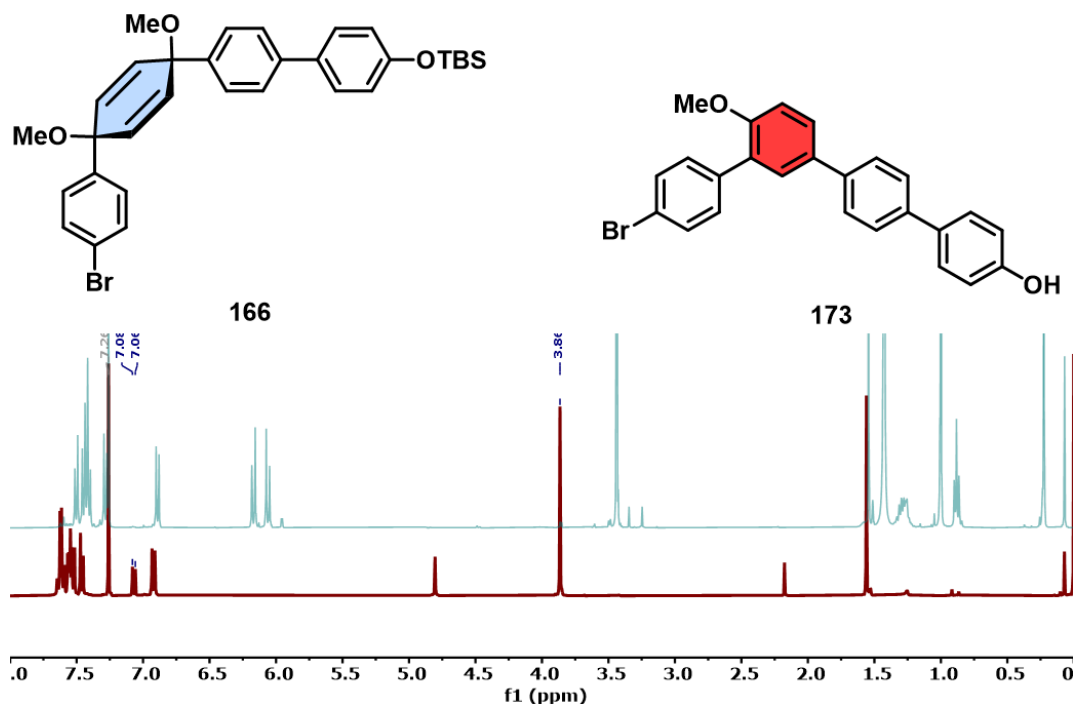
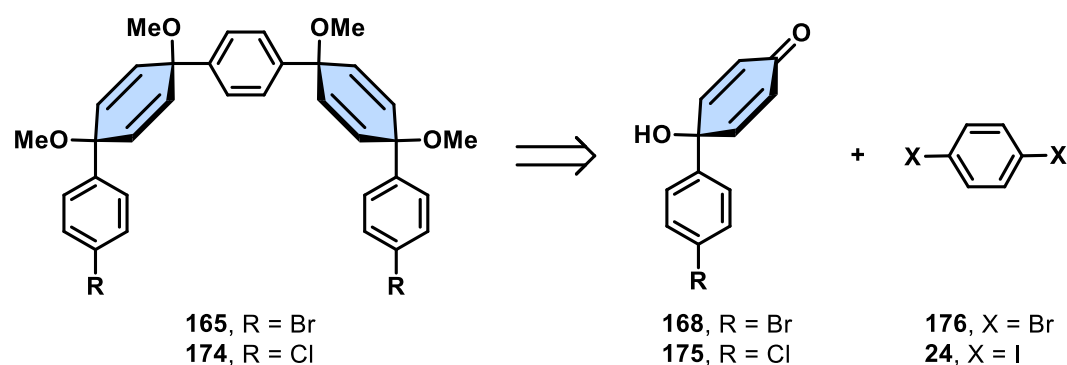


Figure 38. Comparison of the ^1H -NMR spectra in CDCl_3 at room temperature of building block **165** with the obtained spectrum of **173**.

A comparison between the two ^1H -NMR spectra of the starting material **165** and the crude product of the reaction demonstrated the successful cleavage of the silyl-ether, as in the aliphatic region, the signals are vanished (compare 0.5 ppm – 1.5 ppm). Unfortunately, the disappearance of the characteristic multiplet signals originating from the cyclohexadiene motif (around 6.00 ppm and 6.18 ppm) and the disappearance of the signal caused by the protons of the methoxy groups (around 3.40 ppm), indicate that the desired product **167** was not obtained. Moreover, the presence of new signals at around 7.07 ppm and 3.86 ppm indicate that aromatization resulting from a 1,2-aryl shift has taken place. Analyzing 1D- and 2D-NMR spectra additionally revealed that the bromo-phenyl segment of the molecule migrates to form the aromatized product **173**.

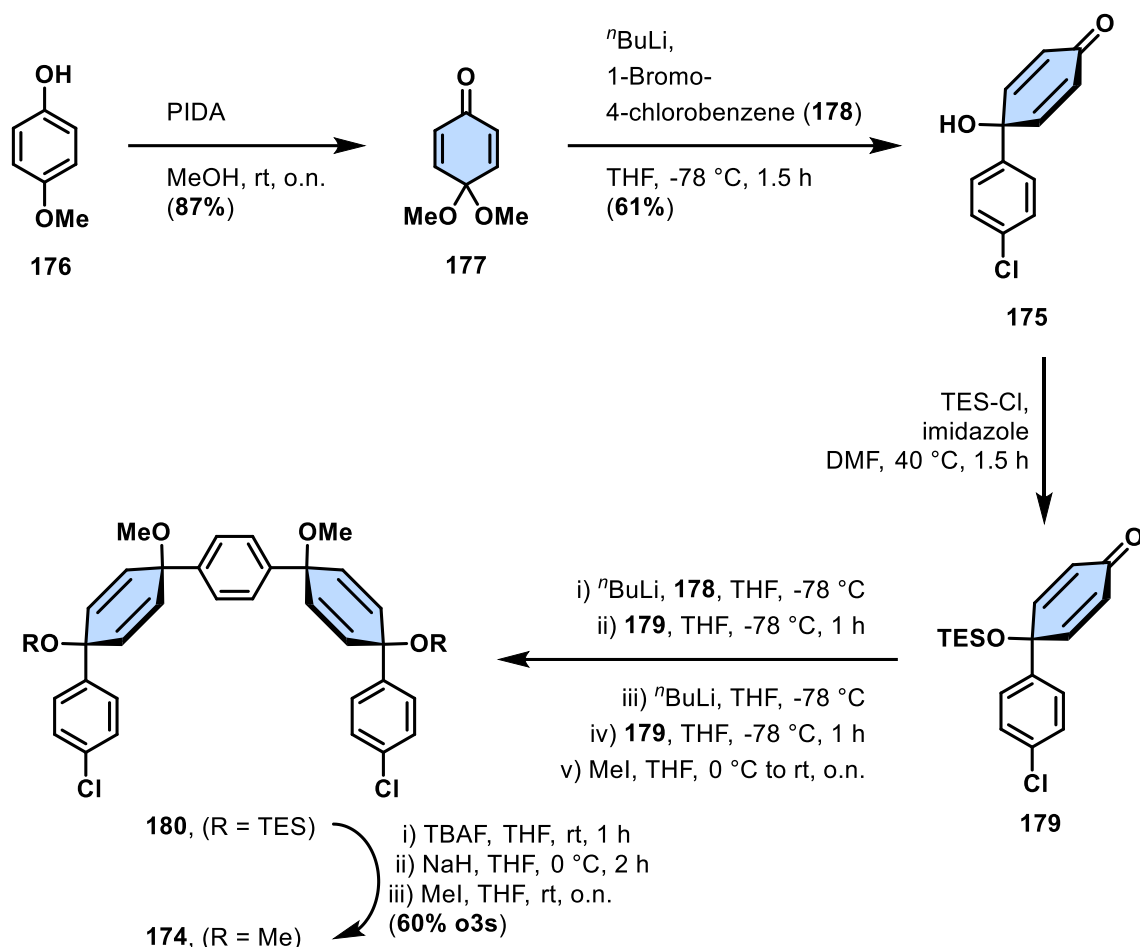
Since the aforementioned circumstances and the low yield in this synthesis could not be resolved after additional attempts, an alternative synthetic approach was devised for the successful synthesis of [10]CPP **155**. By retaining building block **165** as a central motif, it was intended to follow the synthesis approach published by JASTI's group in 2017 (Scheme 31).⁷⁴



Scheme 31. Modified retrosynthetic strategy towards building blocks **165** and **174**.

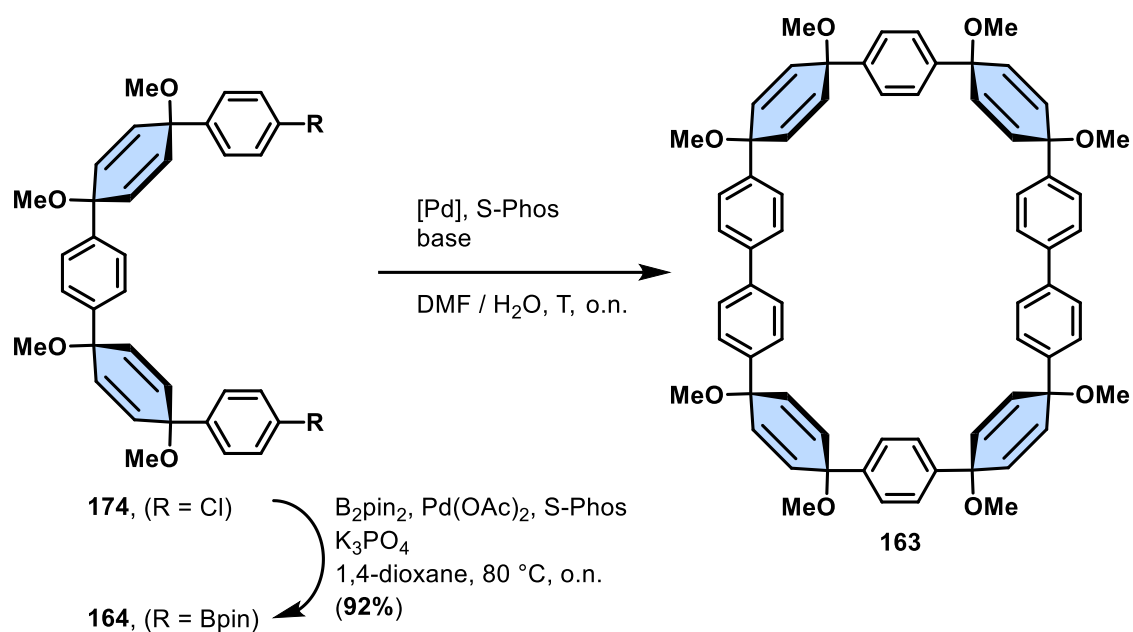
Exploiting the symmetry of this general building block and its high modularity allowed for minor adjustments within the synthesis strategy. Instead of assembling building block **165** or **174** over two steps, a double addition of building block **168** or **175** to 1,4-dibromobenzene (**176**) or 1,4-diiodobenzene (**24**) became the pivotal step.

Starting from 4-hydroxy anisole (**173**), the oxidation towards the acetal through the addition of PIDA concluded in acetal **177** with a yield of 87%. The addition of the mono-lithiated 1-bromo-4-chlorobenzene (**178**) at $-78\text{ }^{\circ}\text{C}$ introduced the cyclohexadiene motif yielding building block **175** in 61% yield. Previous findings from different research groups have demonstrated that incorporating a bulkier triethyl-silyl (TES) protecting group on the alcohol moiety leads to enhanced stereoselectivity during the formation of the pre-bend building blocks. Applying this strategy to this synthesis approach resulted in the formation of compound **174** with a yield of 60% over three steps (Scheme 32).



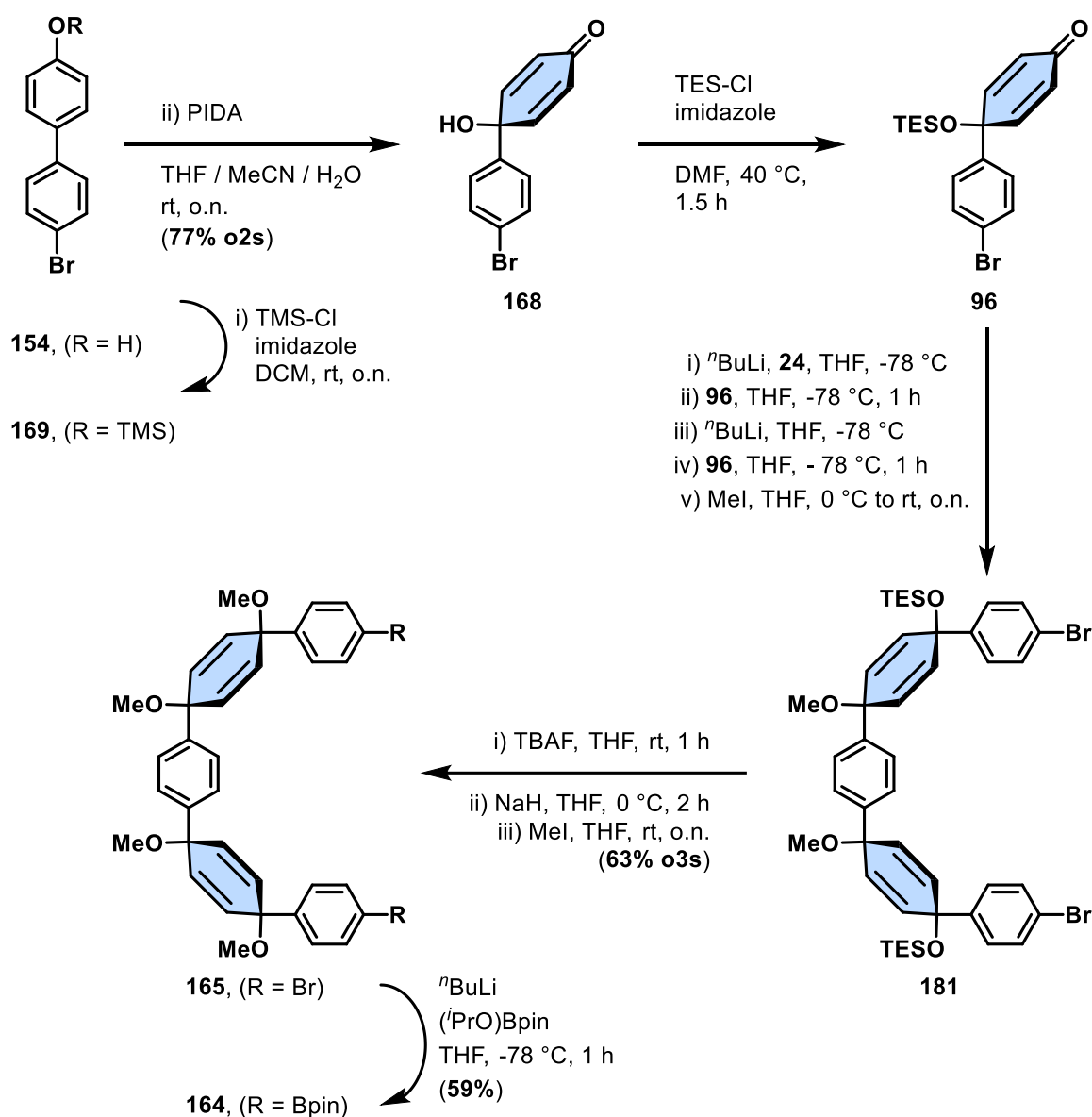
Scheme 32. Synthesis of building block **174** starting from 4-hydroxy anisole (**176**).

Interestingly, higher yields were achieved by the addition of building block **179** as a solution in THF the one-pot synthesis of **170**. The subsequent borylation step concluded the synthesis of building block **164** with a yield of 92%. With both building blocks **174** and **183** at a disposal, initial attempts towards the formation of the macrocyclic precursor **163** were carried out (Scheme 33).



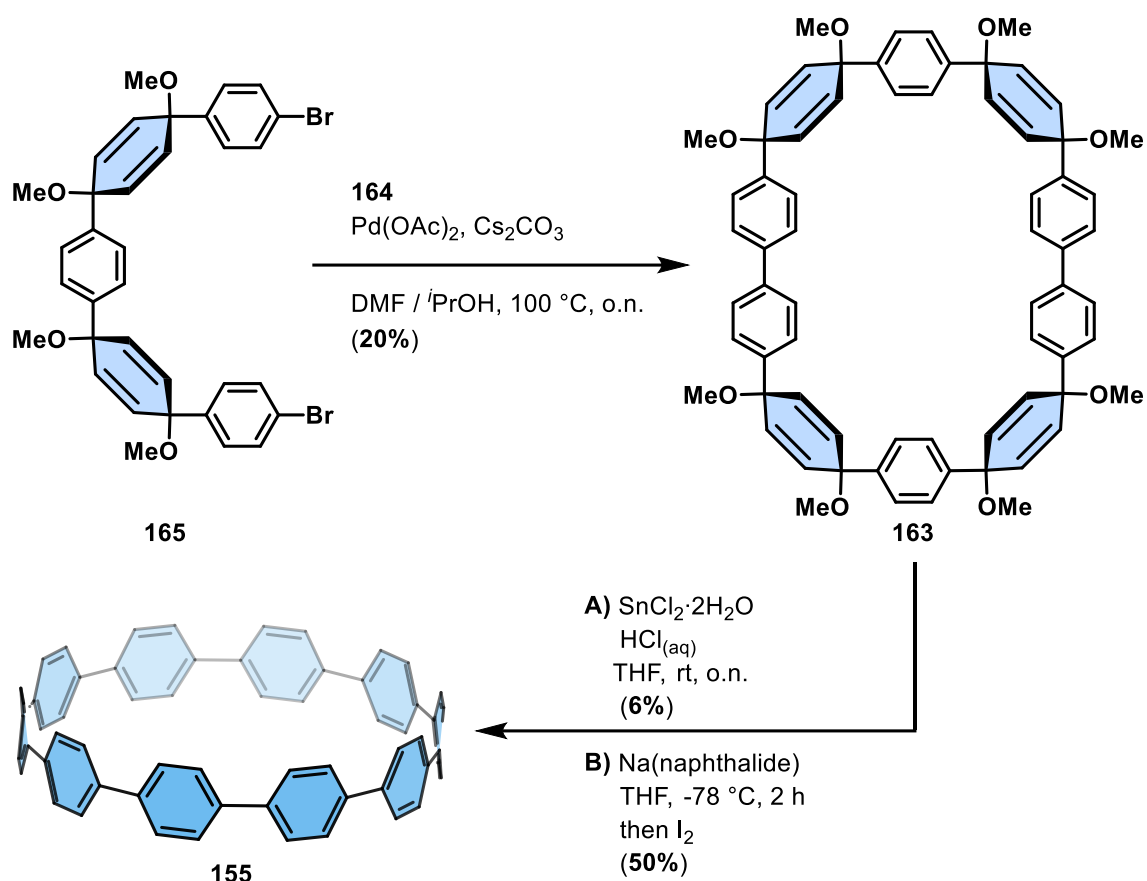
Scheme 33. Synthesis attempt towards macrocyclic precursor **163** through SUZUKI-MIYAUURA cross-coupling reaction.

Unfortunately, applying literature-known conditions for the macrocyclization reaction, using both aryl chloride **174** and aryl boronic ester **164** as coupling partners, did not result in the desired formation of product **163**. Instead, either initial starting material or polymeric compounds were observed. Consequently, it was planned to enhance the reactivity by substituting the aryl chloride **170** with aryl bromide **169** (Scheme 34).



Scheme 34. Modified synthesis route towards building blocks **165a** and **166** as starting materials for the macrocyclization.

Commencing again with 1-bromo-1'-hydroxy biphenyl (**154**), the modified synthesis approach depicted in Scheme 37 was applied. By utilizing the TES-group as protecting group and 1,4-diiodobenzene (**24**), building block **165** was synthesized in yields of 63% over three steps. Subsequent borylation towards **164** enabled the successful synthesis of the macrocyclic precursor **163** using SUZUKI cross-coupling reaction conditions (Scheme 35).



Scheme 35. Concluding the synthesis of [10]CPP **155** through macrocyclization and aromatization.

After optimizing the catalytic system, the precursor was obtained with yields of 20%. This precursor was then aromatized towards [10]CPP **155** with sodium naphthalenide, resulting in yields of 50%. In contrast, the aromatization under the conditions of tin chloric acid only yielded 6%.

Despite encountering various challenges, a convenient synthesis strategy for different building blocks and a successful synthesis of unsubstituted [10]CPP **155** was developed. With this compound in hand, further investigations towards the post-functionalization of **155** using C-H activation was planned. Therefore, various methods have been chosen having the purpose of incorporating a functional handle that facilitates further functionalization of [10]CPP **155** (Figure 39).

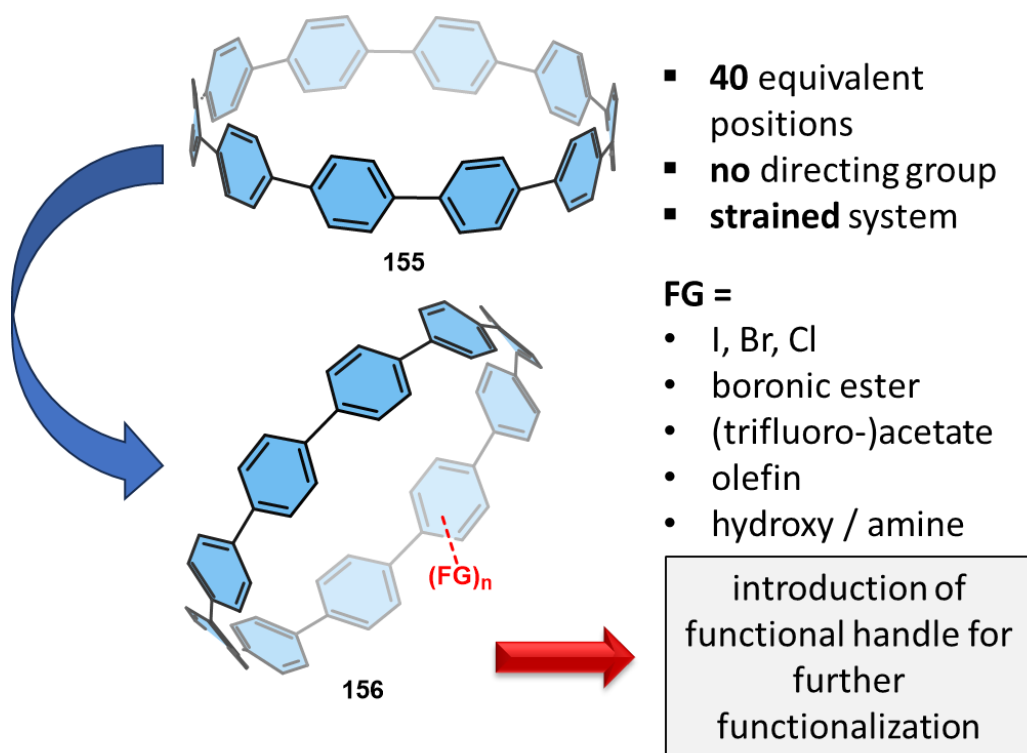
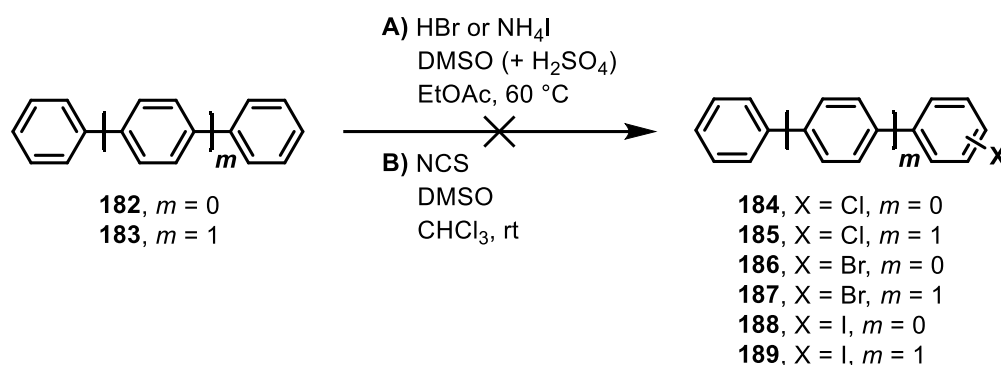


Figure 39. Working hypothesis of the top-down functionalization of [10]CPP **155**.

Initially, the halogenation of [10]CPP **155** was addressed. In general, biphenyl **182** and terphenyl **183** served as simplified model substrates in this case, as they are readily available commercially and represent a small cut-out of **155**. At this point, it must be considered, that in these compounds, three different positions for the reaction are accessible, while in **155** the 1,4-position is blocked. Moreover, these model substrates were only used for a general test to assess if the reaction conditions from the literature were suitable for these aromatic systems, and only a qualitative $^1\text{H-NMR}$ spectrum was measured to evaluate the results.

As already mentioned in the introduction, harsh conditions for electrophilic aromatic substitution often resulted in undesired side reactions. Hypothesizing that milder conditions might be effective for the chosen substrates DMSO-catalyzed halogenation reactions were tested. It is proposed in the literature that the halogen species is oxidized by DMSO and forms a $[\text{X}^+\text{DMSO}]\text{X}^-$ species which subsequently reacts with the π -electrons of the arene species. In the final step, the product is formed with the release of HX^{250} or succinimide²⁵¹ and DMSO or dimethyl sulfide (DMS).

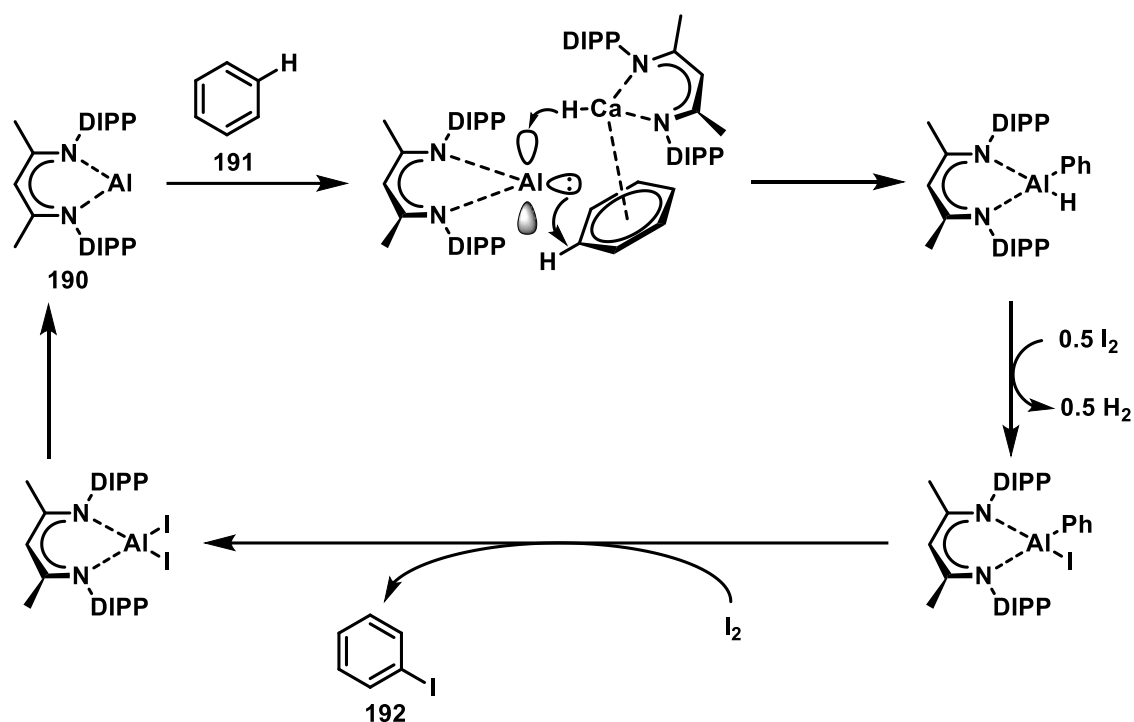
Screening these different reaction conditions for the oxidative halogenation using R-X (R = H, or succinyl; X = Cl, Br, I) did not result in any conversion of the model substrates (Scheme 36).



Scheme 36. Attempts towards oxidative halogenation through DMSO-catalyzed C-H activation.

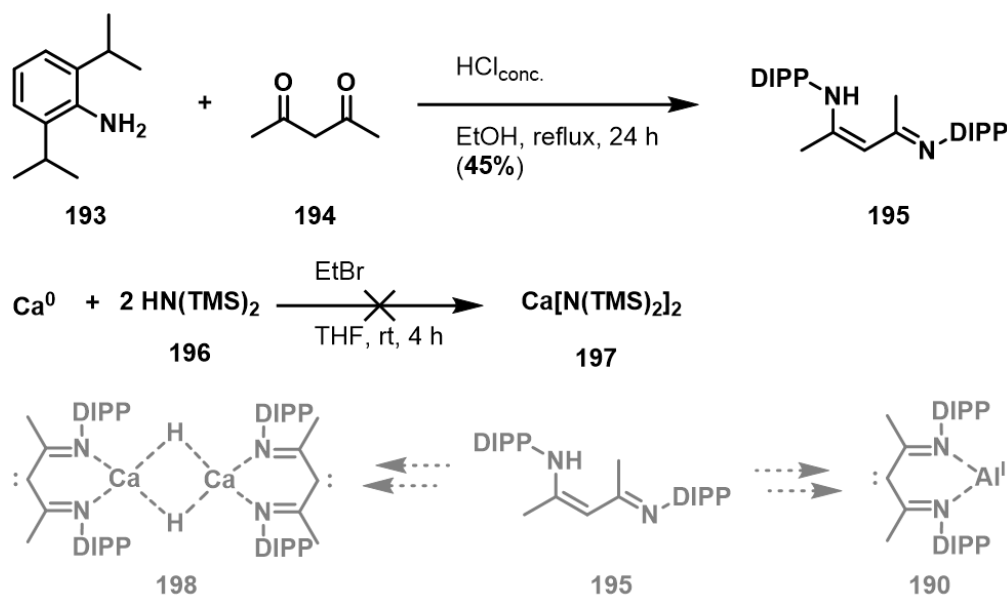
As a result, both arene species could be reisolated, indicating that these attempts were unsuccessful. Although it is known that elemental bromine does not lead to a functionalization of [10]CPP **155**, the iron-catalyzed bromination of arenes has to best of our knowledge, not been investigated on **155** in the literature before. Therefore, the required reaction conditions have been first applied on **182** and **183**. As expected, in both cases, unselective bromination occurred. However, when the same conditions were applied to [10]CPP **155**, only the starting material **155** was reisolated.

In an additional attempt to halogenate [10]CPP **155**, low-valent aluminum catalysis, which is known for its application in the activation of X-H bonds, was chosen as an appealing method (Scheme 37).²⁵²



Scheme 37. Halogenation of arenes through low-valent aluminum and calcium catalysis using catalyst **175**.

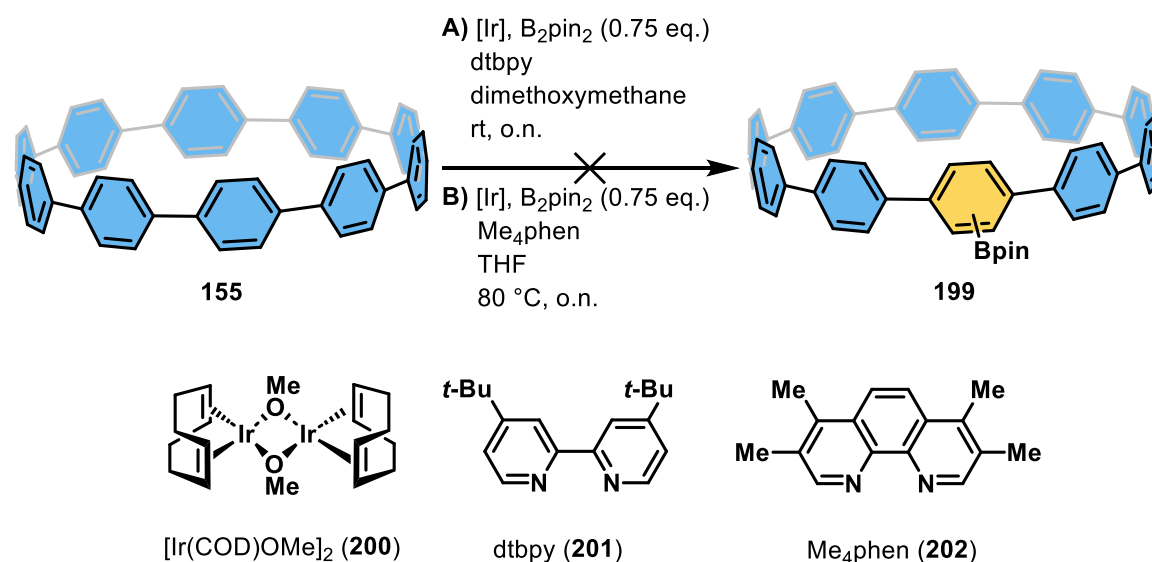
Consequently, it was necessary for us to synthesize the corresponding ligands (Scheme 38).



Scheme 38. Synthesis attempt towards the Ca- (**198**) and Al- (**190**) catalysts.

Commencing from di-isopropyl aniline (**193**) and acetyl acetone **194**, imine **195** was isolated with 45% yield. This compound serves as a pro-ligand for the associated calcium and aluminum complexes **198** and **190**. Unfortunately, different encounters halted the progress in attaining the required complexes.

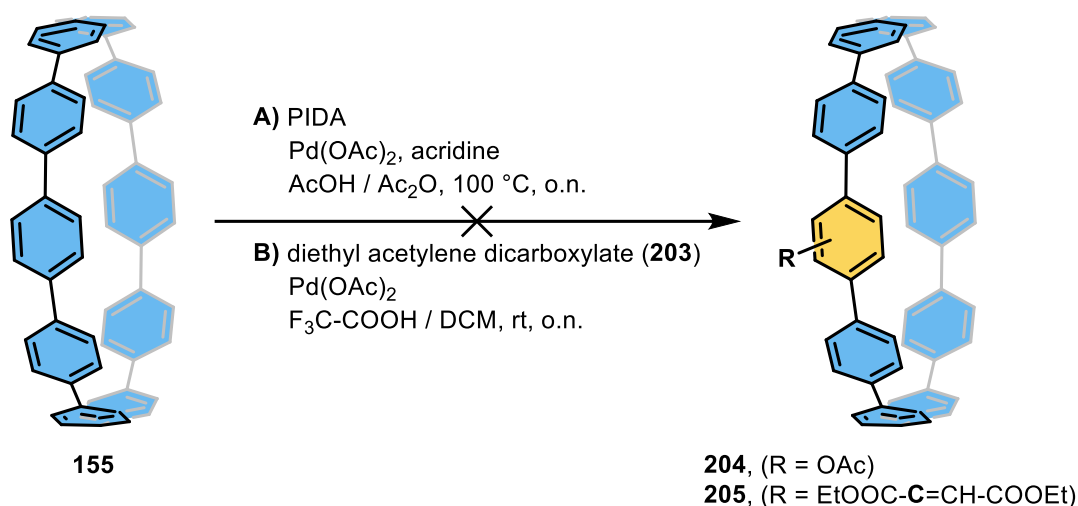
In addition to incorporate halogen functional groups, the boronic pinacol ester (Bpin) was chosen. This versatile functional group facilitates SUZUKI cross-coupling reactions and opens a multitude of possibilities for functionalization. Thus, $[\text{Ir}(\text{COD})\text{OMe}]_2$ **200** and either 4,4'-di-*tert*-butyl-2,2'-dipyridyl (**201**) or 3,4,7,8-tetramethyl-1,10-phenanthroline (Me₄phen, **202**) as the catalytic system were applied for C-H activation of [10]CPP **155** (Scheme 39).^{253,254}



Scheme 39. Towards top-down borylation of [10]CPP **162** through Ir-catalyzed C-H activation.

Unfortunately, after purification only the unreacted [10]CPP **155** was reisolated.

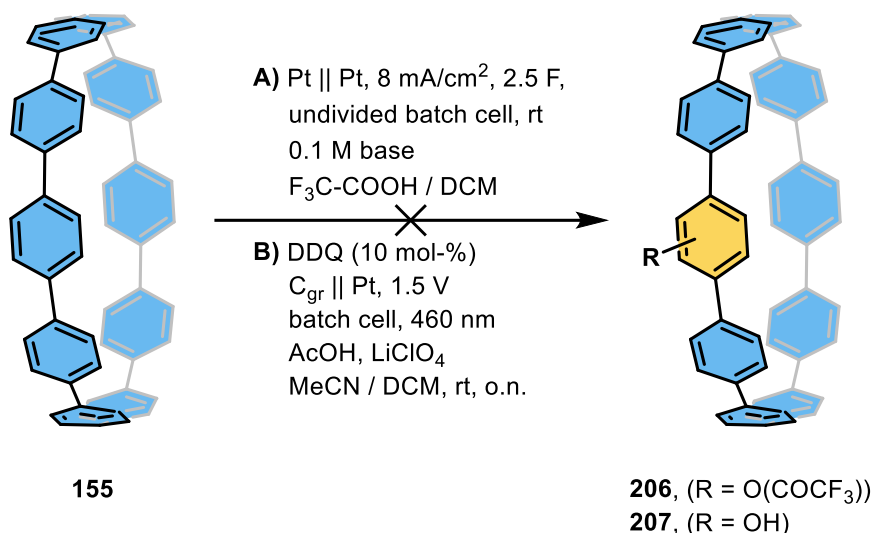
Furthermore, acetoxy functional group should be introduced to [10]CPP **155** using oxidative palladium-catalysis reaction.²⁵⁵ Utilizing similar conditions, an olefination reaction using diethyl acetylene dicarboxylate (**203**) in a solvent mixture of trifluoroacetic acid and dichloromethane (Scheme 40) was planned.²⁵⁶



Scheme 40. Attempts towards acyloxylation (**204**) and olefination (**205**) of [10]CPP **155**.

Again, both attempts resulted only in the reisolated [10]CPP **155**, indicating unsuccessful reactions.

As a last approach, electro(photo-)catalysis should lead to the generation of a radical cation that would subsequently undergo the desired functionalization reaction. Initially, [10]CPP **155** was subjected to cyclic voltammetry measurements in order to determine its oxidation potential. Thus, [10]CPP **155** was measured against the ferrocene/ferrocenium redox pair (Fc/Fc⁺) in dichloromethane at room temperature with a scanning speed of 100 mV s⁻¹. The measurements revealed an oxidation potential of 0.78 V against Fc/Fc⁺, which closely aligns with the literature (0.74 V).⁶⁵ With this result, a trifluoro acetoxylation²⁵⁷ and a hydroxylation²⁵⁸ as two appealing methods for functionalization were selected (Scheme 41).



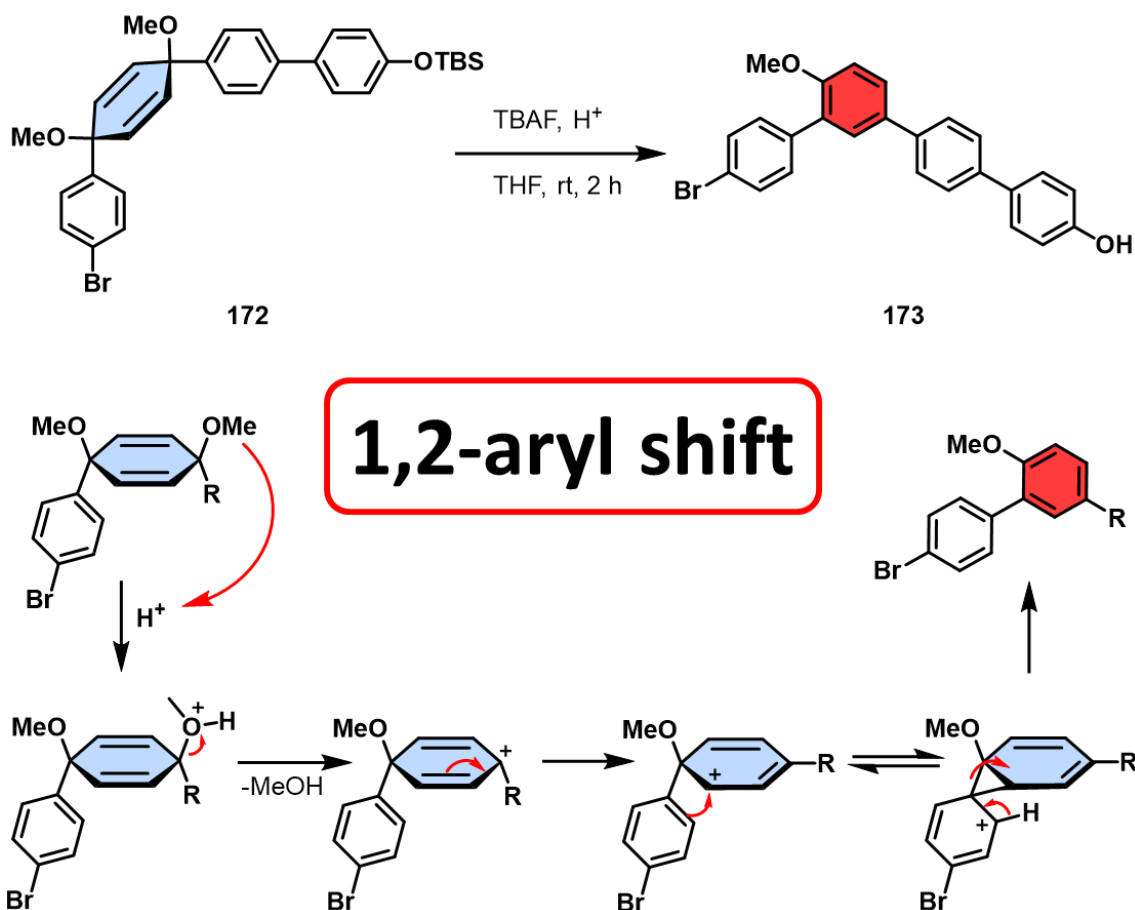
Scheme 41. Towards trifluoro acetoxylation (**206**) and hydroxylation (**207**) of [10]CPP **155** utilizing electro(photo-)catalysis.

After purifying the reaction mixtures and conducting ¹H-NMR measurements, only **155** was recovered in nearly quantitative yields. Thus concludes the unsuccessful chapter of attempting to functionalize [10]CPP **162** from a top-down approach.

In conclusion, a convenient protocol for the fast synthesis of unsubstituted [10]CPP **155** was developed. Minor adjustments from the gram-scale synthesis, resolved the encountered 1,2-aryl shift during the synthesis. Subsequently, various oxidative C-H activation protocols have been applied towards a top-down modification of [10]CPP **155**. Unfortunately, the chosen methodologies for introducing additional functional groups to this remarkable molecule were unsuccessful. It appears that the combination of aromaticity and strain energy presents further obstacles in overcoming the low reactivity of a C-H bond.

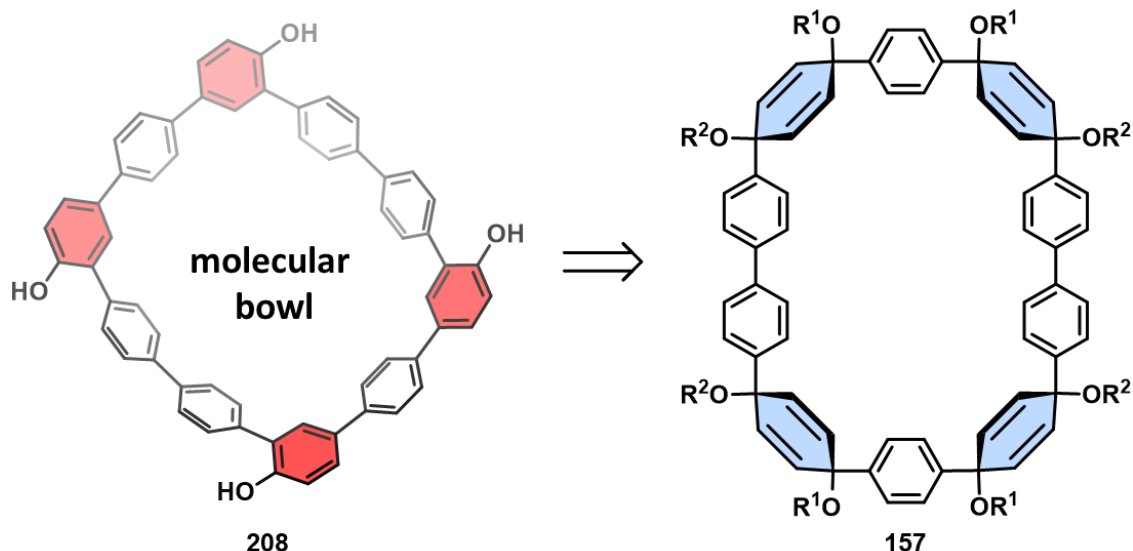
3.2. 1,2-Aryl Shift as Synthetic Tool towards novel Macrocyclic Structures

As presented earlier, the occurrence of the 1,2-aryl was first observed during the synthesis of building block **172** (Scheme 42).



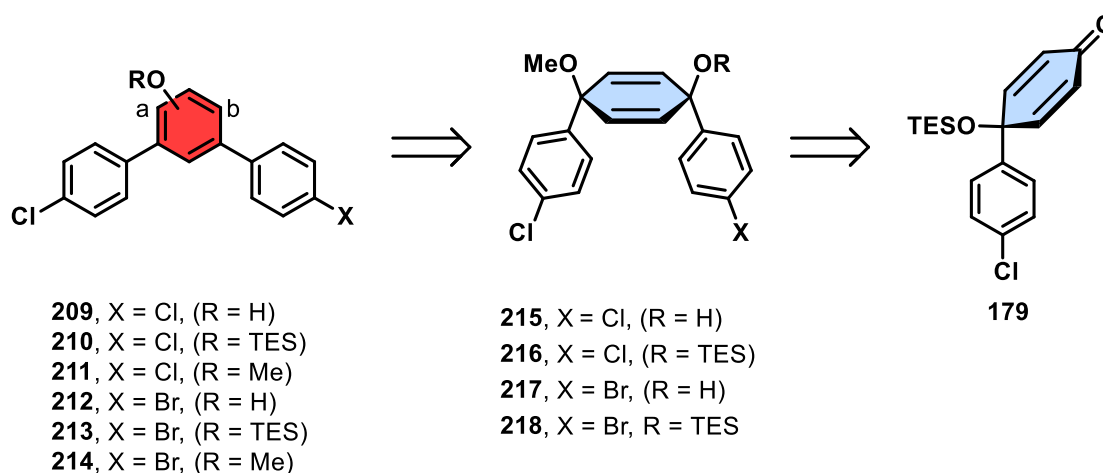
Scheme 42. Project motivation for the investigation of the 1,2-aryl shift as a synthetic tool towards novel macrocyclic structures.

Intrigued by the potential synthesis approach towards a three-fold substituted phenyl unit, a consecutive study to explore the possible application of this rearrangement in the synthesis of novel molecular nanocarbon materials was planned (Scheme 43).



Scheme 43. Schematic retrosynthetic analysis of molecular bowl **208**.

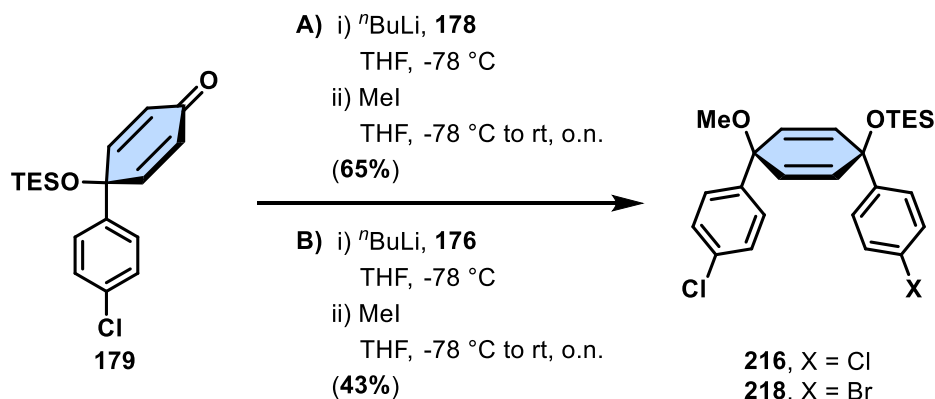
Following an ideal scenario, all cyclohexadiene motifs could undergo the 1,2-aryl shift, resulting in the formation of the bowl-shaped molecule **208**. Consequently, the synthetic precursor was envisioned to be based on macrocycle **157**. Given the fully symmetric nature of this compound and the resulting expected lack of selectivity, smaller pre-bent model substrates were initially used in this project (Scheme 44).



Scheme 44. Synthetic strategy for the consecutive study of the 1,2-aryl shift towards *meta*-terphenyls **209** - **214**.

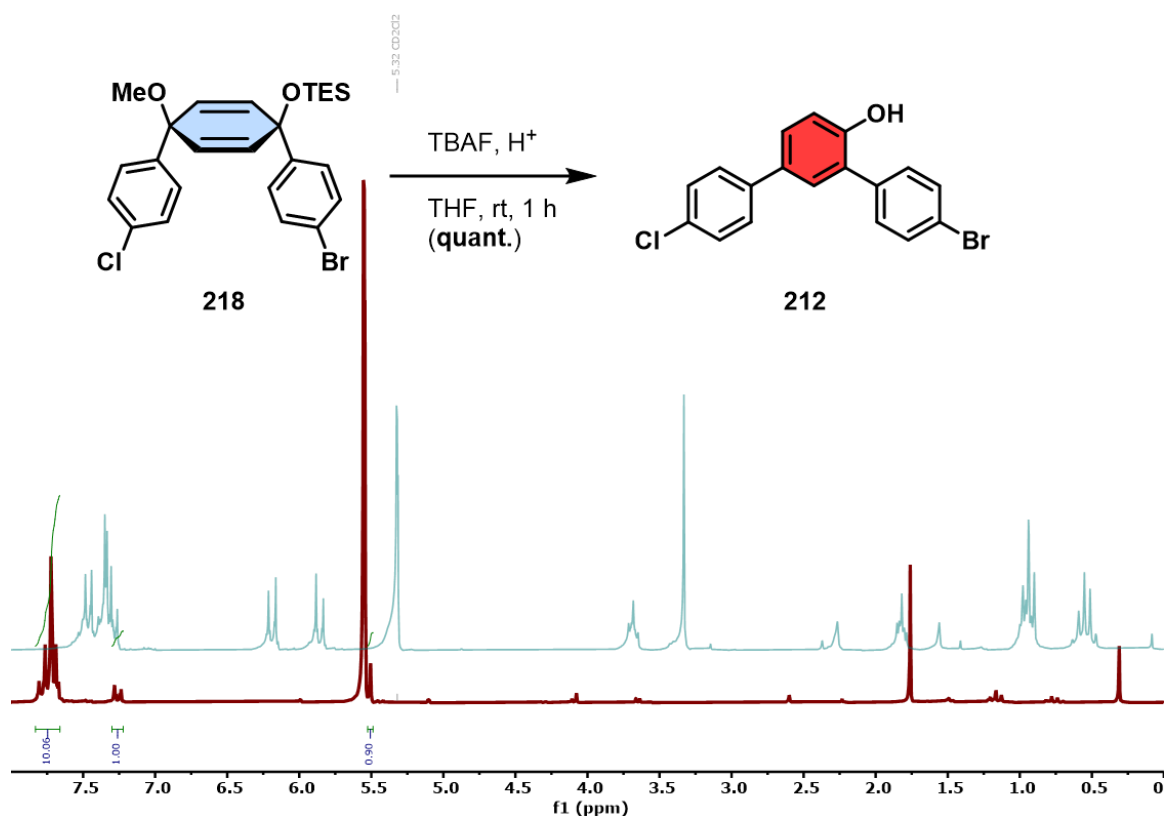
The TES-protected building block **179** was synthesized from *p*-hydroxy anisole (**176**, Scheme 37). The introduction of two different substituents to the cyclohexadiene moiety was aimed at providing a reasonable explanation for any selectivity observed during the rearrangement process. Hence, either 1-bromo-4-

chloro benzene (**178**) or 1,4-dibromo benzene (**176**) was added to the protected ketone **179**, resulting in yields of 65% for **216** and 43% for **218** (Scheme 45).



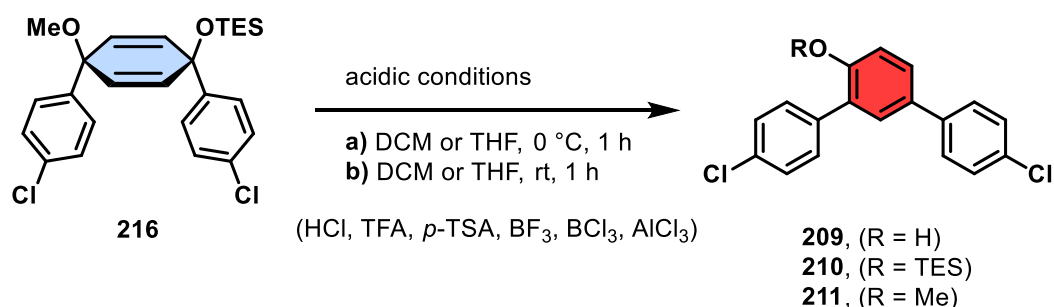
Scheme 45. Synthesis of building blocks **192b** and **193b** as precursors for the investigation of the 1,2-aryl shift.

Unfortunately, the deprotection of the TES-protected groups resulted in the formation of the rearranged products. Consequently, this preliminary study lacks further comparison between a free alcohol functionality and a methoxy group in terms of selectivity. However, TBAF can be used for the deprotection of silyl-groups. Therefore, it can be hypothesized that the deprotection occurred first, followed by the 1,2-aryl shift, leading to the loss of methanol and the aromatization towards the *meta*-substituted product. Initial observations supporting this hypothesis are provided by compound **212**, where the bromo-aryl shifted according to the proposed mechanism (Scheme 46), resulting in a $^1\text{H-NMR}$ signal around 7.25 ppm.



Scheme 46. First observations towards the selectivity of the 1,2-aryl shift during the deprotection of building block **193b**. $^1\text{H-NMR}$ spectra in DCM-d_2 at room temperature of the crude mixture (green) and after the purification attempt (red) are shown.

Additionally, the $^1\text{H-NMR}$ signal corresponding to the methoxy group around 3.40 ppm disappeared. However, further studies have been conducted on **216** by applying different acidic reaction conditions. In order to gain preliminary insights into the kinetics of the 1,2-aryl shift, the reactions were carried out at both room temperature and at $0\text{ }^\circ\text{C}$ (Scheme 47).



Scheme 47. Initial reaction conditions towards the investigation of the 1,2-aryl shift.

The results were evaluated using $^1\text{H-NMR}$ spectroscopy. Thus, the $^1\text{H-NMR}$ spectra of **209** - **211** were compared to the reaction mixtures of the screening (Figure 40). The $^1\text{H-NMR}$ signals of the highlighted protons were used as internal references.

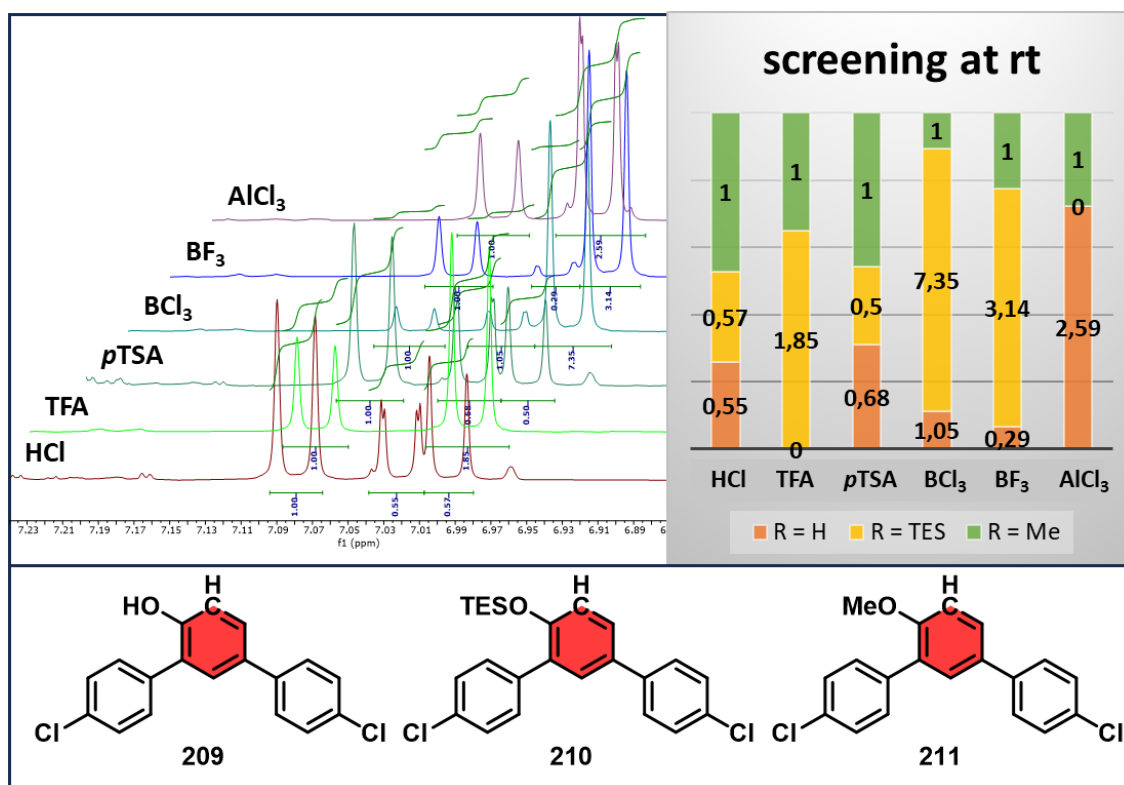


Figure 40. Exemplified evaluation of the screening reactions using different acidic conditions at room temperature. Comparison of $^1\text{H-NMR}$ spectra and columnar diagram. For comparison, highlighted proton was used for the determination of the different ratios between **209** - **211**.

Similarly, the results at a reaction temperature of $0\text{ }^\circ\text{C}$ were evaluated. The two columnar diagrams, summarizing the results, are shown in Figure 41.

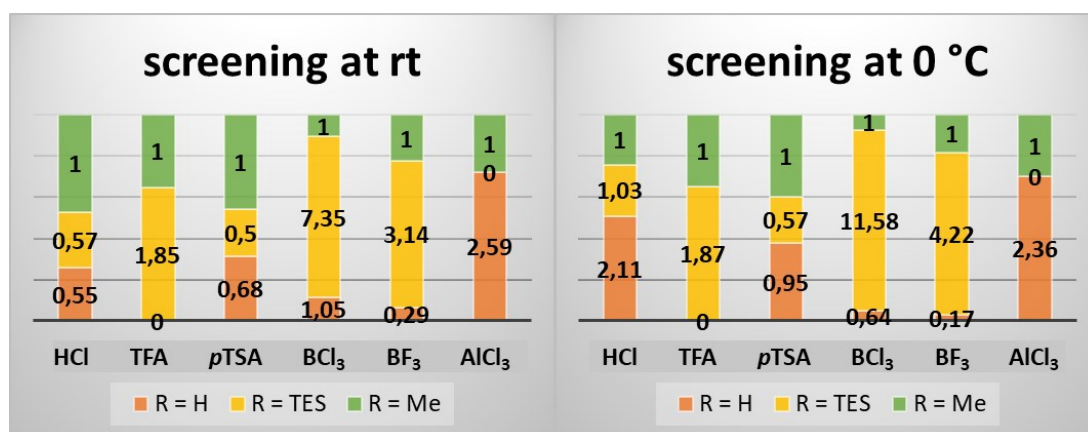
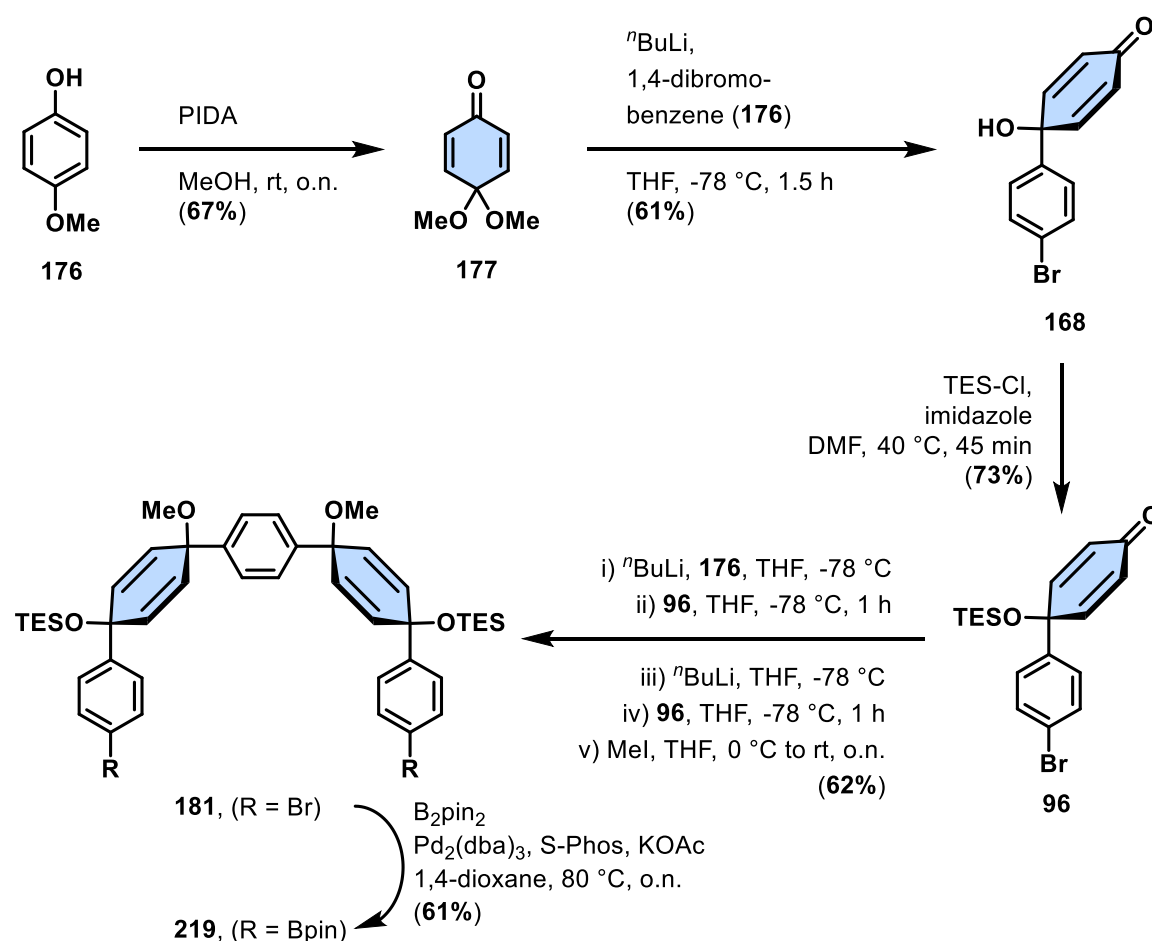


Figure 41. Columnar diagrams obtained after comparison of the different $^1\text{H-NMR}$ spectra obtained after treating **192** under acidic conditions.

In general, the occurrence of a 1,2-aryl shift was observed in all selected cases. However, when HCl and *para*-toluene sulphonic acid (pTSA) were used at $0\text{ }^\circ\text{C}$, the conversion rate was very low, and most of the starting material was still present. This can be attributed to the low stability of the TES-ether towards aqueous/acidic

conditions and its potential for deprotection. Nevertheless, all reactions exhibited selective migration of the left chloro-phenyl segment in the structure. By employing trifluoroacetic acid (TFA) or LEWIS-acids like BCl_3 and BF_3 , the deprotection of the silyl-ether at low temperatures was effectively avoided. Only AlCl_3 demonstrated complete cleavage of the ether. This selectivity can be easily explained by the steric hindrance of the TES-group compared to the methoxy group.

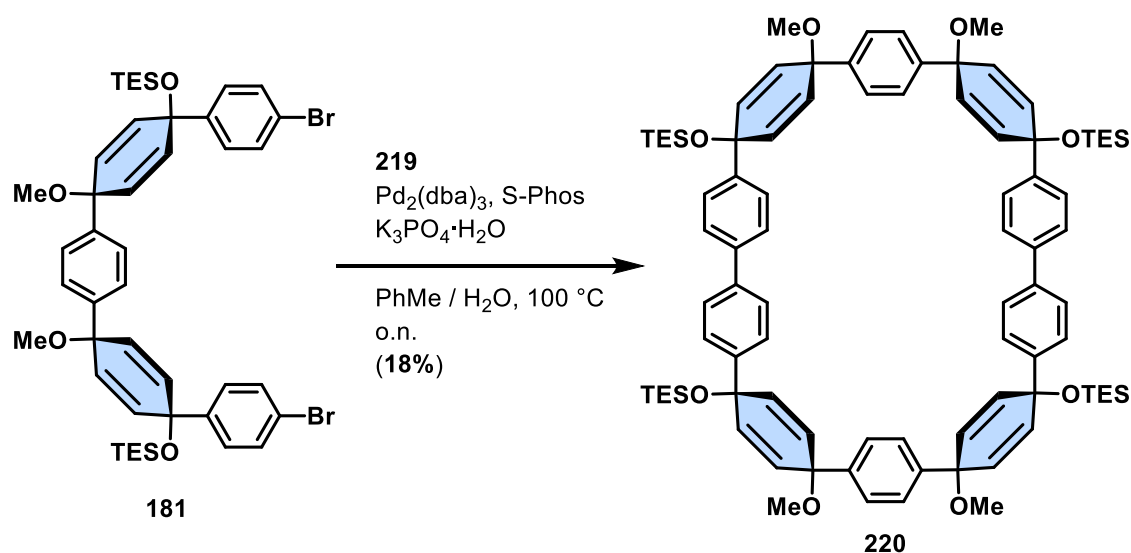
With these qualitative observations of the 1,2-aryl shift, its applicability in the aromatization of a macrocyclic precursor needed to be examined. As a result, the synthesis of the macrocyclic precursor of [10]CPP **163** was modified to create a suitable system for this project (Scheme 48).



Scheme 48. Synthesis of building block **219**, starting from 4-hydroxy anisole (**176**).

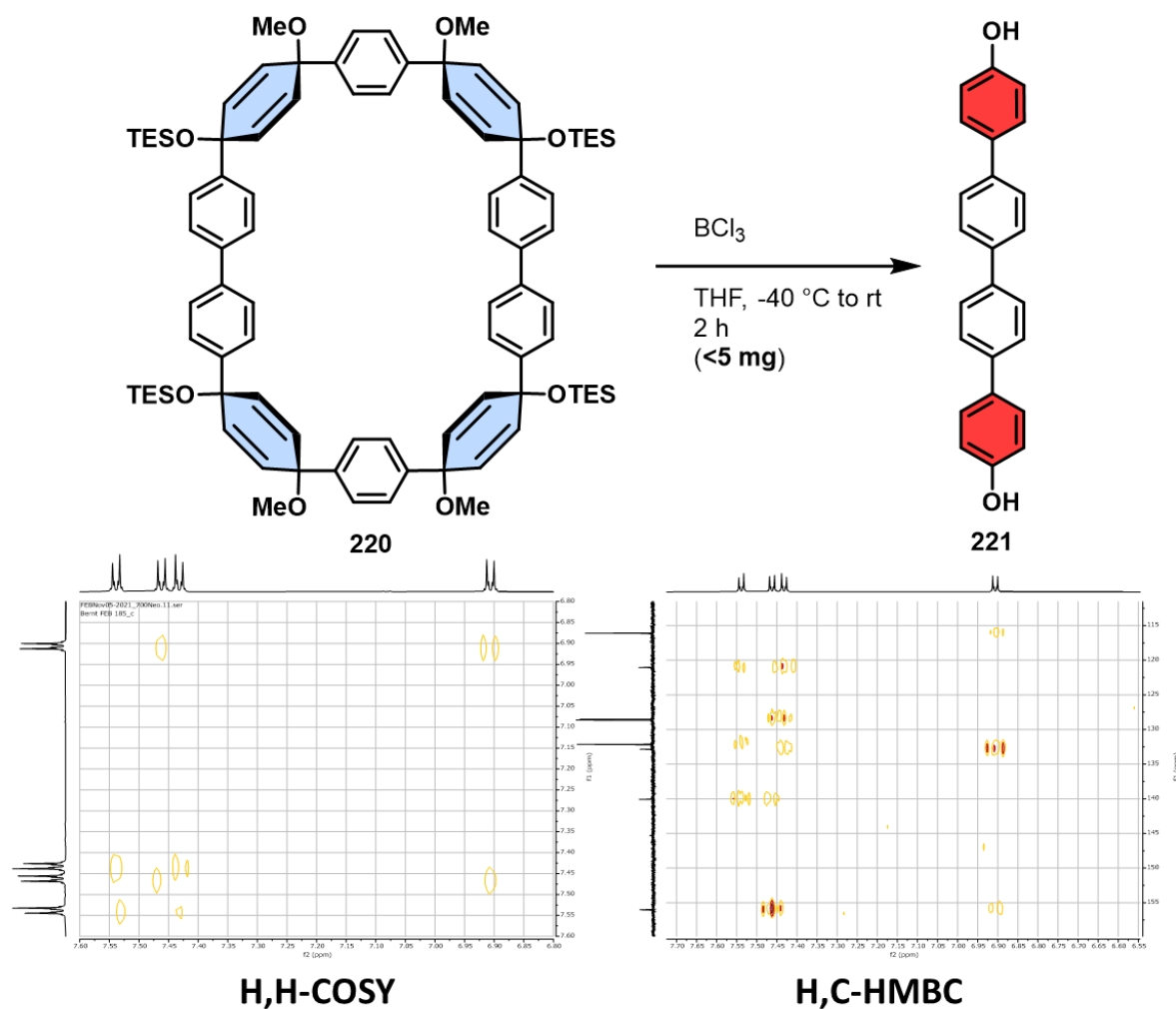
Starting from *p*-hydroxy anisole (**176**), building block **181** was synthesized over four steps with an overall yield of 18%. Surprisingly, borylation through lithium halogen exchange followed by quenching the reaction with *iso*-propoxy-pinacol borane did not yield the desired product and the starting material was recovered.

After altering the reaction conditions to MIYAUURA borylation conditions, the borylated building block **219** was obtained with a yield of 61%. Following optimization for the macrocyclization reaction using SUZUKI-MIYAUURA cross-coupling conditions, the macrocyclic precursor **164b** was obtained with a yield of 18%. Subsequent treatment of this precursor with BCl_3 at $-40\text{ }^\circ\text{C}$ resulted in a complex mixture of products (Scheme 49).



Scheme 49. Macrocyclization reaction towards the precursor **164b** through SUZUKI-MIYAUURA cross-coupling reaction.

Despite several purification attempts, including flash silica gel chromatography and preparative BuckyPrep[®] HPLC, only one pure fraction could be obtained. The corresponding NMR spectra are depicted in Scheme 50.



Scheme 50. Result of the treatment of the macrocyclic precursor **220** with BCl_3 . NMR-spectra which were used for structure determination are shown underneath the reaction scheme.

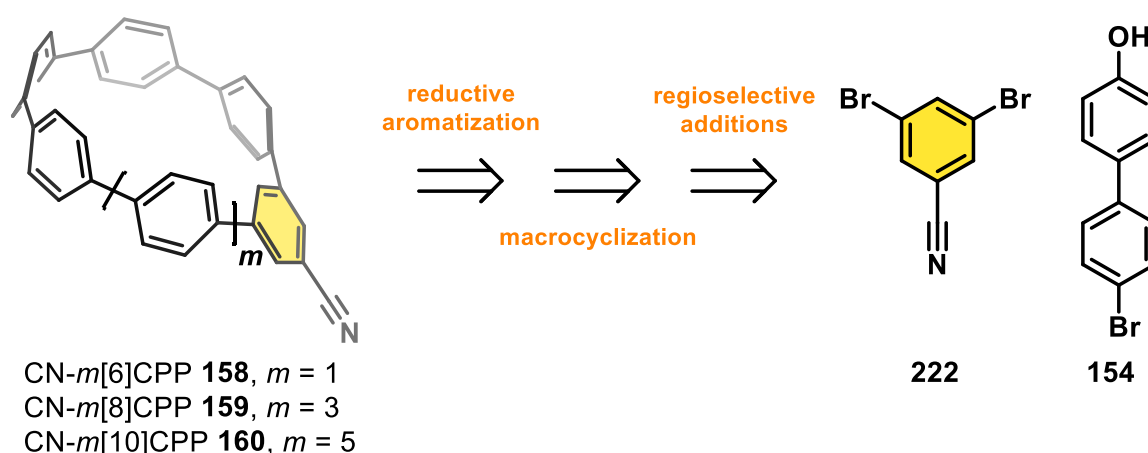
Utilizing both 1D- and 2D-NMR techniques for structure elucidation, revealed that the macrocycle **220** decomposed to form the quaterphenyl-4,4''-diol **221** under partial aromatization through 1,2-aryl migration. It appears that the required increase in strain energy is too high for this specific system, leading to decomposition during aromatization.

Based on these findings, it was decided to not further investigate the 1,2-aryl shift as a synthetic tool for novel aromatic systems, as there are simpler bottom-up approaches that can achieve the same target molecules. However, this project paved the way for the exploration of the *meta*-connectivity within macrocyclic nanocarbon molecules.

3.3. Substituted-*meta*[*n*]Cycloparaphenylenes

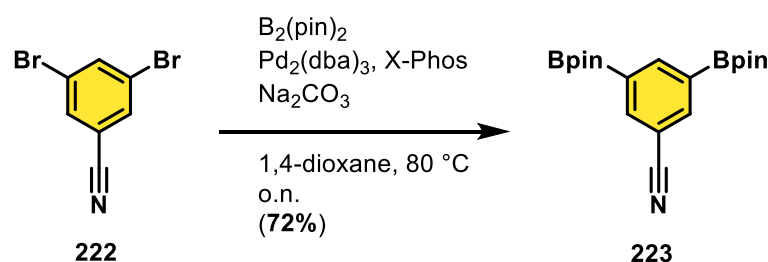
3.3.1. Cyano-*meta*[*n*]Cycloparaphenylenes

Intrigued by the interesting photophysical properties of *meta*[*n*]cycloparaphenylenes (*m*[*n*]CPPs), three different nitrile-substituted *m*[*n*]CPPs were planned. Introduction of the nitrile moiety would allow a functional group, which is inert against the reaction conditions during the SUZUKI cross-coupling macrocyclization and the reductive aromatization using tin chloric acid. Moreover, this functional handle allows convenient one-step transformations into various functional groups (Scheme 51).



Scheme 51. Short retrosynthetic analysis of CN-*m*[*n*]CPPs **165** - **167**.

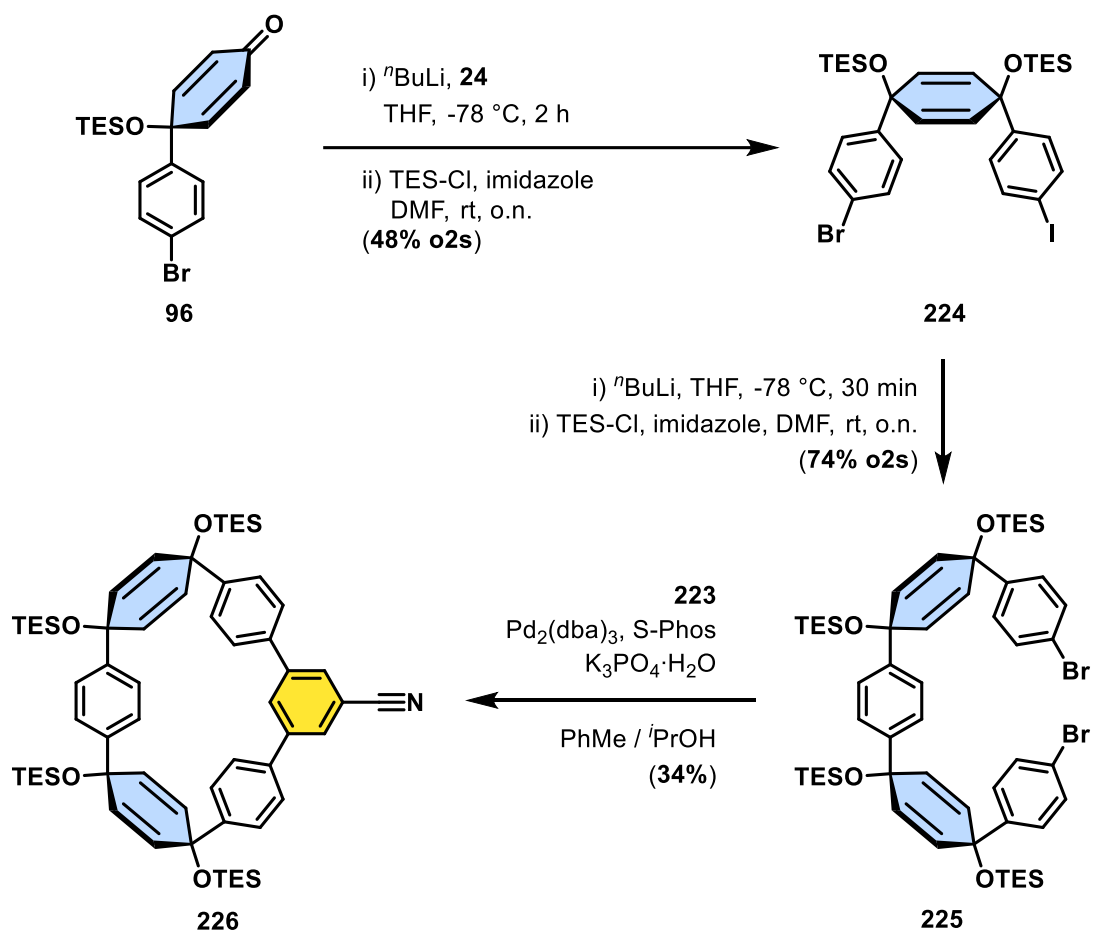
It was envisioned, to introduce the *meta*-connectivity and the nitrile as functional handle within one step during the macrocyclization. Therefore, the building block **223** was synthesized through MIYAUURA borylation (Scheme 52).



Scheme 52. Synthesis of benzonitrile **196b** through MIYAUURA borylation.

Utilizing 3,5-dibromo-benzonitrile (**222**) as starting material, the desired boronic ester functionality was introduced using Pd₂(dba)₃ and X-Phos as catalytic system with a yield of 72%.

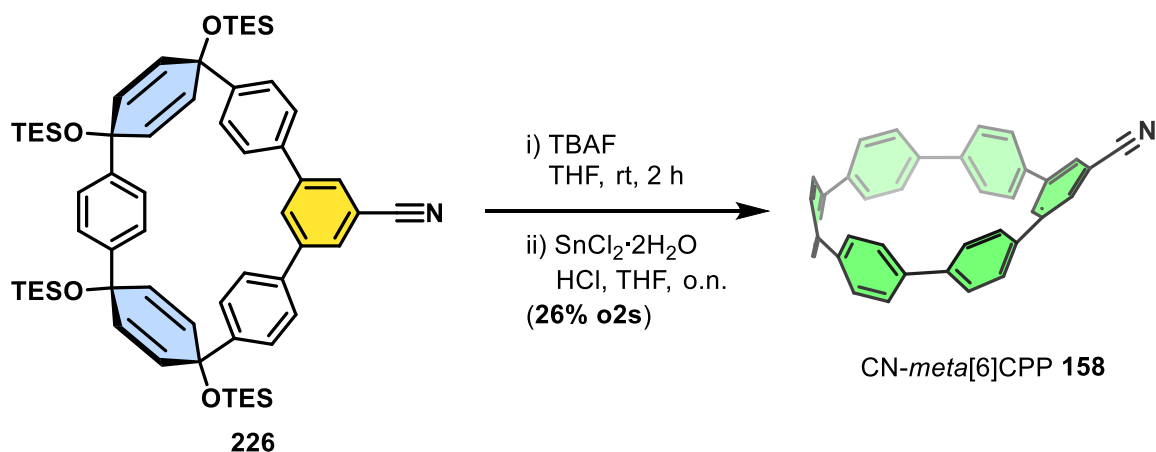
With building block **223** at a disposal, its different sized counterparts for the macrocyclization reaction were required to synthesize. First, the cyano-*m*[6]CPP **158** was addressed. Therefore, the TES-protected building-block **224** was synthesized. Utilizing TES-protecting groups throughout the whole synthesis approach should facilitate the synthesis of building block **225**, as the deprotection and protection sequence was not necessary at this point as it was in comparison for the parent [10]CPP **155** (Scheme 53).



Scheme 53. Synthesis of macrocyclic precursor **199a** utilizing TES-protecting groups throughout the synthesis.

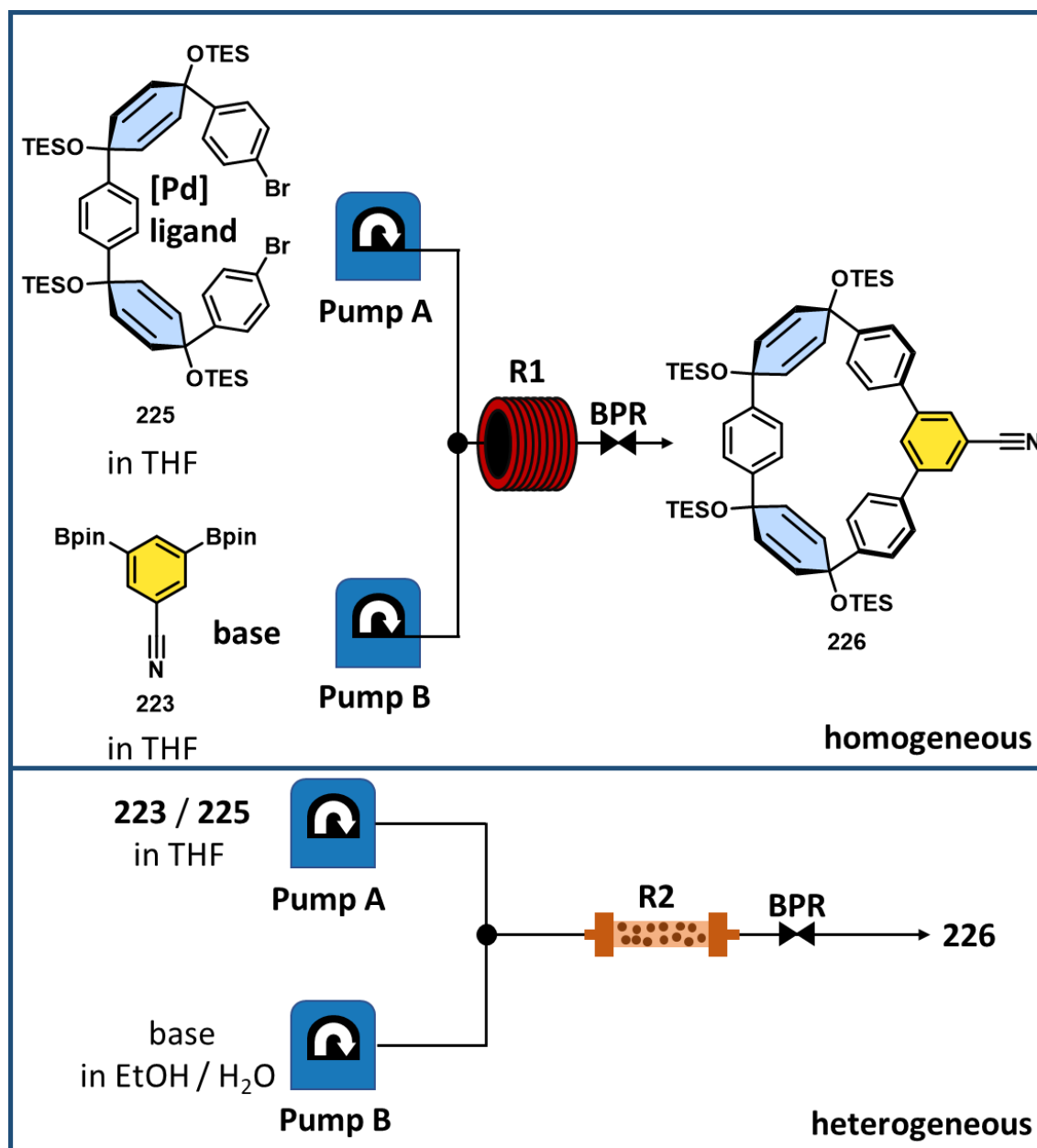
Starting from the TES-protected building block **96**, building block **225** was obtained with 36% over four steps. With **225** and **223** in hand, a SUZUKI-MIYAUARA cross-coupling reaction concluded the synthesis of the macrocyclic precursor **226** in 34% yield. After cleaving the silyl-ethers with TBAF, tin chloric acid was used for reductive aromatization. Already after the deprotection reaction solubility of the macrocyclic precursor became a huge issue. For this reason, sufficient purification was not possible, and the crude product of the reaction was used as is for the next step. Applying reductive conditions onto the system, immediately caused a change

in color of the reaction mixture from colorless to bright yellow. After the reaction was quenched, and the crude product purified through column chromatography, CN-*m*[6]CPP **158** was obtained in low yields of 26% over two steps as a bright yellow solid (Scheme 54).



Scheme 54. Synthesis of cyano-*meta*[6]CPP **158** using tin chloric acid for reductive aromatization.

However, at this time the idea came up, that using flow-chemistry could facilitate and improve the synthesis of the macrocyclic precursor **226**. Especially, scalability, reproducibility and control over the synthesis are frequently discussed in the context of continuous flow synthesis. Moreover, continuous flow-chemistry provides an appealing stage for heterogeneous catalysis.²⁵⁹ Therefore, two different setups were built to screen different reaction conditions for both homogeneous and heterogeneous catalyzed macrocyclization reactions (Scheme 55).



Scheme 55. Homogeneous (top) and heterogeneous (bottom) catalyzed SUZUKI-MIYAUURA cross-coupling reaction for macrocyclization using continuous flow-chemistry. **Pump A/B**: peristaltic pumps. **R1**: coiled tube-reactor. **R2**: backed-bed flow reactor. **BPR**: back-pressure regulator.

To begin with, the macrocyclization within a continuous way was attempted in a homogeneous manner, using similar conditions from the batch synthesis. Due to its sensitivity towards ambient conditions, S-Phos was replaced by X-Phos as a ligand. Moreover, the design of the reactors required THF as a solvent instead of a toluene / DMF mixture. As macrocyclization reactions are usually dependent on their concentration, the same concentration ($c = 3.6 \text{ mM}$) for building block **225** as in the batch reaction was applied in the reactions. Further reaction conditions using the homogeneous catalyst system, are summarized in Table 1. To prevent a

possible reaction between the starting materials at room temperature, the boronic ester **223** was fed to the reactor together with the base.

Table 1. Screening parameters for the homogeneous catalyzed SUZUKI-MIYAUURA cross-coupling reaction towards macrocycle **226** using continuous flow-chemistry. Constant parameters have been the solvent (THF) and the concentration within the reactor **R1** ($c = 3.6$ mM). In all cases X-Phos was utilized as additional ligand. τ = residence time within reactor **R1**, v = combined flowrate within reactor **R1**. *Red: valve of pump **A** was defect and therefore flowrates are not accurate for these experiments.

entry	[Pd] (equiv.)	base (c or equiv.)	T / °C	τ / min	v / mL min ⁻¹
1	Pd ₂ (dba) ₃ (0.1)	K ₃ PO ₄ ·H ₂ O (2.0 M)	60	10	0.40
2	Pd ₂ (dba) ₃ (0.1)	K ₃ PO ₄ ·H ₂ O (2.0 M)	70	10	0.40
3	Pd ₂ (dba) ₃ (1.0)	K ₃ PO ₄ ·H ₂ O (4.0 equiv.)	60	10	0.40
4	Pd ₂ (dba) ₃ (1.0)	K ₃ PO ₄ ·H ₂ O (4.0 equiv.)	70	10	0.40
5	Pd ₂ (dba) ₃ (1.0)	K ₃ PO ₄ ·H ₂ O (4.0 equiv.)	80	10	0.40
6	Pd ₂ (dba) ₃ (1.0)	K ₃ PO ₄ ·H ₂ O (4.0 equiv.)	60	10	0.40
7	Pd ₂ (dba) ₃ (1.0)	K ₃ PO ₄ ·H ₂ O (4.0 equiv.)	70	10	0.40
8	Pd ₂ (dba) ₃ (1.0)	K ₃ PO ₄ ·H ₂ O (4.0 equiv.)	80	10	0.40

Applying a homogeneous catalyst system to the continuous-flow set-up resulted in first successful results regarding the macrocyclization reaction towards **226** (Figure 42). For all entries additional signals within the ¹H-NMR spectra which correspond to the desired product do appear. Unfortunately, quantification of the reactions was not possible due to the number of overlapping signals within the ¹H-NMR spectra. However, a qualitative analysis of these spectra reveals that even stoichiometric amounts of the catalytic system (entries **2 – 8**, Table 1) result in a very low conversion towards the macrocycle **226**. Assumably, in all cases unreacted starting material, as well as open-chain polymeric compounds could be observed as main components in the reactor output, based on the different shapes of the signals in the ¹H-NMR spectra around 6.00 ppm. Moreover, it was observed that at all temperatures during the reaction palladium black formed in the reactor speaking of a deactivated catalytic system.

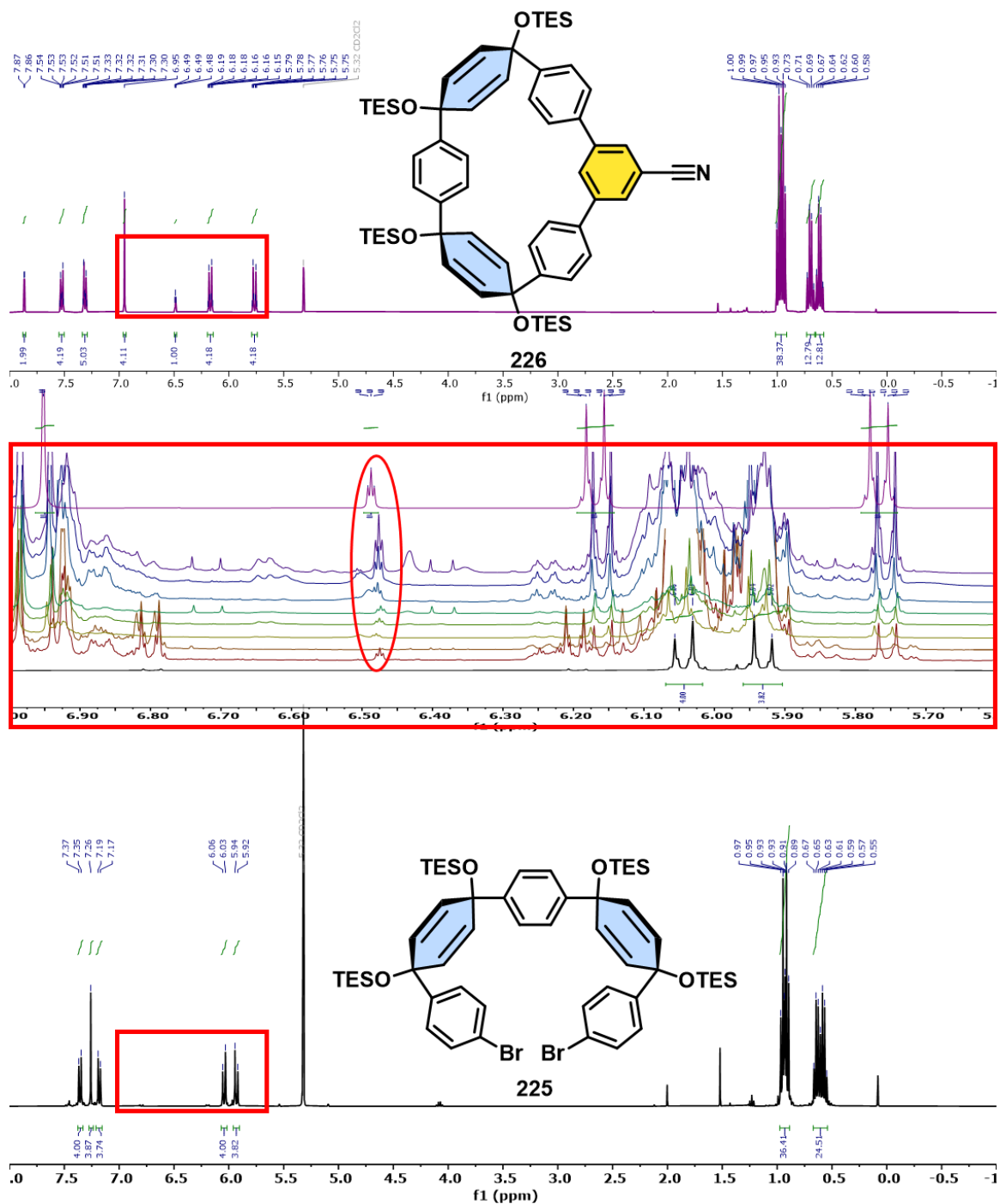


Figure 42. Comparison of the ¹H-NMR spectra derived from the reaction screening towards macrocycle **226** under homogeneous catalyzed SUZUKI-MIYAUURA cross-coupling reaction conditions using continuous-flow chemistry. ¹H-NMR spectrum of building block **225** (black, bottom) and macrocycle **226** (purple, top) are shown for reference. ¹H-NMR spectra of the entries **1** (bottom, brown, Table 1) – **8** (top, blue, Table 1) are shown in the middle of this Figure (red box).

However, at this point it was decided to not further investigate a homogeneous catalytic system, as the advantage of using continuous-flow chemistry is in using heterogeneous catalytic systems. Nevertheless, these preliminary results were intriguing enough, that suitable reaction conditions might be found for a heterogeneous catalytic system as well.

As starting point, four different commercially available solid-supported palladium catalysts were chosen (Figure 43).

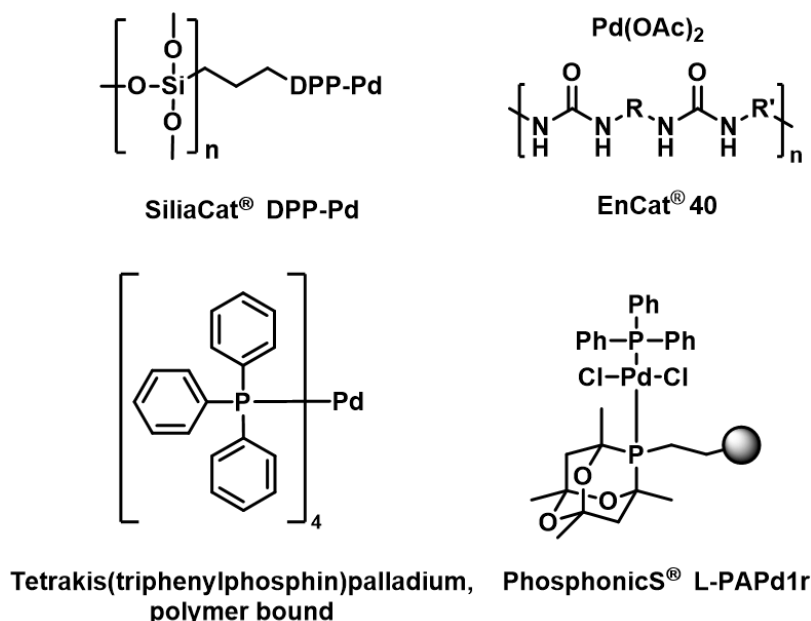


Figure 43. Heterogeneous catalysts applied within the continuous-flow synthesis of macrocycle **199a**.

The amount of catalyst loading was taken from the corresponding product specifications of the suppliers for calculating the amount of catalyst used in the reaction (Table 2).

Table 2. Screening parameters for the heterogeneous catalyzed SUZUKI-MIYAUURA cross-coupling reaction towards macrocycle **226** using continuous flow-chemistry. Constant parameters have been the solvent (THF / EtOH / H₂O) and the concentration within the reactor **R1** ($c = 3.6$ mM). Moreover, the same base was used for all entries (K₂CO₃). τ = residence time within reactor **R1**, v = combined flowrate within reactor **R1**.

entry	[Pd] (loading / mmol g ⁻¹) ^{260–263}	<i>T</i> / °C	τ / min	<i>v</i> / mL min ⁻¹
1	SiliaCat® DPP-Pd (0.2 – 0.3)	60	2	0.4
2	SiliaCat® DPP-Pd (0.2 – 0.3)	70	2	0.2
3	SiliaCat® DPP-Pd (0.2 – 0.3)	80	2	0.2
4	Pd(PPh ₃) ₄ on polymer (~0.6)	80	2	0.2
5	EnCat®40 (0.4)	80	2	0.2
6	PhosphonicS L-PAPd1r® (0.01 -0.03)	80	2	0.2

Using a packed bed-reactor in continuous flow-chemistry, allowed to start with a solution of the starting materials **223** and **225** within one flask. Before entering the reactor, the starting materials were mixed with the base and then got in contact

with the solid-supported catalysts. After collecting the reactor outcome, $^1\text{H-NMR}$ spectra were measured for a qualitative evaluation of the results (Figure 44).

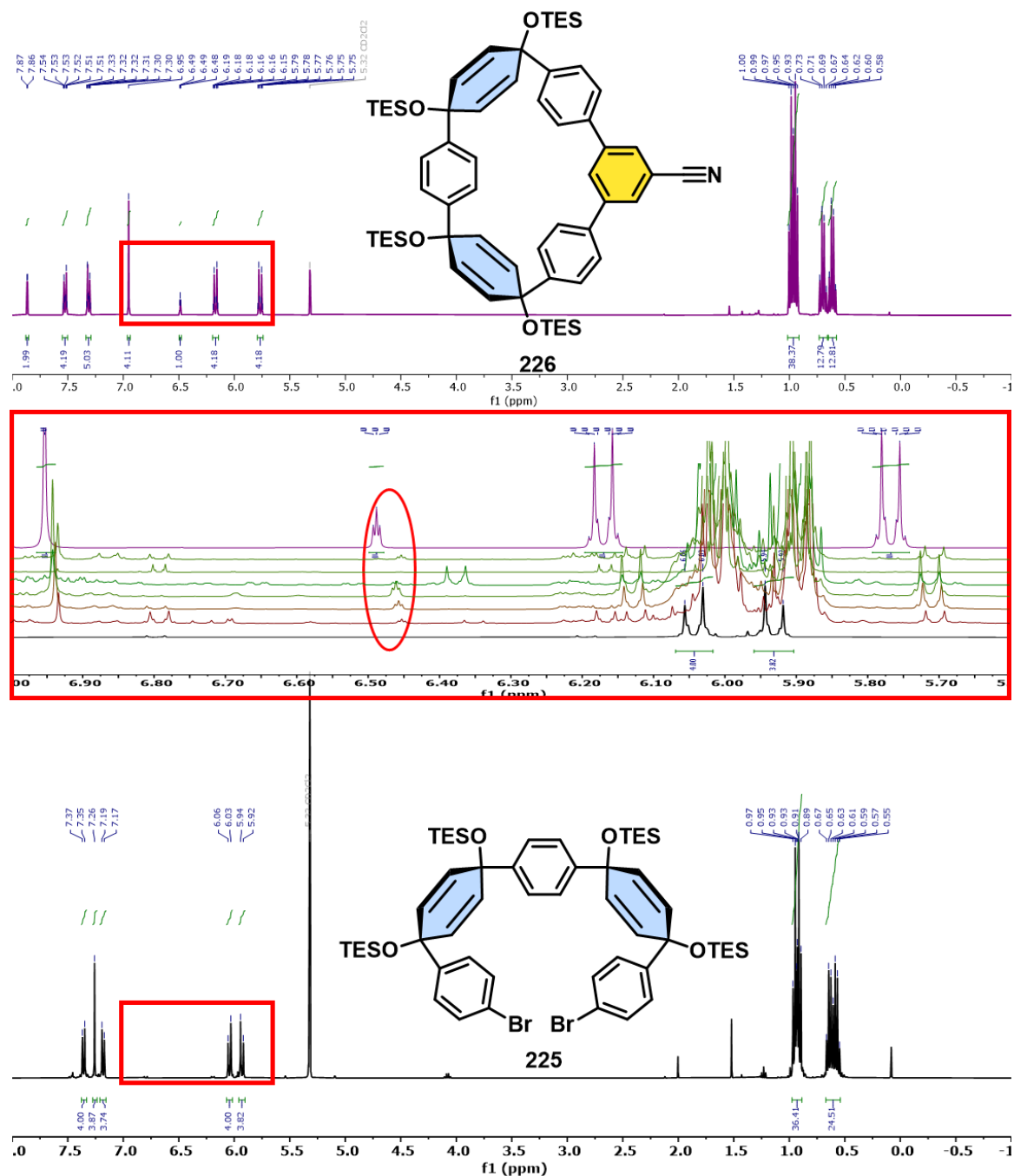
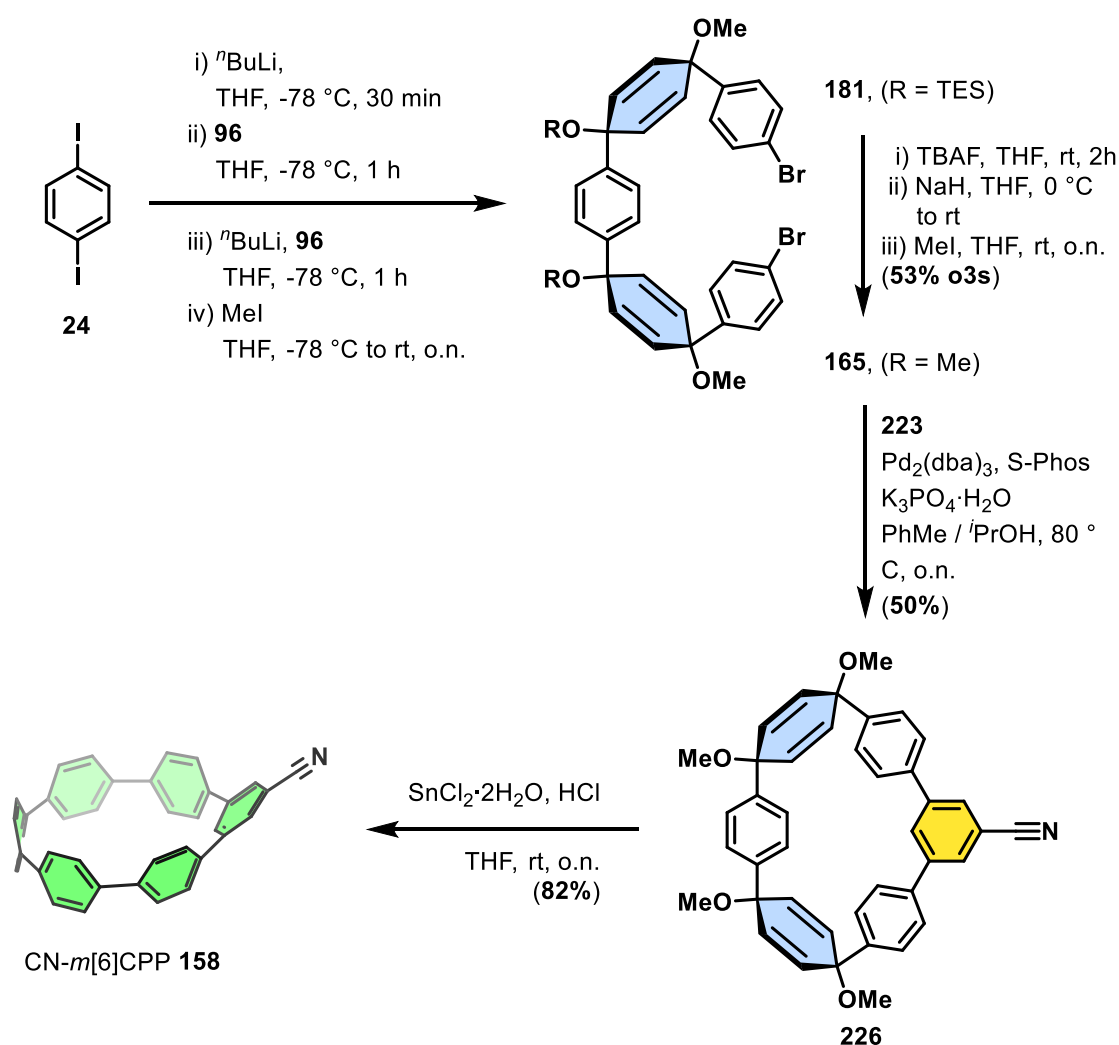


Figure 44. Comparison of the $^1\text{H-NMR}$ spectra derived from the reaction screening towards the macrocycle **199a** under heterogeneous catalyzed SUZUKI-MIYAUURA cross-coupling reaction conditions using continuous-flow chemistry. $^1\text{H-NMR}$ spectrum of building block **225** (black, bottom) and macrocycle **226** (purple, top) are shown for reference. $^1\text{H-NMR}$ spectra of the entries 1 (bottom, brown, Table 2) – 6 (top, dark-green, Table 2) are shown in the middle of this Figure (red box).

Comparing the $^1\text{H-NMR}$ spectra of the reactions show, entries **4** and **5** of Table 2 do not show the formation of the macrocyclic precursor **226**. Moreover, the crude reaction mixtures of the heterogeneous catalyzed macrocyclization reaction do not

display that many $^1\text{H-NMR}$ signals as it is the case for the homogeneous catalyzed reactions. Unfortunately, the formation of the product is still unfavored and mainly starting material **225** is visible. Furthermore, the most promising heterogeneous catalyst seemed to be SiliaCat[®] DPP-Pd (entry **3**, Table 2) whose production was discontinued by the supplier at that time.

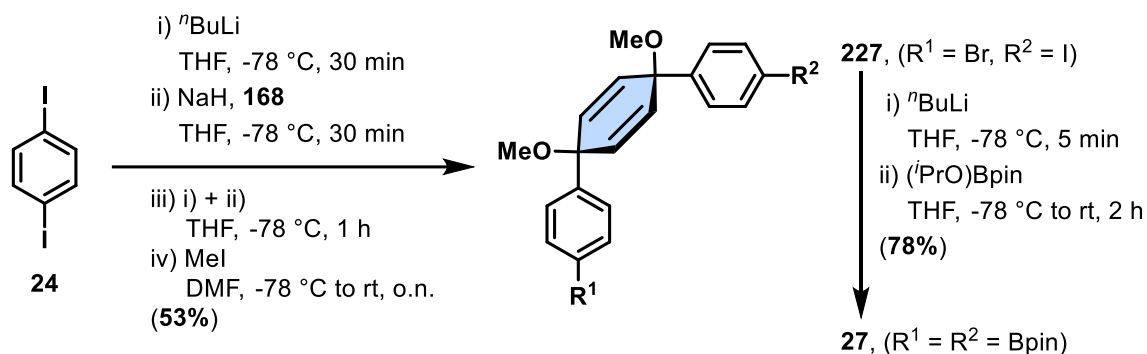
With that and the results of the batch synthesis of **225** further optimization was performed using batch chemistry. Based on the experience in the synthesis of building block **165** and its more convenient handling due to the methoxy groups, the synthetic strategy towards CN-*m*[6]CPP **158** was modified (Scheme 56).



Scheme 56. Synthesis of CN-*m*[6]CPP **158** utilizing methyl-ether as protective groups throughout the synthesis.

Utilizing the methyl-ether protective groups throughout the synthesis of **158** improved the results significantly. CN-*m*[6]CPP **165** is now synthesized in yields of 41% starting from building block **165** over the steps of macrocyclization and

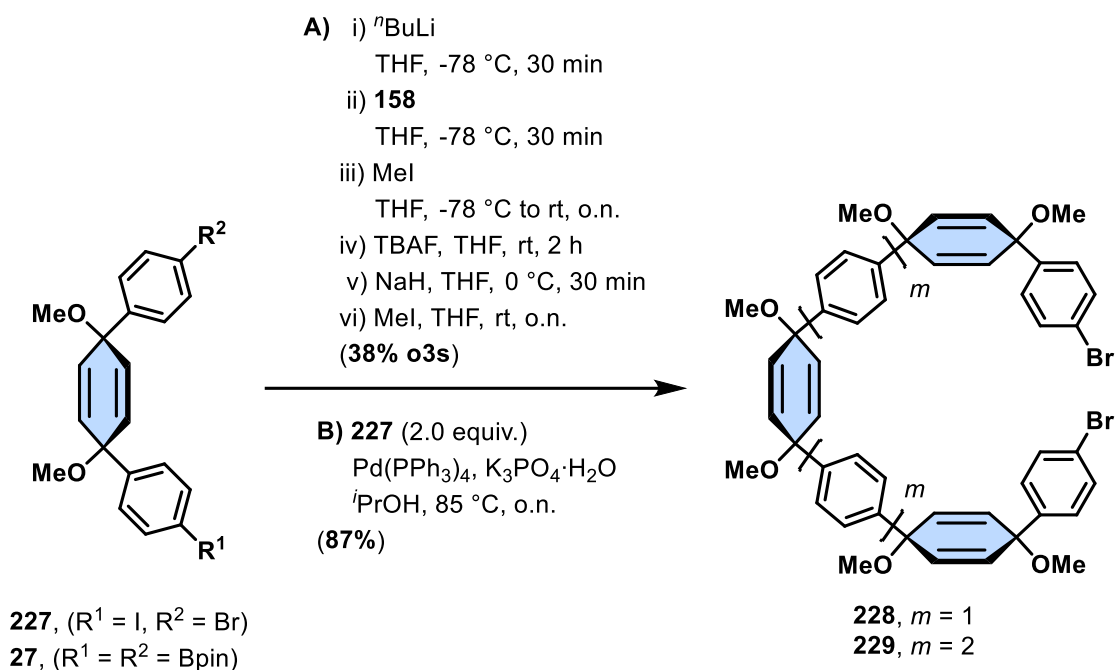
aromatization. As the previous steps worked equally well comparing both synthesis strategies, the methoxy-ether as protecting groups were used for the different sized CN- $m[n]$ CPPs **159** ($n=8$) and **160** ($n=10$) as well. In contrast to CN- $m[6]$ CPP **158**, the other two derivatives rely on the synthesis and combinations of building block **227** and its borylated analog **27** (Scheme 57).



Scheme 57. Synthesis of building block **227** and its borylation through lithium halogen exchange towards **27**.

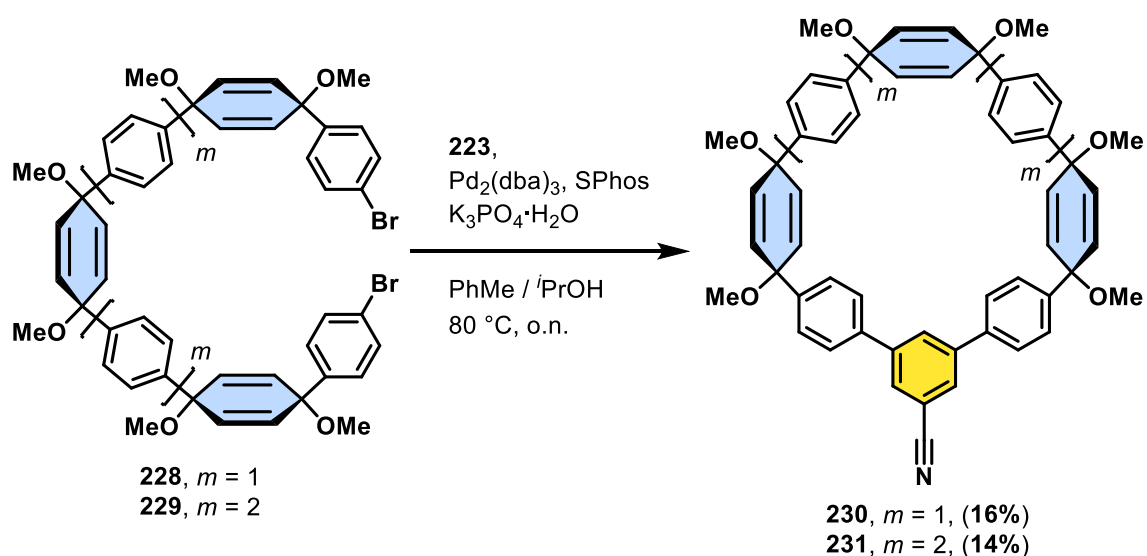
Applying the regioselective addition of the deprotonated building block **168** to 1,4-diodo benzene (**24**) resulted in 53% yield of building block **227**. After purification **227** was borylated through lithium halogen exchange and subsequently quenching of the reaction using *iso*-propoxy pinacol borane. Following this procedure, **27** was obtained with 78% yield.

Commencing from these two building blocks, the two different $[n-1]$ pre-bent building blocks **228** and **229**, where n represents the number of the addressed $m[n]$ CPP, were addressed. While **228** was assembled through the regioselective addition of twice the building block **168** to **227**, **229** was built-up using a SUZUKI-MIYAUURA cross-coupling reaction of **27** with twice the building block **227** (Scheme 58).



Scheme 58. Synthesis of the [$n-1$]pre-bent open-chain precursors **228** and **229**. **A)** synthesis of **228** through regioselective addition of **158** to **227**. **B)** synthesis of **229** through SUZUKI-MIYAUURA cross-coupling reaction of **27** and **227**.

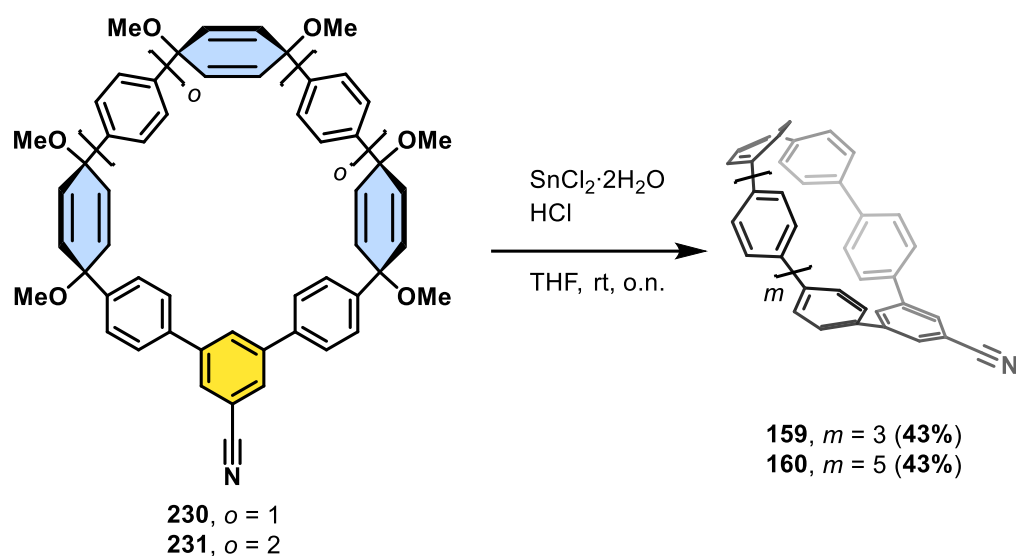
Both building blocks were obtained in decent to good yields of 38% (over three steps for **228**) and 87% (for **229**), respectively. In the subsequent step, these building-blocks were used in a SUZUKI-MIYAUURA cross-coupling reaction together with building block **223** to afford the macrocyclic precursors **230** and **231** (Scheme 59).



Scheme 59. Macrocyclization reactions under SUZUKI-MIYAUURA cross-coupling conditions towards the macrocyclic precursors **230** and **231**.

During the synthesis as well as the purification process of these precursors, solubility and stability started to become an issue. But in the end, both macrocyclic compounds **230** and **231** were successfully isolated in acceptable yields of 16% (**230**) and 14% (**231**), respectively.

To conclude the synthesis of the three different sized cyano-*m* [*n*]CPPs **158** – **160**, reductive conditions using tin chloric acid were applied for the aromatization of the two precursors **230** and **231** (Scheme 60).



Scheme 60. Reductive aromatization of the macrocyclic precursors **230** and **231** using tin chloric acid towards the CN-*m*[*n*]CPPs **159** ($n = 8$) and **166** ($n = 10$).

In both cases, after purification the desired product was obtained in acceptable yields of 43% (**159**) and 43% (**160**), respectively.

Throughout the synthesis of CN-*m*[6]CPP **158** and CN-*m*[10]CPP **160**, suitable crystals for X-ray diffraction measurements were obtained by slow evaporation of DCM (for **158**) or chloroform (for **160**). Their ORTEP drawings at 50% probability and some selected structural parameters are displayed in Figure 45 together with the corresponding crystal packing structures.

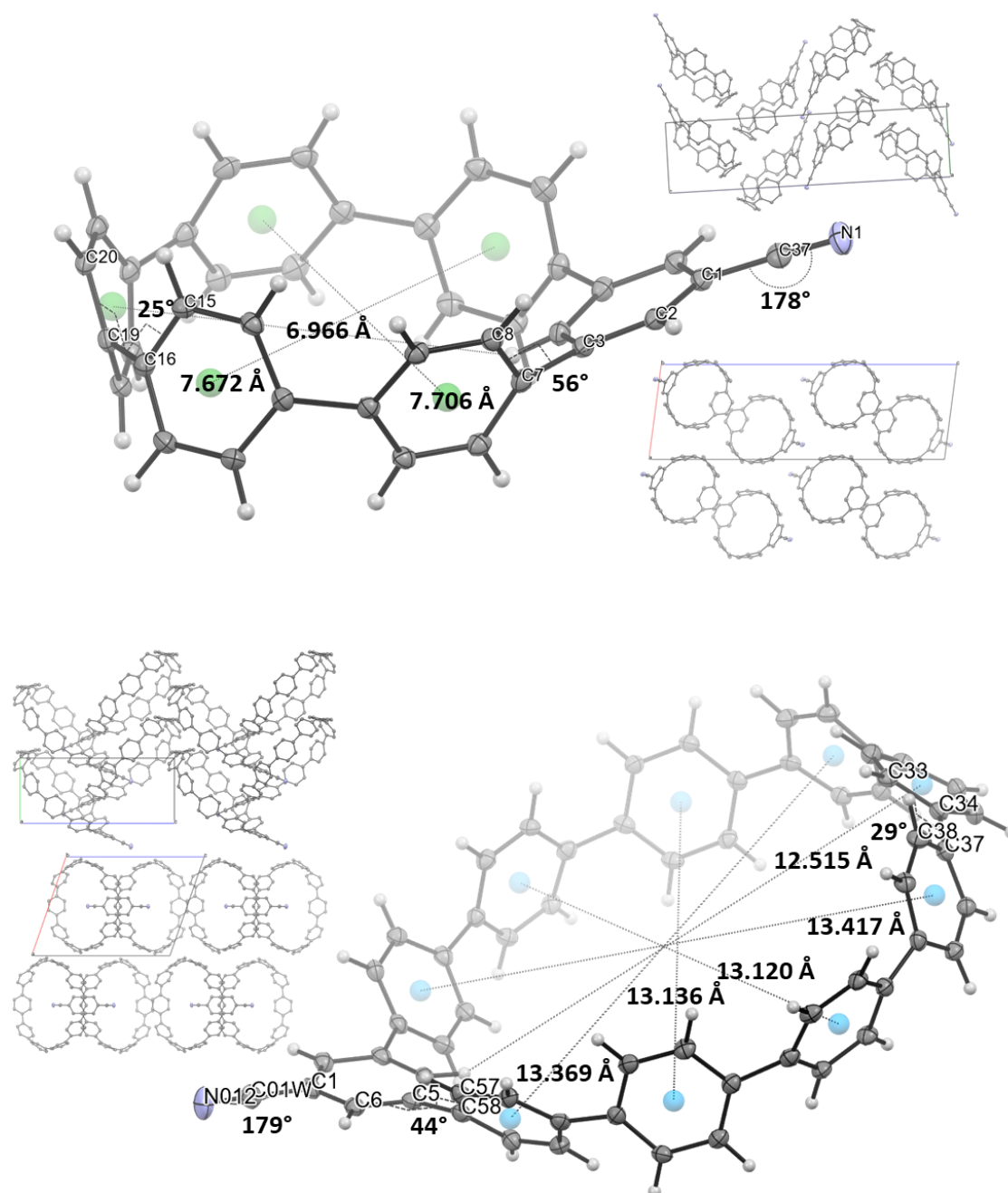


Figure 45. ORTEP drawings of CN-*m*[6]CPP **158** (top, left) at 50% probability, and its corresponding crystal packing from two different angles (top, right). ORTEP drawing of CN-*m*[10]CPP **160** (bottom, right) at 50% probability, and its corresponding crystal packing from two different angles (bottom, left). Structural parameters are shown for the two ORTEP drawings. Solvent molecules have been omitted in all cases, whereas for the crystal packing structures the protons have been omitted as well.

Both the solid-state structure of **158** and **160** revealed that the nitrile group points outside the cyclic structures. The nearly regular shape of the macrocyclic structures is distorted by an inwards pointing proton, which decreases the inner radius by around 0.7 Å. In comparison to unsubstituted *m*[6]CPP the dihedral angles inside CN-*m*[6]CPP **158** are widened throughout the whole molecule. For example, the dihedral angles starting from the *meta*-phenyl diminish from 56° (between C2 and C8) to 23° (between C15 and C20) in CN-*m*[6]CPP **158**, while for CN-*m*[10]CPP **160** these values change from 44° (between C6 and C57) to 29° (between C38 and C33).

Both compounds reveal the typical herring bone structure arrangement which is known for various examples of (*meta*)[*n*]CPPs.^{53,54,68,121,163,264,265} While the functional group of one CN-*m*[10]CPP **160** molecule points into the CPP segment of a second molecule, the functional group of one CN-*m*[6]CPP molecule is pointing into the empty space between the molecules. Moreover, changing the perspective and looking from the top onto the CPP motif of both molecules, reveal the tubular packing of **158** and **160**, which is also characteristic for (*meta*)[*n*]CPPs.

After discussing their synthesis and solid-state structure, the photophysical properties of the CN-*m*[*n*]CPPs **158** – **160** have been characterized. This not only included UV-vis- and fluorescence spectra but additionally their fluorescence quantum yield. The corresponding spectra are shown in Figure 46.

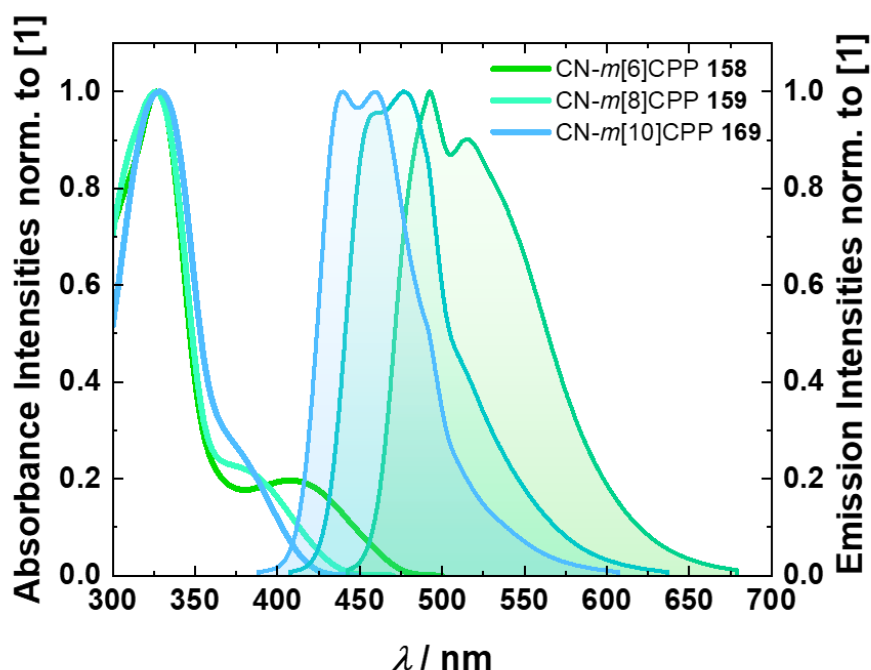


Figure 46. Absorbance (left, blank area underneath the lines, $c = 3 \cdot 10^{-5}$ M) and emission (right, filled area underneath the lines, $c = 3 \cdot 10^{-6}$ M) spectra of CN- $m[n]$ CPPs **158** - **160** measured at room temperature in chloroform.

UV-vis-spectra of all three compounds show a similar absorption maximum around 327 nm corresponding to HOMO – LUMO+1 and HOMO-1 – LUMO transitions.¹⁶³ Moreover, a second absorption shoulder around 419 nm, which corresponds to the HOMO – LUMO transition, is visible. This second shoulder is clearly visible in the UV-vis-spectrum for CN- $m[6]$ CPP **158** and becomes less prominent as the ring size of the CN- $m[n]$ CPPs increases. Fluorescence spectroscopy reveals the size-dependent properties of the CN- $m[n]$ CPPs **158** – **160** as it is also known for their $[n]$ CPP counter parts as well as for their unsubstituted $m[n]$ CPP derivatives. With decreasing ring size there is a bathochromic shift from 440 nm for CN- $m[10]$ CPP **160**, over 477 nm (CN- $m[8]$ CPP **159**) and 519 nm (CN- $m[6]$ CPP **158**). Additionally, all three compounds **158** – **160** show a second emission maximum, which is shifted roughly 10 nm to higher wavelengths. TRETIAK's group suggested in 2014, that the two peaks can be ascribed to vibronic characteristics and a corresponding reduction in vibrational coupling.²⁶⁶

In line with the pattern observed in unsubstituted $m[n]$ CPPs, CN- $m[n]$ CPPs **158** – **160** exhibit a rise in extinction coefficient and quantum yield as the ring size increases. As a result, the brightness also increases when a greater number of

phenyl units are incorporated into the macrocyclic ring. The photophysical characteristics of CN-*m*[*n*]CPPs **158** – **160** are outlined in Table 3.

Table 3. Photophysical characteristics of CN-*m*[*n*]CPPs **158** – **160** measured in chloroform at room temperature. Absorbance maximum ($\lambda_{\text{abs,max}}$), molar extinction coefficient at absorbance maximum ($\epsilon_{\text{abs,max}}$), emission maxima ($\lambda_{\text{em,max1}}$, $\lambda_{\text{em,max2}}$), fluorescence quantum yield at first emission maximum (Φ_{max}), and calculated brightness ($\epsilon_{\text{abs,max}} \cdot \Phi_{\text{max}}$).

	$\lambda_{\text{abs,max}}$ / nm	$\epsilon_{\text{abs,max}}$ / (M·cm) ⁻¹	$\lambda_{\text{em,max1}}$ / nm	$\lambda_{\text{em,max2}}$ / nm	Φ_{max}	$\epsilon_{\text{abs,max}} \cdot \Phi_{\text{max}}$ / (M·cm) ⁻¹
158	327	$5.7 \cdot 10^4 \pm 0.1$	493	519	0.24	$1.4 \cdot 10^4$
158	326	$6.9 \cdot 10^4 \pm 0.4$	465	477	0.52	$3.6 \cdot 10^4$
160	328	$7.3 \cdot 10^4 \pm 0.3$	440	458	0.71	$5.2 \cdot 10^4$

Having investigated the photophysical characteristics of the novel CN-*m*[*n*]CPPs **158** – **160**, their different potentials should be investigated. This discussion not only involved the functional group conversion of the nitrile group for CN-*m*[6]CPP **158** but also the application of CN-*m*[10]CPP **160** in a supramolecular assembly with fullerene C₆₀.

After comparison of the structural parameters of the CN-*m*[10]CPP **160** and its unsubstituted *all-para* analogue [10]CPP **155**, **160** should form a supramolecular assembly with C₆₀, too, as it shows a nearly regular shape. To test this hypothesis, a ¹H-NMR experiment by mixing stoichiometric amounts of CN-*m*[10]CPP **160** with C₆₀ in deuterated tetrachloroethane (TCE-*d*₂) was measured at room temperature. The result is depicted in Figure 47.

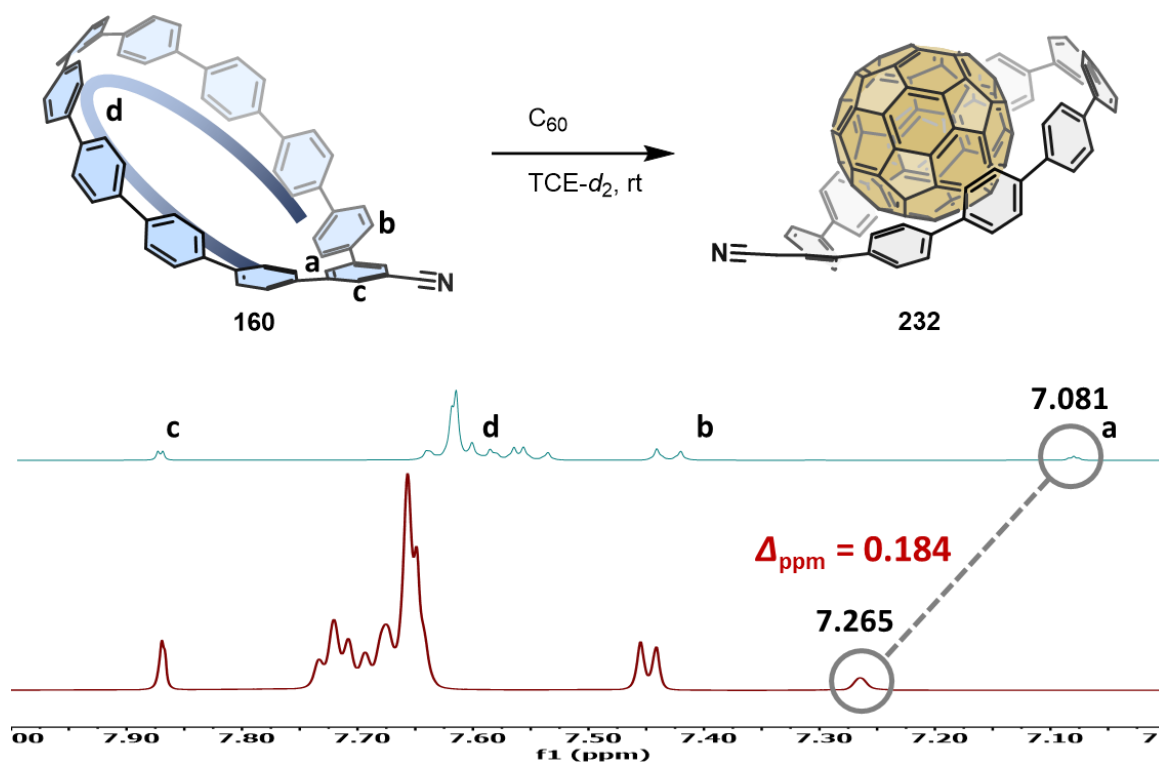


Figure 47. $^1\text{H-NMR}$ spectrum in deuterated tetrachloroethane- d_2 of a 1:1 mixture of CN-*m*[10]CPP **160** at room temperature before (top) and after (bottom) the addition of fullerene C_{60} .

On a first glance, the $^1\text{H-NMR}$ signals of **160** shifted significantly in most cases downfield. This can be rationalized by the electron affinity of the fullerene, which decreases the electron density throughout the *m*[10]CPP **160**. Additionally, the dihedral angle between the *meta*-phenyl and its neighbors resulting in an affection of the inwards pointing proton by the ring current. Taking both effects into account, can be reason enough to rationalize the significant shift by 0.184 ppm downfield of the signal accused by the inwards pointing proton. Furthermore, the signal caused by the four protons next to the *meta*-phenyl are nearly unaffected by the complexation of C_{60} as the protons c next to the nitrile functionality. It is noteworthy that this signal is the only one which shifts to a higher field.

After getting a qualitative insight into the fluorescence quenching of our system, fluorescence titration experiments were used to quantify the binding affinity of C_{60} towards CN-*m*[10]CPP **160** (Figure 48).

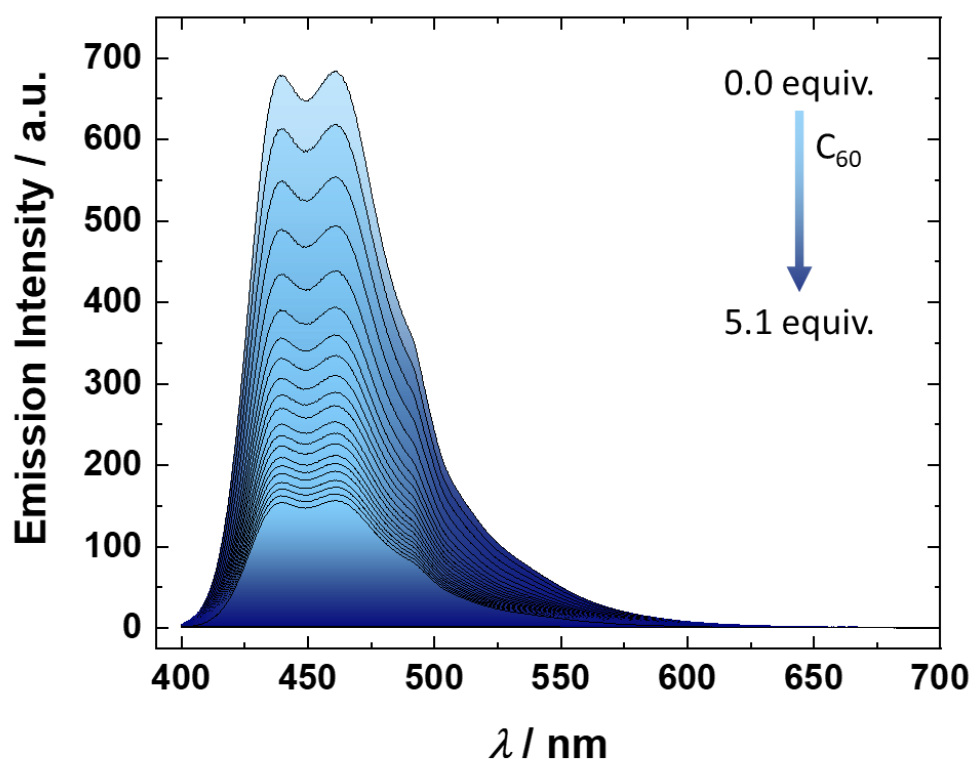
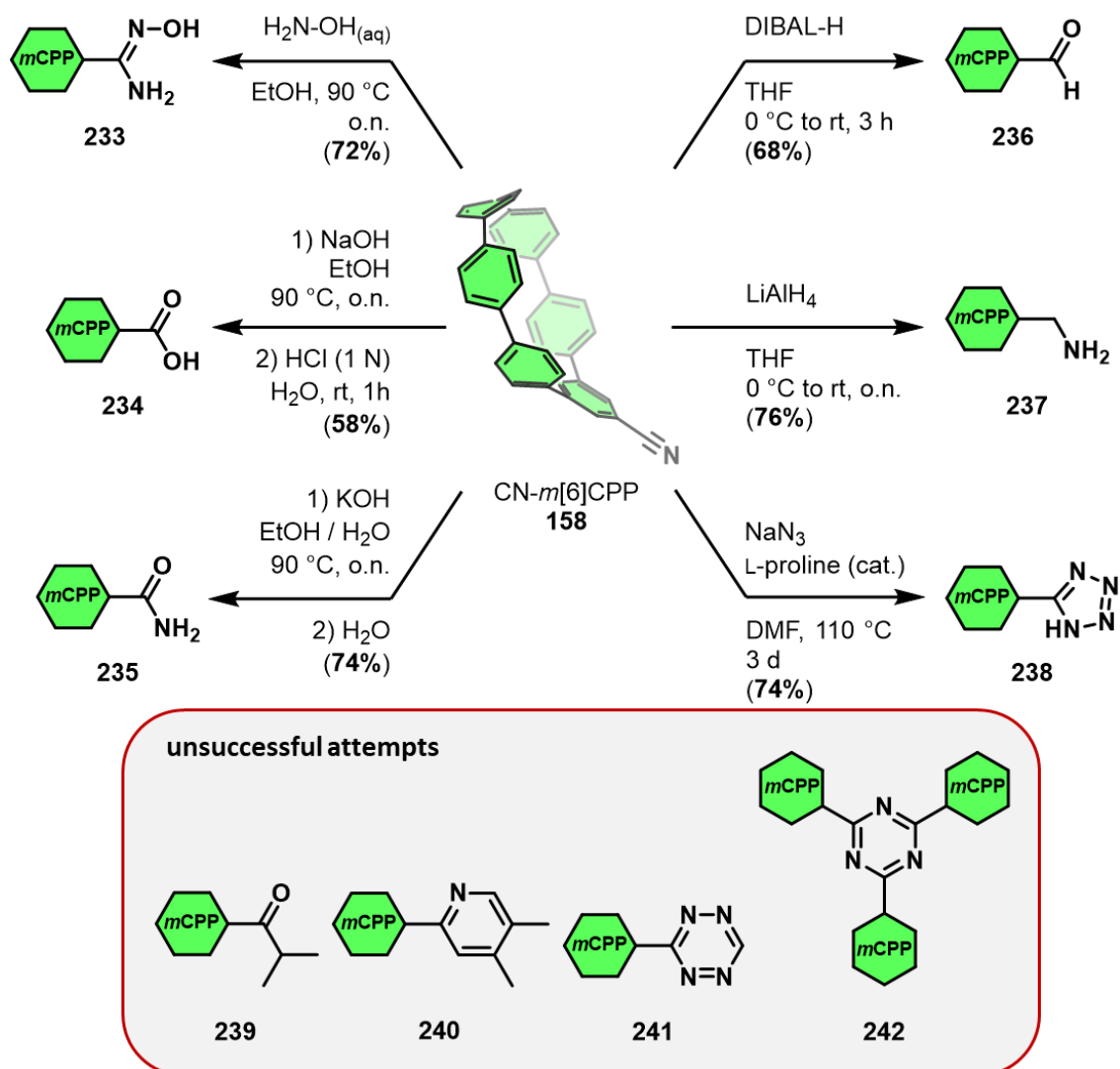


Figure 48. Results of fluorescence quenching experiments.

Utilizing the online-tool *Bindfit*^{267,268}, the association constant (K_a) of the self-assembly system **232** was determined to be $6.73 \cdot 10^4 \text{ M}^{-1}$. The small deviation from the regular circular shape due to the *meta*-connectivity already results in a decrease in K_a when compared to [10]CPP **155**. Nonetheless, the binding strength of the self-assembly system **232** can compete with systems such as calixarenes²⁶⁹ and cycloparaphenyleneacetylenes.²⁷⁰

Further, to proof that the initial hypothesis that the nitrile serves as a valuable functional handle towards different functional groups, different reaction conditions on CN-*m*[6]CPP **158** (Scheme 61) were tested. Therefore, not only simple chemical transformations such as hydrolysis and reduction were chosen, but also more complex reactions towards different nitrogen containing heterocycles (1-*H* tetrazole **215**, pyridine **217**, and tetrazine **218**).



Scheme 61. Functional group conversion of the cyano-functionality attached to the CN-*m*[6]CPP **158**. For clarity, the *m*[6]CPP motif is abbreviated as *m*CPP-labelled green hexagon. For details on the unsuccessful attempts **239** - **242** please refer to the experimental part.

Utilizing hydroxylamine as a nucleophilic base, resulted in the formation of amidoxime **233** in yields of 72%. This functional group is of great importance as precursor of certain heterocycles, which are used in the field of medicinal chemistry.²⁷¹ Applying alkaline conditions towards the hydrolysis of the nitrile-group led to the formation of two distinct products, depending on the quenching conditions of the reaction. The reaction terminated with HCl resulted in the precipitation of the carboxy-*m*[6]CPP **234**, yielding 58%. On the other hand, when water was used to quench the reaction, amide **235** was obtained in 74% yield. Unfortunately, the addition of the *iso*-propyl magnesium GRIGNARD reagent to our CN-*m*[6]CPP **165** just resulted in recovered starting material and not in the formation of the corresponding ketone **239**.

However, it is possible to reduce nitriles using suitable reagents such as DIBAL-H and LiAlH_4 . The utilization of DIBAL-H resulted in the conversion of the nitrile-group to aldehyde **236** with a yield of 68%. By utilizing the stronger reducing agent LiAlH_4 , the benzylic amine **237** could be isolated in yields of 76%. Moreover, the 1*H*-tetrazole **238** was successfully synthesized with a yield of 74% through a 1,3-dipolar cycloaddition using sodium azide and L-proline as organocatalyst. Regrettably, further attempts to synthesize substituted *m*[6]CPPs with larger heterocycles (**240** – **242**) have been unsuccessful, as only starting material was reisolated decomposition of the same was observed. Nonetheless, by synthesizing a small library of substituted *m*[6]CPPs **233** – **238**, the versatility of the nitrile as a functional group could be demonstrated for the *m*[6]CPP scaffold.

Following that, we further investigated their UV-vis- and fluorescence behavior. The spectra of the substituted *m*[6]CPPs **158**, and **233** – **238** are displayed in Figure 49.

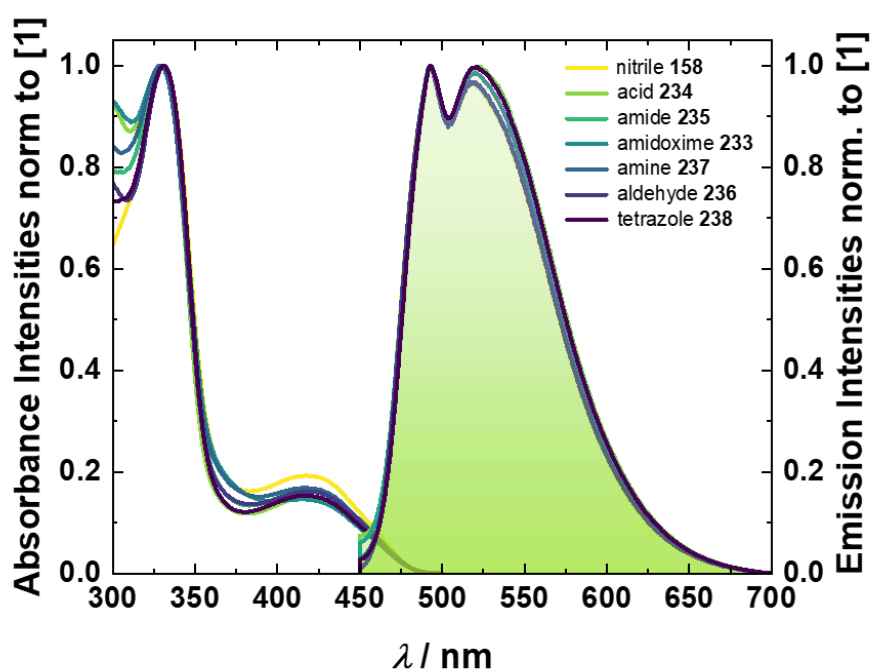


Figure 49. Stacked UV-vis- (left, no colored areas underneath the curves) and emission (right, colored areas underneath the curves) spectra of the different substituted *m*[6]CPPs **165**, **210** – **215**. Measured in DMSO ($c = 10^{-5}$ M) at room temperature.

Demonstrating the very good solubility of the novel *m*[6]CPPs **158**, and **233** – **238** even in polar solvents, the UV-vis- and fluorescence spectra have been recorded in DMSO. Doing so, revealed that the corresponding maxima in absorbance and fluorescence do not change when compared to the parent CN-*m*[6]CPP **158**. Only

a small shift from 327 nm to 330 nm occurred in the absorbance spectrum when measured in DMSO instead of DCM. On a first glance this observation seemed surprising. However, this can be rationalized by the orbital symmetry within the $m[n]$ CPPs and the *meta*-phenyl, where our functional handles are attached, not participating on the conjugation throughout the macrocyclic structure.

Furthermore, the carboxy- $m[6]$ CPP **234** enabled solubility studies in mixtures of water and DMSO for a first insight using similar derivatives in biological applications. Therefore, UV-vis and emission-spectra of **234** were measured in DMSO with different water contents at two different pH levels (Figure 50).

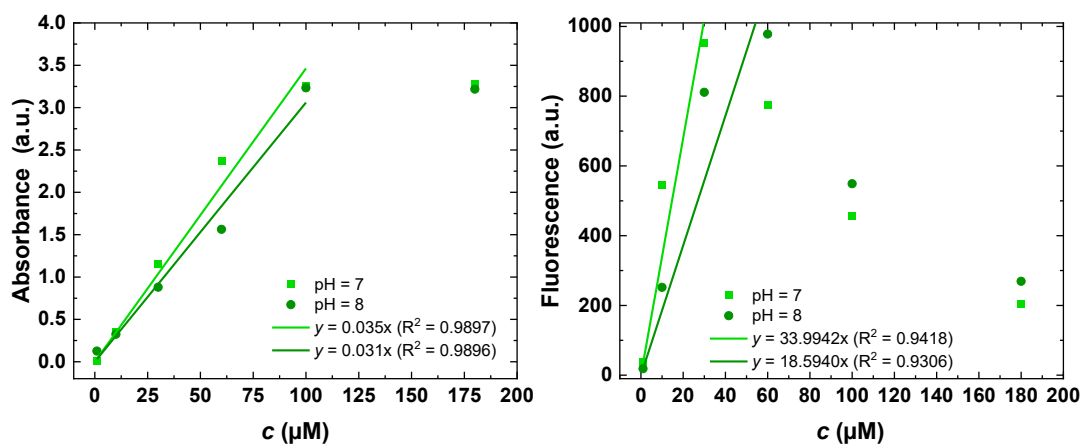


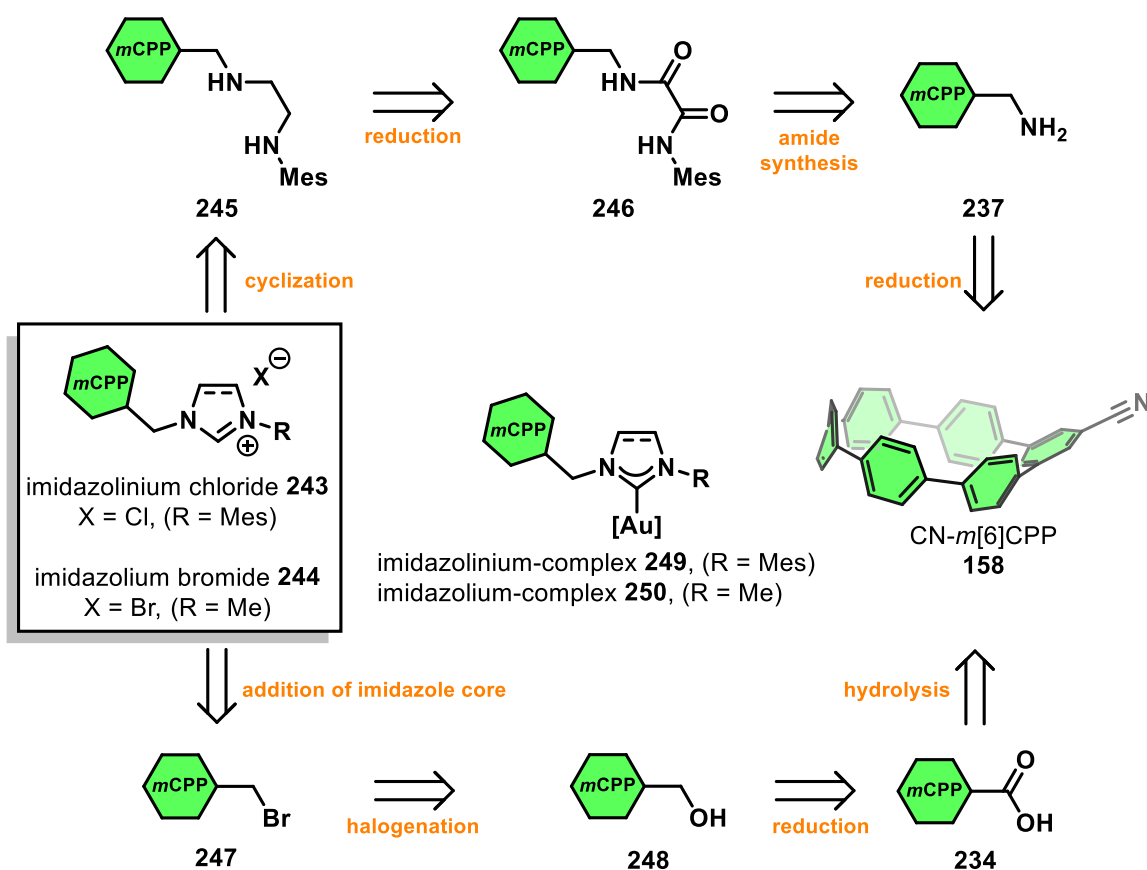
Figure 50. Solubility assessment of carboxy- $m[6]$ CPP **234**. Absorbance (left) and fluorescence (right) over increasing concentrations of **234** at two different pH levels.

At a pH level of 7, the absorbance started to deviate from linearity after a concentration of 100 μM , and the fluorescence after a concentration of 30 μM . Increasing the pH level to 8, using a mono- and dibasic potassium phosphate buffer system, shifted this maximum in concentration towards 60 μM in the fluorescence spectrum. At higher pH levels, the carboxylic acid is in its deprotonated form, thus resulting in a better solubility which fits to our obtained data. The fluorescence intensity can be influenced by several factors, such as aggregation, and static or dynamic fluorescence quenching, though. As **234** is only end-functionalized without additional solubilizing linker, that solubility of at least 60 μM is remarkable. Especially, the facile modification of its properties by simple chemical transformations opens great potential in further development of small molecule fluorophores based on the $m[6]$ CPP scaffold.

After synthesis of a small library of different functionalized *m*[6]CPPs, the *m*CPP scaffold should be incorporated into two different types of ligand systems. This not only allowed for the demonstration of the applicability of the aforementioned synthetic strategies in materials design but also the versatility of the *m*[6]CPP as an intriguing fluorophore.

3.3.2. Synthesis of a Luminescent Gold(I)-Complex

As a contribution to the topics of NHCs and *m*[*n*]CPPs, the synthesis of two different NHC ligands with a methylene bridged *m*[6]CPP scaffold was planned. These ligands should allow for the investigation of the influence of the core structure and the metal center on the *m*[6]CPP scaffold and vice versa. Moreover, this combination might open new research areas in material and life sciences, as well as (metal-)organic chemistry. The synthetic approach is presented in Scheme 62.

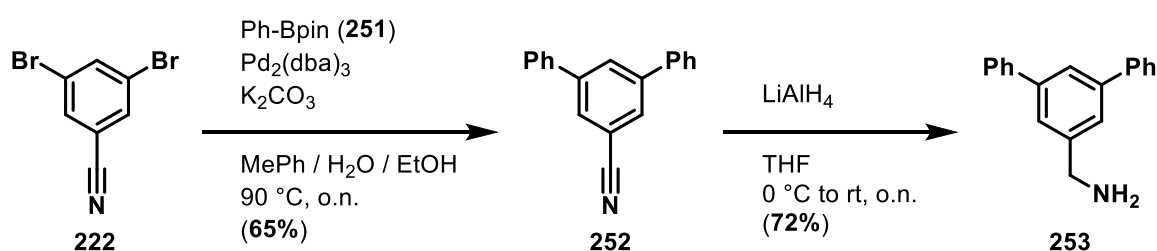


Scheme 62. Retrosynthetic analysis of the synthesis of imidazolium chloride **243** and imidazolium bromide **244** commencing from CN-*m*[6]CPP **158**. For clarity, *m*[6]CPP has been abbreviated as *m*CPP-labelled green hexagon.

A strategy to synthesize the imidazolium precursor **243** uses diamine **245** as starting material, which undergoes a cyclization reaction in the last step with a trialkyl orthoformate. The desired diamine **245** can be afforded through reduction of an oxalamide **246**, which is a product of a STEGLICH-type amide synthesis, commencing from the amine **237**. This amine **237** on the other hand is affordable through the reduction of the CN-*m*[6]CPP **158**.

Following a second strategy, the synthesis of the imidazolium bromide **244** through the addition of the commercially available 1-methyl imidazole to (bromo-methylene)-*m*[6]CPP **247** was addressed. Within that strategy, carboxy-*m*[6]CPP **234** served as lead structure. Thus, *m*[6]CPP **247** can be afforded within two steps starting from **234**. Therefore, the carboxy-group needs to undergo first a reduction followed by a halogenation reaction.

In case of any synthetic challenges, especially during the synthesis of the generally more prone imidazolium precursor **243**, the development of a synthetic strategy based on the *meta*-terphenyl substituted model substrate **252** (Scheme 63).

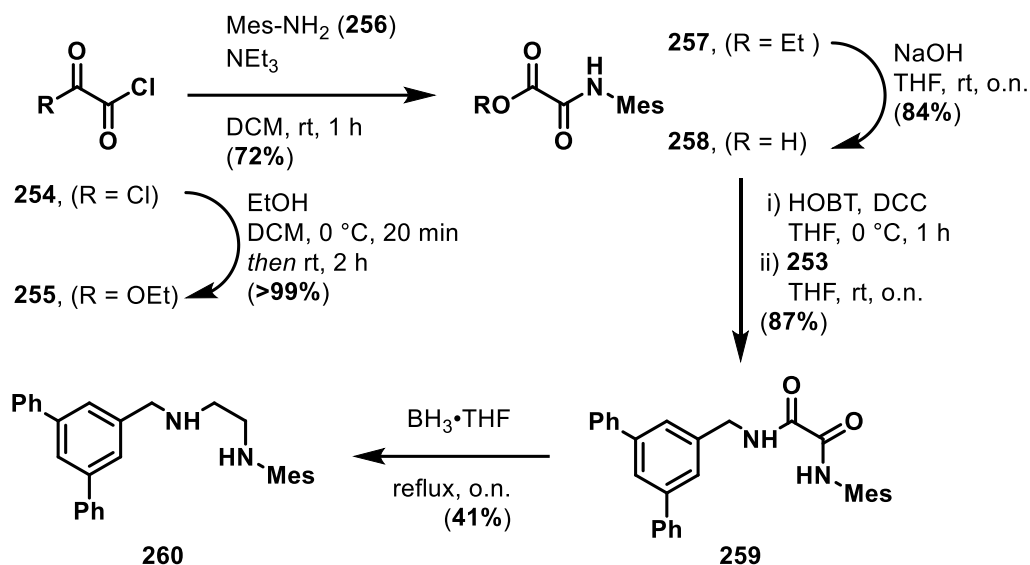


Scheme 63. Synthesis of the corresponding model substrate **230** based on a *meta*-terphenyl.

Commencing from 3,5-dibromo benzonitrile (**222**), the *meta*-terphenyl unit was realized through a SUZUKI-MIYAUURA cross-coupling reaction with pinacol-ester **251**. Using $\text{Pd}_2(\text{dba})_3$ and K_3PO_4 as catalytic system, the nitrile-substituted *meta*-terphenyl **252** was afforded in yields of 65%. Applying reductive conditions, using LiAlH_4 , afforded the corresponding amino-derivative **253**.

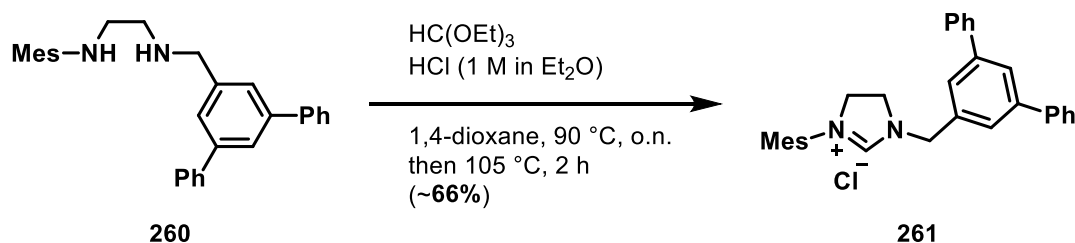
With benzylic amine **253** in hand, the synthesis of the diamine **260** was addressed. Within these steps, not only the synthetic precursor for the backbone of the targeted imidazolium precursor was intended, but the asymmetric substitution pattern as well. Therefore, the synthesis of *N*-(mesityl)-oxanilic acid **258** was required first, which subsequently was used for the synthesis of the oxalamide **259**.

Following this, the diamine **260** was synthesized through reduction utilizing LiAlH_4 (Scheme 64).



Scheme 64. Synthesis of diamine **260** starting from oxalyl chloride (**254**).

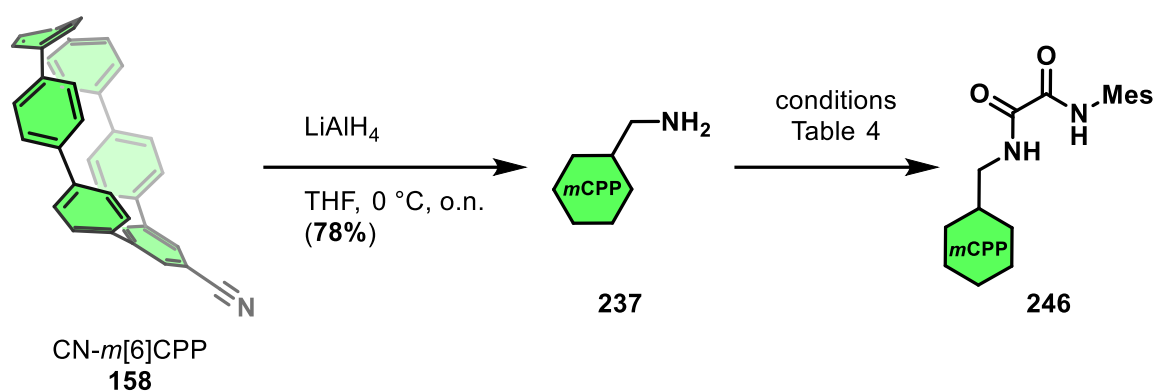
Beginning with oxalyl chloride (**254**), an asymmetric pattern was introduced through the synthesis of the ester **255**, which was obtained in quantitative yields. As now the acid chloride within **255** is more reactive than the ester moiety, *N*-(mesityl)-oxanilic ethyl ester **257** was isolated in good yields of 72%. Subsequent saponification of ester **257** led to the carboxylic acid **258** in yields of 84%. Now combining amine **253** with the acid **258** in a STEGLICH-type amide synthesis afforded the oxalamide **259** in very good yields of 87%. Within the next step, borane-tetrahydrofuran was added to the oxalamide **259** in order to synthesize diamine **260** with a satisfactory yield of 41%. Within the final step, the final imidazolium core structure using triethyl orthoformate, was synthesized (Scheme 65)



Scheme 65. Synthesis of imidazolium **261** through cyclization using triethyl orthoformate.

Under acidic conditions, the imidazolium chloride **261** was synthesized with approximately 66% yield. Unfortunately, solvent residuals could not be removed during the purification attempt as the material decomposed over time.

However, after developing an appealing synthesis strategy towards an imidazolium salt, that strategy was transferred to the *m*[6]CPP scaffold. In doing so, the first step was to transform the nitrile **165** into the primary amine **214** using LiAlH_4 as the reducing agent. After affording the amino-methyl *m*[6]CPP **237** in 78%, the next step was the synthesis of the corresponding oxalamide through STEGLICH esterification-type amide synthesis (Scheme 72).



Scheme 66. Synthesis of *N*-(mesityl)-*N'*-(1-methylene-*m*[6]CPP)oxalamide **246**. For clarity, *m*[6]CPP has been abbreviated as *m*CPP-labelled green hexagon.

Table 4. Optimization screening for the optimization reaction towards oxalamide **246**. The reaction conditions were kept from the model substrate (solvent mixture: THF / DCM, $T = 0\text{ }^\circ\text{C}$ to rt, o.n.,). HOBT – 1-hydroxybenzotriazol, DCC – *N,N'*-dicyclohexylcarbodiimide, EDC – 1-ethyl-3-(3-dimethylaminopropyl)carbodiimide, NMM – *N*-methylmorpholine, DIEPA – diisopropylethylamine.

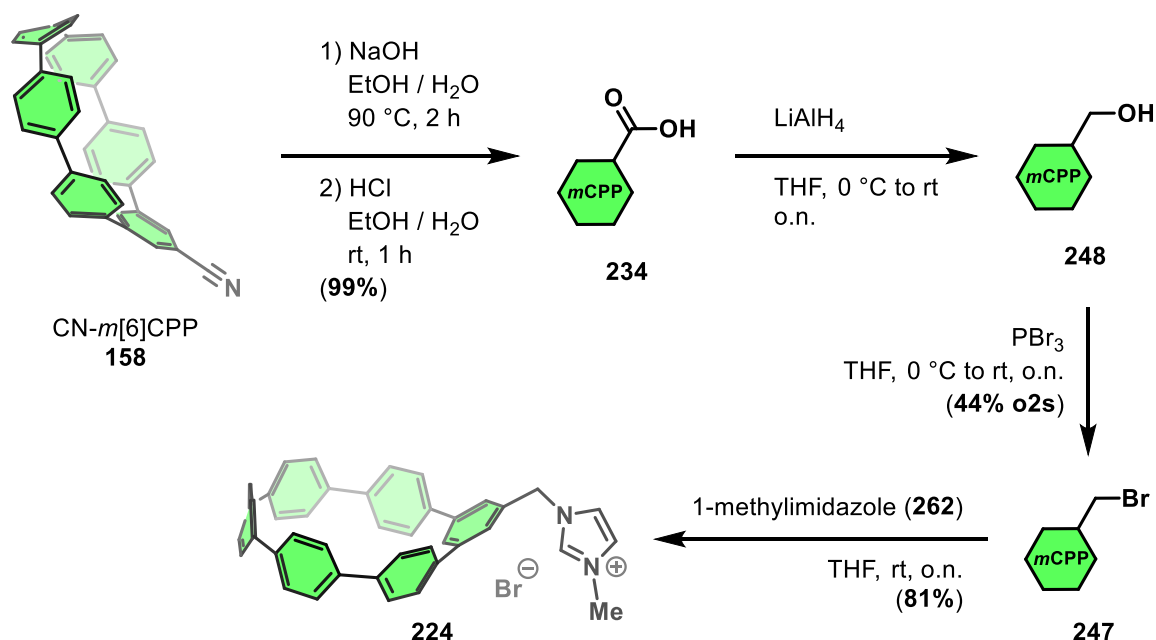
entry	coupling partners	carbodiimide	base	yield / %
1	258 / HOBT	DCC	-	30
2	258 / HOBT	EDC·HCl	-	24
3	258 / HOBT	EDC·HCl	NMM	35
4	258 / HOBT	EDC·HCl	DIPEA	63

Even though the synthesis of oxalamide **259** was straightforward, at this point some optimization of the reaction conditions was required, as the initial conditions only led to 29% yield (Table 4, entry 1).

In a first instance, a change of the carbodiimide derivative to EDC·HCl was tested, as the corresponding urea derivative is water soluble and could be easier removed

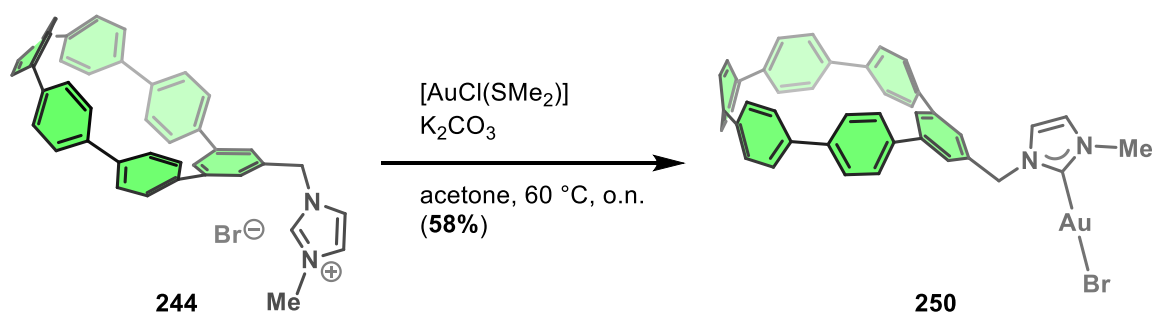
during the aqueous work up. Unfortunately, this modification led to a comparable lower yield of 24% of the desired product **246**. Drawing the conclusion, that the HCl, which was set free during the reaction might interfere somehow with amine **237** and therefore lowers the yield. Thus, *N*-methyl morpholine (NMM) was added to the reaction mixture, as this often facilitates the synthesis of peptides.²⁷² Indeed, the yield now increased to 35% (Table 4, entry 3), which was still not at a satisfactory. Therefore, NMM was displaced with di-*iso*-propyl ethyl amine (DIEPA), resulting in a satisfying yield of 63% of the oxalamide **246**. Unfortunately, despite different attempts to afford the ethylene diamine derivative **245**, this compound could not be isolated due to its instability, concluding this reaction as failed to that point of time.

Starting the second approach, the mesitylene was displaced by a methylene group as additional stabilization effects due to steric wingtips was not required at a first glance. It is common knowledge in the field of NHC synthesis, that the unsaturated backbone on the imidazolium precursor already displays higher stability when compared to an imidazolinium precursor. Moreover, it allows for the utilization of the commercially available 1-methyl imidazole (**228**) as starting material (Scheme 67).



Scheme 67. Synthesis of imidazolium bromide **224** commencing from CN-*m*[6]CPP **158**. For clarity, *m*[6]CPP has been abbreviated as *m*CPP-labelled green hexagon for the intermediate steps.

On a comparable large scale, nitrile **158** was converted to the carboxy-*m*[6]CPP **234** in almost quantitative yields. This substantial improvement in the yield can be attributed to the larger scale, which facilitated the purification of the desired product as column chromatography was not required anymore and washing with cold ethanol and water was sufficient. Within the following two steps, the (bromo-methyl)-*m*[6]CPP **247** was addressed as an important intermediate towards the substituted imidazolium salt **224**. Therefore, LiAlH_4 was used to address the reduction of the carboxylic acid **234** towards the primary alcohol **248**. Subsequently, PBr_3 led to the formation of (bromo-methylene)-*m*[6]CPP **247** in 44% over two steps. After the successful synthesis of the imidazolium bromide **224**, its applicability as a NHC ligand was demonstrated. In general, there exist three main approaches towards the synthesis of metal-NHC complexes, all of which involve the utilization of an imidazolium salt or its derivatives.^{192,273–275} Among these approaches, the so-called weak-base approach, which was independently developed by NOLAN et al.²⁷³ and GIMENO et al.²⁷⁵ in 2013, appeared to be a promising strategy for the synthesis of the $[\text{AuBr}(\text{NHC})]$ complex **250**. This synthetic strategy utilizes a weak, economical base and solvents such as NEt_3 , NaOAc , K_2CO_3 , DCM , or acetone. Furthermore, this method is also compatible with ambient atmospheric conditions. Thus, a linear gold(I)-complex of the general form $[\text{AuX}(\text{NHC})]$ was synthesized (Scheme 68).



Scheme 68. Synthesis of $[\text{N}-(\text{Methyl})-\text{N}'-(1\text{-methylene-}m[6]\text{CPP})\text{-imidazolium}]\text{gold bromide } \mathbf{250}$.

Addressing the $[\text{AuBr}(\text{NHC})]$ complex **250**, imidazolium bromide **244** was stirred in a mixture of K_2CO_3 and $[\text{AuCl}(\text{SMe}_2)]$ in acetone at $60\text{ }^\circ\text{C}$ overnight. After purification, the complex could be isolated with a yield of 58%.

At this point, suitable crystals for X-ray diffraction measurements were isolated for both the imidazolium bromide **244** and the gold(I)-complex **250**. Therefore, vapor

diffusion of *n*-pentane into a saturated solution of the imidazolium bromide **244** in a 1:1 solvent mixture of DCM and acetonitrile was applied. Similarly, the crystals of the gold(I)-complex **250** were obtained. Therefore, a saturated solution of **250** in a 1:1 mixture of 1,2-dichloroethane and 1,2-dichlorobenzene and *n*-pentane for vapor diffusion were used. Structural parameter in addition to the ORTEP drawing at 50% probability and the crystal packing are displayed in Figure 51.

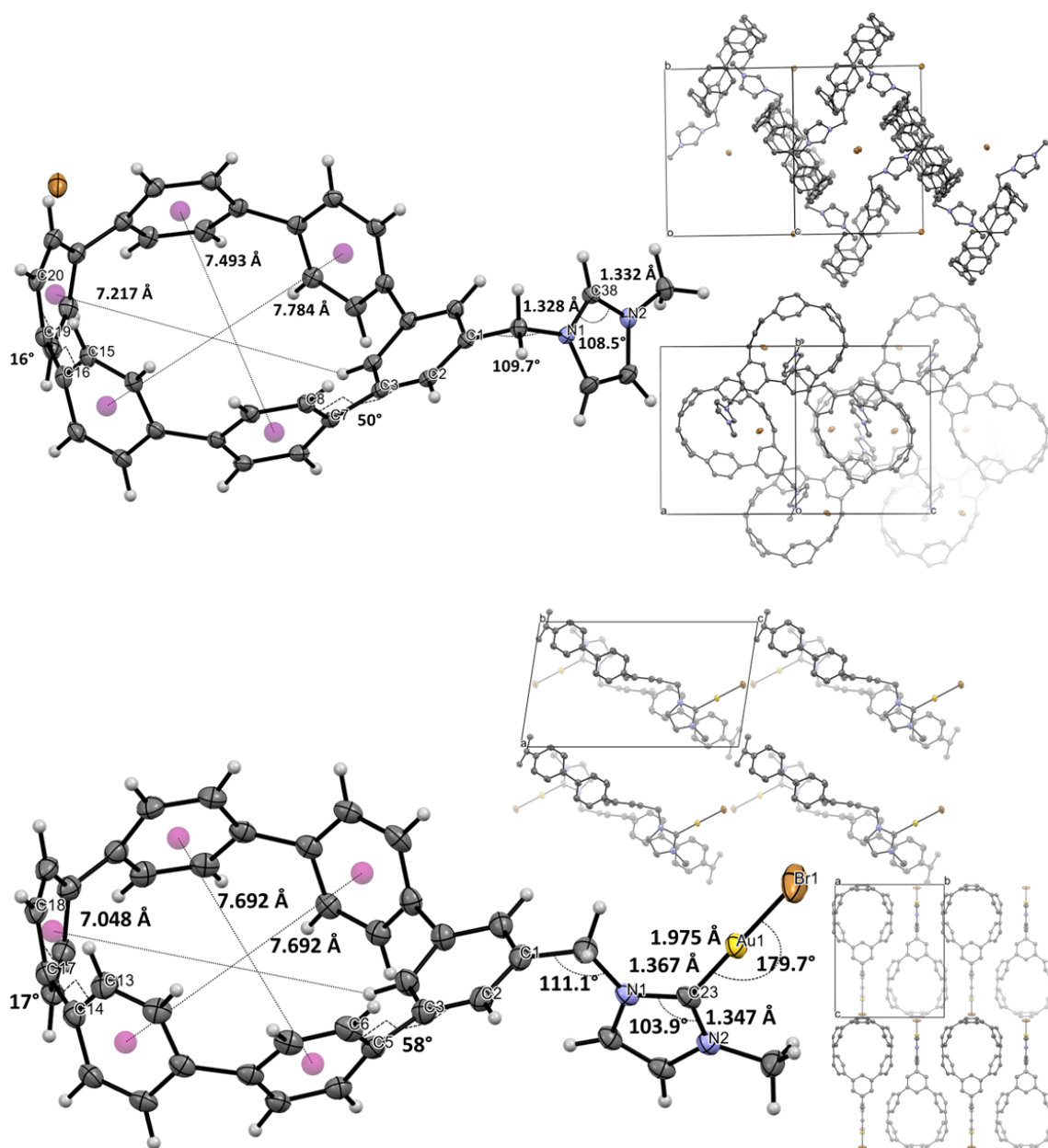


Figure 51. ORTEP drawing of imidazolium bromide **244** (top, left) at 50% probability, and its corresponding crystal packing from two different angles (top, right). ORTEP drawing of the gold(I)-complex **250** (bottom, left) at 50% probability, and its corresponding crystal packing from two different angles (bottom, right). Structural parameters are shown for the two ORTEP drawings. Solvent molecules have been omitted in all cases, whereas for the crystal packing structures the protons have been omitted as well.

In both molecules, the two structural motifs – the *m*[6]CPP as wingtip as well as the imidazole core, are connected through the flexible methylene linker. In imidazolium bromide **244**, the corresponding bond angle between N(1) and C(1) is measured to be 109.7°. Furthermore, in this compound the bond lengths between the nitrogen atoms and the carbenic carbon atom are almost equal ($d_{C(38)-N(2)} = 1.332 \text{ \AA}$; $d_{C(38)-N(1)} = 1.328 \text{ \AA}$), indicating a well-distributed positive charge between the two nitrogen atoms. Upon coordination and formation of the Au(I)-complex **250**, the bond angle between N(1) and C(1) increases to 111.1°. The complex **250** exhibits an approximately linear two-coordinate geometry at the Au(I)-centre, with the C(23)-Au(1)-Br(1) angle measuring 179.7°. Additionally, the bond lengths within the imidazolium core changed to 1.345 Å (N(2)–C(23)) and 1.361 Å (C(23) – N(1)), respectively, while the bond length between C(23) and Au(1) is 1.975 Å.

It is noteworthy that the choice of solvent mixtures for growing suitable single-crystals significantly affects the solid-state arrangement, which is especially true for the complex **250** (Figure 52).

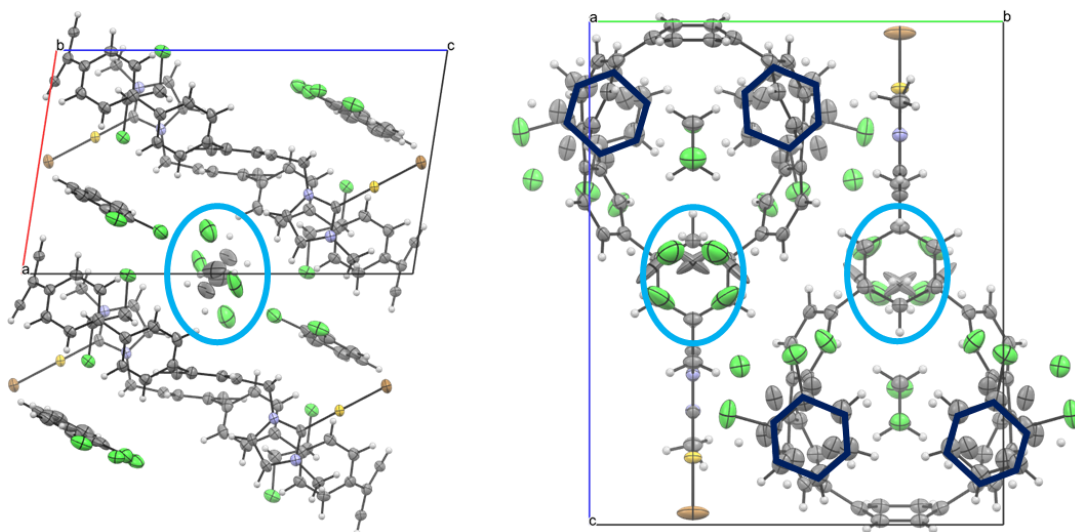


Figure 52. Crystal-packing of the Au(I)-complex **250** from different perspectives. Disordered solvent molecules are highlighted in blue (1,2-dichloroethane) and dark blue (1,2-dichlorobenzene).

As already mentioned in the discussion of the solid-state structures of CN-*m*[*n*]CPPs **158** ($n = 6$) and **160** ($n = 10$), the *m*[6]CPP segment of imidazolium bromide **244** displays a herringbone arrangement as well. Notably, this arrangement is disrupted in the solid-state structure of the gold(I)-complex **250** due to the intercalation of highly disordered solvent molecules, resulting in a sheet-like arrangement. As presented in Figure 52, two 1,2-dichlorobenzene molecules are

distributed on the *m*[6]CPP backbone, where they can wiggle in a certain degree. Additionally, 1,2-dichloroethane is not only placed within the *m*[6]CPP but also intercalated between the *meta*-phenyl units and the 1,2-dichlorobenzene molecules. The latter 1,2-dichloroethane molecules are highly disordered, due to the amount of free space around the solvent molecule.

Furthermore, a different perspective on the solid-state packing structures of **244** and **260** reveals a tubular packing arrangement of the *m*[6]CPP segments. Notably, the methyl group of one imidazolium molecule **244** points inside the ring structure of a second molecule of **244**, thereby intercalating the molecules with each other.

In terms of torsional angles, the *m*[6]CPP segment within **244** exhibits smaller values, ranging from 50° (between C(2) – C(8)) to 16° (between C(15) – C(20)), compared to the CN-*m*[6]CPP **158**. These torsional angles change upon coordination of the gold(I)-species **250**, now ranging from 58° (between C(2) – C(6)) to 17° (between C(13) – C(18)).

Subsequent to the synthesis, solution-state absorption and luminescence spectra were measured for both the imidazolium bromide **244** and the Au(I)-complex **250** in chloroform. The absorption spectra of both substances show the characteristics of the *m*[6]CPP substituent, recognizable on the sharp absorption shoulder around 326 nm and the broad shoulder around 405 nm (Figure 53 and Figure 54). While the main absorption is assigned to the HOMO-1 to LUMO and HOMO to LUMO+1 transitions, the second absorption shoulder is represented by the HOMO to LUMO transition.¹⁶³ It is noteworthy that the nature of the absorption bands do not change upon coordination of the imidazolium salt to Au(I). Therefore, density functional theory (DFT) calculations for the gold(I)-complex **239** at a PBE0/ZORA-def2-TZVPP level,^{276–280} using ORCA 5.0 have been conducted.^{281,282} These calculations support that the absorption energies are still dominated by HOMO-1 to LUMO and HOMO to LUMO+1 transitions as well as the HOMO to LUMO transition, while the gold center and the imidazole core are electronically decoupled from the *m*[6]CPP part (Figure 53).

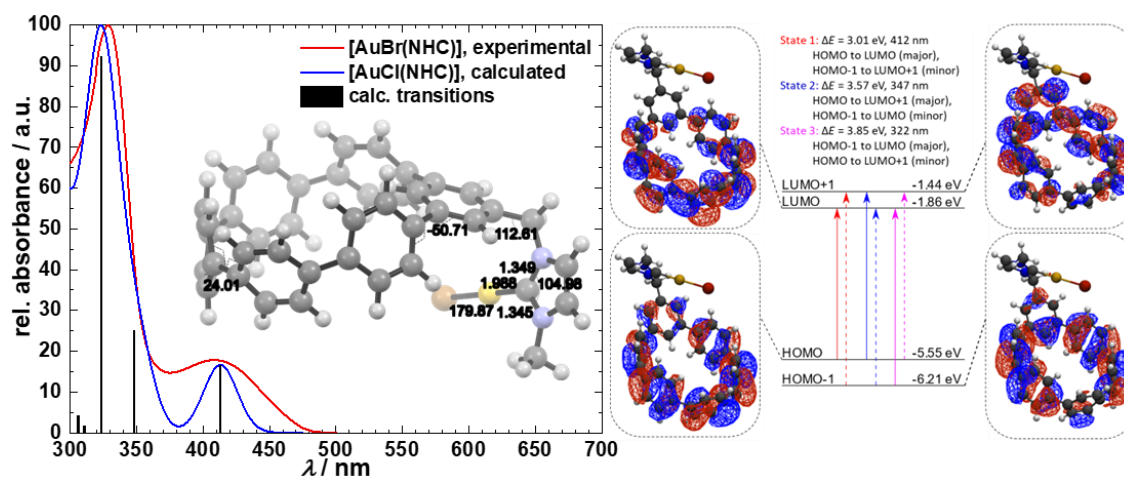


Figure 53. Comparison between the experimentally measured UV-vis-spectrum (red) and the theoretically calculated spectrum (blue) at the PBE0/ZORA-def2-TZVPP level of theory. Within these spectra, the ground state optimized geometry of the gold(I)-complex **250** is shown (left). Visualization of the three main transitions resulting in the observed UV-vis spectrum (right).

The emission spectra of both the imidazolium bromide **244** and the gold(I)-complex **250** show two emission maxima at 493 nm and 519 nm, respectively after irradiation with a wavelength of 326 nm. These maxima fit very well to the maxima of the CN-*m*[6]CPP **158**, which was measured under the same conditions. Fluorescence quantum yields of both substances have been determined to be 0.14 (**244**) and 0.22 (**250**) using CN-*m*[6]CPP **158** ($\Phi = 0.24$) and CN-*m*[10]CPP **160** ($\Phi = 0.71$) as reference substances. The emission spectra are presented together with the experimental absorption spectra in Figure 54.

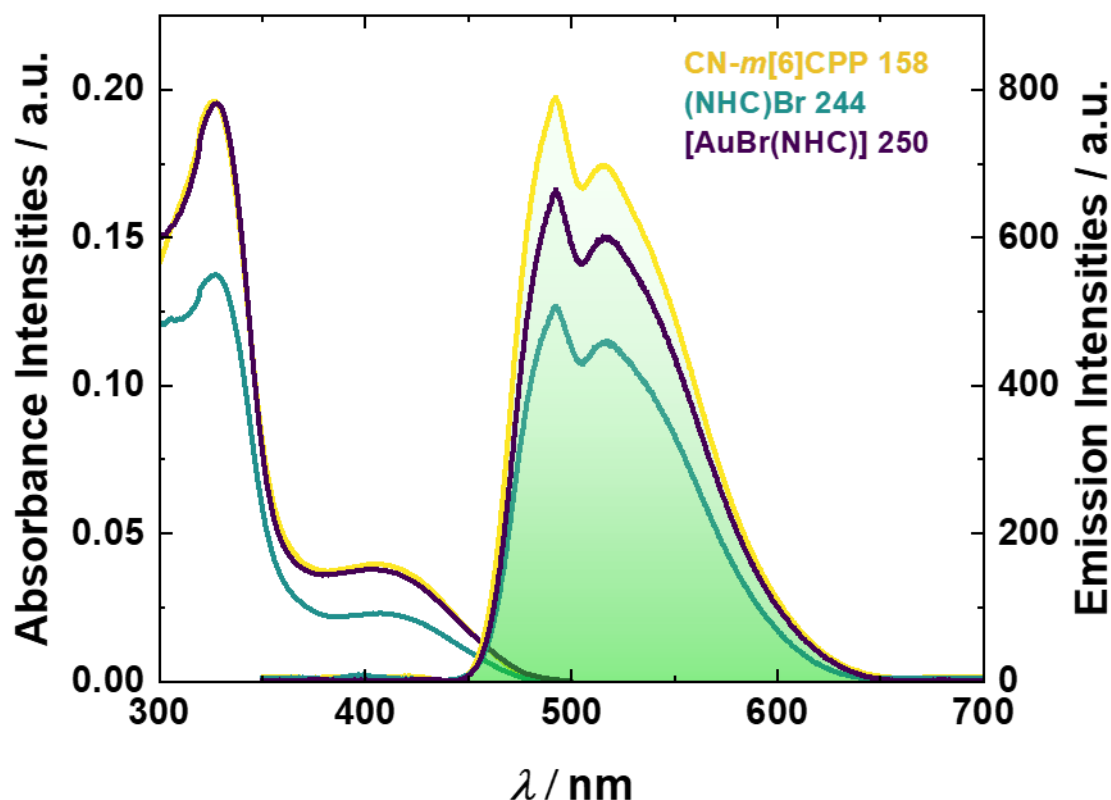


Figure 54. Absorption (left, colorless area underneath the curves) and emission (right, colored areas underneath the curves) spectra of CN-*m*[6]CPP **156**, imidazolium bromide **244** and gold(I)-complex **250**.

For organometallic compounds it is important to know which steric properties the desired ligands possess. With this parameter not only the reactivity but also the stability of a complex can be evaluated.^{283,284} In order to define the steric properties of [AuBr(NHC)] complex **250**, the percent buried volume values (% V_{bur})²⁸⁵ and topographic steric maps²⁸⁶ were calculated using the online-tool *SambVca 2.1*.^{287,288} It represents the occupied coordination sphere space around the metal by a ligand/ligand fragment, using the structure determined either by computational calculations or solid-state structure.^{284,289} The calculation utilized the conventional parameters ($r = 3.5 \text{ \AA}$, representing the radius of the sphere surrounding the metal center, and $d = 2.0 \text{ \AA}$, representing the bond length between C_{NHC} and metal). The bond radii were scaled by a factor of 1.17. The steric distribution surrounding the metal's first coordination sphere (located in the upper hemisphere) is depicted using iso-contour lines originating from a lower point.

Furthermore, the color scale aids in the identification of the less-to-more buried (occupied) zones (Figure 55).

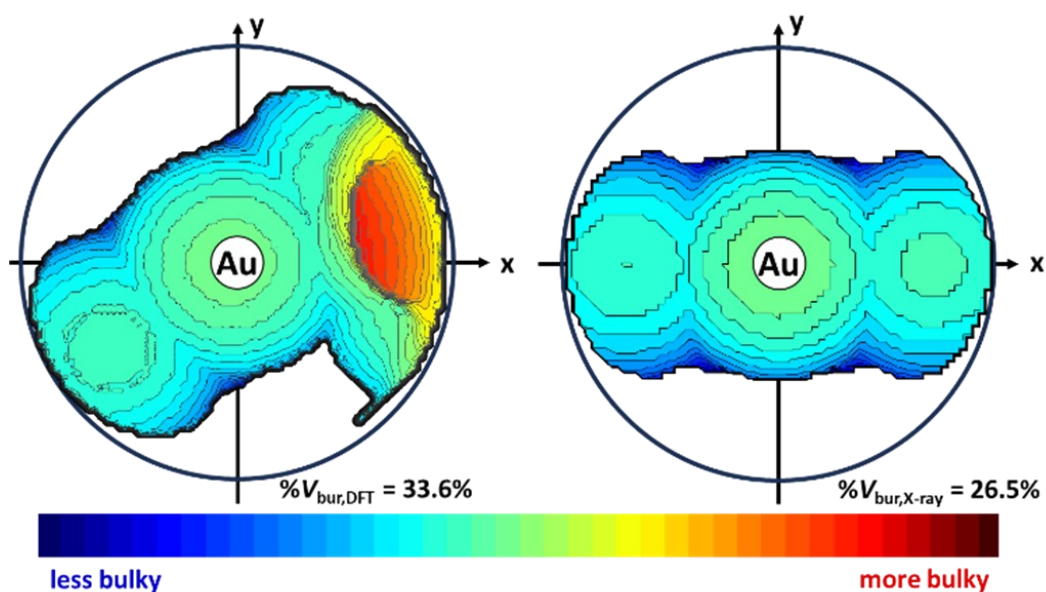


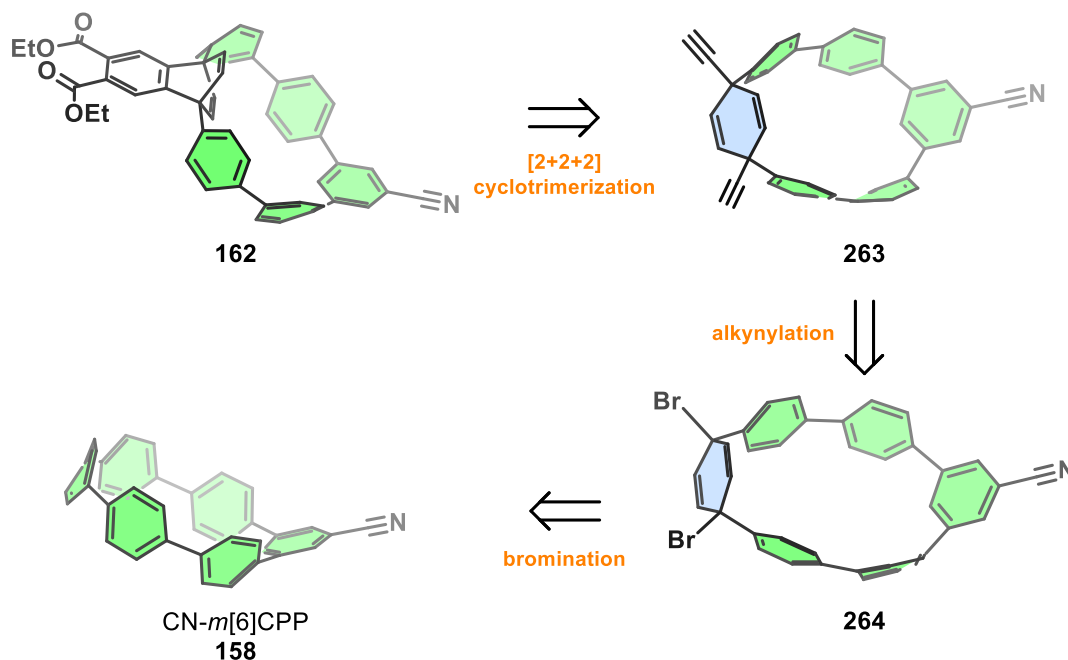
Figure 55. Steric maps gold(I)-complex **250** using the theoretically calculated structure at the PBE0/ZORA-def2-TZVPP level of theory (left) and the solid-state structure (right).

In solution (DFT-calculations) the $\%V_{bur}$ of complex **250** is determined to be 33.6% whereas the $\%V_{bur}$ in the solid-state is only 26.5%. Reason therefore is the orientation of the *m*[6]CPP segment, which points upwards in the solid-state structure and facing towards the gold when calculated in solution.

After the successful incorporation of the *m*[6]CPP scaffold as a fluorescent wingtip for a linear [AuX(NHC)] ligand, the next plan was to incorporate that scaffold into a bidentate ligand system. Moreover, this bidentate character should not be on the exterior of the *m*CPP scaffold but incorporated into the aromatic backbone. Therefore, the idea of a barrelene-incorporated *m*[6]CPP came up, which will be discussed within the next section.

3.3.3. Towards a Barrelene-incorporated *meta*[6]CPP

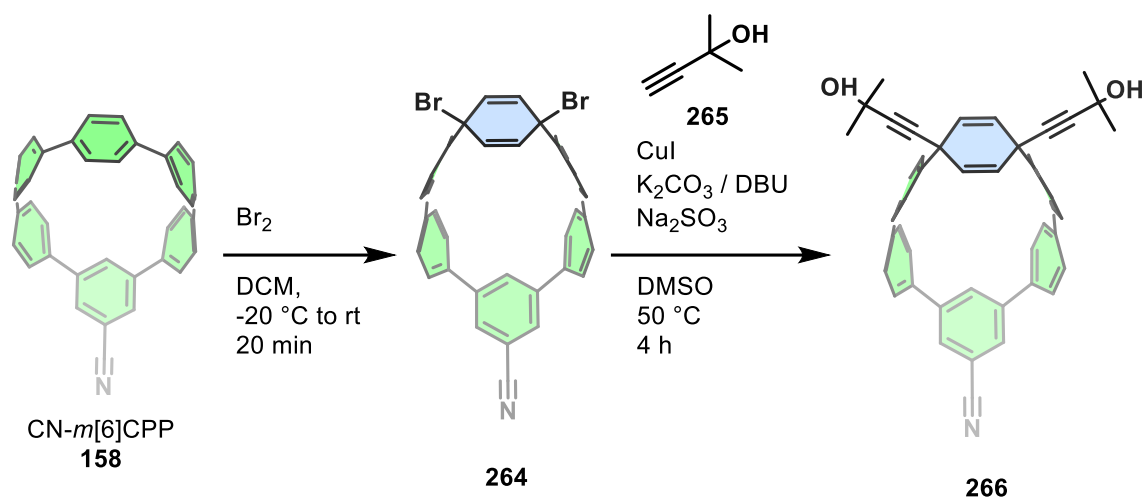
As introduced in **Chapter 1.7**, barrelenes possess intriguing characteristics which enables their application in direct laser writing or as bidentate ligand in organo-metallic compounds. The synthetic strategy towards a barrelene-incorporated CN-*m*[6]CPP **162** is presented in Scheme 69.



Scheme 69. Retrosynthetic strategy towards a barrelene-incorporated *m*[6]CPP **162** commencing from CN-*m*[6]CPP **158**.

Having the [2+2+2] cyclotrimerization protocol of TANAKA's group as key transformation in mind, two terminal alkynes incorporated into the backbone of the *m*[6]CPP backbone, were required (**263**). These alkynes could be rationalized through a Sonogashira-type cross-coupling reaction of a terminal alkyne and the allylic bromines of scaffold **264**.²⁹⁰ The motifs of an allylic bromine incorporated into the *m*[6]CPP backbone, can be introduced through strain induced bromination of the CN-*m*[6]CPP **158** with elemental bromine.²⁹¹

To begin with, CN-*m*[6]CPP **158** was selectively brominated, subsequently followed by the regioselective coupling of alkyne **265** onto the allylic bromine moieties (Scheme 70).



Scheme 70. Synthetic approach towards acetone-protected di-alkyne **266** commencing from CN-*m*[6]CPP **158**.

Unfortunately, purification of the reaction mixture through column chromatography failed due to decomposition of the material on silica. Moreover, due to time constraints, these results were not further verified and are to be handled as preliminary studies for future projects.

4. Perspective on Future Directions

Although the top-down functionalization of [10]CPP **155** did not lead to satisfactory results, it is important to note that the field of C-H activation on unactivated arenes constantly emerges.^{292–294} In order to achieve successful top-down functionalization, it is necessary to address the strain energy of the compound as well as the low-reactivity of the C-H bond need to be tackled. Once a methodology developed, the synthetic work will be greatly simplified regarding functionalized molecules. Thus, a new era of functionalized CPPs and their investigations in various research areas such as materials and life science will emerge.

When acidic conditions were applied to a mixed silyl- and methyl-ether protected macrocyclic precursor, it was observed that the cyclohexadiene motif, which is used in the synthesis of CPPs, is highly reactive. Unfortunately, this reaction resulted in the decomposition of the material, indicating that the 1,2-aryl shift is not suitable for the controlled synthesis of strained 1,3-connected macrocyclic compounds. Thus, a bottom-up approach was applied to introduce the 1,3-connectivity within a macrocyclic structure. Furthermore, the nitrile group was successfully incorporated as a functional handle. At the stage of macrocyclization, the only requirement for a functional group is its stability against the SUZUKI-MIYAUURA cross-coupling and reductive aromatization reaction conditions. Thus, introducing a functionality to the molecule this step is a very convenient way.

The presence of the nitrile functional group allowed the facile synthesis of a small compound library consisting of different substituted *m*[6]CPPs. It is worth noting that this library has the potential to be expanded to include further functional groups. The incorporation of additional one-step transformations²⁹⁵ as well as the utilization of the resulting new functional group in various applications can be envisioned. This work also demonstrated the possibility of further and more complex functionalization reactions starting from the nitrile functionality, as evidenced by the synthesis of the *m*[6]CPP-oxalamide **247** and the *m*[6]CPP-NHC gold(I)-complex **250**. Through the combination of organic and inorganic materials, novel hybrid materials are generated. These hybrid materials usually possess a combination of properties from both materials, thereby opening new pathways for application-related research. In particular, the NHC motif introduces the field of

metal-organic chemistry to (*meta*)[*n*]CPPs, enabling detailed investigations into the structure-property relationship and their application not only in synthetic (metal-)organic chemistry but also in materials and life sciences.

5. Experimental Part

5.1. General Information

Reagents and solvents: In case of no further descriptions, all chemicals were used as received from commercial manufacturers (Acros Organics, Sigma Aldrich, TCI, BLD Pharm, and others). All chemical reactions were done under inert gas atmosphere in dried vessels using Schlenk-technique if not stated otherwise. Technical grade solvents used during work-up and purification were distilled prior to use.

Flow setup: Reactions performed in a flow-setup utilized a Vapourtec *E-Series* system and Vapourtec SF-10 pumps. The reactions were performed in tubular reactors consisting of FEP-tubing (inner diameter 0.75 mm, purchased from Techlab) for all connections. For the heterogeneous catalyzed reactions, an adjustable bed reactor (15 cm x 6.6 mm) was used.

¹H-NMR spectroscopy: Proton-Nuclear Magnetic Resonance (¹H-NMR) spectra were measured on a Bruker Avance II 400 (400 MHz), Avance III 400 MHz HD (400 MHz), Avance 600 (600 MHz) or Avance Neo 700 (700 MHz). All measurements were performed at 295 K. Chemical shifts (δ) are reported in parts per million (ppm) relative to residual solvent signals or tetramethylsilane (TMS), while coupling constants (*J*) are reported in Hertz (Hz). Multiplicities are abbreviated as s (singlet), d (doublet), t (triplet), and m (multiplet).

¹³C-NMR spectroscopy: Carbon-Nuclear Magnetic Resonance (¹³C-NMR) spectra were measured on a Bruker Avance 400 (101 MHz), Avance III 400 MHz HD (101 MHz), Avance 600 (151 MHz) or Avance Neo 700 (176 MHz). All measurements were performed at 295 K. Chemical shifts (δ) are reported in parts per million (ppm) relative to residual solvent signals or tetramethylsilane (TMS).

High-resolution mass spectrometry: ESI-MS spectra were measured on a Bruker Daltonics Micro TOF LC. The samples were dissolved in methanol. A positive voltage of 4500 V was applied to the capillary and -500 V to the End Plate Offset. The nebulizer was set to 0.4 bar. The dry heater was set to 180 °C and the flow of nitrogen as the dry gas to 4.0 L/min.

APCI-MS spectra were measured on a Bruker Daltonics Micro TOF LC. The samples were dissolved in methanol. A positive voltage of 1500 V was applied to the capillary and -500 V to the End Plate Offset. The nebulizer was set to 2.5 bar. The dry heater was set to 200 °C and the flow of nitrogen as the dry gas to 3.0 L/min.

Infra-red spectroscopy: IR spectra were measured on a Bruker ALPHA IR-spectrometer. For the measurements the attenuated total reflection (ATR) methodology was applied. The intensities are abbreviated as w (weak), m (medium), and s (strong).

Column chromatography: For column chromatography, Silica gel 60 (0.04 – 0.063 mm) from Macherey-Nagel GmbH & Co. was used.

Melting points: Melting points were determined on a M5000 melting point meter from A. KRÜSS Optronic GmbH, Germany. A heating rate of 1 °C min⁻¹, a resolution of 0.1 °C were used, with a measurement accuracy of ±0.3 °C (25 – 200 °C), and ±0.5 °C (200 – 400 °C).

UV-vis spectroscopy: SPECORD® 200 PLUS UV-vis spectrophotometer equipped with two automatic eightfold cell changers and a Peltier thermostat system for temperature control manufactured by Analytic Jena was used. The spectrophotometer system is operated by the software ASpect UV from Analytic Jena.

Fluorescence spectroscopy: For fluorescence and excitation spectra a FP-8300 spectrofluorometer (Jasco), was used. For fluorescence spectra, the samples were irradiated with light with the excitation wavelength of the corresponding absorption maximum and a bandwidth of 2.5 nm. The scanning speed was set to 200 nm/min and the data interval to 0.2 nm. For excitation spectra, the samples were irradiated with light with the excitation wavelength of the two corresponding emission maxima. The other parameters were set the same as for the fluorescence spectra. All samples were measured in QS High Precision Cells made of Quartz Suprasi® (Hellma Analytics) with a light path of 10 mm.

The association constant K_a of fullerene C₆₀ and cyano-*meta*[10]cycloparaphenylene **160** was determined using fluorescence quenching

experiments. Therefore, the fluorescence was measured between wavelengths of 400 nm and 700 nm with a scan speed of 200 nm/min and a data interval of 0.2 nm. The response time was set to 0.5 s. The titrations with **160** were irradiated at a wavelength of 328 nm.

The association constant was determined by threefold titrations, where for each titration a solution of **160** in toluene was prepared at a 10^{-6} M concentration. These solutions were used as solvent for a solution of fullerene at a concentration of 10^{-4} M. Starting with 1500 μ L of the solution containing **160**, the fullerene solution was added in 30 steps of 15 μ L. After each addition, the resulting solution was mixed, and a fluorescence spectrum was recorded.

For data evaluation, the fluorescence intensity (in a.u.) at the two emission maxima was used. The data were plotted with non-linear regression utilizing the online tool *Bindfit* by P. Thordarson in combination with the Nelder-Mead method. As error of the mean values the standard deviation was used.

Crystallographic data: Suitable single crystals for X-ray structure determination were selected and transferred in protective perfluoropolyether oil on a microscope slide. The selected and mounted crystals were transferred to the cold gas stream on the diffractometer. The diffraction data were obtained at 100 K on a Bruker D8 three circle diffractometer, equipped with a PHOTON 100 CMOS detector and a 1μ S microfocus sources with Quazar mirror optics (Mo-K α radiation, $\lambda = 0.71073$ Å).

The data obtained were integrated with SAINT and a semi-empirical absorption correction from equivalents with SADABS-2016/2 was applied.²⁹⁶ The structures were solved by direct methods using SHELXT-2018/2.²⁹⁷ Structure refinement was done using SHELXL-2018/3.²⁹⁸ All non-hydrogen atoms were refined anisotropically and C-H hydrogen atoms were positioned at geometrically calculated positions and refined using a riding model. The isotropic displacement parameters of all hydrogen atoms were fixed to 1.2x or 1.5x (CH₃ hydrogens) the U_{eq} value of the atoms they are linked to.

Computational methods: All density functional theory (DFT) computations were carried out using the ORCA software package.^{281,282} The preliminary geometry was obtained from an extended tight binding (XTB) optimization,²⁹⁹ followed by a conformer screening using the conformer rotamer ensemble sampling tool

(CREST).^{300,301} The lowest lying conformer was optimized by the means of DFT using the zeroth-order regular approximation (ZORA) at a PBE0/ZORA-def2-TZVP/D3BJ/CPCM(CHCl₃) level of theory.^{277–280,302–304} For the gold atom, a separate gaussian type orbital (GTO) was defined using the SARC-ZORA-TZVP basis set.²⁷⁶ On all atoms, the SARC/J auxiliary basis set was used for the RIJCOSX approximation.^{305,306}

Due to a tricky potential energy surface, the Hesse matrix was recalculated at every 5th step of the geometry optimization to reach a geometry with no imaginary vibrational modes, which was verified in a separate frequency calculation on the same level of theory. The electronic transitions were computed using time-dependent DFT (TD-DFT) within the Tamm-Dancoff approximation (TDA)³⁰⁷ at a PBE0/ZORA-def2-TZVPP/D3BJ/CPCM(CHCl₃) level of theory with a separate GTO for the gold atom (SARC-ZORA-TZVPP).^{276–280,302–304} On all atoms, the SARC/J auxiliary basis set was used for the RIJCOSX approximation.^{305,306}

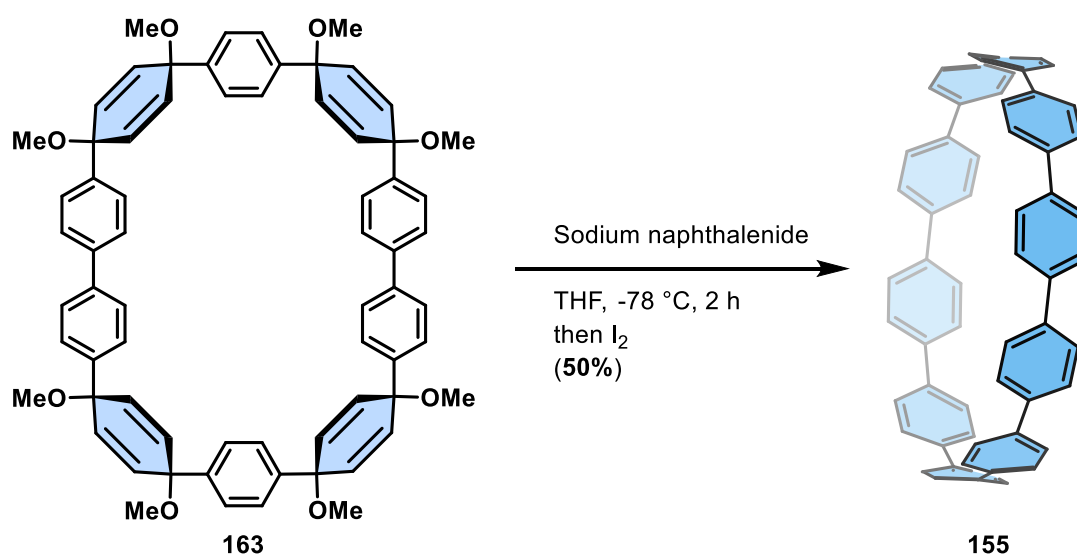
Topographic steric map: The steric demand of the NHC ligand was analysed by using the web application SAMBVCA2.^{287,288,308} As a result, the buried volume²⁸⁵ and the steric map²⁸⁶ were obtained.

5.2. Synthetic procedures

5.2.1. Syntheses of literature-known building blocks and [10]cycloparaphenylene

The synthesis approach of this work started with the synthesis of ketone **168**, following the bottom-up synthesis of [10]cycloparaphenylene by the group of JASTI.⁵³ However, modulation of the strategy allowed the synthesis of building block **165** in a faster and cleaner fashion.⁷⁴ Targeting the larger building blocks, required the synthesis of building block **227** as a key step.⁵⁶ Following the synthesis procedures of DU³⁰⁹ and ESSER,³¹⁰ addressed building block **228**. Building block **229** could be synthesized *via* SUZUKI-cross-coupling reaction using **27** and **227** as coupling partners.⁵⁶

5.2.1.1. [10]Cycloparaphenylene **155**



To a solution of naphthalene (1.92 g, 15.0 mmol, 1.00 equiv.) in THF (30 mL) was carefully added sodium metal (517 mg, 22.5 mmol, 1.50 equiv.) in small portions. The reaction mixture was stirred overnight at rt. The solution was filtered through a glass filter and the concentration was determined through titration with menthol to be 0.384 M.

(note: the THF used for this reaction needs to be stabilizer-free, as it catches the radicals of the solution and thus, aromatization reaction will not work.)

The macrocyclic precursor **163** (400 mg, 396 μmol , 1.00 equiv.) was dissolved in THF (50 mL) and cooled down to $-78\text{ }^{\circ}\text{C}$. At this point, freshly prepared sodium naphthalenide (12.5 mL, 0.384 M in THF, 12.0 equiv.) was added and the reaction mixture was stirred for 2 h at $-78\text{ }^{\circ}\text{C}$. Afterwards, the reaction was quenched by the addition of I_2 (4.00 mL, 1 M in THF, 10.1 equiv.). The reaction mixture was allowed to warm up to rt, and before the careful addition of saturated aqueous $\text{Na}_2\text{S}_2\text{O}_3$ solution until the excess I_2 was removed. H_2O (30 mL) was then added and the aqueous phase was extracted with DCM (3x150 mL). The combined organic phase was washed with brine (50 mL) and dried over Na_2SO_4 . After filtration, all volatiles were removed under reduced pressure to obtain the crude product. This was further purified through flash silica gel column chromatography (hexanes / DCM = 1:0 – 1:1) to obtain the product **155** as yellow solid (152 mg, 200 μmol , 50%).

$^1\text{H-NMR}$ (400 MHz, 296 K, CDCl_3): δ = 7.56 (s, 40H) ppm.

$^{13}\text{C-NMR}$ (400 MHz, 297 K, CDCl_3): δ = 138.32 (20C_q); 127.51 (40C_{CH}) ppm.

Analytical data correspond to the literature.⁵³

5.2.2. General procedure for the (LEWIS-)acid screening towards the investigation of the 1,2-aryl shift (GP 1)

Diene (100 mg, 217 μmol , 1.00 equiv.) was dissolved in diethyl ether (2 mL). To this solution was added the corresponding (LEWIS-)acid (1.20 equiv.). After 1 h stirring, the resulting reaction mixture was quenched with water (1 mL), extracted with diethyl ether (2x3 mL). The combined organic phase was dried over Na_2SO_4 , and the volatiles were removed under reduced pressure.

5.2.3. General procedure for the macrocyclization reactions (GP 2)

Dibromide (1.00 equiv.) and diboronate (1.00 equiv.) were added to a round-bottomed three-neck-flask connected to the Schlenk-line. The flask was evacuated for 5 min and purged 3x with nitrogen. After adding the solvent mixture (MePh / *i*PrOH = 10:1, 3.6 mM), the mixture was flushed with nitrogen for 2 h at $40\text{ }^{\circ}\text{C}$ (oil bath). Aqueous $\text{K}_3\text{PO}_4\cdot\text{H}_2\text{O}$ (2.0 M, 4.0 equiv.) was purged with nitrogen in a

separate flask for 2 h at rt. After 2 h, Pd₂(dba)₃ (10 mol%), S-Phos (20 mol%), and the base were added to the flask in this order. The reaction mixture was allowed to stir at 80 °C (oil bath) overnight.

After cooling to rt, the reaction mixture was then filtered through a plug of Celite[®]. The round bottom flask was rinsed 3x with DCM and filtered through the Celite[®] plug. The filtrate was added to a separatory funnel along with water and the product was extracted 3x with DCM. The organic layers were washed with brine, dried over sodium sulfate and concentrated to yield the crude product.

The crude product was further purified by flash silica gel chromatography.

5.2.3.1. General procedure for the homogeneous-catalyzed macrocyclization using continuous flow-chemistry (GP 2.1)

Two solutions were prepared and each filled into a reservoir. In reservoir A, the dibromide **225** was dissolved in THF (20 mL). In reservoir B, the diboronic ester **223** was dissolved in THF and an aqueous solution of the base was added. Both solutions were continuously stirred and purged with a stream of nitrogen for 1 h. Then the catalytic system was added to reservoir A. Both solutions were pumped from the reservoirs using peristaltic pumps (E-Series, Vapourtec) through loops and check valves before entering the mixer. Following the mixer (inner diameter = 1.0 mm), the tubular reactor ($V = 10$ mL, heated to different temperatures) and a cooling loop were placed in combination with a back-pressure regulator (BPR, 2.76 bar). The reactor output was collected for 50 min. The reactor output was filtrated over a plug of Celite[®], and H₂O (10 mL) was added. The aqueous phase was extracted with DCM (3x20 mL). The combined organic phase was washed with brine (20 mL) and dried over MgSO₄. After filtration, the volatiles were removed under reduced pressure. The crude product was analyzed by means of ¹H-NMR spectroscopy.

5.2.3.1. General procedure for the heterogeneous-catalyzed macrocyclization using continuous flow-chemistry (GP 2.2)

Two solutions were prepared and each filled into a reservoir. In reservoir A, dibromide **225** and diboronic ester **223** were dissolved in THF (20 mL). In reservoir B, the base was dissolved in a mixture of EtOH / H₂O (v / v = 4:1; 20 mL). Both solutions were continuously stirred and purged with a stream of nitrogen for 1 h. The solid-supported catalytic system was placed into the packed-bed reactor until reactor was filled to a height of 10 cm. Both solutions were pumped from the reservoirs using peristaltic pumps (E-Series, Vapourtec) through loops and check valves before entering the mixer. Following the mixer (inner diameter = 1.0 mm), the packed-bed reactor (V = 10 mL, heated to different temperatures) and a cooling loop were placed in combination with a back-pressure regulator (BPR, 2.76 bar). The reactor output was collected for 50 min. The reactor output was filtrated over a plug of Celite[®], and H₂O (10 mL) was added. The aqueous phase was extracted with DCM (3x20 mL). The combined organic phase was washed with brine (20 mL) and dried over MgSO₄. After filtration, the volatiles were removed under reduced pressure. The crude product was analyzed by means of ¹H-NMR spectroscopy.

5.2.4. General procedure for the aromatization reactions using tin chloric acid (GP 3)

Stock solution of H₂SnCl₄: Into a Schlenk tube SnCl₂·2H₂O (0.040 M, 2.0 equiv./OMe) was added together with THF, followed by dropwise addition of concentrated HCl (4.0 equiv./OMe). This solution was allowed to stir at rt for 30 min. (*note: if the tin chloride is too old, then the solution becomes cloudy during the addition of HCl, and the reaction does not work properly*)

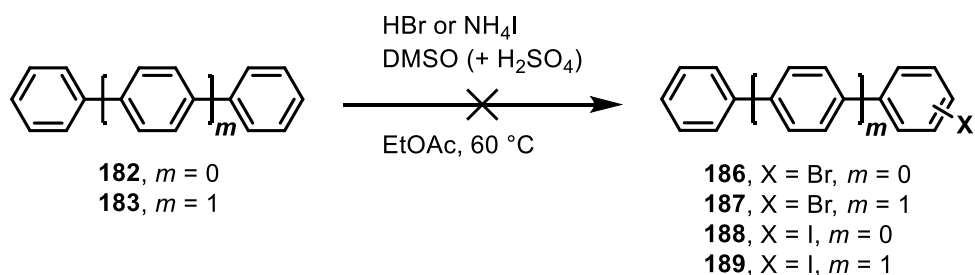
Aromatization: The freshly prepared H₂SnCl₄ solution was added to the macrocyclic precursors at rt. After stirring overnight, the reaction was quenched with aqueous saturated NaHCO₃ solution, and the product was extracted 3x with DCM. The combined organic layers were washed with water and brine, dried over magnesium sulfate, and concentrated to dryness resulting in the crude product.

Purification of the addressed compound was achieved by flash column chromatography on silica gel if not stated otherwise.

5.2.5. Synthetic procedures towards C-H activation of unactivated arenes

Within this section, the general procedures towards different strategies of C-H activation are given.

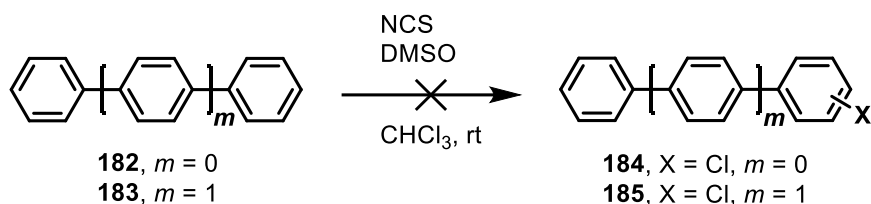
5.2.5.1. DMSO-catalyzed halogenation using hydrogen halides



According to a literature procedure,²⁵⁰ to a solution of arenes **182** or **183** (0.50 mmol, 1.0 equiv.) and DMSO (0.55 mmol, 1.1 equiv.) in EtOAc (2.0 mL) was added hydrobromic acid (48%, 0.55 mmol, 1.1 equiv.) at 60 °C under air. The mixture was stirred at this temperature over night. After cooling to rt, the volatiles were removed under reduced pressure, and the crude product was analyzed by ¹H-NMR spectroscopy.

For iodination, NH₄I (0.55 mmol, 1.1 equiv.) and catalytic amounts of conc. H₂SO₄ were used, following the same procedure.

5.2.5.2. DMSO-catalyzed chlorination using *N*-chlorosuccinimide

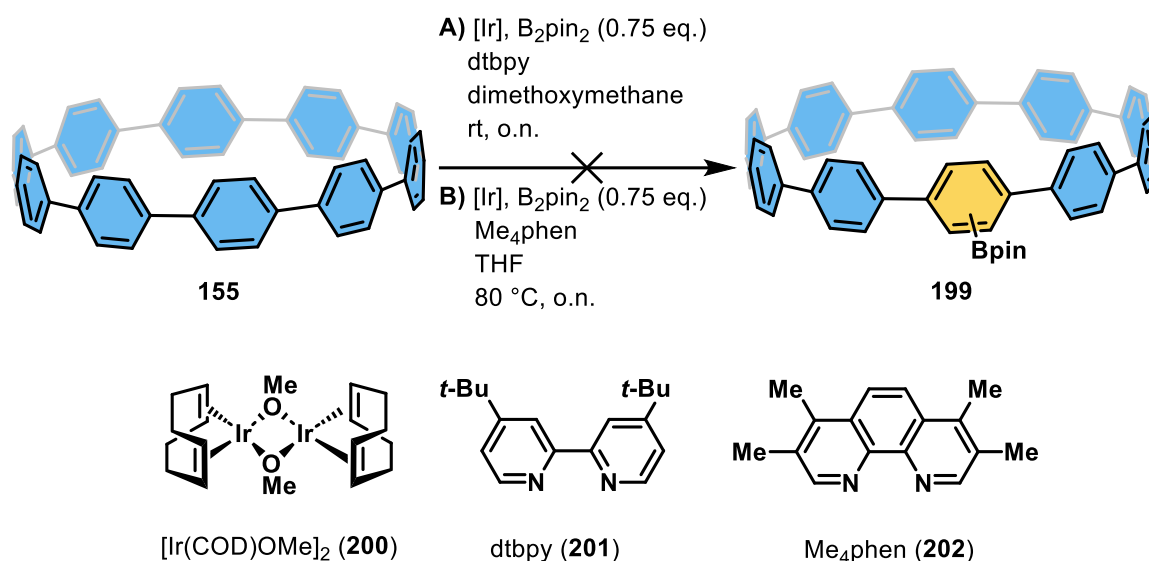


According to a literature procedure,²⁵¹ to a solution of arenes **182** or **183** (0.50 mmol, 1.0 equiv.) and NCS (0.60 mmol, 1.2 equiv.) in chloroform (2.0 mL) was added DMSO (0.10 mmol, 0.20 equiv.). The reaction mixture was allowed to stir overnight at rt. The next day, the volatiles were removed under reduced pressure, and the crude product was analyzed by ¹H-NMR spectroscopy.

5.2.5.3. Calcium-catalyzed arene C-H Bond activation by low-valent Al(I)

According to a literature procedure,²⁵² the low-valent β -diketiminato complex (^{DIPP}BDI)Al (BDI = CH[C(CH₃)N]) needed to be synthesized.³¹¹ Unfortunately, following the literature procedures did not lead to the desired products. Thus, this functionalization reaction was not executed.

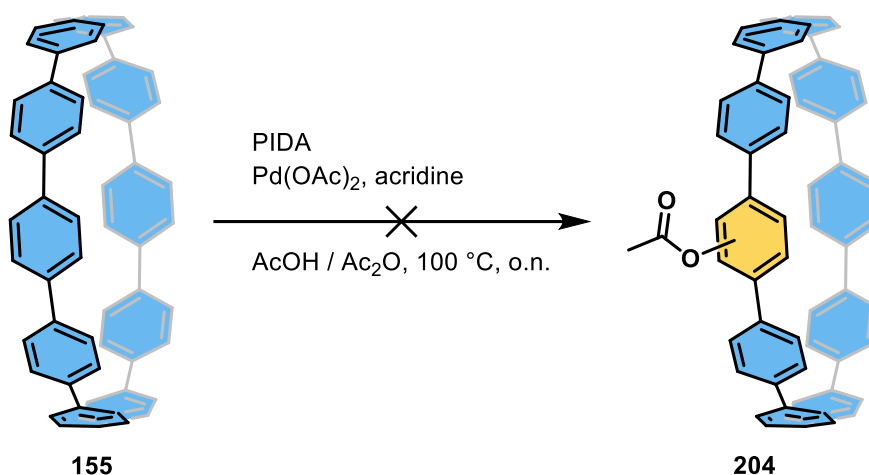
5.2.5.4. Iridium-catalyzed borylation



According to literature procedures,^{253,254} solutions of $[\text{IrOMe}(\text{COD})]_2$ (32 μL , 0.010 M in THF, 4.8 mol%) and 3,4,7,8-tetramethyl-1,10-phenanthroline (32 μL , 0.020 M in THF, 9.7 mol%) were added to a solution of [10]CPP **155** (5.00 mg, 6.57 μmol , 1.00 equiv.) and bis(pinacolato)diboron (16 μL , 0.30 M in THF, 0.73 equiv.) in THF (1.0 mL). The reaction was stirred at 80 °C overnight. After cooling to rt, the reaction was exposed to air, followed by filtration over a plug of Celite[®] with DCM as the eluent. After removing all volatiles, the crude product was analyzed by means of ¹H-NMR spectroscopy.

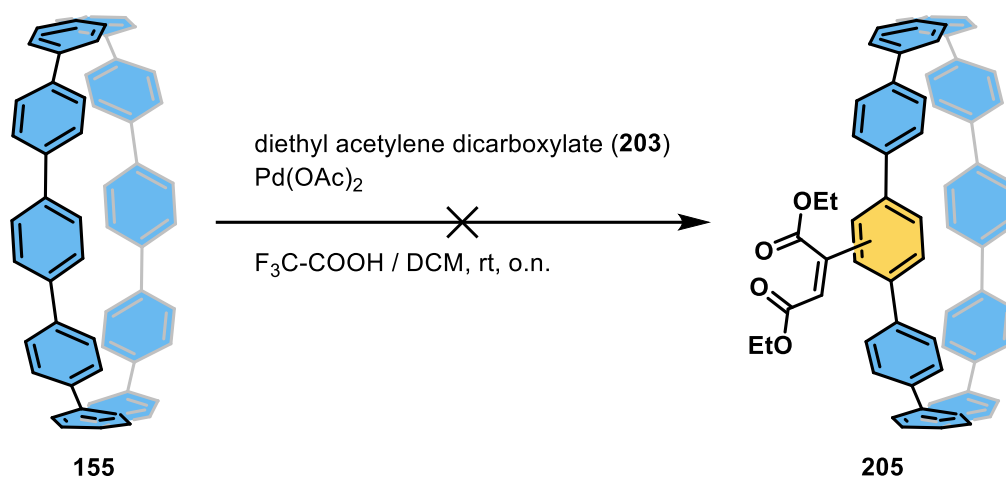
4,4''-Bis(di-*tert*-butyl)-2,2''-bipyridine (32 μL , 0.020 M in THF, 9.7 mol%) was used in the same manner as a ligand.

5.2.5.5. Pd-catalyzed C-H acetoxylation



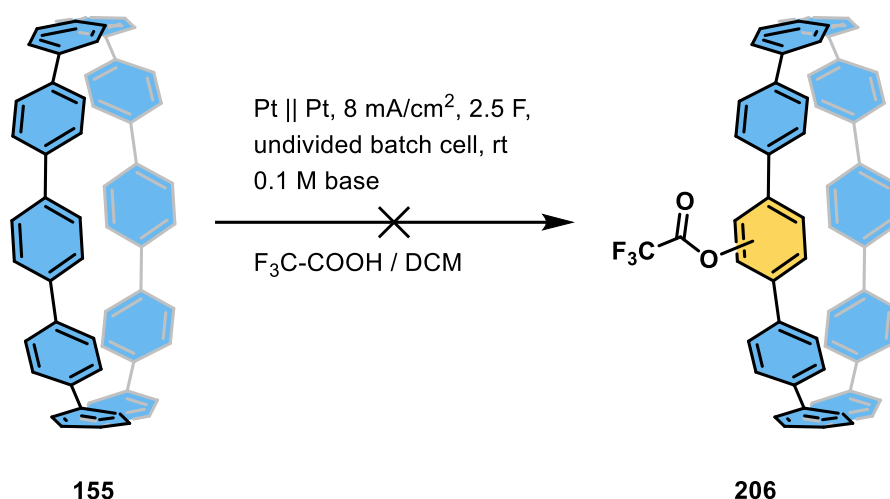
According to a literature procedure,²⁵⁵ to a solution of [10]CPP **155** (10.0 mg, 12.9 μmol , 1.00 equiv.) in acetic acid Pd(OAc)₂ (0.10 mg, 0.44 μmol , 3.3 mol%) and (diacetoxyiodo)benzene (4.30 mg, 12.9 μmol , 1.00 equiv.) were added. After the addition of catalytic amounts of Ac₂O and acridine (0.14 mg, 0.78 μmol , 6.0 mol%), the reaction mixture was stirred at rt for 10 min. Afterwards, the reaction vessel was placed into a preheated oil bath at 100 °C and the reaction mixture was stirred overnight. After cooling to rt, the reaction mixture was filtered over a plug of Celite[®] and the filtrate was diluted with Et₂O (5 mL). After shaking for 2 min, the organic phase was washed with saturated aqueous solution of K₂CO₃ (3x2 mL). After separation, the organic layer was dried over MgSO₄, filtered and the volatiles were removed under reduced pressure. The crude product was analyzed by ¹H-NMR spectroscopy.

5.2.5.6. Pd-catalyzed C-H olefination



According to a literature procedure,²⁵⁶ arene (1.0 equiv.) and diethyl acetylenedicarboxylate (1.0 equiv.) were dissolved in DCM (2 mL). To this solution, catalytic amounts of TFA were added at 0 °C. Afterwards, the reaction was allowed to warm up to rt, and further stirred overnight. After a short silica plug, the reaction mixture was washed with saturated aqueous NaHCO₃ solution (3x5 mL), brine (15 mL), and dried over MgSO₄. After filtration, all volatiles were removed under reduced pressure. The crude product was analyzed by ¹H-NMR spectroscopy.

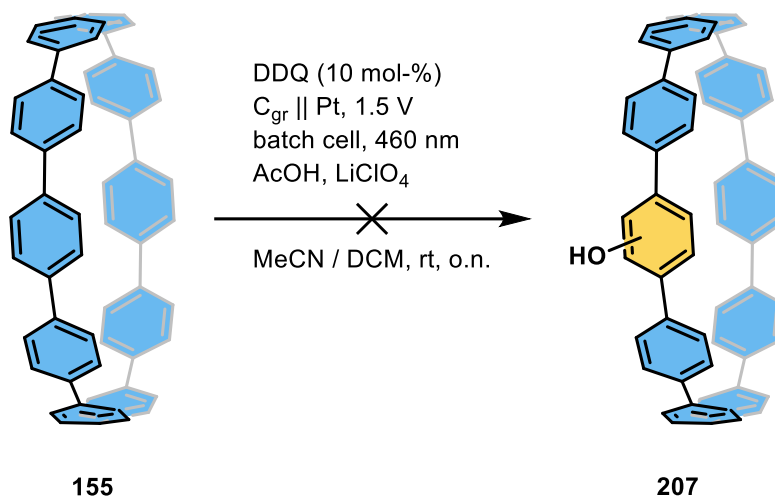
5.2.5.7. Electrochemical C-H trifluoro acetoxylation



According to a literature procedure,²⁵⁷ [10]CPP **155** (11.4 mg, 15.0 μmol, 1.00 equiv.), TFA (4.26 μL, 30.0 mmol, 2.00 equiv.) and 2,6-lutidine (357 μL, 3.00 mmol, 200 equiv.) were dissolved in DCM (8.0 mL). This solution was placed

into an undivided glass cell (C_{gr} – 1.5 cm in solution, 1 cm thickness | Pt – 1.5 cm in solution, 1 cm thickness) at a current of 87 mA and an electricity of 3.0 F/mol. During the reaction a total charge of 4 A·s is transferred. After the reaction is over, saturated aqueous NaHCO_3 solution was added, and the aqueous phase was extracted with DCM (3x5 mL). To remove the base, the combined organic phase was washed with 2 N HCl (3x10 mL). After removing the volatiles under reduced pressure, flash silica gel column chromatography (DCM / Cy = 1:1) was used for purification.

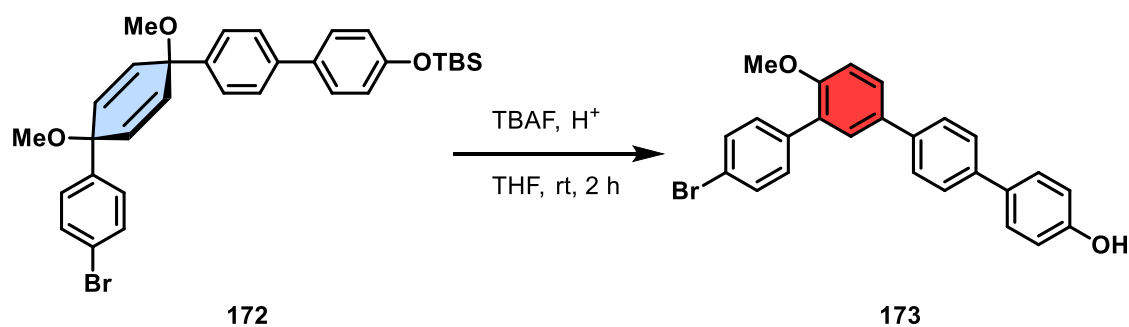
5.2.5.8. Electrochemical C-H hydroxylation



According to a literature procedure,²⁵⁸ an Electra-Syn vial equipped with stirring bar, a graphite anode and a platinum cathode was filled with DDQ (0.93 mg, 4.0 μmol , 0.10 equiv.), [10]CPP **155** (30.4 mg, 40.0 μmol , 1.00 equiv.), and LiClO_4 (25.8 mg, 240 μmol , 6.00 equiv.) in a mixture of MeCN / DCM (v : v = 1:9). The cell was sealed using parafilm and then flushed with N_2 gas of a N_2 balloon. Following this, H_2O (36 μL , 2.0 mmol, 50 equiv.) and AcOH (22.9 μL , 400 μmol , 10.0 equiv.) were added through a syringe. The reaction mixture was then purged with N_2 three more times. The solution was then stirred at rt with irradiation from a blue LED lamp (460 nm) and under a controlled potential of 1.5 V for 48 h. The reaction mixture was cooled using a ventilation fan during this time. After the corresponding time, the reaction mixture was poured into H_2O (10 mL). The carbon felt anode was rinsed with EtOAc (3x5 mL) in an ultrasonic bath. The aqueous layer was separated and extracted with EtOAc (3x10 mL), and the combined organic layers

were washed with brine and dried over Na₂SO₄. After removing all volatiles under reduced pressure, the crude product was further subjected to flash silica gel column chromatography (Cy / DCM = 1:1).

5.2.6. 1,2-Aryl shift of building block **172** towards 4-bromo-4'-methoxy-[1,1':3',1'':4'',1''':4''']-quarter-phenyl]-4''-ol (**173**)



To a stirred solution of the enhanced building block **172** (17.0 g, 29.4 mmol, 1.00 equiv.) in THF (400 mL) was added TBAF (35 mL, 1.0 M in THF, 1.19 equiv.). The reaction was allowed to stir at room temperature overnight. H₂O (100 mL) was then added, and the reaction mixture was extracted with diethyl ether (3x150 mL). The combined organic phase was washed with H₂O (3x100 mL) and dried over Na₂SO₄. After concentrating under reduced pressure, the crude yellow solid was recrystallized from cyclohexane to afford a colorless solid.

The ¹H-NMR did not fit to the literature and revealed that a 1,2-aryl shift had occurred quantitatively towards **173**.

¹H-NMR (400 MHz, 299 K, CDCl₃): δ = 7.61 – 7.55 (m, 5H); 7.54 – 7.51 (m, 3H); 7.50 – 7.47 (m, 2H); 7.45 – 7.42 (m, 2H); 7.05 – 7.03 (m, 1H); 6.90 – 6.86 (m, 2H); 4.76 (s, 1H); 3.87 (s, 3H) ppm.

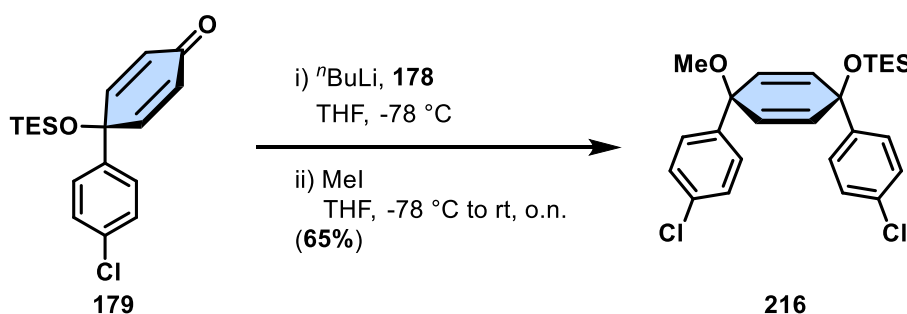
¹H-NMR (400 MHz, 299 K, CS₂+DCM-*d*₂): δ = 6.98 – 6.92 (m, 5H); 6.91 – 6.89 (m, 3H); 6.87 – 6.85 (m, 2H); 6.83 – 6.81 (m, 2H); 6.42 – 6.40 (m, 1H); 6.26 – 6.24 (m, 2H); 4.28 (s, 1H); 3.23 (s, 3H) ppm.

¹³C-NMR (400 MHz, 299 K, CS₂+CDCl₃): δ = 155.83 (1C_q); 155.17 (1C_q); 139.26 (1C_q); 138.75 (1C_q); 137.27 (1C_q); 133.61 (1C_q); 133.42 (1C_q); 131.25 (2C_{CH});

131.15 (2C_{CH}); 129.84 (1C_q); 129.23 (1C_{CH}); 128.23 (2C_{CH}); 127.33 (1C_{CH}); 127.06 (2C_{CH}); 127.04 (2C_{CH}); 121.44 (1C_q); 115.72 (2C_{CH}); 111.66 (1C_{CH}); 55.56 (1C_{CH₃}) ppm.

¹³C-NMR (400 MHz, 299 K, CS₂+DCM-*d*₂): δ = 135.60 (1C_q); 134.88 (1C_q); 118.83 (1C_q); 118.41 (1C_q); 117.06 (1C_q); 113.15 (1C_q); 113.01 (1C_q); 111.12 (2C_{CH}); 110.94 (2C_{CH}); 109.41 (1C_q); 108.95 (1C_{CH}); 108.01 (2C_{CH}); 107.15 (1C_{CH}); 106.83 (4C_{CH}); 101.09 (1C_q); 95.57 (2C_{CH}); 91.51 (1C_{CH}); 35.39 (1C_{CH₃}) ppm.

5.2.7. 4,4''-Dichloro-4'-methoxy-[1,1':4',1''-terphenyl]-1'(4'*H*)-yl)oxy)triethylsilane (216)

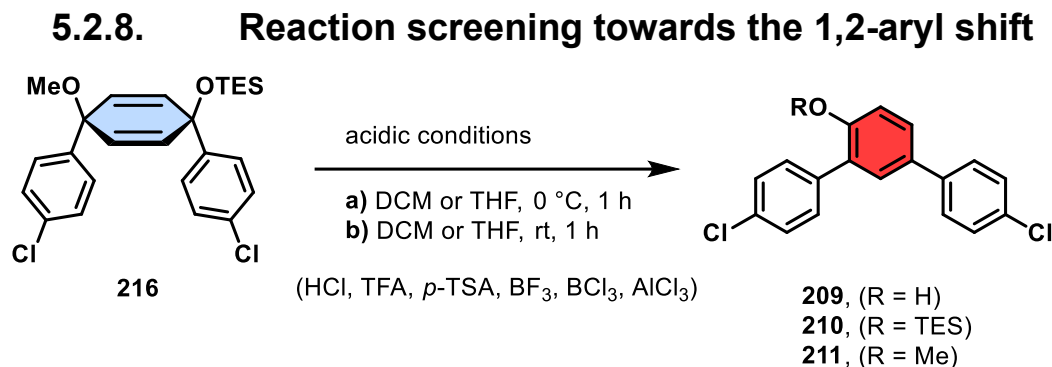


1-bromo-4-chlorobenzene (**178**, 1.74 g, 9.00 mmol, 1.00 eq.) was dissolved in THF (100 mL) and the solution was cooled to -78 °C. To this *n*-BuLi (4.4 mL, 2.5 M in hexanes, 1.2 equiv.) was added dropwise over a time of 5 min to give a clear solution, which was stirred for 30 min at this temperature.

4'-chloro-1-((triethylsilyl)oxy)-[1,1'-biphenyl]-4(1*H*)-one (**179**, 3.10 g, 9.26 mmol, 1.03 equiv.) dissolved in THF (0.5 M) was added at -78 °C. This was allowed to stir at -78 °C for 1 h. The color turned bright red during the addition. The reaction was quenched by the addition of neat MeI (1.20 mL, 19.1 mmol, 2.12 equiv.) and changed to bright yellow. The cold bath was allowed to expire, and the reaction was allowed to stir overnight.

EtOAc (30 mL) was added, and the organic phase was washed with brine (150 mL), dried over MgSO₄, and the volatiles were removed under reduced pressure. The crude product was obtained as a yellow oil which was further purified by flash silica gel column chromatography (Cy / DCM = 9:1). The product was obtained as a colorless liquid (2.66 g, 5.77 mmol, 64%).

¹H-NMR (200 MHz, 296 K, CDCl₃) δ = 7.28 (s, 4H.); 7.23 (s, 4H); 6.14 (m, 2H); 5.92 (m, 2H); 3.35 (s, 3H); 0.96 (q, 9H); 0.66 (t, 6H) ppm.



Concentrated HCl (16.0 μ L, 520 μ mol, 1.20 equiv.), trifluoroacetic acid (20.0 μ L, 257 μ mol, 1.18 equiv.), *p*-toluenesulfonic acid monohydrate (98.8 mg, 520 μ mol, 1.20 equiv.), boron trichloride solution (0.500 mL, 1.00 M in DCM, 1.15 equiv.), boron trifluoride diethyl etherate (32 μ L, 0.26 mmol, 1.2 equiv.) and aluminium chloride (69.3 mg, 520 μ mol, 1.20 equiv.) have been used for triggering the 1,2-aryl shift. Compounds have not been isolated. The ratio of the different products was determined within the result and discussion (Figure 42).

4,4''-dichloro-[1,1':3',1''-terphenyl]-4'-ol (209)

¹H-NMR (400 MHz, 297 K, DCM-*d*₂): δ = 7.54 – 7.51 (m, 2H); 7.50 – 7.48 (m, 4H); 7.47 – 7.46 (m, 2H); 7.42 – 7.38 (m, 2H); 7.04 – 7.01 (m, 1H); 5.21 (s, 1H) ppm.

Due to bad solubility, no ¹³C-NMR spectrum was recorded.

((4,4''-dichloro-[1,1':3',1''-terphenyl]-4'-yl)oxy)triethylsilane (210)

¹H-NMR (400 MHz, 297 K, DCM-*d*₂): δ = 7.56 – 7.51 (m, 5H); 7.46 – 7.43 (m, 1H); 7.42 – 7.38 (m, 4H); 7.00 – 6.98 (m, 1H); 0.87 (t, *J* = 7.78 Hz, 9H); 0.60 (t, *J* = 7.78 Hz, 6H) ppm.

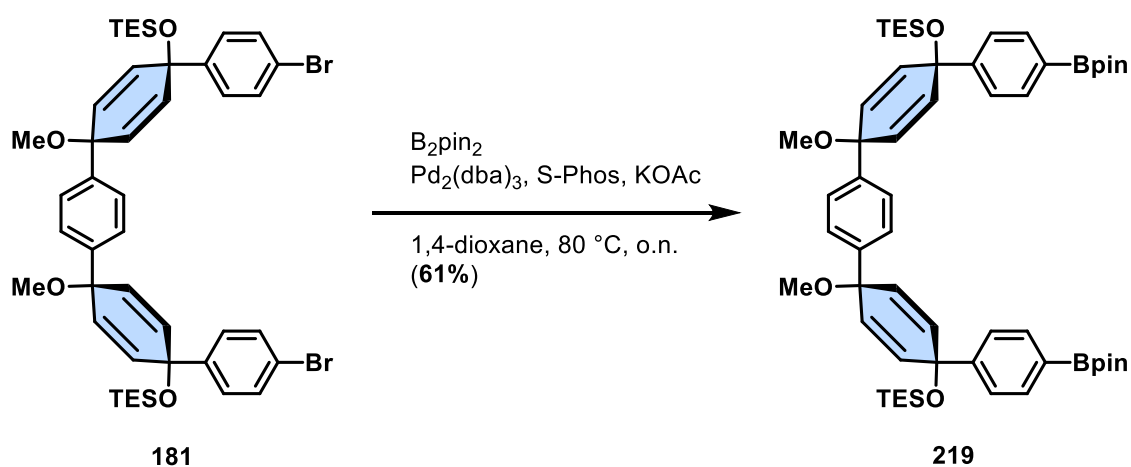
¹³C-NMR (101 MHz, 297 K, DCM-*d*₂): δ = 152.98 (1C); 139.50 (1C); 137.74 (1C); 133.64 (1C); 133.15 (1C); 132.51 (1C); 131.40 (2C); 129.45 (1C); 129.22 (1C); 128.41 (2C); 128.37 (2C); 127.55 (2C); 120.82 (1C); 6.69 (3C); 56.07 (3C) ppm.

*one carbon is missing due to bad signal to noise ratio

4,4''-dichloro-4'-methoxy-1,1':3',1''-terphenyl (211)

¹H-NMR (400 MHz, 297 K, DCM-*d*₂): δ = 7.57 – 7.50 (m, 6H); 7.42 – 7.38 (m, 4H); 7.09 – 7.07 (m, 1H); 3.85 (s, 3H) ppm.

¹³C-NMR (101 MHz, 297 K, DCM-*d*₂): δ = 156.67 (1C); 139.41 (1C); 137.29 (1C); 133.29 (1C); 133.12 (1C); 132.86 (1C); 131.36 (2C); 130.14 (1C); 129.49 (1C); 129.24 (2C); 128.51 (2C); 128.35 (2C); 127.73 (1C); 112.12 (1C); 56.07 (1C) ppm.

5.2.9. Borylation of mixed-protected building block 219

Dibromide **181** (2.00 g, 2.31 mmol, 1.00 equiv.), bis(pinacolato)diboron (1.50 g, 5.91 mmol, 2.56 equiv.), $\text{Pd}_2(\text{dba})_3$ (155 mg, 169 μmol , 7.3 mol%), X-Phos (225 mg, 462 μmol , 0.200 equiv.) and KOAc (1.15 g, 11.7 mmol, 5.07 equiv.) were placed in a flame dried Schlenk tube and dissolved in 1,4-dioxane (50 mL). The reaction mixture was heated to 80 °C overnight. After cooling down to rt, the reaction mixture was stirred with active carbon for 15 min. After filtration over Celite[®], the volatiles were evaporated. After titrating with *n*-pentane and sonification, a grey solid was obtained, which was further washed with cold *n*-pentane until the solution became colorless. The product **219** was obtained as colorless solid (1.35 g, 1.41 mmol, 61%).

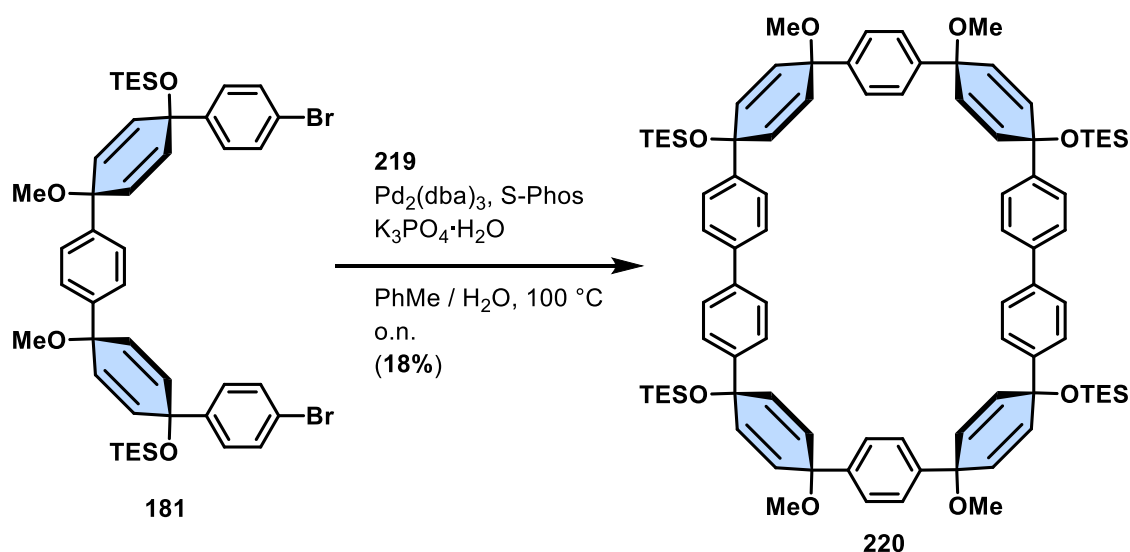
¹H-NMR (400 MHz, 298 K, CDCl_3): δ = 7.72 – 7.69 (m, 4H); 7.37 – 7.34 (m, 4H), 7.32 (s, 4H); 6.17 – 6.13 (m, 4H); 5.95 – 5.91 (m, 4H); 3.36 (s, 3H); 1.33 (s, 24H); 0.95 (t, J = 7.81 Hz, 18H); 0.65 (q, J = 7.81 Hz, 12H) ppm.

$^{13}\text{C-NMR}$ (101 MHz, 298 K, CDCl_3): δ = 149.11 (2C); 142.85 (2C); 135.42 (4C); 134.87 (4C); 129.26 (4C); 126.41 (4C); 125.16 (4C); 83.85 (4C); 74.58 (2C), 72.06 (2C); 52.13 (2C); 25.01 (8C); 7.20 (6C); 6.70 (6C) ppm.

*two carbons are missing most likely due to signal overlap.

HRMS (ESI) m/z for $\text{C}_{56}\text{H}_{80}\text{B}_2\text{O}_8\text{Si}_2$ $[\text{M}+\text{Na}]^+$ calculated 981.546; found 981.544.

5.2.10. Mixed-protected macrocycle 220



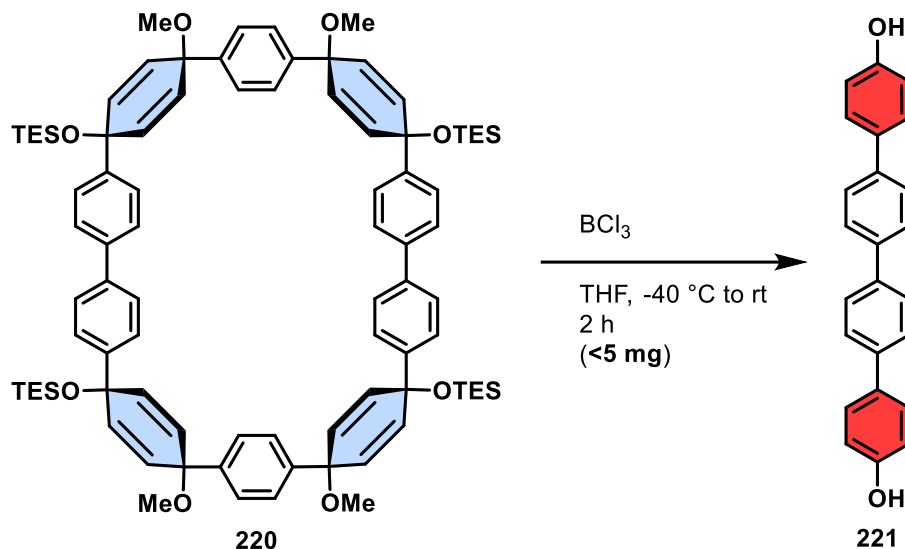
Following **GP 2**, dibromide **181** (435 mg, 503 μmol , 1.00 equiv.), diboronate **219** (484 mg, 505 μmol , 1.00 equiv.), $\text{K}_3\text{PO}_4 \cdot \text{H}_2\text{O}$ (470 mg, 1.94 mmol, 3.86 equiv.), S-Phos (40.3 mg, 96.2 μmol , 0.191 equiv.), and $\text{Pd}_2(\text{dba})_3$ (45.2 mg, 47.9 μmol , 9.5 mol%) have been used in a solvent mixture of PhMe / H_2O (10:1, 132 mL) and DMF (2.0 mL). The crude product was purified through flash silica gel column chromatography (1st: Cy / DCM / EtOAc = 1:1:0 – 0:1:1; 2nd: DCM / EtOAc = 5:1:1 – 4:1:1) to afford a colorless solid (36.0 mg, 25.2 μmol , 18%)

$^1\text{H-NMR}$ (400 MHz, 297 K, DCM-d_2): δ = 7.42 – 7.39 (m, 8H); 7.35 – 7.32 (m, 8H); 7.26 (s, 8H); 6.17 – 6.13 (m, 8H); 5.91 – 5.87 (m, 8H); 3.38 (s, 12H); 0.97 (t, J = 7.87 Hz, 36H); 0.67 (q, J = 7.87 Hz, 24H) ppm.

$^{13}\text{C-NMR}$ (101 MHz, 297 K, DCM-d_2): δ = 145.41 (4C); 143.26 (4C); 139.72 (4C); 135.71 (4C); 129.78 (4C); 126.97 (8C); 126.55 (8C); 126.49 (8C); 75.03 (8C); 72.20 (8C); 52.36 (4C); 7.23 (12C); 6.86 (12C) ppm.

* ^1H - ^{13}C -HMBC spectrum and ^1H - ^1H -COSY-NMR spectra give proof of one compound although corresponding mass could not be detected using ESI- and APCI-MS.

5.2.11. 1,2-Aryl shift on mixed-protected macrocycle **220**



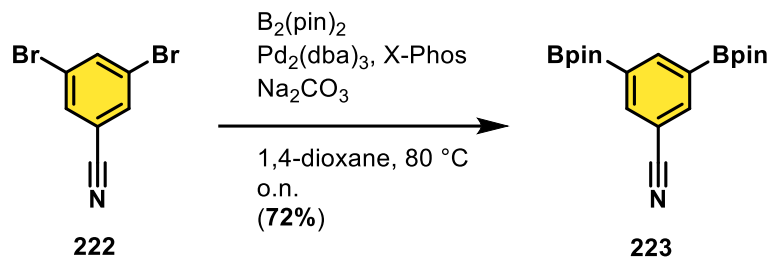
Macrocycle **220** (35.3 mg, 25.0 μmol , 1.00 equiv.) was dissolved in DCM (2.0 mL) and was cooled to $-40\text{ }^\circ\text{C}$. After 10 min stirring at $-40\text{ }^\circ\text{C}$, BCl_3 solution (0.25 mL, 1.0 M in DCM, 10 equiv.) was added dropwise. After 1 h the reaction mixture was allowed to warm up to rt and was stirred for one additional hour at this temperature. After the addition of H_2O (2.0 mL), the reaction mixture was extracted with DCM (3x2 mL), washed with brine (10 mL), dried over MgSO_4 , and concentrated under reduced pressure. After using preparative HPLC for purification, one fraction could be analyzed and revealed the decomposition of the material.

[1,1':4',1'':4'',1''':4''']-Quarterphenyl]-4,4''-diol (**221**)

$^1\text{H-NMR}$ (600 MHz, 298 K, DCM-d_2): δ = 7.55 – 7.53 (m, 4H); 7.47 – 7.45 (m, 4H); 7.44 – 7.42 (m, 4H); 6.92 – 6.89 (m, 4H) ppm.

$^{13}\text{C-NMR}$ (151 MHz, 298 K, DCM-d_2): δ = 156.02 (2C_q); 140.08 (2C_q); 132.86 (2C_q); 132.15 (4C_{CH}); 128.64 (4C_{CH}); 128.54 (4C_{CH}); 121.05 (2C_q); 116.11 (4C_{CH}) ppm.

5.2.1. 3,5-Bis(4,4,5,5-tetramethyl-1,3,2-dioxaborolan-2-yl)benzonitrile (**223**)



Into a flask potassium acetate (4.42 g, 45.1 mmol, 6.00 equiv.) was placed and flame dried three times. Then 3,5-dibromobenzonitrile (**222**, 2.00 g, 7.67 mmol, 1.00 equiv.), bis(pinacolato)diboron (4.87 g, 18.8 mmol, 2.45 equiv.), $Pd_2(\text{dba})_3$ (284 mg, 0.301 mmol, 3.92 mol%), and X-Phos (365 mg, 0.750 mmol, 9.78 mol%) were added and dissolved in anhydrous 1,4-dioxane (50 mL). The reaction was heated to 80 °C overnight.

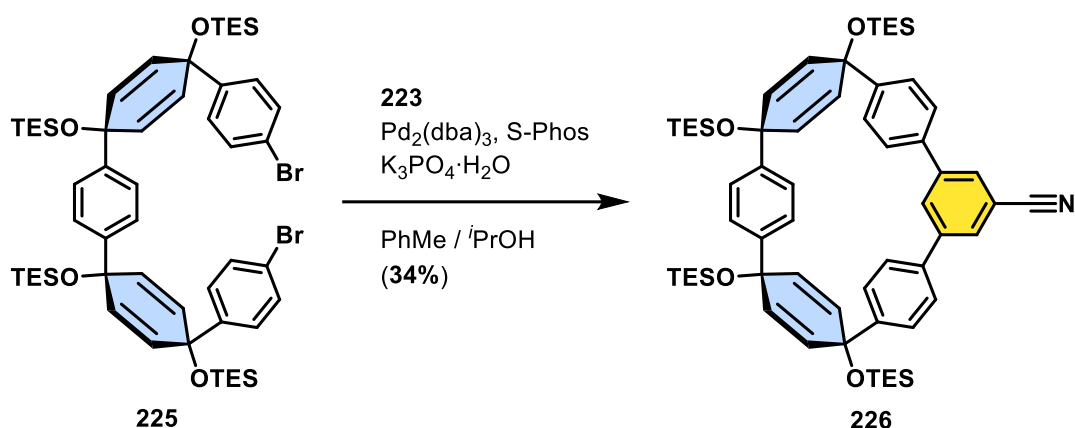
After cooling down to rt, the reaction mixture was stirred with active carbon for 15 min. Afterwards, it was filtered over Celite[®], which was rinsed with additional DCM until the filtrate came out colorless. The volatiles were evaporated under reduced pressure, resulting in a red, highly viscous liquid. After triturating with *n*-pentane and ultra-sonication for 15 min, a grey solid could be filtrated. This solid was carefully washed with cold *n*-pentane until the filtrate became colorless. The desired product **223** could be obtained as a colorless solid (1.95 g, 5.5 mmol, 72%).

Mp. = 69.7 °C.

¹H-NMR (400 MHz, 297 K, DCM-*d*₂): δ = 8.34 (t, J = 1.28 Hz 1 H), 8.11 (d, J = 1.28 Hz, 2 H), 1.34 (s, 24 H) ppm.

Analytical data correspond to the literature.³¹²

5.2.2. Macrocyclic precursor 226



Following **GP 2**, pre-bent building block **225** (1.05 g, 986 μmol , 1.00 equiv.), diboronate ester **223** (423 mg, 1.19 mmol, 1.21 equiv.), $\text{K}_3\text{PO}_4 \cdot \text{H}_2\text{O}$ (971 mg, 4.01 mmol, 4.06 equiv.), $\text{Pd}_2(\text{dba})_3$ (94.0 mg, 99.6 μmol , 10.1 mol%), S-Phos (88.0 mg, 210 μmol , 21.3 mol%) were stirred in a mixture of PhMe / *i*PrOH (77 mL) at 80 °C overnight. After flash silica purification (1st: Cy / DCM / EtOAc + 1% NEt_3 = 8:1:1 – 1:1:2; 2nd: Hex / DCM / EtOAc + 1% NEt_3 = 10:1:1) a colorless solid was obtained (338 mg, 336 μmol , 34%).

$^1\text{H-NMR}$ (400 MHz, 298 K, DCM-d_2): δ = 7.87 (d, J = 1.85 Hz, 2H); 7.54 – 7.51 (m, 4H); 7.33 – 7.30 (m, 5H)*; 6.95 (s, 4H); 6.49 (t, J = 1.85 Hz, 1H); 6.19 – 6.15 (m, 4H); 5.79 – 5.76 (m, 4H); 1.00 – 0.93 (m, 36H)^(a); 0.70 (q, J = 7.78 Hz, 12H); 0.61 (q, J = 7.78 Hz, 12H) ppm.

*should have an integral of 4 – chloroform residues are underneath.

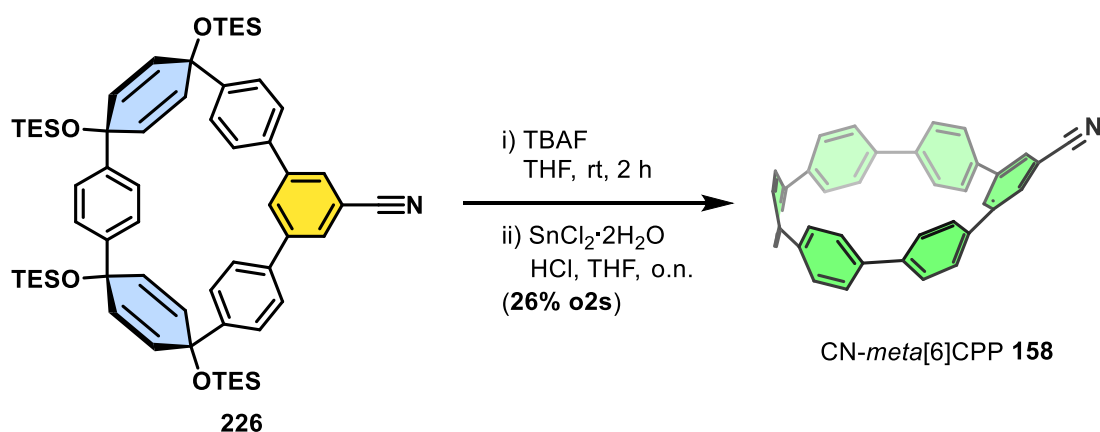
^(a)two overlapping triplets which protons usually couple with the protons of the quartets.

$^{13}\text{C-NMR}$ (101 MHz, 299 K, DCM-d_2): δ = 146.40 (2 C_q); 146.22 (1 C_{CH}); 145.35 (2 C_q); 143.64 (2 C_q); 141.35 (2 C_q); 132.04 (4 C_{CH}); 131.84 (4 C_{CH}); 129.17 (4 C_{CH}); 126.74 (4 C_{CH}); 126.71 (2 C_{CH}); 125.64 (4 C_{CH}); 119.50 (1 C_{CN}), 113.13 (1 C_q); 71.57 (2 C_q); 70.97 (2 C_q); 7.30 (6 C_{CH_2}); 7.20 (6 C_{CH_2}); 6.94 (6 C_{CH_3}); 6.79 (6 C_{CH_3}) ppm

*signal at 77.96 corresponds to chloroform residues.

HRMS (ESI) m/z for $\text{C}_{61}\text{H}_{83}\text{NO}_4\text{Si}_4$ [$M+\text{Na}$]⁺ calculated 1028.5291; found 1028.5288.

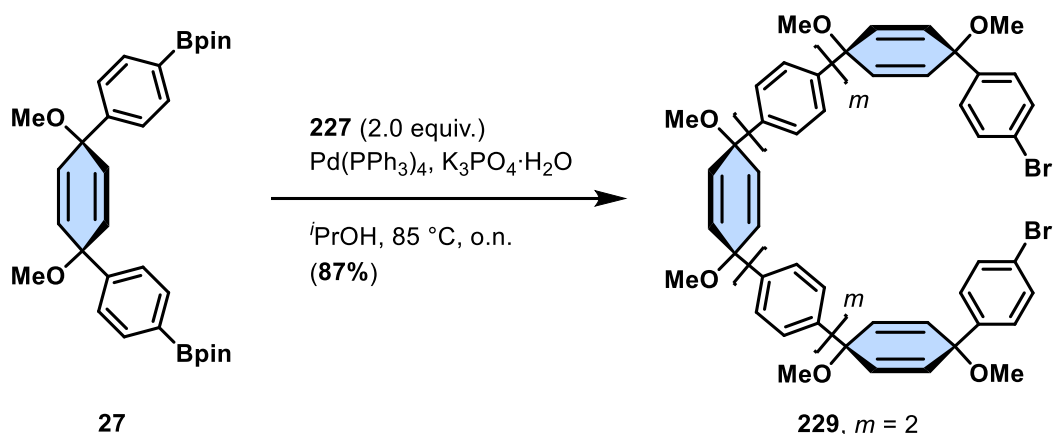
5.2.3. Cyano-*meta*[6]cycloparaphenylene **158**



To a solution of the silyl-ether protected macrocyclic precursor **226** (40.0 mg, 39.7 μmol , 1.00 equiv.) in THF (0.5 mL), was added TBAF (0.32 mL, 1.00 M in THF, 8.05 equiv.). The reaction mixture was stirred for 2 h at rt and subsequently quenched by the addition of H₂O (3.0 mL). After removing the THF under reduced pressure, the colorless precipitate was washed on a Celite[®] plug with H₂O (3x2 mL), DCM (3x5 mL) and eluted with acetone. After removing all volatiles under reduced pressure, the deprotected macrocyclic precursor was obtained as colorless solid, which was used as received for the aromatization reaction.

Following **GP 3**, freshly prepared H₂SnCl₄ solution (4.96 mL, 198 μmol , 5.00 equiv.) was added to the flask. After purification using aluminum oxide flash column chromatography (Cy / DCM = 5:1 – 1:1 + 2% EtOAc), the product **158** was obtained as bright yellow solid (5.00 mg, 10.4 μmol , 26.2% o2s).

*This procedure was later modified. Therefore, the structure characterization is given to a later stage of the synthetic procedures.

5.2.4. Building block **227**

Mixing diboronate **27** (600 mg, 1.10 mmol, 1.00 equiv.), building block **227** (1.09 g, 2.19 mmol, 1.99 equiv.), and Pd(PPh₃)₄ (127 mg, 0.110 mmol, 9.99 mol%) in a 250 mL round-bottomed three-neck flask, the solids were degassed by pouring vacuum three times and purging with nitrogen in between. Inside a separate 100 mL round-bottom three-neck flask, aqueous sodium bicarbonate (1M, 12 mL) and 2-propanol (45 mL) were flushed with nitrogen for 1 h. After transferring the liquid phase into the reaction flask, the reaction mixture was heated to 85 °C and vigorously stirred overnight.

After cooling to rt, the reaction was extracted with DCM (3×100 mL), washed with water (3×100 mL) and brine (100 mL). Drying over magnesium sulfate and concentrating under reduced pressure resulted in a yellow/brown foam. The crude product was further purified by flash silica column chromatography (1st: Cy/EtOAc/DCM = 3:1:1, 2nd: Cy/EtOAc/DCM = 5:1:1 + 1 % TEA) resulting **229** as a colorless solid (1.65 g, 1.60 mmol, 87%).

Mp. = 129 – 130 °C.

¹H-NMR (600 MHz, 298 K, CDCl₃): δ = 7.54 – 7.53 (m, 8H); 7.49 – 7.48 (m, 4H); 7.44 – 7.42 (m, 8H); 7.29 – 7.28 (m, 4H); 6.17 – 6.15 (m, 8H); 6.08 – 6.06 (m, 4H); 3.47 (s, 6H); 3.44 (s, 6H); 3.43 (s, 6H) ppm.

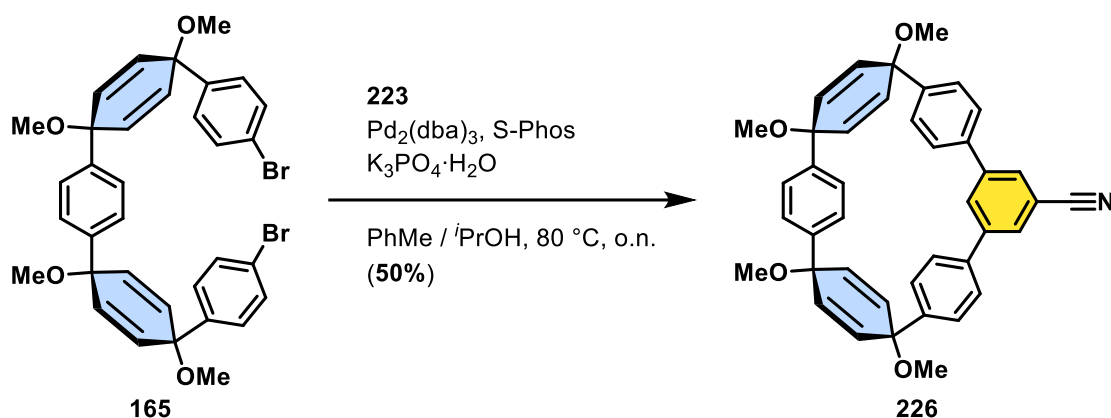
¹³C-NMR (151 MHz, 298 K, CDCl₃): δ = 142.72 (2C); 142.69 (2C); 142.40 (2C); 140.26 (2C); 140.06 (2C); 133.86 (4C); 133.54 (4C); 133.14 (4C); 131.60 (4C); 127.98 (4C); 127.29 (4C); 127.25 (4C); 126.60 (4C); 126.52 (4C); 121.75 (2C); 74.86 (2C); 74.75 (2C); 74.69 (2C); 52.19 (3C); 52.17 (3C) ppm.

HRMS (ESI) m/z for $C_{60}H_{54}Br_2O_6$ $[M+Na]^+$ calculated 1051.2179; found 1051.2177.

5.2.5. Macrocyclization reactions towards nitrile-substituted *meta*[*n*]cycloparaphenylenes

Following the general procedure **GP 2** for the macrocyclization reaction, three different macrocycles were synthesized.

5.2.5.1. Macrocylic precursor **226**



Dibromide **165** (1.99 g, 3.00 mmol, 1.00 equiv.) and diboronate **223** (1.17 g, 3.30 mmol, 1.10 equiv.), $Pd_2(dba)_3$ (283 mg, 300 μ mol, 10.0 mol%), S-Phos (251 mg, 600 μ mol, 20 mol%), and $K_3PO_4 \cdot H_2O$ (2.91 g, 12.0 mmol, 4.00 equiv.) were used. After purification through recrystallization from cyclohexane, the product **226** was obtained as bright yellow solid (914 mg, 1.51 mmol, 50%).

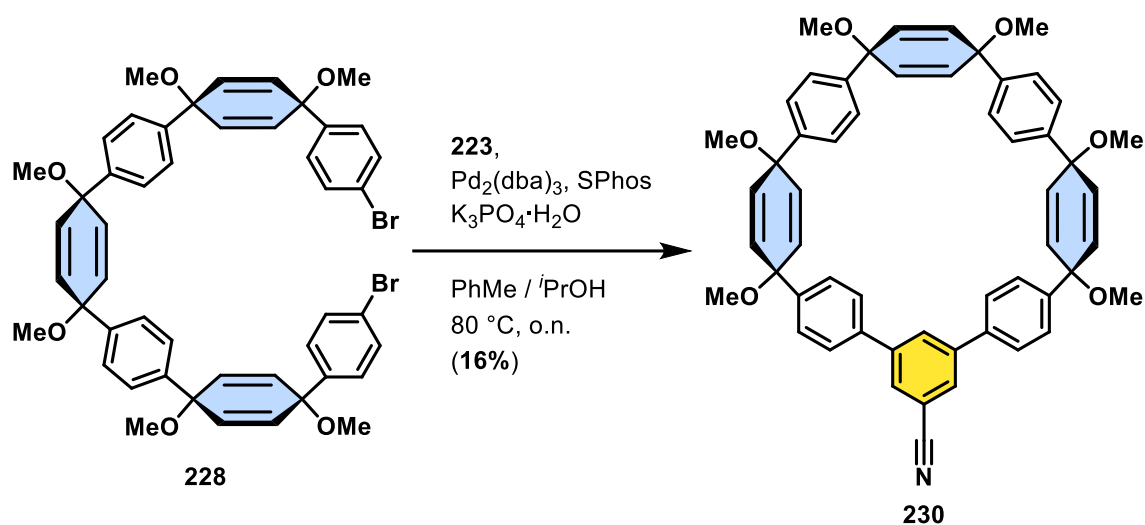
Mp. = >295 °C (slow decomposition).

1H -NMR (400 MHz, 298 K $DCM-d_2$): δ = 7.86 (d, J = 1.86 Hz, 2H); 7.52 – 7.49 (m, 4H); 7.33 – 7.31 (m, 4H); 7.00 (s, 4H); 6.48 (t, J = 1.86 Hz, 1H); 6.31 – 6.29 (m, 4H); 5.85 – 5.82 (m, 4H); 3.45 (s, 6H); 3.35 (s, 6H) ppm.

^{13}C -NMR (101 MHz, 298 K, $DCM-d_2$): δ = 146.29 (1C); 143.91 (2C); 143.53 (2C); 143.32 (2C); 141.52 (2C); 134.03 (4C); 133.82 (4C); 129.24 (4C); 126.88 (4C); 126.74 (2C); 126.05 (4C); 119.44 (1C); 113.11 (1C); 74.79 (2C); 74.67 (2C); 52.84 (2C); 51.58 (2C) ppm.

HRMS (ESI) m/z for $C_{41}H_{35}NO_4$ $[M+Na]^+$ calculated 628.2358; found 628.2351.

5.2.5.2. Macrocyclic precursor 230



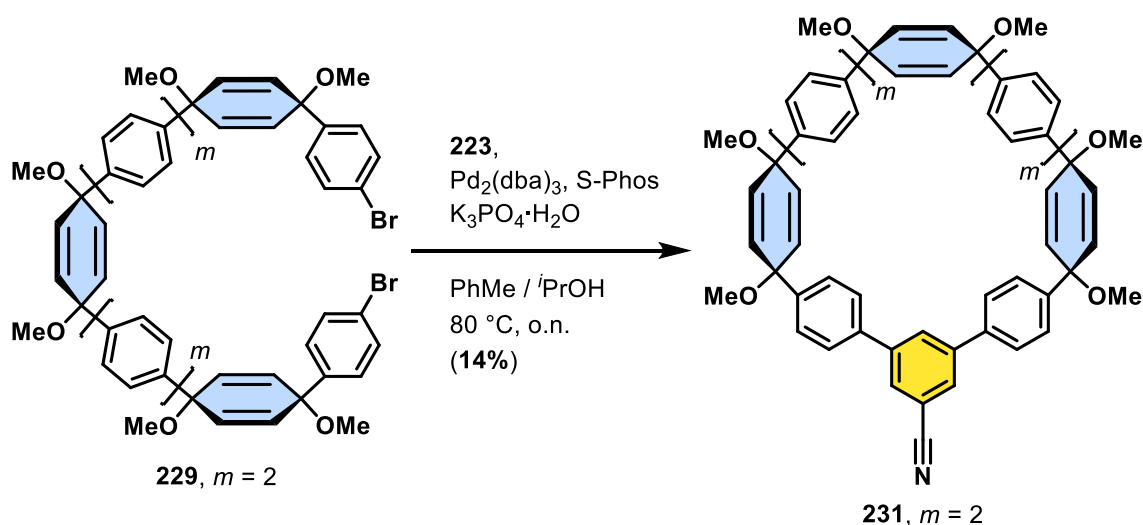
Dibromide **228** (400 mg, 455 μ mol, 1.00 equiv.) and diboronate **223** (194 mg, 546 μ mol, 1.10 equiv.), Pd₂(dba)₃ (41.7 mg, 45.5 μ mol, 10 mol%), S-Phos (41.9 mg, 100 μ mol, 22 mol%), and K₃PO₄·H₂O (441 mg, 1.82 mmol, 4.00 equiv.) were used. After purification through flash silica column chromatography (PhMe / EtOAc = 5:1 + 1% NEt₃; twice) the product **231** was obtained as yellow solid (60 mg, 74 μ mol, 16%).

Mp. = >280 °C (slow decomposition).

¹H-NMR (600 MHz, 298 K, DCM-*d*₂): δ = 8.03 (t, *J* = 1.68 Hz, 1H); 7.87 (d, *J* = 1.68 Hz, 2H); 7.62 – 7.61 (m, 4H); 7.53 – 7.52 (m, 4 H); 7.50 (s, 8H); 6.17 (s, 4H); 6.15 – 6.13 (m, 4H); 6.10 – 6.09 (m, 4H); 3.48 (s, 6H); 3.41 (s, 6H); 3.25 (s, 6H) ppm.

¹³C-NMR (151 MHz, 298 K, DCM-*d*₂): δ = 144.70 (1C); 143.84 (2C); 143.76 (2C); 142.46 (2C); 137.92 (2C); 134.21 (4C); 133.60 (4C); 133.50 (4C); 131.19 (2C); 128.86 (2C); 127.32 (4C); 127.00 (4C); 126.82 (4C); 126.55 (4C); 119.24 (1C); 113.90 (1C); 74.22 (2C); 74.57 (2C); 73.01 (2C); 52.48 (2C); 52.07 (2C); 51.51 (2C) ppm.

HRMS (ESI) *m/z* for C₅₅H₄₉NO₆ [*M*+Na]⁺ calculated 842.3451; found 842.3444.

5.2.5.3. Macrocyclic precursor **231**

Dibromide **229** (764 mg, 741 μmol , 1.00 equiv.) and diboronate **231** (289 mg, 815 μmol , 1.10 equiv.), $\text{Pd}_2(\text{dba})_3$ (70.0 mg, 74.1 μmol , 10 mol%), S-Phos (68.3 mg, 16.3 μmol , 22 mol%), and $\text{K}_3\text{PO}_4 \cdot \text{H}_2\text{O}$ (718 mg, 2.96 mmol, 4.00 equiv.) were used. After purification through flash silica column chromatography (PhMe / EtOAc = 8:1 - 5:1 + 1% NEt_3 ; twice) the product **231** was obtained as yellow solid (97.2 mg, 100 μmol , 14%).

Mp. = $>270^\circ\text{C}$ (slow decomposition)

$^1\text{H-NMR}$ (700 MHz, 303 K, DCM-d_2): δ = 7.95 (t, J = 1.68 Hz, 1H); 7.83 (d, J = 1.68, 2H); 7.58 (s, 8H); 7.54 – 7.51 (m, 8H); 7.49 – 7.48 (m, 4H); 7.45 – 7.44 (m, 4H); 6.20 – 6.18 (m, 4H); 6.16 – 6.14 (m, 4H); 6.11 (s, 4H); 3.46 (s, 12H); 3.44 (s, 6H) ppm.

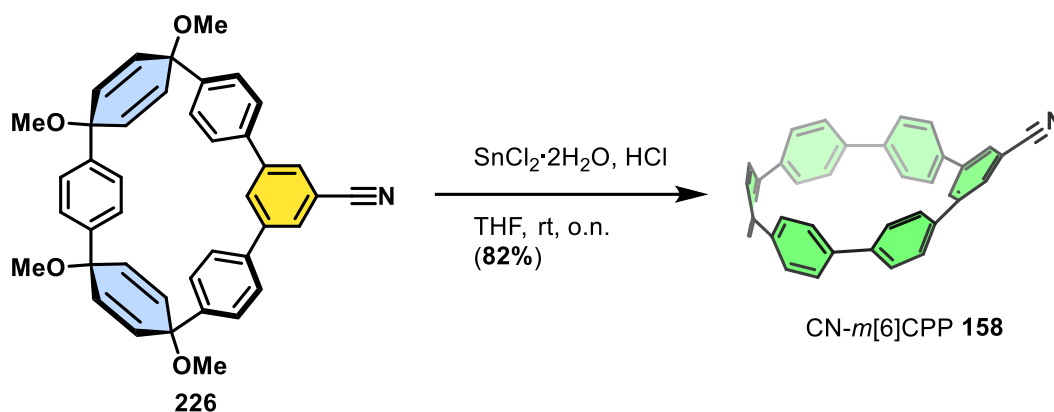
$^{13}\text{C-NMR}$ (176 MHz, 303 K, DCM-d_2): δ = 144.56 (1C); 143.59 (2C); 143.25 (2C); 143.21 (2C); 140.15 (2C); 140.08 (2C); 138.88 (2C); 134.34 (4C); 133.88 (4C); 133.58 (4C); 130.86 (2C); 129.89 (2C); 127.73 (4C); 127.32 (4C); 127.24 (4C); 127.20 (4C); 126.87 (4C); 119.15 (1C); 113.87 (1C); 75.12 (2C); 74.93 (2C); 74.91 (2C); 52.31 (2C); 52.28 (2C); 52.25 (2C) ppm.

HRMS (ESI) m/z for $\text{C}_{67}\text{H}_{57}\text{NO}_6$ [$M+\text{Na}$] $^+$ calculated 994.4077; found 994.4067.

5.2.6. Aromatization reactions towards nitrile-substituted *meta*[*n*]cycloparaphenylenes derived from methyl-ether protected macrocycles

Following **GP 3**, three different CN-*m*[*n*]CPPs were synthesized.

5.2.6.1. Cyano-*meta*[6]cycloparaphenylene **158**



Macrocyclic precursor **226** (914 mg, 1.51 mmol, 1.00 equiv.) and H₂SnCl₄ (0.30 L, 0.040 M, 4.00 equiv.) were used. After purification through flash silica column chromatography (Cy / DCM / EtOAc = 5:1:1 – 5:2:2) the product was obtained as bright yellow solid (593 mg, 1.24 mmol, 82%).

On a different scale, macrocyclic precursor **226** (825 mg, 1.36 mmol, 1.00 equiv.) and H₂SnCl₄ (273 mL, 0.0400 M in THF, 4.00 equiv.) were used. After purification through flash silica column chromatography (Cy / DCM / EtOAc = 6:1:1) the product **158** was obtained as bright yellow solid (631 mg, 1.32 mmol, 97%).

Mp. = >290 °C (slow decomposition).

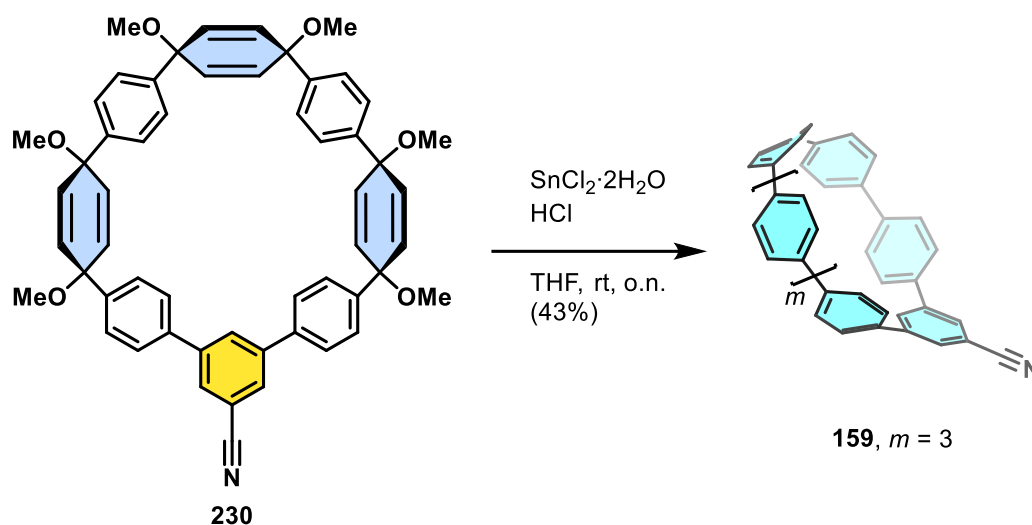
¹H-NMR (400 MHz, 297 K, DCM-*d*₂): δ = 7.73 (d, *J* = 1.86 Hz, 2H); 7.47 – 7.41 (m, 16H); 7.14 – 7.12 (m, 4H); 6.04 (t, *J* = 1.86 Hz, 1H) ppm.

¹³C-NMR (101 MHz, 297 K, DCM-*d*₂): δ = 144.03 (1C); 143.83 (2C); 140.97 (2C); 139.95 (2C); 137.99 (2C); 136.95 (2C); 136.52 (2C); 129.83 (4C); 128.41 (4C); 128.27 (4C); 128.21 (4C); 127.95 (4C); 126.35 (2C); 119.41 (1C); 113.28 (1C) ppm.

IR (ATR): $\tilde{\nu}$ = 3052 (m); 2926 (m); 2225 (m); 1715 (w); 1577 (s); 1482 (s) cm⁻¹.

HRMS (APCI) *m/z* for C₃₇H₂₃N [*M*+H]⁺ calculated 482.1903; found 482.1909.

HRMS (ESI) *m/z* for C₃₇H₂₃N [*M*+Na]⁺ calculated 504.1722; found 504.1723.

5.2.6.2. Cyano-*meta*[8]cycloparaphenylene **159**

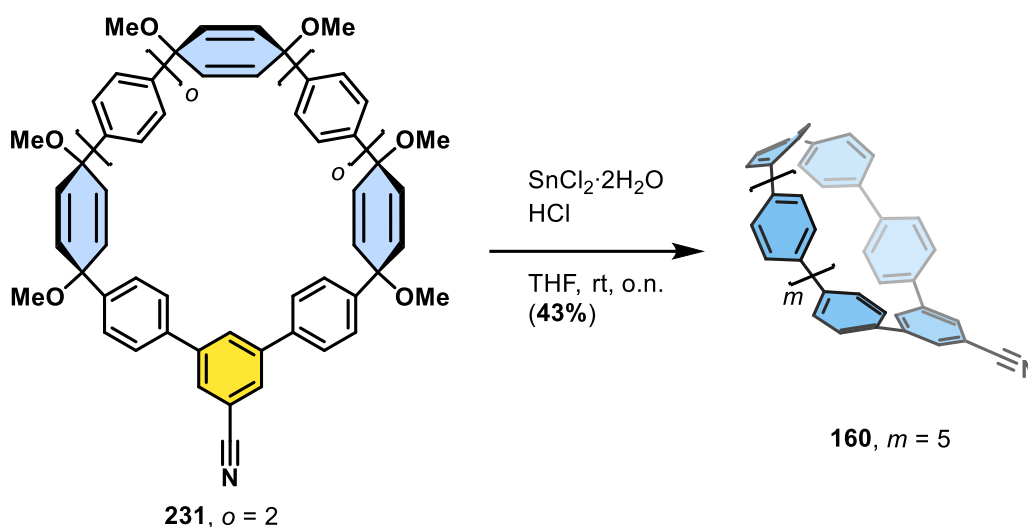
Macrocyclic precursor **230** (30.0 mg, 36.6 μmol , 1.00 equiv.) and H_2SnCl_4 (11 mL, 0.040 M, 12 equiv.) were used. After purification through flash silica column chromatography (Cy / DCM = 3:1 – 1:1) the product **159** was obtained as yellow solid (10.0 mg, 15.8 μmol , 43%).

Mp. = >290 °C (slow decomposition).

$^1\text{H-NMR}$ (400 MHz, 298 K, DCM-d_2): δ = 7.85 (d, J = 1.72 Hz, 2H); 7.54 – 7.46 (m, 20H); 7.43 – 7.41 (m, 4H); 7.33 – 7.30 (m, 4H); 6.60 (t, J = 1.72 Hz, 1H) ppm.

$^{13}\text{C-NMR}$ (101 MHz, 300 K, DCM-d_2): δ = 143.85 (1C); 140.91 (2C); 140.79 (2C); 139.65 (2C); 138.84 (2C); 138.52 (2C); 138.46 (2C); 138.02 (2C); 137.68 (2C); 129.22 (4C); 128.10 (4C); 128.06 (8C); 127.95 (4C); 127.87 (4C); 127.76 (4C); 127.50 (2C); 119.33 (1C); 113.58 (1C) ppm.

HRMS (ESI) m/z for $\text{C}_{49}\text{H}_{31}\text{N}$ [$M+\text{Na}$] $^+$ calculated 656.2348; found 656.2346.

5.2.6.3. Cyano-*meta*[10]cycloparaphenylene **160**

Macrocyclic precursor **231** (97.2 mg, 100 μmol , 1.00 equiv.) and H_2SnCl_4 (20 mL, 0.060 M, 12 equiv.) were used. After purification through flash silica column chromatography (Cy / DCM = 3:1 – 1:1) the product was obtained as pale yellow solid (34 mg, 43 μmol , 43%).

Mp. = >280 °C (slow decomposition).

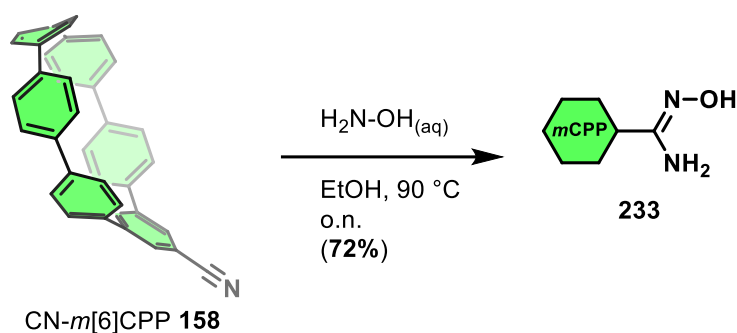
$^1\text{H-NMR}$ (700 MHz, 303 K, CDCl_3): δ = 7.85 (d, J = 1.72 Hz, 2H); 7.63 – 7.61 (m, 8H); 7.58 – 7.57 (m, 16H); 7.54 – 7.52 (m, 8H); 7.40 – 7.39 (m, 4H); 7.07 (t, J = 1.72 Hz, 1H) ppm.

$^{13}\text{C-NMR}$ (176 MHz, 303 K CDCl_3): δ = 143.64 (1C); 140.74 (2C); 138.94 (2C); 138.92 (2C); 138.83 (2C); 138.77 (2C); 138.41 (2C); 138.25 (2C); 138.18 (2C); 137.99 (2C); 137.77 (2C); 128.64 (4C); 127.89 (2C); 127.86 (4C); 127.79 (4C); 127.70 (4C); 127.65 (4C); 127.62 (4C); 127.60 (4C); 127.42 (4C); 127.35 (4C); 119.09 (1C); 113.36 (1C) ppm.

IR (ATR): $\tilde{\nu}$ = 3024 (s); 2919 (s); 2230 (w^*); 1726 (m); 1589 (m); 1482 (s) cm^{-1} .

*CN intensity low because of dominating CH, and CC vibrations.

HRMS (ESI) m/z for $\text{C}_{61}\text{H}_{39}\text{N}$ [$M+\text{H}$] $^+$ calculated 786.3155; found 786.3157.

5.2.7. Amidoxime-*meta*[6]cycloparaphenylene 233

Cyano-*meta*[6]cycloparaphenylene **158** (20.0 mg, 41.5 μmol , 1.00 equiv.) was added to a mixture of 50% aq. NH_2OH / EtOH (2.00 mL, v / v = 3:1). After stirring overnight at 90°C, the mixture was cooled to rt and concentrated under reduced pressure to obtain the target compound **233** as a yellow solid (15.3 mg, 29.7 μmol , 72%).

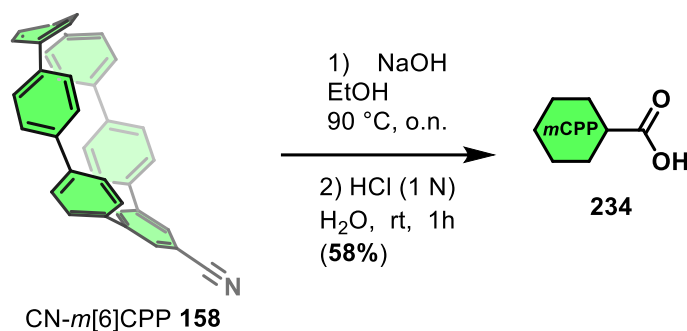
Mp. = >280 °C (slow decomposition).

$^1\text{H-NMR}$ (600 MHz, 298 K, $\text{DMSO-}d_6$): δ = 9.75 (s, 1H); 7.80 (d, J = 1.74 Hz, 2H); 7.59 – 7.52 (m, 16H); 7.23 – 7.21 (m, 4H); 5.98 (s, 2H); 5.47 (t, J = 1.74 Hz, 1H) ppm.

$^{13}\text{C-NMR}$ (151 MHz, 298 K $\text{DMSO-}d_6$): δ = 150.82 (1C); 141.95 (2C); 141.74 (2C); 138.39 (1C); 138.32 (2C); 136.73 (2C); 135.63 (2C); 135.05 (2C); 134.96 (1C); 129.17 (4C); 128.05 (4C); 127.79 (4C); 127.70 (4C); 127.44 (4C); 119.23 (2C) ppm.

HRMS(ESI) m/z for $\text{C}_{37}\text{H}_{26}\text{N}_2\text{O}$ [$M+\text{H}$]⁺ calculated 515.2118; found 515.2122.

5.2.8. Carboxy-*meta*[6]cycloparaphenylene **234**



Cyano-*meta*[6]cycloparaphenylene **158** (20.0 mg, 41.5 μmol , 1.00 equiv.) was suspended in an ethanolic solution of NaOH (2.0 mL, 10 N). The mixture was stirred at 90 °C overnight. After cooling to rt, the solution was acidified by 1 N HCl (pH~2). After stirring for 30 min at rt, the organic phase was extracted with ethyl acetate and the combined organic phase was washed with brine. After drying over MgSO₄, and subsequent filtration, the volatiles were evaporated under reduced pressure. The crude product was further purified through flash silica gel chromatography (Cy / EtOAc / MeOH = 5:1:0 – 4:1:1) obtaining the product as yellow solid (12 mg, 24 μmol , 58%).

On a larger scale cyano-*meta*[6]cycloparaphenylene **158** (300 mg, 623 μmol , 1.00 equiv.) in a solution of NaOH (5 N, 80 mL (EtOH/H₂O = 1:1)) was stirred for 3 h at 90 °C. After cooling to rt, the solution was acidified to pH~2 and further stirred at rt for 1 h. The precipitate was filtered and washed with cold EtOH and water to remove excess of acid and inorganic salts. After drying under reduced pressure, the product **234** was obtained as a bright yellow solid (310 mg, 619 μmol , 99%).

Mp. = >280 °C (slow decomposition).

¹H-NMR (400 MHz, 297 K, DMSO-*d*₆): δ = 13.23 (s, 1H)*; 8.05 (d, *J* = 1.85 Hz, 2H); 7.60 – 7.52 (m, 16H), 7.24 – 7.21 (m, 4H); 5.67 (t, *J* = 1.85 Hz, 1H) ppm.

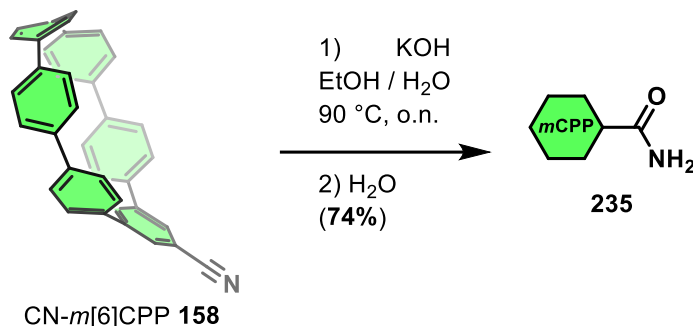
(*proton of carboxylic acid exchanges with water from solvent.)

¹³C-NMR (101 MHz, 297 K DMSO-*d*₆): δ = 167.19 (1C); 142.33 (2C); 142.22 (1C); 141.03 (2C); 138.55 (2C); 136.80 (2C); 135.62 (2C); 134.96 (2C); 132.52 (1C); 129.33 (4C); 128.02 (4C); 127.78 (4C); 127.72 (4C); 127.40 (4C); 122.96 (2C) ppm.

IR (ATR): $\tilde{\nu}$ = 2853 (m); 1898 (w); 1716 (m); 1681 (s); 1578 (s); 1483 (m) cm⁻¹.

HRMS (ESI) m/z for $C_{37}H_{24}O_2$ $[M+H]^+$: 501.1849 $[M+H]^+$; found 501.1842.

5.2.9. Amide-*meta*[6]cycloparaphenylene **235**



Cyano-*meta*[6]cycloparaphenylene **158** (20.0 mg, 41.5 μ mol, 1.00 equiv.) was suspended in a solution of KOH (20.0 mg, 356 μ mol, 8.59 equiv.) in EtOH / H₂O (2.5 mL, v / v = 4:1) and stirred overnight at 90 °C. After cooling to rt, H₂O (20 mL) was added, and the reaction was extracted with ethyl acetate (3x20 mL). The combined organic layers were washed with brine (50 mL). After drying over MgSO₄ and filtration, the volatiles were evaporated. The obtained crude product was further purified by flash silica gel chromatography (Cy / EtOAc / MeOH = 5:1:1). The product **235** was obtained as yellow solid (15.3 mg, 30.6 μ mol, 74%).

Mp. = >280°C (slow decomposition).

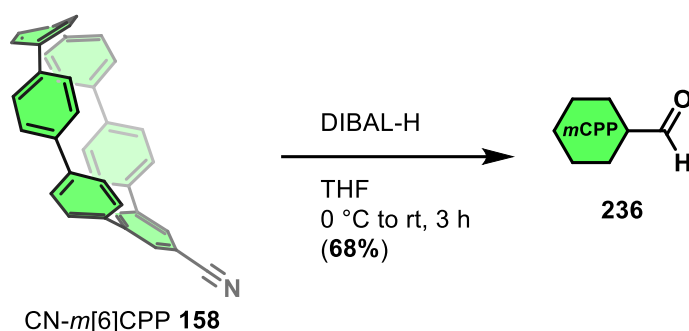
¹H-NMR (400 MHz, 296 K, DMSO-*d*₆): δ = 8.13 (s, 1H); 8.00 (d, J = 1.76 Hz, 2H); 7.60 – 7.52 (m, 16H); 7.23 – 7.21 (m, 4H); 5.99 (t, J = 1.76 Hz, 1H) ppm.

*One proton of the amide is missing most likely due to H-D exchange with water.

¹³C-NMR (101 MHz, 297 K, DMSO-*d*₆): δ = 167.78 (1C); 142.06 (2C); 141.38 (1C); 140.56 (1C); 138.43 (2C); 136.76 (2C); 136.08 (1C); 135.62 (2C); 135.00 (1C); 129.25 (4C); 128.03 (4C); 127.78 (4C); 127.71 (4C); 127.44 (4C); 121.30 (2C) ppm.

HRMS (ESI) m/z for $C_{37}H_{25}NO$ $[M+Na]^+$ calculated 522.1828; found 522.1832.

5.2.10. Aldehyde-*meta*[6]cycloparaphenylene **236**



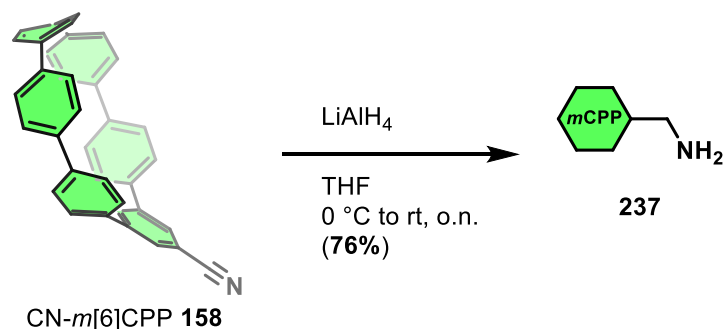
Cyano-*meta*[6]cycloparaphenylene **158** (20.0 mg, 41.5 μmol , 1.00 equiv.) was dissolved in DCM (0.5 mL), cooled to 0 °C, and treated slowly dropwise with DIBAL-H (0.10 mL, 1.0 M in *n*-hexane, 2.4 equiv.). The reaction was allowed to warm up to rt and then stirred for 3 h. Under vigorous stirring, 6 M HCl solution (2 mL) was added together with some ice to the reaction mixture. After stirring for 1 h at rt, the aqueous phase was extracted with DCM (3x20 mL). The combined organic phase was washed with saturated aqueous NaHCO₃ solution (20 mL) and distilled H₂O (50 mL), dried over MgSO₄, and filtered. After removing the volatiles under reduced pressure, the crude product was further purified by flash silica gel chromatography (CHCl₃ / hexanes = 4:1). The product **236** was obtained as yellow solid (13.6 mg, 28.1 μmol , 68%).

Mp. = >250 °C (slow decomposition).

¹H-NMR (400 MHz, 296 K, DMSO-*d*₆): δ = 10.14 (s, 1H); 8.05 (d, *J* = 1.85 Hz, 2H); 7.60 – 7.52 (m, 16H); 7.26 – 7.24 (m, 4H); 5.75 (t, *J* = 1.85, 1H) ppm.

¹³C-NMR (101 MHz, 297 K DMSO-*d*₆): δ = 193.16 (1C); 143.71 (1C); 142.86 (2C); 140.71 (2C); 138.71 (2C); 137.86 (1C); 136.84 (2C); 135.62 (2C); 134.93 (2C); 129.37 (4C); 128.02 (4C); 127.78 (4C); 127.75 (4C); 127.45 (4C); 123.30 (2C) ppm.

HRMS (APCI) *m/z* for C₃₇H₂₄O [M+H]⁺ calculated 485,1900; found 485.1899.

5.2.11. (Amino-methylene)-*meta*[6]cycloparaphenylene**237**

LiAlH₄ (5.20 mg, 130 μmol, 3.14 equiv.) was added in small portions to a solution of cyano-*meta*[6]cycloparaphenylene **158** (20.0 mg, 41.5 μmol, 1.00 equiv.) in THF (2.00 mL) at 0 °C. The resulting mixture was warmed up to rt and stirred overnight. The next day, a saturated solution of sodium/potassium tartrate (20 mL) was added and allowed to stir for 1 h at rt. The aqueous phase was extracted with EtOAc (4x25 mL). The combined organic layers were dried over MgSO₄ and filtrated. After removing the volatiles under reduced pressure, the crude product was further purified by flash silica gel chromatography (DCM / MeOH = 19:1 + 0.5% NEt₃). The product **237** was obtained as yellow solid (15.3 mg, 31.5 μmol, 76%).

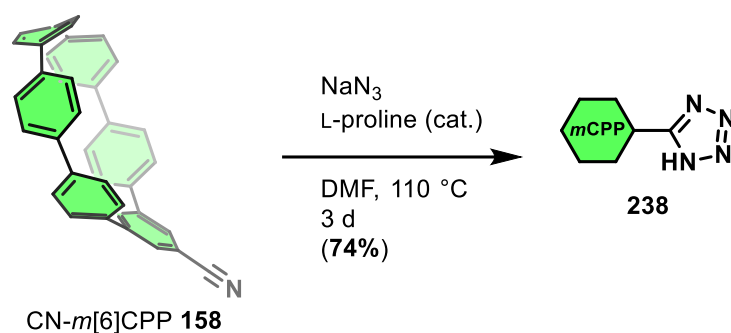
On a larger scale, LiAlH₄ (52.5 mg, 1.24 mmol, 3.00 equiv.), and cyano-*meta*[6]cycloparaphenylene **1** (200 mg, 415 μmol, 1.00 equiv.) in THF (10 mL) at 0 °C were used. For quenching the reaction, sodium/potassium tartrate (150 mL) was added. The crude product **237** was further purified by flash silica gel chromatography (SiO₂, DCM/MeOH = 19:1 + 0.5% TEA) to obtain the desired product (157 mg, 323 μmol, 78%)

Mp. = slow decomposition >250 °C

¹H-NMR (400 MHz, 298 K, DMSO-*d*₆): δ = 7.60 – 7.51 (m, 16H); 7.48 (d, *J* = 1.90 Hz, 2H); 7.18 – 7.16 (m, 4H); 5.29 (t, *J* = 1.90 Hz, 1H), 3.84 (s, 2H) ppm.

¹³C-NMR (101 MHz, 297 K DMSO-*d*₆): δ = 145.84 (1C); 142.31 (2C); 142.02 (2C); 138.05 (2C); 136.64 (2C); 136.09 (1C); 135.59 (2C); 135.07 (2C); 129.09 (4C); 128.01 (4C); 127.76 (4C); 127.60 (4C); 127.28 (4C); 120.89 (2C); 45.71 (1C) ppm.

HRMS (ESI) *m/z* calc. for C₃₇H₂₇N + H⁺: 486.2216 [*M*+H]⁺; found: 486.2219.

5.2.12. 1*H*-Tetrazole-5-*meta*[6]cycloparaphenylene **238**

A mixture of cyano-*meta*[6]cycloparaphenylene **158** (20.0 mg, 41.5 μmol , 1.00 equiv.), NaN_3 (5.00 mg, 76.1 μmol , 1.83 equiv.), and L-proline (1.50 mg, 13.0 μmol , 31.0 mol%) was stirred at 110 °C in DMF (2.00 mL) for 3 d. After completion of the reaction, the mixture was allowed to cool to rt and afterwards poured in ice water under rigorous stirring. This mixture was acidified with aqueous HCl solution (2 N). The resulting precipitate was dissolved with ethyl acetate and the combined organic phase was washed with water (6x50 mL), brine (100 mL), and dried over MgSO_4 . After filtration, the volatiles were evaporated under reduced pressure and the pure product **238** was obtained (16.2 mg, 30.9 μmol , 74%).

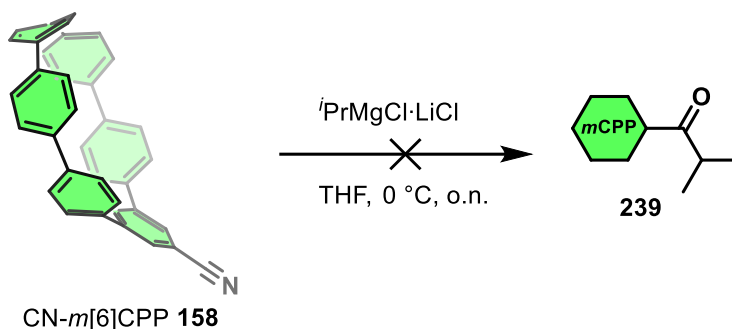
Mp. = >280°C (slow decomposition).

$^1\text{H-NMR}$ (400 MHz, 298 K $\text{DMSO-}d_6$): δ = 8.17 (d, J = 1.75 Hz, 2H); 7.60 – 7.53 (m, 16H); 7.28 – 7.26 (m, 4H); 5.64 (t, J = 1.75 Hz, 1H) ppm.

$^{13}\text{C-NMR}$ (101 MHz, 298 K $\text{DMSO-}d_6$): δ = 155.47 (C_q , 1C - HMBC); 143.05 (C_q , 2C); 140.85 (C_q , 2C); 140.49 (C_q , 1C); 138.71 (C_q , 2C); 136.85 (C_q , 2C); 135.63 (C_q , 2C); 134.92 (C_q , 2C); 129.28 ($\text{C}_{\text{sp}2}$, 4C); 128.04 ($\text{C}_{\text{sp}2}$, 4C); 127.78 ($\text{C}_{\text{sp}2}$, 4C); 127.74 ($\text{C}_{\text{sp}2}$, 4C); 127.51 ($\text{C}_{\text{sp}2}$, 4C); 125.67 (C_q , 1C); 120.74 (C_q , 2C) ppm.

HRMS(ESI) m/z for $\text{C}_{37}\text{H}_{24}\text{N}_4[\text{M}+\text{Na}]^+$ calculated 547.1893; found 547.1888.

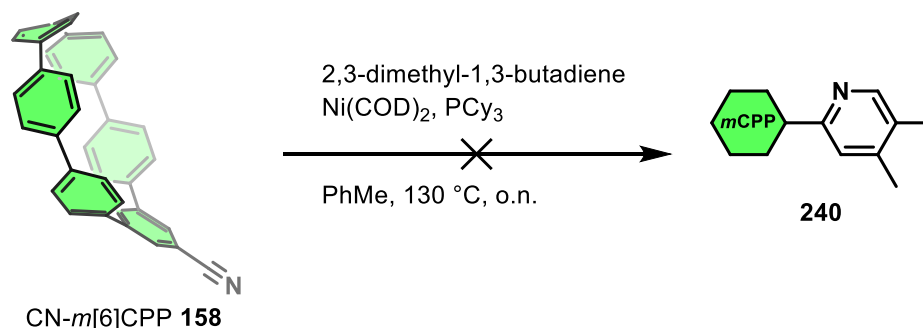
5.2.13. 1-(*meta*[6]cycloparaphenylene)-2-methylpropane-1-one **239**



iso-propyl magnesium chloride lithium chloride complex solution (48.0 μ L, 1.30 M in THF, 1.50 equiv.) was slowly added to a solution of cyano-*meta*[6]cycloparaphenylene **158** (20.0 mg, 41.5 μ mol, 1.00 equiv.) in dry THF (1.0 mL) at 0 °C. The reaction was allowed to stir at rt overnight. The next day, the reaction was quenched through the addition of saturated aqueous NH_4Cl solution, and 1 M was added to the reaction mixture. The reaction mixture was stirred for 1 h at rt, and subsequently extracted with Et_2O (3x20 mL). The combined organic phase was washed with brine and dried over Na_2SO_4 . The volatiles were evaporated under reduced pressure to afford the crude product.

Decomposition of the starting material was observed when measured $^1\text{H-NMR}$ spectrum.

5.2.14. 4,5-Dimethylpyridinyl-2-(*meta*[6]cycloparaphenylene) **240**

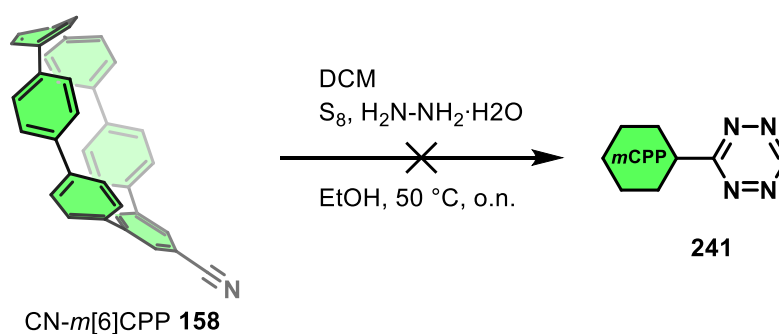


To a solution of $\text{Ni}(\text{cod})_2$ (2.00 mg, 7.27 μ mol, 0.18 equiv.), tricyclohexylphosphin (5.00 mg, 17.3 μ mol, 0.42 equiv.) and cyano-*meta*[6]cycloparaphenylene **158**

(20.0 mg, 41.5 μmol , 1.00 equiv.) in toluene (1.0 mL) was added 2,3-dimethyl-1,3-butadiene (19.0 μL , 165 μmol , 3.97 equiv.). The resulting mixture was transferred into a pressure-tight vial (volume: 4.0 mL). The vial was tightly sealed up and heated at 130 $^{\circ}\text{C}$ overnight. After the reaction mixture was cooled to rt, all volatiles were removed under reduced pressure after a short plug of Celite[®]. Short flash silica gel column chromatography (Cy / DCM = 4:1) led to the reisolation of the starting material.

5.2.15. 3-(*meta*[6]cycloparaphenylene)-1,2,4,5-tetrazine

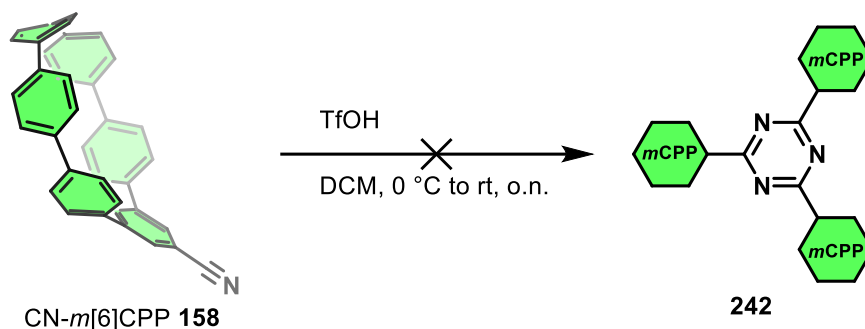
241



Cyano-*meta*[6]cycloparaphenylene **158** (20.0 mg, 41.5 μmol , 1.00 equiv.) were added together with DCM (5.00 μL , 79.7 μmol , 1.92 equiv.), sulfur (2.70 mg, 83.8 μmol , 2.02 equiv.) and EtOH (2.0 mL) into a screw cap vial. Hydrazine monohydrate (16.2 μL , 332 μmol , 8.00 equiv.) was added slowly with stirring afterwards. The tube was sealed, and the reaction mixture was heated to 50 $^{\circ}\text{C}$ overnight. Then DCM (1.0 mL) and aqueous sodium nitrite (28.6 mg, 415 μmol , 10.0 equiv.) were added to the mixture. Excess acetic acid (2.0 mL) was then added. The reaction mixture was extracted with DCM (3x20 mL), and the combined organic phase was dried over MgSO₄. After filtration, the volatiles were removed under reduced pressure and a crude ¹H-NMR spectrum was measured.

Unfortunately, only cyano-*meta*[6]cycloparaphenylene **158** was reisolated.

5.2.16. 2,4,6-(*meta*[6]cycloparaphenylene)-1,3,5-triazine **242**

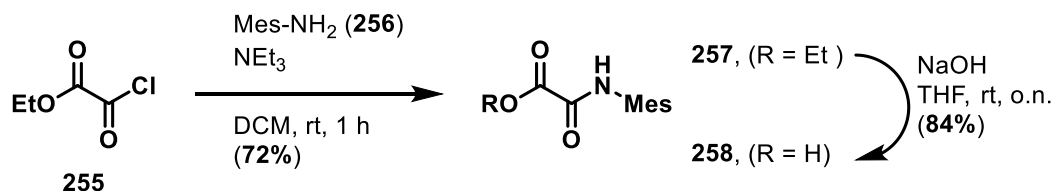


To a vigorously stirred solution of cyano-*meta*[6]cycloparaphenylene **158** (20.0 mg, 41.5 μmol , 1.00 equiv.) in DCM (2.0 mL) trifluoromethanesulfonic acid (3 droplets from Pasteur pipette) was added at 0 °C. The reaction mixture was stirred for 2 h at 0 °C before warmed up to rt. After being stirred overnight at room temperature, aqueous NaOH solution (10%) was added dropwise until the appearance of the solution became colorless. The reaction mixture was extracted with CHCl_3 (10 mL) and the organic phase was separated, washed with H_2O (2x10 mL), and dried over MgSO_4 . After filtration, the volatiles were removed under reduced pressure and a crude $^1\text{H-NMR}$ spectrum was measured.

Unfortunately, the $^1\text{H-NMR}$ spectrum showed decomposition of the cyano-*meta*[6]cycloparaphenylene **158**.

*using Sml_2 instead of TfOH resulted in the reisolation of the starting material.

5.2.17. *N*-(Mesityl)-oxanilic acid (**258**)



This compound was synthesized according to literature.³¹³

A solution of 2,4,6-trimethylaniline (**256**) (3.65 mL, 25.1 mmol, 1.00 equiv.) and triethylamine (3.65 mL, 24.9 mmol, 0.994 equiv.) in anhydrous THF (20 mL) was cooled to 0 °C. At this temperature, ethyl chlorooxoacetate (**255**) (2.80 mL, 25.1 mmol, 1.00 equiv.) was added slowly via syringe. Precipitation of a colorless

solid occurred immediately upon addition. The mixture was allowed to stir for 2 h after warming to rt. At this point, the solid was filtered off, and the organic layer was washed with 2 M HCl solution (2x20 mL). The aqueous layer was washed with ethyl acetate, and the combined organic layers were washed with brine (50 mL) and dried over MgSO₄. The solvent was then removed under reduced pressure, leaving a pale yellow solid. Recrystallization from hexanes afforded the *N*-(mesityl)-oxanilic acid ethyl ester as colorless solid (4.24 g, 18.0 mmol, 72%).

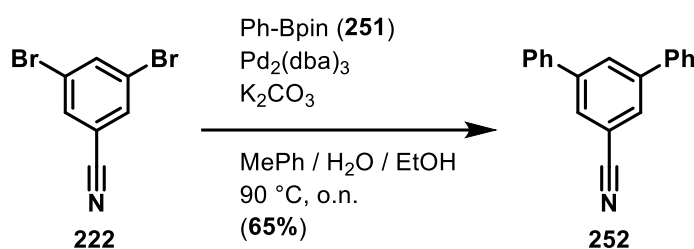
The *N*-(mesityl)-oxanilic ethyl ester **257** (518 mg, 2.20 mmol, 1.00 equiv.) was subsequently dissolved in THF (10 mL). To this solution was added 1 M NaOH solution (40 mL), and the mixture was stirred overnight at rt. Diethyl ether (20 mL) was added, and the layers were separated. The organic layer was washed with 1 M NaOH solution (20 mL). The aqueous layer was then acidified with 2 M HCl until precipitation occurred. The aqueous phase was then extracted with ethyl acetate (2x20 mL). The ethyl acetate was washed with brine (20 mL), and then dried over MgSO₄. Removal of the solvent under reduced pressure provided the *N*-(mesityl)-oxanilic acid (**258**) as a colorless solid (383 mg, 1.85 mmol, 84%).

Mp. = 106 °C.

¹H-NMR (400 MHz, 297 K, CDCl₃): δ = 8.47 (s, 1H); 6.94 (s, 2H); 2.29 (s, 3H); 2.20 (s, 6H) ppm.

¹³C-NMR (101 MHz, 297 K, CHCl₃): δ = 159.80 (1C); 155.97 (1C); 138.57 (1C); 134.65 (2C); 129.45 (2C); 128.85 (1C); 21.11 (1C); 18.41 (2C) ppm.

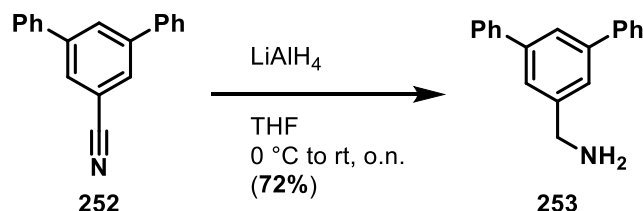
HRMS (ESI) m/z for. C₁₁H₁₃NO₃ [*M*+Na]⁺ calculated 230.0787; found: 230.0788.

5.2.18. [1,1':3',1''-Terphenyl]-5'-carbonitrile (252)

To a solution of 3,5-dibromobenzonitrile (**222**, 209 mg, 800 μ mol, 1.00 equiv.) in 1,4-dioxane (20 mL) was added phenyl boronic pinacol ester **251** (390 mg, 1.87 mmol, 2.34 equiv.) and Pd(dppf)₂ (1:1 complex with DCM; 269 mg, 323 μ mol, 40 mol%). To this mixture, aqueous Na₂CO₃ solution (1.4 mL, 2.0 M, 3.5 equiv.) was added, and the reaction was stirred under refluxing conditions overnight. After cooling to rt, the reaction mixture was filtered through a plug of Celite[®]. The organic phase was washed with H₂O (3x20 mL), brine (50 mL), and dried over MgSO₄. After filtration, the volatiles were removed under reduced pressure and the crude product was further purified by flash silica gel chromatography (Cy / EtOAc = 8:1). The product **252** was isolated as colorless solid (132 mg, 517 μ mol, 65%).

¹H-NMR (600 MHz, 298 K, CDCl₃): δ = 8.00 (t, J = 1.76 Hz, 1H); 7.83 (d, J = 1.76 Hz, 2H); 7.63 – 7.61 (m, 4H); 7.52 – 7.49 (m, 4H); 7.46 – 7.43 (m, 4H) ppm.

¹³C-NMR (151 MHz, 298 K, CHCl₃): δ = 143.16 (2C); 139.08 (2C); 130.51 (1C); 129.45 (2C); 129.30 (4C); 128.63 (2C); 127.32 (4C); 119.00 (1C); 113.56 (1C) ppm.

5.2.19. [1,1':3',1''-Terphenyl]-5'-yl-methanamine (253)

LiAlH₄ (63.0 mg, 1.58 mmol, 2.01 equiv) was slowly added to a solution of carbonitrile **252** (200 mg, 783 μ mol, 1.00 equiv.) in THF (10 mL) at 0 °C. The resulting mixture was warmed up to rt and stirred overnight. The next day, a saturated solution of sodium/potassium tartrate (20 mL) was added to the reaction mixture. After stirring for 30 min at rt, the aqueous phase was extracted with EtOAc

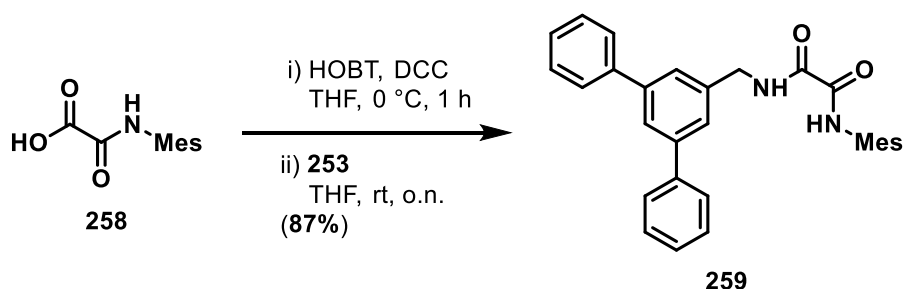
(4x50 mL). The combined organic phase was dried over MgSO_4 , filtered, and concentrated under reduced pressure. The crude product was further purified by flash silica gel chromatography (DCM / MeOH = 19:1 + 1% NEt_3). The product **253** slowly crystallized in slightly yellow needles (121.6 mg, 468.9 μmol , 60%).

$^1\text{H-NMR}$ (600 MHz, 298 K, CDCl_3): δ = 7.70 – 7.69 (m, 1H); 7.67 – 7.68 (m, 4H); 7.54 (m, 2H); 7.47 – 7.45 (m, 4H); 7.38 – 7.36 (2H); 4.02 (s, 2H) ppm.

$^{13}\text{C-NMR}$ (151 MHz, 298 K, CHCl_3): δ = 142.28 (2C); 141.25 (2C); 128.94 (4C); 127.61 (4C); 127.44 (4C); 119.00 (1C); 113.56 (1C); 46.65 (1C) ppm.

HRMS (ESI) m/z for. $\text{C}_{19}\text{H}_{17}\text{N}$ [$M+\text{Na}$] $^+$ calculated 282.1253; found: 282.1257.

5.2.20. *N*-(Mesityl)-*N'*-([1,1':3',1''-terphenyl]-5'-ylmethyl)-oxalamide (**259**)



N-(Mesityl)-oxalamic acid **258** (58.2 mg, 281 μmol , 1.00 equiv.) and 1-HOBT (58.7 mg, 422 μmol , 1.50 equiv.) were dissolved in THF (2.0 mL) and cooled to 0 °C. To this solution was then added DCC (70.3 mg, 1 M in DCM, 1.20 equiv.). The reaction mixture was allowed to stir 1 h. During this time, a colorless precipitation occurred. After 1 h, amine **253** (50.0 mg, 193 μmol , 0.686 equiv.) was added to the suspension and allowed to stir overnight at rt. The next day, all volatiles were removed under reduced pressure, and EtOAc was added to form a suspension, which was then filtered to remove the solid. The filtrate was washed with 10% citric acid solution (2x5 mL), 5% NaHCO_3 (2x5 mL) and brine (5 mL). Afterwards, the organic phase was dried over MgSO_4 , and the volatiles were removed under reduced pressure. After recrystallization from *n*-hexane, the product was afforded as colorless solid (75.0 mg, 167 μmol , 87%).

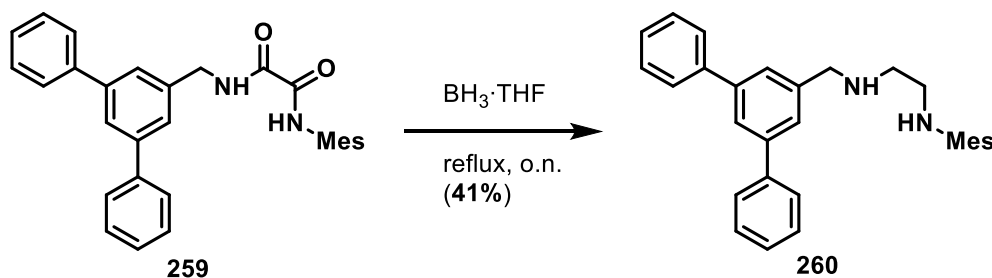
¹H-NMR (600 MHz, 299 K, CDCl₃): δ = 8.74 (s, 1H); 7.92 (s, 7.92); 7.76 (t, *J* = 1.71 Hz, 1H); 7.66 – 7.63 (m, 4H); 7.53 (d, *J* = 1.71 Hz, 2H); 7.49 – 7.45 (m, 4H); 7.41 – 7.36 (m, 4H); 6.92 (s, 2H); 4.69 (d, *J* = 6.09 Hz, 2H); 2.28 (s, 3H); 2.20 (s, 6H) ppm.

¹³C-NMR (151 MHz, 300 K, CHCl₃): δ = 160.03 (1C); 158.16 (1C); 142.73 (2C); 140.83 (2C); 137.84 (1C); 134.87 (2C); 129.24 (2C); 129.03 (4C); 127.84 (2C); 127.46 (4C); 126.04 (1C); 125.97 (2C); 44.26 (1C); 21.08 (1C); 18.52 (2C) ppm.

*two carbons are missing due to bad signal to noise ratio.

HRMS (ESI) *m/z* for. C₃₀H₂₈N₂O₂ [*M*+Na]⁺ calculated 471.2043; found: 471.2041.

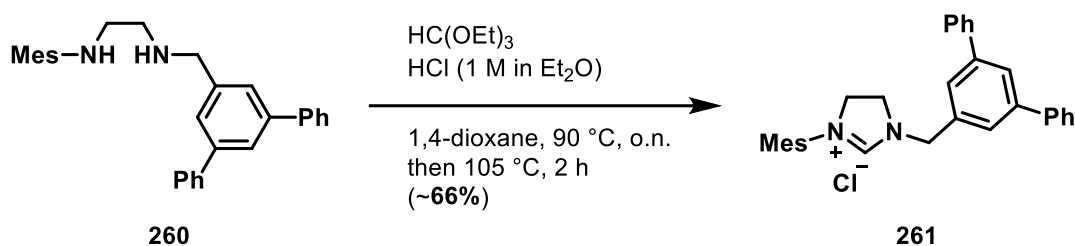
5.2.21. *N*-(Mesityl)-*N'*-([1,1':3',1''-terphenyl]-5'-ylmethyl)-diamine (**260**)



Oxalamide **259** (70.0 mg, 156 μmol, 1.00 equiv.) was dissolved in BH₃·THF (1.1 mL, 1.0 M in THF, 7.1 equiv.) and heated to reflux overnight. After cooling to rt, the solution was poured into a mixture of ice, H₂O, and HCl (1 M). The precipitate was filtered off and was dissolved in THF / H₂O (1:4). The solution was basified with NaOH (pH~12). The aqueous phase was extracted with Et₂O (3x10 mL). The combined organic phase was washed with brine (20 mL), dried over MgSO₄. After filtration, the volatiles were removed under reduced pressure and the crude product was further purified through flash silica gel column chromatography (Cy / EtOAc = 3:1 + 1% NEt₃ – DCM / MeOH = 1:1 + 1% NEt₃). The product **260** was obtained as colorless solid, which crystallized very slowly (30.6 mg, 72.8 μmol, 47%).

¹H-NMR (200 MHz, 296 K, CDCl₃): δ = 7.75 – 7.65 (m, 6H); 7.59 (m, 2H); 7.53 – 7.35 (m, 7H); 6.83 (s, 2H); 3.99 (s, 2H); 3.14 – 3.09 (m, 2H); 2.97 – 2.91 (m, 2H); 2.30 (s, 6H); 2.24 (s, 3H) ppm.

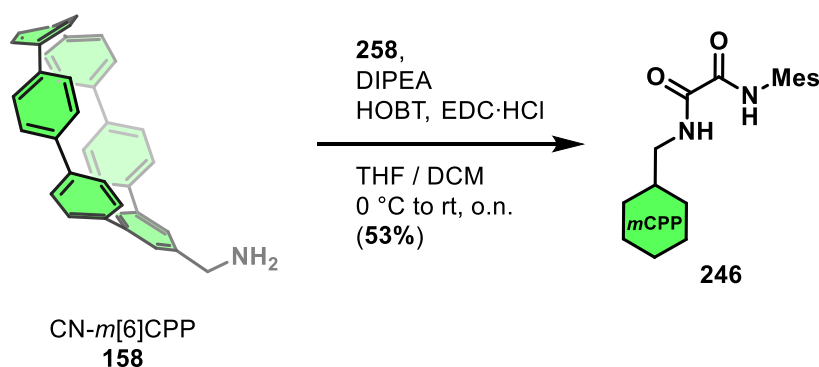
5.2.22. *N*-(Mesityl)-*N'*-(1-([1,1':3',1''-terphenyl]-5'-ylmethyl)-imidazolinium chloride (261)



A mixture of diamine **260** (30.0 mg, 71.3 μmol , 1.00 equiv.), triethyl orthoformate (200 μL , 1.18 mmol, 16.6 equiv.), and HCl (150 μL , 1.00 M in Et_2O , 2.10 equiv.), and 1,4-dioxane (0.5 mL) was heated in an open vial at $90\text{ }^\circ\text{C}$ overnight. The next day, the reaction mixture was heated at $105\text{ }^\circ\text{C}$ for 2 h. After cooling to rt, the volatiles were removed under reduced pressure to one-third of its volume. The mixture was cooled to rt and filtered over a short pipette filled with Celite[®]. The solid was washed with cold diethyl ether (5x10 mL) and finally eluted with DCM. The product **261** was obtained as orange solid (22.0 mg, 47.1 μmol , 66%).

¹H-NMR (200 MHz, 297 K, CDCl_3): δ = 10.28 (s, 1H); 7.78 (s, 1H); 7.65 – 7.58 (m, 6H); 7.46 – 7.42 (m, 4H); 7.38 – 7.35 (m, 2H); 6.85 (s, 2H); 5.30 (s, 2H); 4.10 (s, 4H); 2.27 (s, 6H); 2.22 (s, 3H) ppm.

5.2.23. *N*-(Mesityl)-*N'*-(1-methylene-*meta*[6]cycloparaphenylene)-oxalamide 246



N-(Mesityl)-oxanilic acid **258** (59.7 mg, 288 μmol , 1.00 equiv.) and Pr_2NEt (DIPEA, 123 μL , 720 μmol , 2.50 equiv.) were dissolved in THF (6 mL) and cooled to $0\text{ }^\circ\text{C}$. After addition of 1-hydroxybenzotriazole (60.2 mg, 432 μmol , 1.50 equiv.) and 1-

ethyl-3-[3-dimethylaminopropyl]carbodiimide hydrochloride (66.3 mg, 346 μmol , 1.00 M in CH_2Cl_2 , 1.20 equiv.) the reaction was stirred at this temperature until TLC showed full conversion (~ 1 h) of the oxanilic acid. At this point, (amino-methylene)-*meta*[6]cycloparaphenylene **X** (140 mg, 288 μmol , 1.00 equiv., in 2 mL THF) was added to the suspension and was allowed to stir overnight at rt. The next day, the reaction mixture was quenched with sodium bicarbonate, extracted with CH_2Cl_2 (3x50 mL), washed with water (3x50 mL), and brine (100 mL). The organic phase was dried over magnesium sulphate, and the volatiles were removed under reduced pressure, leaving a yellow solid, which was further purified by column chromatography (SiO_2 , Cy/DCM/EtOAc = 5:1:1). The product was obtained as a bright yellow solid (103 mg, 152 μmol , 53%).

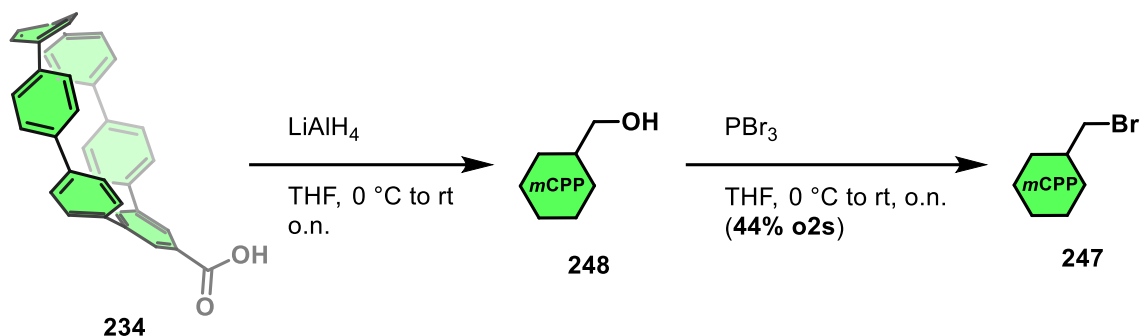
Mp.: slow decomposition >230 $^\circ\text{C}$.

$^1\text{H-NMR}$ (400 MHz, 299 K; DCM- d_2): δ = 8.77 (s, 1H); 7.94 (s, 1H); 7.47 – 7.39 (m, 18H); 7.17 (m, 4H); 6.94 (s, 2H); 5.72 (t, J = 1.76 Hz, 1H); 4.65 (d, J = 6.36 Hz, 2H); 2.29 (s, 3H), 2.20 (s, 6H) ppm.

$^{13}\text{C-NMR}$ (101 MHz, 300 K; DCM- d_2): δ = 160.23 (1C), 158.64 (1C), 143.56 (2C), 142.73 (2C), 139.33 (2C), 139.08 (1C), 138.77 (1C), 138.01 (1C), 137.84 (2C), 136.97 (2C), 136.73 (2C), 135.30 (2C), 130.41 (1C), 129.75 (4C), 129.31 (2C), 128.46 (4C), 128.24 (4C), 128.09 (4C), 127.73 (4C), 122.28 (2C), 44.42 (1C), 21.05 (1C), 18.50 (2C) ppm.

IR (ATR): $\tilde{\nu}$ = 3304 (m), 3014 (m), 2919 (m), 2852 (m), 1659 (v), 1582 (m), 1496 (v) cm^{-1} .

HRMS (ESI) m/z for $\text{C}_{48}\text{H}_{38}\text{N}_2\text{O}_2$ [$M+\text{Na}$] $^+$ calculated 697.2825; found: 697.2817.

5.2.24. Bromo-methylene-*meta*[6]cycloparaphenylene**247**

A solution of carboxy-*meta*[6]cycloparaphenylene **234** (250 mg, 500 μmol , 1.00 equiv.) in THF (20 mL) was cooled to -20 °C. After careful addition of LiAlH_4 (40.0 mg, 1.00 μmol , 2.00 equiv.) the reaction mixture was allowed to warm up to rt and stirred overnight. The reaction was quenched at 0 °C using a saturated sodium/potassium tartrate solution (200 mL). After warming up to rt, diethyl ether (100 mL) was added, and the organic layer was separated. After extraction with diethyl ether (3x100 mL), the combined organic layers were washed with saturated sodium bicarbonate solution (3x100 mL). After drying over magnesium sulphate, and subsequent filtration, the volatiles have been removed at the rotary evaporator to afford the crude benzylic alcohol **248**, which was used without further purification.

After cooling a solution of the afforded crude alcohol in THF (10 mL) to 0 °C, PBr_3 (68 μL , 0.25 mmol, 0.50 equiv.) was added dropwise to the reaction. The reaction was warmed up to rt and stirred overnight. After dropwise addition of water (5 mL), diethyl ether (50 mL) was added, and the organic phase has been separated. After extraction with diethyl ether (3 x 50 mL), the combined organic layers were washed with saturated sodium bis carbonate solution (3 x 50 mL). After drying over magnesium sulphate, and subsequent filtration, the volatiles have been removed at the rotary evaporator to afford the crude benzylic bromine. Further purification using flash column chromatography (SiO_2 , Cy/DCM = 6:1) afforded the desired product **247** (120 mg, 218 μmol , 44%).

Mp. = >290 °C (slow decomposition).

¹H-NMR (400 MHz, 297 K, DCM-*d*₂): δ = 7.49 (d, *J* = 1.68 Hz, 2H)*; 7.45 – 7.39 (m, 16H)*; 7.16 – 7.13 (m, 4H)*; 5.72 (t, *J* = 1.68 Hz, 1H); 4.64 (s, 2H) ppm.

*Partial hydrolysis under ambient conditions while attempting to remove solvent residues (DCM worked well, but diethyl ether still inside). Water (1.53 ppm) from NMR solvent.

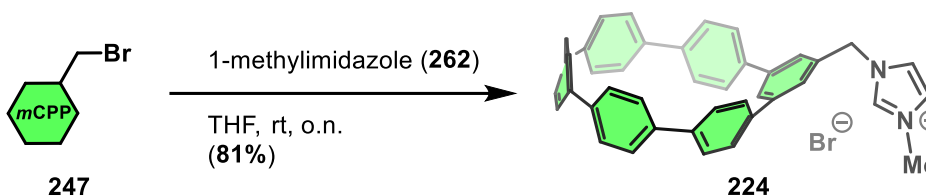
¹³C-NMR (101 MHz, CD₂Cl₂): δ = 143.52 (2C); 142.42 (2C); 139.76 (2C); 139.45 (1C); 139.36 (1C); 137.83 (2C); 136.95 (2C); 136.70 (2C); 129.75 (4C); 128.45 (4C); 128.24 (4C); 128.10 (4C); 127.75 (4C); 123.35 (2C); 34.35 (1C) ppm.

* δ = 66.07 (2C); 15.51 (2C) ppm correspond to diethyl ether which could not be removed.

IR (ATR): $\tilde{\nu}$ = 2850 (m); 1892 (w); 1638 (m); 1580 (s) 1482 (m) cm⁻¹.

HRMS (APCI) *m/z* for C₃₇H₂₅Br [*M*+H]⁺ calculated 549.1213; found 549.1213.

5.2.25. *N*-(Methyl)-*N'*-(1-methylene-*meta*[6]cycloparaphenylene)-imidazolium bromide **224**



To a solution of bromo-methylene-*meta*[6]cycloparaphenylene **247** (100 mg, 182 μ mol, 1.00 equiv.) in THF (10 mL) *N*-methyl-imidazole (0.10 mL, 1.2 mmol, 6.6 equiv.) was added at rt and was stirred overnight. The next day, the precipitate was filtered over a plug of Celite® and washed with cold diethyl ether until the filtrate became colourless. Then, the solvent has been changed to MeCN, and the desired product was eluted. After removing the volatiles at the rotary evaporator, the imidazolium bromide **224** was obtained as a yellow solid (93.0 mg, 147 μ mol, 81%).

Mp. = >290 °C (slow decomposition)

¹H-NMR (400 MHz, 297 K, MeCN-*d*₃): δ = 8.91 (s, 1H); 7.57 – 7.50 (m, 11H); 7.49 – 7.46 (m, 8H); 7.40 (t, *J* = 1.86 Hz, 1H)^(a); 7.24 – 7.18 (m, 4H); 5.54 (t, *J* = 1.76 Hz, 1H); 5.48 (s, 1H); 3.87 (s, 3H) ppm.

^(a)Coupling partner underneath the multiplet 7.57 – 7.50 ppm.

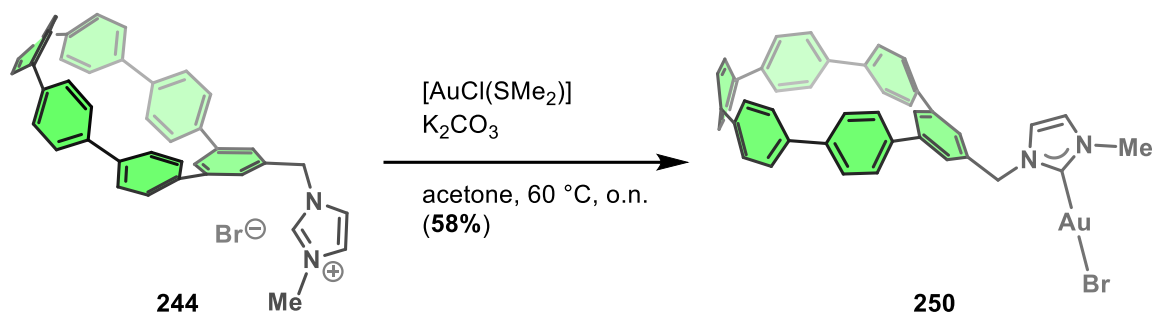
*Water (2.16 ppm) from NMR solvent.

$^{13}\text{C-NMR}$ (101 MHz, 298 K, DCM-d_2): δ = 144.46 (2C); 142.84 (2C); 140.35 (1C); 140.19 (2C); 138.71 (2C); 137.62 (2C); 137.50 (1C); 137.11 (2C); 136.72 (1C); 130.29 (4C); 129.26 (4C); 129.10 (4C); 128.81 (4C); 128.45 (4C); 125.08 (1C); 123.47 (2C); 123.36 (1C); 53.73 (1C); 37.05 (1C) ppm.

IR (ATR): $\tilde{\nu}$ = 3012 (m); 1890 (w); 1570 (s); 1481 (m) cm^{-1} .

HRMS (ESI) m/z for $\text{C}_{41}\text{H}_{31}\text{BrN}_2$ [$M\text{-Br}$] $^+$ calculated 551.2482; found 551.2498.

5.2.26. **[*N*-(Methyl)-*N'*-(1-methylene-*meta*[6]cycloparaphenylene)-imidazolium]gold bromide **250****



To a solution of imidazolium bromide **244** (20.0 mg, $31.7\text{ }\mu\text{mol}$, 1.00 equiv.) in acetone (2 mL) was added grinded K_2CO_3 (13.1 mg, $95.1\text{ }\mu\text{mol}$, 3.0 equiv.) and $[\text{Au}(\text{SMe}_2)]$ (9.63 mg, $31.7\text{ }\mu\text{mol}$, 1.0 equiv.). The solution was stirred at $60\text{ }^\circ\text{C}$ overnight. After cooling to rt, the solvent was evaporated, and the resulting solid was suspended in diethyl ether before filtered over a Celite[®] plug. After washing with excess cold diethyl ether, the yellow solid was eluted using DCM. After evaporation of the volatiles, the product was further purified by flash column chromatography (SiO_2 , Cy/DCM = 1:3) to obtain complex **250** as a yellow solid (15.2 mg, $18.3\text{ }\mu\text{mol}$, 58%).

Mp. = $>290\text{ }^\circ\text{C}$ (slow decomposition)

$^1\text{H-NMR}$ (400 MHz, 297 K, CDCl_3): δ = 7.44 – 7.38 (m, 16H); 7.34 (d, J = 1.76 Hz, 2H); 7.14 – 7.11 (m, 4H); 6.95 (d, J = 7.77 Hz, 1H)^(a); 6.95 (d, J = 7.77 Hz, 2H)^(a); 5.58 (t, J = 1.76 Hz, 1H); 5.48 (s, 2H); 3.88 (s, 3H) ppm.

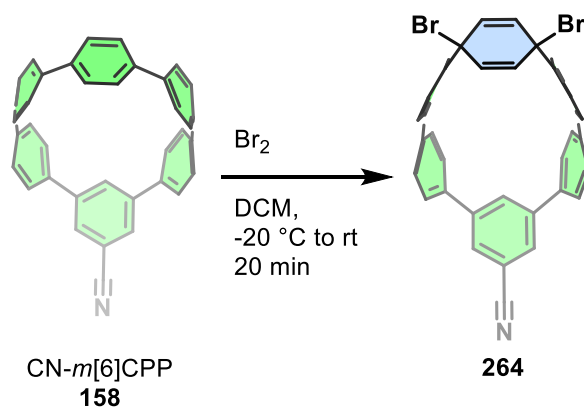
(a) Overlapping dublets caused by the imidazolium backbone.

^{13}C -NMR (101 MHz, 297 K, CDCl_3): δ = 175.55 (1C); 143.66 (2C); 141.74 (2C); 140.06 (1C); 139.57 (2C); 137.68 (2C); 136.55 (2C); 136.32 (2C); 136.29 (1C); 129.57 (4C); 128.22 (4C); 128.00 (4C); 127.74 (4C); 127.41 (4C); 122.41 (1C); 121.86 (2C); 120.52 (1C); 55.31 (1C); 38.41 (1C) ppm.

IR (ATR): $\tilde{\nu}$ = 3013 (m); 1885 (w); 1568 (s); 1482 (m) cm^{-1} .

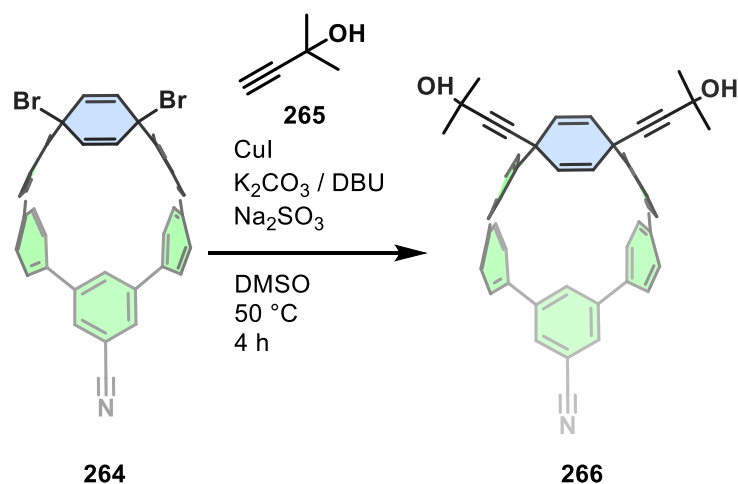
HRMS (APCI) m/z for $\text{C}_{41}\text{H}_{31}\text{AuBrN}_2$ [M] $^+$ calculated 827.1336; found 827.1334.

5.2.27. Bromination of cyano-*meta*[6]cycloparaphenylene **158**



According to a literature procedure,²⁹¹ cyano-*m*[6]cycloparaphenylene **158** (16.9 mg, 35.0 μmol , 1.00 equiv.) was dissolved in DCM (10.0 mL) and cooled to -20 $^\circ\text{C}$. A solution of Br_2 (120 μL , 38.5 μmol , 1.10 equiv.) in DCM (0.8 mL) was prepared in a separate vial. The bromine solution was added dropwise to the CPP solution, and the reaction mixture was stirred at -20 $^\circ\text{C}$ for 20 min. The contents of the flask were passed through a PTFE syringe filter and the volatiles were removed under reduced pressure to obtain a yellow solid, which was used as is for the next reaction.

^1H -NMR (200 MHz, 296 K, CDCl_3): δ = 7.68 (d, J = 1.78 Hz, 2H); 7.36 – 7.28 (m, 8H); 7.19 – 7.13 (m, 4H); 7.05 – 6.99 (m, 4H); 6.32 (s, 4H); 4.88 (t, J = 1.78 Hz, 1H) ppm.

5.2.28. Alkynylation of the allyl-bromides 264

In order to a literature procedure,²⁹⁰ the crude product of the aforementioned bromination reaction was dissolved in DMSO (1.0 mL). To this solution, 2-methyl-3-butyn-2-ol (**X**, 10.0 μ L, 102 μ mol, 2.92 equiv.), Na₂SO₃ (5.62 mg, 35.0 μ mol, 1.00 equiv.), CuI (0.29 mg, 1.5 μ mol, 4.3 mol%); K₂CO₃ (9.67 mg, 70.0 μ mol, 2.00 equiv.) and DBU (1 drop) were added. The reaction mixture was stirred at 40 °C for 4 h. After acidic work-up and extraction with DCM (3x4 mL), the crude product was obtained.

¹H-NMR (400 MHz, 297 K, CDCl₃): δ = 7.75 (d, J = 1.88 Hz, 2H); 7.43 – 7.35 (m, 8H); 7.24 – 7.17 (m, 4H); 7.12 – 7.06 (m, 4H); 6.15 (s, 4H); 4.93 (t, J = 1.88 Hz, 1H), 2.55 (s, 18H) ppm.

*further attempts of purification of this compound only led to decomposition

6. Zusätzliche Veröffentlichungen

Neben den oben aufgeführten Veröffentlichungen als Erstautor, wurden zusätzliche Arbeiten in Zusammenarbeit mit weiteren Autoren veröffentlicht.

Jannis Volkmann, Daniel Kohrs, Felix Bernt, Hermann A. Wegner

„Synthesis of a Substituted [10]Cycloparaphenylene through [2+2+2] Cycloaddition”

Eur. J. Org. Chem. **2022**, e202101357.

Jannis Volkmann, Daniel Kohrs, Felix Bernt, Hermann A. Wegner

„Front Cover: Synthesis of a Substituted [10]Cycloparaphenylene through [2+2+2] Cycloaddition” – Cover Design von Felix Bernt

Eur. J. Org. Chem. **2022**, e202200044.

Anne Kunz, Nils Oberhof, Frederik Scherz, Leon Martins, Prof. Dr. Andreas Dreuw, Hermann A. Wegner

„Cover Feature: Azobenzene-Substituted Triptycenes: Understanding the Exciton Coupling of Molecular Switches in Close Proximity” – Cover Design von Felix Bernt

Chem. Eur. J. **2022**, 28, e202201762.



7. Danksagung

Zuallererst möchte ich meinem Doktorvater Herrn Prof. Dr. Hermann A. Wegner für die Möglichkeit danken meine Dissertation in seiner Arbeitsgruppe während der letzten Jahre anzufertigen. Seine wissenschaftliche Leitung und das in mich gesetzte Vertrauen wurden während der gesamten Zeit in seiner Arbeitsgruppe von tiefgründigen fachlichen Diskussionen begleitet. Auch wenn die Projekte nicht immer nach meinen Vorstellungen verlaufen sind, verstand Prof. Dr. Hermann Wegner stets die richtigen Worte zu finden, mich zu motivieren und zu neuen Ideen zu inspirieren. Zusätzlich möchte ich Prof. Dr. R. Göttlich für das Anfertigen eines Zweitgutachtens meiner Arbeit danken.

Weiterhin gilt mein aufrichtiger Dank allen Mitarbeitenden aus weiteren Arbeitsgruppen, die einen Teil dazu beigetragen haben, dass meine Arbeit nun in dieser Form vorliegen kann. Hier seien zunächst Lisa Marie Wagner und Dr. Christian Würtele zu nennen, welche durch ihre fachlichen Kompetenzen es ermöglicht haben, dass ich vier verschiedene Festkörperstrukturen von meinen Kernverbindungen erhalten konnte. Weiterhin danke ich Dr. L. Patalak von der Arbeitsgruppe Prof. Dr. D. Werz, der die absoluten Quantenausbeuten von drei meiner Verbindungen bestimmen konnte. Außerdem danke ich F. Sprang aus der Arbeitsgruppe von Prof. Dr. Waldvogel für die Einführung in die Thematik der Elektro(photo-)katalyse und ihrer Betreuung während meines kurzen Forschungsaufenthalts in Mainz.

Weiterhin bedanke ich mich bei allen Angehörigen des organisch chemischen Instituts der Justus-Liebig-Universität Gießen, die sowohl mit ihrer technischen als auch administrativen Hilfe mir zur Seite standen. Hier seien auch die beiden Teams aus der Chemikalienausgabe und der Glasbläserei genannt. Zusätzlich bedanke ich mich auch bei Dr. K. Maaß, der die Organisation und Durchführung des Nebenfachpraktikums für alle Seiten so angenehm wie möglich gestaltet hat. An dieser Stelle möchte ich mich auch bei Johannes C. Voigt und Pia A. Mader für ihre tatkräftige Unterstützung im Labor und das Anfertigen ihrer jeweiligen Abschlussarbeit unter meiner Leitung bedanken. Es hat mich sehr gefreut, dass ihr euer Vertrauen in mich als Betreuer gesetzt und den jeweiligen Abschluss erfolgreich bestanden habt.

Für die finanzielle Unterstützung während der Promotion möchte ich mich nicht nur bei TCI und den Europäischen und Hessischen Regierungen bedanken, sondern auch bei der GDCh, die mir für das WiFo 2023 ein Reisestipendium ausgestellt hat. Zusätzlich gilt mein Dank über die finanzielle Unterstützung während des Beilstein Symposiums 2023 in Limburg und die Möglichkeit der zusätzlichen Weiterbildung in den Bereichen Projektmanagement und GMP dem Gießener Graduiertenzentrum für Naturwissenschaften und Psychologie.

Ein besonderer Dank geht an die gesamte Arbeitsgruppe Wegner. Hier möchte ich vor allem Jan H. Griwatz, Daniel Kohrs und Jannis Volkmann erwähnen. Sie haben mich sehr offen und freundlich in der *Molecular Nanocarbon* Gruppe willkommen geheißen und mir mit ihren Erfahrungen einen sehr angenehmen Einstieg in die Thematik der Cycloparaphenylene ermöglicht. Ich habe die Atmosphäre und wissenschaftlichen Diskussionen in unserem Labor immer sehr genossen und hatte eine sehr gute Zeit mit euch. Auch möchte ich Nathaniel Ukah für seine anregenden Diskussionen während der Bearbeitung meines NHC-Projektes danken. Weiterhin möchte ich mich bei Dominic Schatz bedanken, der mich nicht nur auf die Position als Wissenschaftlicher Mitarbeiter in dieser Arbeitsgruppe hingewiesen hat, sondern auch immer hilfreiche Beiträge zu meinen wissenschaftlichen Problemstellungen gegeben hat. Zudem war Dominic ein Teil der DnD Spielgruppe, die ich während meiner Zeit in dieser Arbeitsgruppe leiten durfte. Hier möchte ich auch den weiteren Teilnehmern der Gruppe danken, die es gewagt haben, ein Abenteuer zu bestreiten und gemeinsam abends bei Würfeln und Essen die Zeit miteinander zu verbringen. Daher geht ein großer Dank auch an Daniel Kohrs, Julia Ruhl, Dominic Schatz, Michel Große, Christopher M. Leonhardt, Finn Schneider, Kai Hanke und Anne Kunz. „Aushilfskraft“ Conrad Averdunk gilt ebenfalls ein Dankeschön, da er es geschafft hat an einigen Tagen, Spieler ehrwürdig zu vertreten. Es hat mir immer sehr viel Spaß gemacht euch dabei zu beobachten, wie ihr knifflige Situationen im Abenteuer gemeinsam zu lösen versucht habt.

Ein sehr großes Dankeschön möchte ich meiner Familie und meinen Freunden außerhalb des universitären Lebens danken. Ich konnte mich immer auf euch verlassen und dem Stress während der gesamten Studienzeit auch mal

beiseitelassen. Ohne diesen Ausgleich hätte ich diesen gesamten Lebensabschnitt nicht geschafft und bin daher einfach nur unglaublich dankbar.

Abschließend bleiben die Worte von uneingeschränkter Dankbarkeit und Wertschätzung für meine Partnerin Lisa. Du hast es immer verstanden mir die richtigen Worte entgegenzubringen. Deine gute Laune und Energie geben mir auch in den schwierigsten Zeiten genug Kraft, um meinen Weg weiterzugehen und an mich zu glauben. Von daher ein riesiges Dankeschön zum Abschluss auch an dich!

8. Abbreviations

$\%V_{\text{bur}}$	buried volume / %
[<i>n</i>]CPPs	[<i>n</i>]cycloparaphenylenes
[<i>n</i>]OPPs	[<i>n</i>]oligo-paraphenylenes
Ar	aryl
BODIPY	4,4-difluoro-4-bora-3a,4a-diaza-s-indazene
Bpin	pinacol boranyl
Bu	butyl
BuLi	butyl lithium
<i>c</i>	concentration / mol·L ⁻¹
C[<i>n</i>]A	calix[<i>n</i>]arenes
CNTs	carbon nanotubes
COD	1,5-cyclooctadiene
CPL	circularly polarized luminescence
Cy	Cyclohexane
dba	dibenzylidene acetone
DCC	<i>N,N'</i> -dicyclohexylcarbodiimide
DCM	dichloromethane
DDQ	2,3-dichloro-5,6-dicyano-1,4-benzoquinone
DFT	density functional theory
DIEPA	diisopropylamine
DMF	dimethyl formamide
DMS	dimethyl sulfide
dtbpy	4,4'-di- <i>tert</i> -butyl-2,2'-dipyridyl
EDC	1-ethyl-3-(3-dimethylaminopropyl)carbodiimide
EPR	electron paramagnetic resonance
equiv.	Equivalents
Fc / Fc ⁺	ferrocene / ferrocenium redox pair
FRET	FÖRSTER resonance energy transfer
Hex	hexyl
HOBT	1-hydroxybenzotriazol
HOMO	highest occupied molecular orbital
HPLC	high-pressure liquid chromatography

IC	internal conversion
ISC	intersystem crossing
K_a	association constant / M^{-1}
LUMO	lowest unoccupied molecular orbital
$m[n]$ CPPs	<i>meta</i> [n]cycloparaphenylenes
Me ₄ phen	3,4,7,8-tetramethyl-1,10-phenanthroline
NHC	<i>N</i> -heterocyclic carbene
NMM	<i>N</i> -methylmorpholine
NMR	nuclear magnetic resonance
o.n.	overnight
OLED	organic light-emitting diode
$P[n]$ A	pillar[n]arenes
Pent	pentyl
PG	protecting group
PhMe	Toluene
PIDA	phenyliodo diacetate
<i>p</i> TSA	<i>para</i> -toluene sulphonic acid
RET	resonance energy transfer
rISC	reverse intersystem crossing
ROMP	ring-opening polymerization
S_0	electronic ground state of a chromophore
$S_1, S_2, S_3 \dots S_n$	higher electronic states of a chromophore
T_1	first triplet excited state
TADF	thermally activated delayed fluorescence
TBAF	tetra-butylammonium fluoride
TBS	<i>tert</i> Butyl dimethyl silyl group
TD-DFT	time-dependent density functional theory
TES	triethyl silyl group
TFA	trifluoro acetic acid
TMS	trimethyl silyl group
ν	combined flow-rate / $mL \cdot min^{-1}$
$\epsilon_{abs,max}$	molar extinction coefficient at absorbance maximum / $M \cdot cm^{-1}$
$\lambda_{abs,max}$	absorbance maximum / nm

λ_{em}	emission wavelength / nm
τ	residence time / min
ϕ_F	fluorescence quantum yield

9. List of Figures

Figure 1. Chemical structure of quinine 6	1
Figure 2. JABLONSKY diagram of the various comprehend mechanisms at play when a fluorescent molecule assimilates light (left). Absorption (blue arrows), fluorescence (green arrows), phosphorescence (red), internal conversion (dashed orange arrows), vibrational relaxation (dashed black arrows), (reverse) intersystem crossing (yellow arrows), quenching (purple arrow). Illustrative energy diagram of the FRANCK-CONDON principle (right).	2
Figure 3. Corresponding emission color dependent on the energy gap between the excited state (S_1) and ground state (S_0).	3
Figure 4. Schematic representation of the FÖRSTER and DEXTER energy transfer mechanisms upon photoexcitation of an electronic ground state donor.	4
Figure 5. Core frameworks of the four organic dye classes that are most frequently utilized. (oxazole: deep red, fluorescein 8 and rhodamine 9 ; cyanine 10 : blue; BODIPY 11 : green; oxazines: red, Nile red 12 and ATTO 655 13	5
Figure 6. Structure of a graphene sheet and corresponding armchair 14 and zigzag 15 carbon nanotubes. .	6
Figure 7. Schematic representation of the electron-poor (blue) and -rich (red) surfaces of [6]CPP 16	7
Figure 8. Different strategies by the group of VÖGTLE towards the synthesis of [n]cycloparaphenylenes	8
Figure 9. Schematic representation of the different synthetic strategies towards [n]CPPs reported by the groups of JASTI, ITAMI, YAMAGO, and OSAKADA.	10
Figure 10. Modular synthesis approach towards different sized [n]CPPs for $n = 5 - 12$ based on the three building blocks.	11
Figure 11. Schematic representation of the HOMO and LUMO energies of oligo-paraphenylenes (orange) and cycloparaphenylenes (blue) using the theoretically calculated values of YAMAGO's group at the B3LYP/6-31G* level of theory. ⁶⁵	12
Figure 12. Schematic representation of the size-dependent emission represented by the color of the maximum wavelength of [n]CPPs ($n = 5 - 12$).	13
Figure 13. General representation of the top-down and bottom-up approaches towards functionalized [n]CPPs.	14
Figure 14. Design concept of donor- / acceptor-incorporated CPPs (adjusted from literature ⁹²).	17
Figure 15. Schematic representation of the metallofullerene-[12]CPP complex 53 . Double bonds of fullerene C_{80} have been omitted for clarity.	19
Figure 16. Examples of [n]CPP-containing polymers within the main-chain and the side-chain.	20
Figure 17. Representative scheme of the synthesis of substituted [n]CPPs 62 - 65 through [2+2+2] cyclotrimerization.	23
Figure 18. Design of the molecular squid 67	24
Figure 19. Design principle of [n]CPP-P[5]As 71 and 72	25
Figure 20. Structures realized through the active template synthesis approach: catenane 73 , trefoil knot 74 , and all-benzene catenane 75 . Additionally, JASTI's modified active template approach towards interlocked molecules is shown using the substituted alkyne and the macrocyclic precursor structure.	27
Figure 21. Turn-on of the fluorescence in smaller CPP derivatives through the incorporation of a meta-linkage.	33
Figure 22. Chemical structure of [c2]daisy chain rotaxane 108 based on pyridinyl-m[6]CPP 104	35
Figure 23. Chemical structure of polyyne[3]rotaxane 109 based on pyridinyl-m[6]CPP 104	36
Figure 24. Molecular orbital diagram of a FISHER-type N-heterocyclic carbene.	39
Figure 25. BERTRAND's carbene 116 stabilized through P- and Si substituents (left). ARDUENGO's carbene 117 stabilized through the nitrogen heterocycle (right).	40
Figure 26. Relative energies of the normally degenerated p-orbitals and possible ground state electron configuration of carbenes.	40
Figure 27. Applicational fields of NHC gold-complexes.	41
Figure 28. 1,10-Phenanthroline mimicking NHC 119 and 10-hydroxybenzo[h]quinolone mimicking NHC 120	42

Figure 29. Tetra-naphthalimide substituted NHC coinage-metal complexes 131 - 134	43
Figure 30. BODIPY NHC-transition-metal complexes 135 with Ru, Rh, Ir, Pd, and Au.	44
Figure 31. Modified structure of BODIPY NHC-transition-metal complexes tested as photosensitizers for the generation of ^1O	45
Figure 32. Coumarin NHC-transition-metal complexes 137 and 138 , which can be used as CO sensor.	45
Figure 33. Fluorophore-NHC-Au complexes 142 and 143 for cytotoxicity studies.	47
Figure 34. Bicyclo[2.2.2]octa-2,5,7-triene (144) and its arrangement of p-orbitals.	48
Figure 35. Project aim for the investigation of m[n]CPPs 158 - 160	52
Figure 36. Meta[6]CPP 158 serving as platform for different transition-metal ligands.	53
Figure 37. General research purpose of this work.	53
Figure 38. Comparison of the $^1\text{H-NMR}$ spectra in CDCl_3 at room temperature of building block 165 with the obtained spectrum of 173	59
Figure 39. Working hypothesis of the top-down functionalization of [10]CPP 155	65
Figure 40. Exemplified evaluation of the screening reactions using different acidic conditions at room temperature. Comparison of $^1\text{H-NMR}$ spectra and columnar diagram. For comparison, highlighted proton was used for the determination of the different ratios between 209 - 211	75
Figure 41. Columnar diagrams obtained after comparison of the different $^1\text{H-NMR}$ spectra obtained after treating 192 under acidic conditions.	75
Figure 42. Comparison of the $^1\text{H-NMR}$ spectra derived from the reaction screening towards macrocycle 226 under homogeneous catalyzed SUZUKI-MIYAUURA cross-coupling reaction conditions using continuous-flow chemistry. $^1\text{H-NMR}$ spectrum of building block 225 (black, bottom) and macrocycle 226 (purple, top) are shown for reference. $^1\text{H-NMR}$ spectra of the entries 1 (bottom, brown, Table 1) – 8 (top, blue, Table 1) are shown in the middle of this Figure (red box).	84
Figure 43. Heterogeneous catalysts applied within the continuous-flow synthesis of macrocycle 199a	85
Figure 44. Comparison of the $^1\text{H-NMR}$ spectra derived from the reaction screening towards the macrocycle 199a under heterogeneous catalyzed SUZUKI-MIYAUURA cross-coupling reaction conditions using continuous-flow chemistry. $^1\text{H-NMR}$ spectrum of building block 225 (black, bottom) and macrocycle 226 (purple, top) are shown for reference. $^1\text{H-NMR}$ spectra of the entries 1 (bottom, brown, Table 2) – 6 (top, dark-green, Table 2) are shown in the middle of this Figure (red box).	86
Figure 45. ORTEP drawings of CN-m[6]CPP 158 (top, left) at 50% probability, and its corresponding crystal packing from two different angles (top, right). ORTEP drawing of CN-m[10]CPP 160 (bottom, right) at 50% probability, and its corresponding crystal packing from two different angles (bottom, left). Structural parameters are shown for the two ORTEP drawings. Solvent molecules have been omitted in all cases, whereas for the crystal packing structures the protons have been omitted as well.	91
Figure 46. Absorbance (left, blank area underneath the lines, $c = 3 \cdot 10^{-5} \text{ M}$) and emission (right, filled area underneath the lines, $c = 3 \cdot 10^{-6} \text{ M}$) spectra of CN-m[n]CPPs 158 - 160 measured at room temperature in chloroform.	93
Figure 47. $^1\text{H-NMR}$ spectrum in deuterated tetrachloroethane- d_2 of a 1:1 mixture of CN-m[10]CPP 160 at room temperature before (top) and after (bottom) the addition of fullerene C_{60}	95
Figure 48. Results of fluorescence quenching experiments.	96
Figure 49. Stacked UV-vis- (left, no colored areas underneath the curves) and emission (right, colored areas underneath the curves) spectra of the different substituted m[6]CPPs 165, 210 – 215 . Measured in DMSO ($c = 10^{-5} \text{ M}$) at room temperature.	98
Figure 50. Solubility assessment of carboxy-m[6]CPP 234 . Absorbance (left) and fluorescence (right) over increasing concentrations of 234 at two different pH levels.	99
Figure 51. ORTEP drawing of imidazolium bromide 244 (top, left) at 50% probability, and its corresponding crystal packing from two different angles (top, right). ORTEP drawing of the gold(I)-complex 250 (bottom, left) at 50% probability, and its corresponding crystal packing from two different angles (bottom, right). Structural parameters are shown for the two ORTEP drawings. Solvent molecules have been omitted in all cases, whereas for the crystal packing structures the protons have been omitted as well.	106
Figure 52. Crystal-packing of the Au(I)-complex 250 from different perspectives. Disordered solvent molecules are highlighted in blue (1,2-dichloroethane) and dark blue (1,2-dichlorobenzene).	107

Figure 53. Comparison between the experimentally measured UV-vis-spectrum (red) and the theoretically calculated spectrum (blue) at the PBE0/ZORA-def2-TZVPP level of theory. Within these spectra, the ground state optimized geometry of the gold(I)-complex **250** is shown (left). Visualization of the three main transitions resulting in the observed UV-vis spectrum (right)..... 109

Figure 54. Absorption (left, colorless area underneath the curves) and emission (right, colored areas underneath the curves) spectra of CN-m[6]CPP **156**, imidazolium bromide **244** and gold(I)-complex **250**. 110

Figure 55. Steric maps gold(I)-complex **250** using the theoretically calculated structure at the PBE0/ZORA-def2-TZVPP level of theory (left) and the solid-state structure (right). 111

10. List of Schemes

<i>Scheme 1.</i> Chemical structure of mauveine A 1 and B 2 , which consist of o-toluidine 3 , aniline (4) and p-toluidine 5	1
<i>Scheme 2.</i> Schematic representation of the idea of a bottom-up synthesis of CNTs from a small molecule template (adapted from literature ⁴⁰).	6
<i>Scheme 3.</i> Synthetic attempt towards [2]CPP by PAREKH and GUHA in 1934 through desulfurization. ⁴²	7
<i>Scheme 4.</i> Synthesis approach of BERTOZZI's group in 2008 towards the first reported [n]CPPs (n = 9, 12, 18).	9
<i>Scheme 5.</i> Top-down functionalization of [9]CPP 31 and [12]CPP 32 by metal complexation.	15
<i>Scheme 6.</i> Top-down functionalization of [5]CPP 42 through bromination. Depending on the conditions, different substitutions could be achieved.	16
<i>Scheme 7.</i> Synthesis of benzothiadiazole [10]CPP (BT[10]CPP) 50 and tetra-benzothiadiazole [12]CPP (TB[12]CPP) 52 following different approaches.....	18
<i>Scheme 8.</i> Synthesis of poly(nb[n]CPP)s poly-59 - poly-61 using ring-opening metathesis polymerization (ROMP).	21
<i>Scheme 9.</i> Synthesis towards car-[n]CPPs 78 (n = 9) and 79 (n = 11). Boron atoms within the boron cluster have been omitted for clarity and are shown as blue cage structure.	28
<i>Scheme 10.</i> Representative synthesis scheme of Ru ₂ (40-COO) 81	29
<i>Scheme 11.</i> General representation of the [n]CPP synthesis using two different protected cyclohexadiene scaffolds.	30
<i>Scheme 12.</i> Proposed mechanism for the 1,2-aryl shift on a protected cyclohexadiene scaffold.	31
<i>Scheme 13.</i> 1,2-aryl shift on phenyl-substituted [8]CPP 82	31
<i>Scheme 14.</i> Application of the 1,2-aryl shift in the synthesis of natural products (A), carbo- and heterocycles (B) and functionalization of pillar[5]arenes (C).....	32
<i>Scheme 15.</i> Schematic representation of the synthesis towards different sized m[n]CPPs 94 , 99 - 103 and the corresponding key building blocks.....	34
<i>Scheme 16.</i> Schematic representation of the rotaxane synthesis based on pyridinyl-m[n]CPPs 104 – 105 . .	34
<i>Scheme 17.</i> Schematic representation of the synthesis of the all-benzene catenane 112 , deriving from the tetra-substituted azobenzene 110	36
<i>Scheme 18.</i> Synthesis of lysosome targeted m[6]CPP 114 derived from alkynyl-m[6]CPP 112 under azide-alkyne click-reaction conditions.....	37
<i>Scheme 19.</i> Schematic representation of the synthesis towards monomer 116 derived from alkynyl-m[6]CPP 113	38
<i>Scheme 20.</i> Synthesis of acridine-NHC-Au complexes 126 - 128 for the investigation of their luminescent properties depending on the alkyl-chain lengths on the second wingtip.	43
<i>Scheme 21.</i> Synthesis of anthracene-NHC-transition-metal complexes 138 and 139 with cytotoxic properties.	46
<i>Scheme 22.</i> Singlet- and triplet-mediated photo transformations of barrelene 144 towards cyclooctatetraene (145) and semibullvalene (146).....	48
<i>Scheme 23.</i> Co-polymerization of barrelene 144 and norbornene 147 for direct laser writing.....	49
<i>Scheme 24.</i> Synthesis of substituted 157 through Rh-catalyzed [2+2+2] cyclootrimerization.	49
<i>Scheme 25.</i> Rh-catalyzed cyclootrimerization towards barrelene 152	50
<i>Scheme 26.</i> Synthesis of [10]CPP 155 and its top-down functionalization through C-H activation.....	51
<i>Scheme 27.</i> Investigation of a 1,2-aryl shift on the macrocyclic precursor 157	52
<i>Scheme 28.</i> Retrosynthetic analysis of the C-H functionalization and the synthesis of [10]CPP 155 starting from biphenyl 154	55
<i>Scheme 29.</i> Synthesis of building block 172 through the combination of the silylated building blocks 169 and 170	57
<i>Scheme 30.</i> Synthesis attempt towards building block 166 after cleavage of the silyl-ether group on 172 . .	58
<i>Scheme 31.</i> Modified retrosynthetic strategy towards building blocks 165 and 174	60
<i>Scheme 32.</i> Synthesis of building block 174 starting from 4-hydroxy anisole (176).	61

Scheme 33. Synthesis attempt towards macrocyclic precursor 163 through SUZUKI-MIYAUURA cross-coupling reaction.....	62
Scheme 34. Modified synthesis route towards building blocks 165a and 166 as starting materials for the macrocyclization.	63
Scheme 35. Concluding the synthesis of [10]CPP 155 through macrocyclization and aromatization.	64
Scheme 36. Attempts towards oxidative halogenation through DMSO-catalyzed C-H activation.	66
Scheme 37. Halogenation of arenes through low-valent aluminum and calcium catalysis using catalyst 175	67
Scheme 38. Synthesis attempt towards the Ca- (198) and Al- (190) catalysts.	67
Scheme 39. Towards top-down borylation of [10]CPP 162 through Ir-catalyzed C-H activation.....	68
Scheme 40. Attempts towards acyloxylation (204) and olefination (205) of [10]CPP 155	69
Scheme 41. Towards trifluoro acetoxylation (206) and hydroxylation (207) of [10]CPP 155 utilizing electro(photo)-catalysis.	70
Scheme 42. Project motivation for the investigation of the 1,2-aryl shift as a synthetic tool towards novel macrocyclic structures.	71
Scheme 43. Schematic retrosynthetic analysis of molecular bowl 208	72
Scheme 44. Synthetic strategy for the consecutive study of the 1,2-aryl shift towards meta-terphenyls 209 - 214	72
Scheme 45. Synthesis of building blocks 192b and 193b as precursors for the investigation of the 1,2-aryl shift.	73
Scheme 46. First observations towards the selectivity of the 1,2-aryl shift during the deprotection of building block 193b . ¹ H-NMR spectra in DCM-d ₂ at room temperature of the crude mixture (green) and after the purification attempt (red) are shown.	74
Scheme 47. Initial reaction conditions towards the investigation of the 1,2-aryl shift.....	74
Scheme 48. Synthesis of building block 219 , starting from 4-hydroxy anisole (176).	76
Scheme 49. Macrocyclization reaction towards the precursor 164b through SUZUKI-MIYAUURA cross-coupling reaction.....	77
Scheme 50. Result of the treatment of the macrocyclic precursor 220 with BCl ₃ . NMR-spectra which were used for structure determination are shown underneath the reaction scheme.	78
Scheme 51. Short retrosynthetic analysis of CN-m[n]CPPs 165 - 167	79
Scheme 52. Synthesis of benzonitrile 196b through MIYAUURA borylation.....	79
Scheme 53. Synthesis of macrocyclic precursor 199a utilizing TES-protecting groups throughout the synthesis.	80
Scheme 54. Synthesis of cyano-meta[6]CPP 165 using tin chloric acid for reductive aromatization.....	81
Scheme 55. Homogeneous (top) and heterogeneous (bottom) catalyzed SUZUKI-MIYAUURA cross-coupling reaction for macrocyclization using continuous flow-chemistry. Pump A/B : peristaltic pumps. R1 : coiled tube-reactor. R2 : backed-bed flow reactor. BPR : back-pressure regulator.	82
Scheme 56. Synthesis of CN-m[6]CPP 158 utilizing methyl-ether as protective groups throughout the synthesis.	87
Scheme 57. Synthesis of building block 227 and its borylation through lithium halogen exchange towards 27	88
Scheme 58. Synthesis of the [n-1]pre-bent open-chain precursors 228 and 229 . A) synthesis of 228 through regioselective addition of 158 to 227 . B) synthesis of 229 through SUZUKI-MIYAUURA cross-coupling reaction of 27 and 227	89
Scheme 59. Macrocyclization reactions under SUZUKI-MIYAUURA cross-coupling conditions towards the macrocyclic precursors 230 and 231	89
Scheme 60. Reductive aromatization of the macrocyclic precursors 230 and 231 using tin chloric acid towards the CN-m[n]CPPs 159 (n = 8) and 166 (n = 10).	90
Scheme 61. Functional group conversion of the cyano-functionality attached to the CN-m[6]CPP 158 . For clarity, the m[6]CPP motif is abbreviated as mCPP-labelled green hexagon. For details on the unsuccessful attempts 239 - 242 please refer to the experimental part.	97

Scheme 62. Retrosynthetic analysis of the synthesis of imidazolinium chloride 243 and imidazolium bromide 244 commencing from CN-m[6]CPP 158 . For clarity, m[6]CPP has been abbreviated as mCPP-labelled green hexagon.	100
Scheme 63. Synthesis of the corresponding model substrate 230 based on a meta-terphenyl.....	101
Scheme 64. Synthesis of diamine 260 starting from oxalyl chloride (254).	102
Scheme 65. Synthesis of imidazolinium 261 through cyclization using triethyl orthoformate.	102
Scheme 66. Synthesis of N-(mesityl)-N'-(1-methylene-m[6]CPP)oxalamide 246 . For clarity, m[6]CPP has been abbreviated as mCPP-labelled green hexagon.....	103
Scheme 67. Synthesis of imidazolium bromide 224 commencing from CN-m[6]CPP 158 . For clarity, m[6]CPP has been abbreviated as mCPP-labelled green hexagon for the intermediate steps.....	104
Scheme 68. Synthesis of [N-(Methyl)-N'-(1-methylene-m[6]CPP)-imidazolium]gold bromide 250	105
Scheme 69. Retrosynthetic strategy towards a barrelene-incorporated m[6]CPP 162 commencing from CN-m[6]CPP 158	112
Scheme 70. Synthetic approach towards acetone-protected di-alkyne 266 commencing from CN-m[6]CPP 158	113

11. List of Tables

Table 1. Screening parameters for the homogeneous catalyzed SUZUKI-MIYAUURA cross-coupling reaction towards macrocycle 226 using continuous flow-chemistry. Constant parameters have been the solvent (THF) and the concentration within the reactor R1 ($c = 3.6 \text{ mM}$). In all cases X-Phos was utilized as additional ligand. τ = residence time within reactor R1 , v = combined flowrate within reactor R1 . *Red: valve of pump A was defect and therefore flowrates are not accurate for these experiments.	83
Table 2. Screening parameters for the heterogeneous catalyzed SUZUKI-MIYAUURA cross-coupling reaction towards macrocycle 226 using continuous flow-chemistry. Constant parameters have been the solvent (THF / EtOH / H ₂ O) and the concentration within the reactor R1 ($c = 3.6 \text{ mM}$). Moreover, the same base was used for all entries (K ₂ CO ₃). τ = residence time within reactor R1 , v = combined flowrate within reactor R1	85
Table 3. Photophysical characteristics of CN-m[n]CPPs 158 – 160 measured in chloroform at room temperature. Absorbance maximum ($\lambda_{abs,max}$), molar extinction coefficient at absorbance maximum ($\epsilon_{abs,max}$), emission maxima ($\lambda_{em,max1}$, $\lambda_{em,max2}$), fluorescence quantum yield at first emission maximum (Φ_{max}), and calculated brightness ($\epsilon_{abs,max} \cdot \Phi_{max}$).	94
Table 4. Optimization screening for the optimization reaction towards oxalamide 246 . The reaction conditions were kept from the model substrate (solvent mixture: THF / DCM, $T = 0 \text{ }^\circ\text{C}$ to rt, o.n.,). HOBT – 1-hydroxybenzotriazol, DCC – N,N'-dicyclohexylcarbodiimide, EDC – 1-ethyl-3-(3-dimethylaminopropyl)carbodiimide, NMM – N-methylmorpholine, DIEPA – diisopropylethylamine.....	103

12. References

- 1 R. Brightman, *Nature*, 1956, **177**, 815–821.
- 2 M. R. Hartings, *Nat. Rev. Chem.*, 2021, **5**, 219.
- 3 J. F. W. Herschel, *Phil. Trans. R. Soc.*, 1845, **135**, 143–145.
- 4 G. G. Stokes, *Phil. Trans. R. Soc.*, 1852, **142**, 463–562.
- 5 J. R. Lakowicz, in *Principles of Fluorescence Spectroscopy*, ed. J. R. Lakowicz, Springer US, Boston, MA, 2006, pp. 27–61.
- 6 J. B. Grimm and L. D. Lavis, *Nat. Methods*, 2022, **19**, 149–158.
- 7 M. Kasha, *Discuss. Faraday Soc.*, 1950, **9**, 14.
- 8 T. J. Bruno, *CRC handbook of fundamental spectroscopic correlation charts*, CRC Press, Boca Raton, FL, 2006.
- 9 L. D. Lavis, *Biochem.*, 2017, **56**, 5165–5170.
- 10 Y. Tao, R. Chen, H. Li, C. Zheng and W. Huang, in *Highly efficient OLEDs*, ed. H. Yersin, Wiley-VCH, Weinheim, 1st edn., 2019, pp. 377–423.
- 11 D. L. Andrews, C. Curutchet and G. D. Scholes, *Laser Photonics Rev.*, 2011, **5**, 114–123.
- 12 E. A. Jares-Erijman and T. M. Jovin, *Nat. Biotechnol.*, 2003, **21**, 1387–1395.
- 13 T. Förster, *Annalen der Physik*, 1948, **437**, 55–75.
- 14 R. B. Sekar and A. Periasamy, *J. Cell Biol.*, 2003, **160**, 629–633.
- 15 J. A. Broussard, B. Rappaz, D. J. Webb and C. M. Brown, *Nat Protoc*, 2013, **8**, 265–281.
- 16 A. Köhler and H. Bässler, *J. Mater. Chem.*, 2011, **21**, 4003–4011.
- 17 D. L. Dexter, *J. Chem. Phys.*, 1953, **21**, 836–850.
- 18 D. Cavazos-Elizondo and A. Aguirre-Soto, *Anal. Sens.*, 2022, **2**, e202200004.
- 19 M. Zimmer, *Chem. Rev.*, 2002, **102**, 759–781.
- 20 U. Kubitschek, *Fluorescence microscopy. From principles to biological applications*, Wiley-VCH, Weinheim, 2017.
- 21 J. Wiedenmann, F. Oswald and G. U. Nienhaus, *IUBMB life*, 2009, **61**, 1029–1042.
- 22 S. M. Ng, M. Koneswaran and R. Narayanaswamy, *RSC Adv.*, 2016, **6**, 21624–21661.
- 23 U. Resch-Genger, M. Grabolle, S. Cavaliere-Jaricot, R. Nitschke and T. Nann, *Nat. Methods*, 2008, **5**, 763–775.
- 24 W. Li, G. S. Kaminski Schierle, B. Lei, Y. Liu and C. F. Kaminski, *Chem. Rev.*, 2022, **122**, 12495–12543.
- 25 B. Li, M. Zhao, J. Lin, P. Huang and X. Chen, *Chem. Soc. Rev.*, 2022, **51**, 7692–7714.
- 26 L. D. Lavis and R. T. Raines, *ACS Chem. Biol.*, 2008, **3**, 142–155.
- 27 M. Vendrell, D. Zhai, J. C. Er and Y.-T. Chang, *Chem. Rev.*, 2012, **112**, 4391–4420.
- 28 H. Li, D. Kim, Q. Yao, H. Ge, J. Chung, J. Fan, J. Wang, X. Peng and J. Yoon, *Angew. Chem.*, 2021, **133**, 17408–17429.
- 29 Q. Zheng and L. D. Lavis, *Curr. Opin. Chem. Biol.*, 2017, **39**, 32–38.
- 30 H.-H. Han, H. Tian, Y. Zang, A. C. Sedgwick, J. Li, J. L. Sessler, X.-P. He and T. D. James, *Chem. Soc. Rev.*, 2021, **50**, 9391–9429.
- 31 Z. Yao, H. W. C. Postma, L. Balents and C. Dekker, *Nature*, 1999, **402**, 273–276.
- 32 D. K. Patel, H.-B. Kim, S. D. Dutta, K. Ganguly and K.-T. Lim, *Materials (Basel, Switzerland)*, 2020, **13**. DOI: 10.3390/ma13071679.
- 33 H. Karimi-Maleh, R. Darabi, M. Baghayeri, F. Karimi, L. Fu, J. Rouhi, D. E. Niculina, E. S. Gündüz and E. N. Dragoi, *J. Food Meas. Charact.*, 2023, **17**, 5371–5389.
- 34 L. Rajeshkumar, M. Ramesh, V. Bhuvaneshwari and D. Balaji, *Carbon Lett.*, 2023, **33**, 661–690.

- 35 W. Yang, K. R. Ratinac, S. P. Ringer, P. Thordarson, J. J. Gooding and F. Braet, *Angew. Chem. Int. Ed.*, 2010, **49**, 2114–2138.
- 36 M. Zhong, M. Zhang and X. Li, *Carbon Energy*, 2022, **4**, 950–985.
- 37 A. Hirsch, *Angew. Chem.*, 2002, **41**, 1853.
- 38 M. U. Zahid, E. Pervaiz, A. Hussain, M. I. Shahzad and M. B. K. Niazi, *Mater. Res. Express*, 2018, **5**, 52002.
- 39 T. W. Ebbesen, *Annu. Rev. Mater. Sci.*, 1994, **24**, 235–264.
- 40 R. Jasti and C. R. Bertozzi, *Chem. Phys. Lett.*, 2010, **494**, 1–7.
- 41 U. H. F. Bunz, S. Menning and N. Martín, *Angew. Chem.*, 2012, **51**, 7094–7101.
- 42 V. C. Parekh and P. C. Guha, *J. Indian Chem. Soc.*, 1934, 95–100.
- 43 R. Friederich, M. Nieger and F. Vögtle, *Chem. Ber. (Chemische Berichte)*, 1993, **126**, 1723–1732.
- 44 Y. Miyahara, T. Inazu and T. Yoshino, *Tetrahedron Lett.*, 1983, **24**, 5277–5280.
- 45 L. A. Paquette, R. E. Moerck, B. Harirchian and P. D. Magnus, *J. Am. Chem. Soc.*, 1978, 1597–1599.
- 46 H. Omachi, Y. Segawa and K. Itami, *Acc. Chem. Res.*, 2012, **45**, 1378–1389.
- 47 S. E. Lewis, *Chem. Soc. Rev.*, 2015, **44**, 2221–2304.
- 48 Di Wu, W. Cheng, X. Ban and J. Xia, *Asian J. Org. Chem.*, 2018, **7**, 2161–2181.
- 49 M. Srinivasan, S. Sankararaman, H. Hopf and B. Varghese, *Eur. J. Org. Chem.*, 2003, **2003**, 660–665.
- 50 R. Jasti, J. Bhattacharjee, J. B. Neaton and C. R. Bertozzi, *J. Am. Chem. Soc.*, 2008, **130**, 17646–17647.
- 51 T. J. Sisto, M. R. Golder, E. S. Hirst and R. Jasti, *J. Am. Chem. Soc.*, 2011, **133**, 15800–15802.
- 52 T. J. Sisto, X. Tian and R. Jasti, *J. Org. Chem.*, 2012, **77**, 5857–5860.
- 53 J. Xia, J. W. Bacon and R. Jasti, *Chem. Sci.*, 2012, **3**, 3018.
- 54 J. Xia and R. Jasti, *Angew. Chem.*, 2012, **51**, 2474–2476.
- 55 J. Xia, M. R. Golder, M. E. Foster, B. M. Wong and R. Jasti, *J. Am. Chem. Soc.*, 2012, **134**, 19709–19715.
- 56 E. R. Darzi, T. J. Sisto and R. Jasti, *J. Org. Chem.*, 2012, **77**, 6624–6628.
- 57 P. J. Evans, E. R. Darzi and R. Jasti, *Nat. Chem.*, 2014, **6**, 404–408.
- 58 H. Omachi, S. Matsuura, Y. Segawa and K. Itami, *Angew. Chem.*, 2010, **49**, 10202–10205.
- 59 H. Takaba, H. Omachi, Y. Yamamoto, J. Bouffard and K. Itami, *Angew. Chem.*, 2009, **48**, 6112–6116.
- 60 S. Yamago, Y. Watanabe and T. Iwamoto, *Angew. Chem.*, 2010, **49**, 757–759.
- 61 E. Kayahara, T. Iwamoto, T. Suzuki and S. Yamago, *Chem. Lett.*, 2013, **42**, 621–623.
- 62 Y. Tsuchido, R. Abe, T. Ide and K. Osakada, *Angew. Chem.*, 2020, **59**, 22928–22932.
- 63 Y. Yoshigoe, Y. Tanji, Y. Hata, K. Osakada, S. Saito, E. Kayahara, S. Yamago, Y. Tsuchido and H. Kawai, *JACS Au*, 2022, **2**, 1857–1868.
- 64 R. B. Kręćjasz, J. Malinčík and T. Šolomek, *Synthesis*, 2023, **55**, 1355–1366.
- 65 T. Iwamoto, Y. Watanabe, Y. Sakamoto, T. Suzuki and S. Yamago, *J. Am. Chem. Soc.*, 2011, **133**, 8354–8361.
- 66 E. Kayahara, V. K. Patel and S. Yamago, *J. Am. Chem. Soc.*, 2014, **136**, 2284–2287.
- 67 Y. Ishii, Y. Nakanishi, H. Omachi, S. Matsuura, K. Matsui, H. Shinohara, Y. Segawa and K. Itami, *Chem. Sci.*, 2012, **3**, 2340.
- 68 E. Kayahara, Y. Sakamoto, T. Suzuki and S. Yamago, *Org. Lett.*, 2012, **14**, 3284–3287.
- 69 J. H. Griwatz and H. A. Wegner, *Organic Materials*, 2020, **02**, 306–312.
- 70 J. H. Griwatz, M. L. Kessler and H. A. Wegner, *Chem. Eur. J.*, 2023, e202302173.
- 71 H. Kim, H.-J. Lee and D.-P. Kim, *Angew. Chem.*, 2016, **55**, 1422–1426.

- 72 Y. Segawa, T. Kuwabara, K. Matsui, S. Kawai and K. Itami, *Tetrahedron*, 2015, **71**, 4500–4503.
- 73 V. K. Patel, E. Kayahara and S. Yamago, *Chem. Eur. J.*, 2015, **21**, 5742–5749.
- 74 E. R. Darzi, B. M. White, L. K. Loventhal, L. N. Zakharov and R. Jasti, *J. Am. Chem. Soc.*, 2017, **139**, 3106–3114.
- 75 E. Kayahara, V. Patel, J. Xia, R. Jasti and S. Yamago, *Synlett*, 2015, **26**, 1615–1619.
- 76 T. Kawanishi, K. Ishida, E. Kayahara and S. Yamago, *J. Org. Chem.*, 2020, **85**, 2082–2091.
- 77 R. Frydrych, T. Lis, W. Bury, J. Cybińska and M. Stępień, *J. Am. Chem. Soc.*, 2020, **142**, 15604–15613.
- 78 E. R. Darzi and R. Jasti, *Chem. Soc. Rev.*, 2015, **44**, 6401–6410.
- 79 Y. Segawa, A. Fukazawa, S. Matsuura, H. Omachi, S. Yamaguchi, S. Irle and K. Itami, *Org. Biomol. Chem.*, 2012, **10**, 5979–5984.
- 80 P. Li, T. J. Sisto, E. R. Darzi and R. Jasti, *Organic letters*, 2014, **16**, 182–185.
- 81 O. Laporte and W. F. Meggers, *J. Opt. Soc. Am.*, 1925, **11**, 459.
- 82 C. Camacho, T. A. Niehaus, K. Itami and S. Irle, *Chem. Sci.*, 2013, **4**, 187–195.
- 83 P. L. Burn, A. Kraft, D. Baigent, D. D. C. Bradley, A. R. Brown, R. H. Friend, R. W. Gymer, A. B. Holmes and R. W. Jackson, *J. Am. Chem. Soc.*, 1993, **115**, 10117–10124.
- 84 U. Scherf and K. Müllen, in *Photonic and optoelectronic polymers*, ed. S. A. Jenekhe and K. J. Wynne, American Chemical Soc, Washington, DC, 1997, pp. 358–380.
- 85 S. Dellsperger, F. Dötz, P. Smith and C. Weder, *Macromol. Chem. Phys.*, 2000, **201**, 192–198.
- 86 J. Morgado, F. Cacialli, R. H. Friend, R. Iqbal, G. Yahioğlu, L. R. Milgrom, S. C. Moratti and A. B. Holmes, *Chem. Phys. Lett.*, 2000, **325**, 552–558.
- 87 K. Horie, S. Kondo and K. Akagi, *J. Mater. Chem. C*, 2023, **11**, 943–952.
- 88 M. E. Kleybolte, S. I. Vagin and B. Rieger, *Macromol. Chem. Phys.*, 2023, **224**. DOI: 10.1002/macp.202200441.
- 89 N. Kubota, Y. Segawa and K. Itami, *J. Am. Chem. Soc.*, 2015, **137**, 1356–1361.
- 90 E. Kayahara, R. Qu and S. Yamago, *Angew. Chem.*, 2017, **129**, 10564–10568.
- 91 E. J. Leonhardt and R. Jasti, *Nat. Rev. Chem.*, 2019, **3**, 672–686.
- 92 M. Hermann, D. Wassy and B. Esser, *Angew. Chem. Int. Ed.*, 2021, **60**, 15743–15766.
- 93 T. C. Lovell, Z. R. Garrison and R. Jasti, *Angew. Chem.*, 2020, **132**, 14469–14473.
- 94 Z.-L. Qiu, C. Tang, X.-R. Wang, Y.-Y. Ju, K.-S. Chu, Z.-Y. Deng, H. Hou, Y.-M. Liu and Y.-Z. Tan, *Angew. Chem. Int. Ed.*, 2020, **59**, 20868–20872.
- 95 J. Zhang, Z. Qiu, C. Zhao, Y. Lu, W. Li, L. Liu, C. Wang, Y. Tan and T. Wang, *Nano Res.*, 2023, **16**, 3372–3378.
- 96 C. Graham, M. Moral, L. Muccioli, Y. Olivier, Á. J. Pérez-Jiménez and J.-C. Sancho-García, *Int. J. Quantum Chem.*, 2018, **118**. DOI: 10.1002/qua.25562.
- 97 D. Chen, Y. Wada, Y. Kusakabe, L. Sun, E. Kayahara, K. Suzuki, H. Tanaka, S. Yamago, H. Kaji and E. Zysman-Colman, *Organic letters*, 2023, **25**, 998–1002.
- 98 E. Kayahara, M. Nakano, L. Sun, K. Ishida and S. Yamago, *Chem. Asian J.*, 2020, **15**, 2451–2455.
- 99 V. Bliksted Roug Pedersen, T. W. Price, N. Kofod, L. N. Zakharov, B. W. Laursen, R. Jasti and M. Brøndsted Nielsen, *Chem. Eur. J.*, 2023. DOI: 10.1002/chem.202303490.
- 100X. Li, L. Jia, W. Wang, Y. Wang, Di Sun and H. Jiang, *J. Mater. Chem. C*, 2023, **11**, 1429–1434.
- 101D. Ari, E. Dureau, O. Jeannin, J. Rault-Berthelot, C. Poriel and C. Quinton, *Chem. Commun.*, 2023. DOI: 10.1039/d3cc04924h.
- 102C. W. Struck and W. H. Fonger, *J. Appl. Phys.*, 1971, **42**, 4515–4516.
- 103Q. Huang, G. Zhuang, M. Zhang, J. Wang, S. Wang, Y. Wu, S. Yang and P. Du, *J. Am. Chem. Soc.*, 2019, **141**, 18938–18943.

- 104E. Peterson, R. L. Maust, R. Jasti, M. Kertesz and J. D. Tovar, *J. Am. Chem. Soc.*, 2022, **144**, 4611–4622.
- 105G. M. Peters, G. Grover, R. L. Maust, C. E. Colwell, H. Bates, W. A. Edgell, R. Jasti, M. Kertesz and J. D. Tovar, *J. Am. Chem. Soc.*, 2020, **142**, 2293–2300.
- 106S. Wang, F. Chen, G. Zhuang, K. Wei, T. Chen, X. Zhang, C. Chen and P. Du, *Nano Res.*, 2023, **16**, 10342–10347.
- 107P. Seitz, M. Bhosale, L. Rzesny, A. Uhlmann, J. S. Wössner, R. Wessling and B. Esser, *Angew. Chem. Int. Ed.*, 2023, e202306184.
- 108R. L. Maust, P. Li, B. Shao, S. M. Zeitler, P. B. Sun, H. W. Reid, L. N. Zakharov, M. R. Golder and R. Jasti, *ACS Cent. Sci.*, 2021, **7**, 1056–1065.
- 109T. Kawase and H. Kurata, *Chem. Rev.*, 2006, **106**, 5250–5273.
- 110J. M. Lehn, *Science*, 1993, **260**, 1762–1763.
- 111E. Fischer, *Ber. Dtsch. Chem. Ges.*, 1894, **27**, 2985–2993.
- 112The Nobel Prize in Chemistry 1987,
<https://www.nobelprize.org/prizes/chemistry/1987/summary/>, (accessed 22 December 2023).
- 113T. Iwamoto, Y. Watanabe, T. Sadahiro, T. Haino and S. Yamago, *Angew. Chem.*, 2011, **50**, 8342–8344.
- 114Q. Huang, G. Zhuang, H. Jia, M. Qian, S. Cui, S. Yang and P. Du, *Angew. Chem. Int. Ed.*, 2019, **58**, 6244–6249.
- 115Y. Xu, B. Wang, R. Kaur, M. B. Minameyer, M. Bothe, T. Drewello, D. M. Guldi and M. von Delius, *Angew. Chem.*, 2018, **130**, 11723–11727.
- 116F. Schwer, S. Zank, M. Freiberger, R. Kaur, S. Frühwald, C. C. Robertson, A. Görling, T. Drewello, D. M. Guldi and M. von Delius, *Organic Materials*, 2022, **4**, 7–17.
- 117X. Chang, Y. Xu and M. von Delius, *Chem. Soc. Rev.*, 2023. DOI: 10.1039/D2CS00937D.
- 118J. Volkmann, D. Kohrs and H. A. Wegner, *Chem. Eur. J.*, 2023, **29**, e202300268.
- 119D. Kohrs, J. Volkmann and H. A. Wegner, *Eur. J. Org. Chem.*, 2023, **26**.
- 120J. Volkmann, D. Kohrs, F. Bernt and H. A. Wegner, *Eur. J. Org. Chem.*, 2022, **2022**. DOI: 10.1002/ejoc.202101357.
- 121D. Kohrs, J. Becker and H. A. Wegner, *Chem. Eur. J.*, 2022, **28**, e202104239.
- 122T. Ogoshi, T.-A. Yamagishi and Y. Nakamoto, *Chem. Rev.*, 2016, **116**, 7937–8002.
- 123M. Xue, Y. Yang, X. Chi, Z. Zhang and F. Huang, *Acc. Chem. Res.*, 2012, **45**, 1294–1308.
- 124S. B. Nimse and T. Kim, *Chem. Soc. Rev.*, 2013, **42**, 366–386.
- 125P. Della Sala, C. Talotta, A. Capobianco, A. Soriente, M. de Rosa, P. Neri and C. Gaeta, *Organic Letters*, 2018, **20**, 7415–7418.
- 126Y. Xu, F. Steudel, M.-Y. Leung, B. Xia, M. von Delius and V. W.-W. Yam, *Angew. Chem. Int. Ed.*, 2023, **62**, e202302978.
- 127Y. Fan, S. Fan, L. Liu, S. Guo, J. He, X. Li, Z. Lian, W. Guo, X. Chen, Y. Wang and H. Jiang, *Chem. Sci.*, 2023. DOI: 10.1039/D3SC04358D.
- 128C. J. Bruns and J. F. Stoddart, *The nature of the mechanical bond. From molecules to machines*, John Wiley & Sons, Hoboken, New Jersey, 2017.
- 129M. Xue, Y. Yang, X. Chi, X. Yan and F. Huang, *Chem. Rev.*, 2015, **115**, 7398–7501.
- 130G. Gil-Ramírez, D. A. Leigh and A. J. Stephens, *Angew. Chem. Int. Ed.*, 2015, **54**, 6110–6150.
- 131N. H. Evans, *Chem. Eur. J.*, 2018, **24**, 3101–3112.
- 132The Nobel Prize in Chemistry 2016,
<https://www.nobelprize.org/prizes/chemistry/2016/summary/>, (accessed 22 December 2023).

- 133Y. Xu, R. Kaur, B. Wang, M. B. Minameyer, S. Gsänger, B. Meyer, T. Drewello, D. M. Guldi and M. von Delius, *J. Am. Chem. Soc.*, 2018, **140**, 13413–13420.
- 134S. Saito, E. Takahashi and K. Nakazono, *Organic letters*, 2006, **8**, 5133–5136.
- 135V. Aucagne, K. D. Hänni, D. A. Leigh, P. J. Lusby and D. B. Walker, *J. Am. Chem. Soc.*, 2006, **128**, 2186–2187.
- 136Y.-Y. Fan, D. Chen, Z.-A. Huang, J. Zhu, C.-H. Tung, L.-Z. Wu and H. Cong, *Nature communications*, 2018, **9**, 3037.
- 137Y. Segawa, M. Kuwayama, Y. Hijikata, M. Fushimi, T. Nishihara, J. Pirillo, J. Shirasaki, N. Kubota and K. Itami, *Science*, 2019, **365**, 272–276.
- 138Y. Segawa, D. R. Levine and K. Itami, *Acc. Chem. Res.*, 2019, **52**, 2760–2767.
- 139J. H. May, J. M. van Raden, R. L. Maust, L. N. Zakharov and R. Jasti, *Nat. Chem.*, 2023, **15**, 170–176.
- 140Z. Jiang, W. Duan, W. Lin, L. Yang, Z. Wu, J. Wang, S. Wang, P. Du and Q. Li, *Mater. Today Chem.*, 2022, **25**, 100973.
- 141M. Zhu, Q. Zhou, H. Cheng, Y. Sha, V. I. Bregadze, H. Yan, Z. Sun and X. Li, *Angew. Chem. Int. Ed.*, 2023, **62**, e202213470.
- 142T. A. Schaub, J. T. Margraf, L. Zakharov, K. Reuter and R. Jasti, *Angew. Chem. Int. Ed.*, 2018, **57**, 16348–16353.
- 143S. Hashimoto, E. Kayahara, Y. Mizuhata, N. Tokitoh, K. Takeuchi, F. Ozawa and S. Yamago, *Org. Lett.*, 2018, **20**, 5973–5976.
- 144E. J. Leonhardt, J. M. van Raden, D. Miller, L. N. Zakharov, B. Alemán and R. Jasti, *Nano Lett.*, 2018, **18**, 7991–7997.
- 145J. M. van Raden, E. J. Leonhardt, L. N. Zakharov, A. Pérez-Guardiola, A. J. Pérez-Jiménez, C. R. Marshall, C. K. Brozek, J. C. Sancho-García and R. Jasti, *J. Org. Chem.*, 2020, **85**, 129–141.
- 146H. Shudo, M. Kuwayama, M. Shimasaki, T. Nishihara, Y. Takeda, N. Mitoma, T. Kuwabara, A. Yagi, Y. Segawa and K. Itami, *Nature communications*, 2022, **13**, 3713.
- 147H. Shudo, M. Kuwayama, Y. Segawa, A. Yagi and K. Itami, *Half-substituted fluorocycloparaphenylenes with high symmetry: Synthesis, properties and derivatization to densely substituted carbon nanorings*, 2023.
- 148A. A. Kamin, T. D. Clayton, C. E. Otteson, P. M. Gannon, S. Krajewski, W. Kaminsky, R. Jasti and D. J. Xiao, *Chem. Sci.*, 2023, **14**, 9724–9732.
- 149M. R. Golder, L. N. Zakharov and R. Jasti, *Pure Appl. Chem.*, 2017, **89**, 1603–1617.
- 150P. Wipf and J. K. Jung, *Chem. Rev.*, 1999, **99**, 1469–1480.
- 151T. J. Sisto, L. N. Zakharov, B. M. White and R. Jasti, *Chem. Sci.*, 2016, **7**, 3681–3688.
- 152R. T. Arnold and J. S. Buckley, *J. Am. Chem. Soc.*, 1949, **71**, 1781–1784.
- 153H. Budzikiewicz and W. Metlesics, *J. Org. Chem.*, 1959, **24**, 1125–1126.
- 154G. W. Morrow and B. Schwind, *Synth. Commun.*, 1995, **25**, 269–276.
- 155C. A. Ramsden, ed., *Synthesis from Nonaromatic Precursors*, Georg Thieme Verlag, Stuttgart, 2007, 31a.
- 156S. Goodwin and B. Witkop, *J. Am. Chem. Soc.*, 1957, 179–185.
- 157B. Miller, *J. Am. Chem. Soc.*, 1970, **92**, 432–433.
- 158A. M. Sauer, W. E. Crowe, G. Henderson and R. A. Laine, *Tetrahedron Lett.*, 2007, **48**, 6590–6593.
- 159C. DJERASSI and C. R. SCHOLZ, *J. Am. Chem. Soc.*, 1948, **70**, 1911–1913.
- 160R. K. Mallick, S. Dutta, M. Protim Gogoi and A. K. Sahoo, *Helv. Chim. Acta*, 2022, **105**. DOI: 10.1002/hlca.202100198.
- 161Z. Xia, J. Hu, Z. Shen, Q. Yao and W. Xie, *RSC Adv.*, 2015, **5**, 38499–38502.
- 162Z. Wang, Y. A. Liu, H. Yang, W.-B. Hu and K. Wen, *Org. Lett.*, 2022, **24**, 1822–1826.

- 163T. C. Lovell, C. E. Colwell, L. N. Zakharov and R. Jasti, *Chem. Sci.*, 2019, **10**, 3786–3790.
- 164J. M. van Raden, B. M. White, L. N. Zakharov and R. Jasti, *Angew. Chem. Int. Ed.*, 2019, **58**, 7341–7345.
- 165J. M. van Raden, N. N. Jarenwattananon, L. N. Zakharov and R. Jasti, *Chem. Eur. J.*, 2020, **26**, 10205–10209.
- 166C. E. Otteson, C. M. Levinn, J. M. van Raden, M. D. Pluth and R. Jasti, *Org. Lett.*, 2021, **23**, 4608–4612.
- 167C. W. Patrick, J. F. Woods, P. Gawel, C. E. Otteson, A. L. Thompson, T. D. W. Claridge, R. Jasti and H. L. Anderson, *Angew. Chem.*, 2022, **61**, e202116897.
- 168T. C. Lovell, S. G. Bolton, J. P. Kenison, J. Shangguan, C. E. Otteson, F. Civitci, X. Nan, M. D. Pluth and R. Jasti, *ACS Nano*, 2021, **15**, 15285–15293.
- 169An Bu, Y. Zhao, H. Xiao, C.-H. Tung, L.-Z. Wu and H. Cong, *Angew. Chem.*, 2022, **61**, e202209449.
- 170B. M. White, Y. Zhao, T. E. Kawashima, B. P. Branchaud, M. D. Pluth and R. Jasti, *ACS Cent. Sci.*, 2018, **4**, 1173–1178.
- 171J. Zhang, H. Cheng, Z. Meng, H. Zhang, Z. Luo, M. Muddassir, X. Li and Y. Sha, *Polym. Chem.*, 2023. DOI: 10.1039/D3PY01058A.
- 172L. Mercks and M. Albrecht, *Chem. Soc. Rev.*, 2010, **39**, 1903–1912.
- 173P. Bellotti, M. Koy, M. N. Hopkinson and F. Glorius, *Nat. Rev. Chem.*, 2021, **5**, 711–725.
- 174M. N. Hopkinson, C. Richter, M. Schedler and F. Glorius, *Nature*, 2014, **510**, 485–496.
- 175R. Visbal and M. C. Gimeno, *Chem. Soc. Rev.*, 2014, **43**, 3551–3574.
- 176R. H. Crabtree, *The Organometallic Chemistry of the Transition Metals*, Wiley, 2014.
- 177S. P. Nolan, ed., *N-heterocyclic carbenes. Effective tools for organometallic synthesis*, Wiley-VCH, Weinheim, Germany, 2014.
- 178J.-B. Dumas and E. Péligot, *Mémoire sur l'esprit de bois et sur les divers composés éthers qui en proviennent*, Imprimerie de E-J Bailly et Co, Paris, 1835.
- 179A. J. Arduengo and R. Krafczyk, *Chem. Unserer Zeit*, 1998, **32**, 6–14.
- 180A. Igau, H. Grutzmacher, A. Baceiredo and G. Bertrand, *J. Am. Chem. Soc.*, 1988, **110**, 6463–6466.
- 181A. J. Arduengo, R. L. Harlow and M. Kline, *J. Am. Chem. Soc.*, 1991, **113**, 361–363.
- 182W. Jeong, E. J. Shin, D. A. Culkin, J. L. Hedrick and R. M. Waymouth, *J. Am. Chem. Soc.*, 2009, **131**, 4884–4891.
- 183J. Raynaud, C. Absalon, Y. Gnanou and D. Taton, *J. Am. Chem. Soc.*, 2009, **131**, 3201–3209.
- 184A. J. Boydston, Y. Xia, J. A. Kornfield, I. A. Gorodetskaya and R. H. Grubbs, *J. Am. Chem. Soc.*, 2008, **130**, 12775–12782.
- 185B. R. Galan, M. Pitak, M. Gembicky, J. B. Keister and S. T. Diver, *J. Am. Chem. Soc.*, 2009, **131**, 6822–6832.
- 186T. Iwai, T. Fujihara, J. Terao and Y. Tsuji, *J. Am. Chem. Soc.*, 2009, **131**, 6668–6669.
- 187G. G. Dubinina, H. Furutachi and D. A. Vivic, *J. Am. Chem. Soc.*, 2008, **130**, 8600–8601.
- 188Y. Lee and A. H. Hoveyda, *J. Am. Chem. Soc.*, 2009, **131**, 3160–3161.
- 189V. W.-W. Yam, J. K.-W. Lee, C.-C. Ko and N. Zhu, *J. Am. Chem. Soc.*, 2009, **131**, 912–913.
- 190W. A. Herrmann and C. Köcher, *Angewandte Chemie*, 1997, **109**, 2256–2282.
- 191S. F. Clewing and J. P. Wagner, *J. Org. Chem.*, 2021, **86**, 15247–15252.
- 192W. A. Herrmann, M. Elison, J. Fischer, C. Köcher and G. R. J. Artus, *Chem. Eur. J.*, 1996, **2**, 772–780.
- 193C. Lorber and L. Vendier, *Dalton Trans.*, 2009, 6972–6984.
- 194D. Zhang and G. Zi, *Chem. Soc. Rev.*, 2015, **44**, 1898–1921.
- 195C. Heinemann, T. Müller, Y. Apeloig and H. Schwarz, *J. Am. Chem. Soc.*, 1996, **118**, 2023–2038.

- 196J. C. Y. Lin, R. T. W. Huang, C. S. Lee, A. Bhattacharyya, W. S. Hwang and I. J. B. Lin, *Chem. Rev.*, 2009, **109**, 3561–3598.
- 197M. Mora, M. C. Gimeno and R. Visbal, *Chem. Soc. Rev.*, 2019, **48**, 447–462.
- 198H. Amouri, *Chem. Rev.*, 2023, **123**, 230–270.
- 199S. P. Nolan, *Acc. Chem. Res.*, 2011, **44**, 91–100.
- 200L. Rocchigiani and M. Bochmann, *Chem. Rev.*, 2021, **121**, 8364–8451.
- 201M. Pažický, A. Loos, M. J. Ferreira, D. Serra, N. Vinokurov, F. Rominger, C. Jäkel, A. S. K. Hashmi and M. Limbach, *Organometallics*, 2010, **29**, 4448–4458.
- 202N. Marion, S. Díez-González, P. de Frémont, A. R. Noble and S. P. Nolan, *Angewandte Chemie (International ed. in English)*, 2006, **45**, 3647–3650.
- 203T. J. Robilotto, J. Bacsa, T. G. Gray and J. P. Sadighi, *Angewandte Chemie (International ed. in English)*, 2012, **51**, 12077–12080.
- 204K. Salorinne, R. W. Y. Man, P. A. Lummis, M. S. A. Hazer, S. Malola, J. C.-H. Yim, A. J. Veinot, W. Zhou, H. Häkkinen, M. Nambo and C. M. Crudden, *Chem. Commun.*, 2020, **56**, 6102–6105.
- 205R. W. Y. Man, H. Yi, S. Malola, S. Takano, T. Tsukuda, H. Häkkinen, M. Nambo and C. M. Crudden, *J. Am. Chem. Soc.*, 2022, **144**, 2056–2061.
- 206A. I. Sullivan, J. F. DeJesus, S. Malola, S. Takano, T. Tsukuda, H. Häkkinen and C. M. Crudden, *Chem. Mater.*, 2023, **35**, 2790–2796.
- 207M. R. Narouz, S. Takano, P. A. Lummis, T. I. Levchenko, A. Nazemi, S. Kaappa, S. Malola, G. Yousefalizadeh, L. A. Calhoun, K. G. Stamplecoskie, H. Häkkinen, T. Tsukuda and C. M. Crudden, *J. Am. Chem. Soc.*, 2019, **141**, 14997–15002.
- 208V. K. Kulkarni, B. N. Khiarak, S. Takano, S. Malola, E. L. Albright, T. I. Levchenko, M. D. Aloisio, C.-T. Dinh, T. Tsukuda, H. Häkkinen and C. M. Crudden, *J. Am. Chem. Soc.*, 2022, **144**, 9000–9006.
- 209P. A. Lummis, K. M. Osten, T. I. Levchenko, M. Sabooni Asre Hazer, S. Malola, B. Owens-Baird, A. J. Veinot, E. L. Albright, G. Schatte, S. Takano, K. Kovnir, K. G. Stamplecoskie, T. Tsukuda, H. Häkkinen, M. Nambo and C. M. Crudden, *JACS Au*, 2022, **2**, 875–885.
- 210M.-L. Teyssot, A.-S. Jarrousse, M. Manin, A. Chevy, S. Roche, F. Norre, C. Beaudoin, L. Morel, D. Boyer, R. Mahiou and A. Gautier, *Dalton Trans.*, 2009, 6894–6902.
- 211J. Jiang, X. Xiong and T. Zou, *Acc. Chem. Res.*, 2023, **56**, 1043–1056.
- 212R. T. Mertens, S. Gukathasan, A. S. Arojojoye, C. Olelewe and S. G. Awuah, *Chem. Rev.*, 2023, **123**, 6612–6667.
- 213H. Yersin, ed., *Highly Efficient OLEDs with Phosphorescent Materials*, Wiley-VCH, Weinheim, 1st edn., 2008.
- 214V. Wing-Wah Yam and E. Chung-Chin Cheng, eds., *Photochemistry and Photophysics of Coordination Compounds: Gold*, vol. 281.
- 215A. Laguna, ed., *Modern supramolecular gold chemistry. Gold-metal interactions and applications*, Wiley-VCH, Weinheim, Chichester, 2008.
- 216L. Gao, N. Deligonul and T. G. Gray, *Inorg. Chem.*, 2012, **51**, 7682–7688.
- 217C.-W. Hsu, C.-C. Lin, M.-W. Chung, Y. Chi, G.-H. Lee, P.-T. Chou, C.-H. Chang and P.-Y. Chen, *J. Am. Chem. Soc.*, 2011, **133**, 12085–12099.
- 218V. W.-W. Yam and K. M.-C. Wong, *Chem. Commun.*, 2011, **47**, 11579–11592.
- 219T. Li, D. S. Muthiah Ravinson, R. Haiges, P. I. Djurovich and M. E. Thompson, *J. Am. Chem. Soc.*, 2020, **142**, 6158–6172.
- 220M. Kriechbaum, M. List, R. J F Berger, M. Patzschke and U. Monkowius, *Chem. Eur. J.*, 2012, **18**, 5506–5509.
- 221M. Kriechbaum, G. Winterleitner, A. Gerisch, M. List and U. Monkowius, *Eur. J. Inorg. Chem.*, 2013, **2013**, 5567–5575.

- 222M. Vaddamanu, A. Sathyanarayana, Y. Masaya, S. Sugiyama, O. Kazuhisa, K. Velappan, M. Nandeshwar, K. Hisano, O. Tsutsumi and G. Prabusankar, *Chem. Asian. J.*, 2021, **16**, 521–529.
- 223H.-Q. Dong, T.-B. Wei, X.-Q. Ma, Q.-Y. Yang, Y.-F. Zhang, Y.-J. Sun, B.-B. Shi, H. Yao, Y.-M. Zhang and Q. Lin, *J. Mater. Chem. C*, 2020, **8**, 13501–13529.
- 224A. S. Oshchepkov, M. S. Oshchepkov, M. V. Oshchepkova, A. Al-Hamry, O. Kanoun and E. A. Kataev, *Adv. Opt. Mater.*, 2021, **9**, 2001913.
- 225Z. Hendi, S. Jamali, S. M. J. Chabok, A. Jamjah, H. Samouei and Z. Jamshidi, *Inorg. Chem.*, 2021, **60**, 12924–12933.
- 226P. Kos and H. Plenio, *Chem. Eur. J.*, 2015, **21**, 1088–1095.
- 227S. Popov and H. Plenio, *Eur. J. Inorg. Chem.*, 2022, **2022**, e202200335.
- 228O. Halter and H. Plenio, *Eur. J. Inorg. Chem.*, 2018, **2018**, 2935–2943.
- 229A. Citta, E. Schuh, F. Mohr, A. Folda, M. L. Massimino, A. Bindoli, A. Casini and M. P. Rigobello, *Metallomics.*, 2013, **5**, 1006–1015.
- 230B. Bertrand, A. de Almeida, E. P. M. van der Burgt, M. Picquet, A. Citta, A. Folda, M. P. Rigobello, P. Le Gendre, E. Bodio and A. Casini, *Eur. J. Inorg. Chem.*, 2014, **2014**, 4532–4536.
- 231R. Visbal, V. Fernández-Moreira, I. Marzo, A. Laguna and M. C. Gimeno, *Dalton Trans.*, 2016, **45**, 15026–15033.
- 232J. Hine, J. A. Brown, L. H. Zalkow, W. E. Gardener and M. Hine, *J. Am. Chem. Soc.*, 1955, **1955**, 594–598.
- 233H. E. Zimmerman and R. M. Paufler, *J. Am. Chem. Soc.*, 1960, **82**, 1514–1515.
- 234H. E. Zimmerman and G. L. Grunewald, *J. Am. Chem. Soc.*, 1966, **88**, 183–184.
- 235R. Altundas, A. Dastan, N. S. Ünalı, K. Güven, O. Uzun and M. Balci, *Eur. J. Org. Chem.*, 2002, **2002**, 526–533.
- 236H. E. Zimmerman, G. L. Grunewald, R. M. Paufler and M. A. Sherwin, *J. Am. Chem. Soc.*, 1969, **91**, 2330–2338.
- 237R. Schulte, M. Löcker, H. Ihmels, M. Heide and C. Engelhard, *Chem. Eur. J.*, 2023, **29**, e202203203.
- 238T. Nishimura, T. Kawamoto, M. Nagaosa, H. Kumamoto and T. Hayashi, *Angew. Chem. Int. Ed.*, 2010, **49**, 1638–1641.
- 239R. Shintani, M. Takeda, T. Nishimura and T. Hayashi, *Angew. Chem. Int. Ed.*, 2010, **49**, 3969–3971.
- 240M. A. Esteruelas and L. A. Oro, *Coord. Chem. Rev.*, 1999, **193-195**, 557–618.
- 241M. Shiotsuki, N. Onishi, F. Sanda and T. Masuda, *Polym. J.*, 2011, **43**, 51–57.
- 242L. Pu, M. W. Wagaman and R. H. Grubbs, *Macromolecules*, 1996, **29**, 1138–1143.
- 243T. Tang, G. Ahumada and C. W. Bielawski, *Polym. Chem.*, 2020, **11**, 5437–5443.
- 244C. G. Krespan, B. C. McKusick and T. L. Cairns, *J. Am. Chem. Soc.*, 1961, **83**, 3428–3432.
- 245R. S. H. Liu and C. G. Krespan, *J. Org. Chem.*, 1969, **34**, 1271–1278.
- 246R. G. Miller and M. Stiles, *J. Am. Chem. Soc.*, 1963, **85**, 1798–1800.
- 247K. Chow and H. W. Moore, *J. Org. Chem.*, 1990, **55**, 370–372.
- 248Y. Miyauchi, Y. Shibata and K. Tanaka, *Chem. Lett.*, 2016, 86–88.
- 249N. Hayase, Y. Miyauchi, Y. Aida, H. Sugiyama, H. Uekusa, Y. Shibata and K. Tanaka, *Org. Lett.*, 2017, **19**, 2993–2996.
- 250S. Song, X. Sun, X. Li, Y. Yuan and N. Jiao, *Org. Lett.*, 2015, **17**, 2886–2889.
- 251S. Song, X. Li, J. Wei, W. Wang, Y. Zhang, L. Ai, Y. Zhu, X. Shi, X. Zhang and N. Jiao, *Nat. Catal.*, 2020, **3**, 107–115.
- 252S. Brand, H. Elsen, J. Langer, S. Grams and S. Harder, *Angew. Chem. Int. Ed.*, 2019, **58**, 15496–15503.

- 253T. Ishiyama, J. Takagi, K. Ishida, N. Miyaoura, N. R. Anastasi and J. F. Hartwig, *J. Am. Chem. Soc.*, 2002, **124**, 390–391.
- 254S. M. Preshlock, B. Ghaffari, P. E. Maligres, S. W. Krska, R. E. Maleczka and M. R. Smith, *J. Am. Chem. Soc.*, 2013, **135**, 7572–7582.
- 255A. K. Cook, M. H. Emmert and M. S. Sanford, *Org. Lett.*, 2013, **15**, 5428–5431.
- 256C. Jia, D. Piao, J. Oyamada, W. Lu, T. Kitamura and Y. Fujiwara, *Science*, 2000, **287**, 1992–1995.
- 257T. Tajima, Y. Kishi and A. Nakajima, *Electrochimica Acta*, 2009, **54**, 5959–5963.
- 258H. Huang and T. H. Lambert, *Angew. Chem. Int. Ed.*, 2021, **60**, 11163–11167.
- 259M. B. Plutschack, B. Pieber, K. Gilmore and P. H. Seeberger, *Chem. Rev.*, 2017, **117**, 11796–11893.
- 260SiliaCat DPP-Pd Heterogeneous Catalyst (RD-R390-100) | Portfolio | SiliaCat - Heterogeneous Catalysts | Products, <https://www.silicycle.com/products/siliacat-heterogeneous-catalysts/portfolio/rd-r390-100>, (accessed 1 December 2023).
- 261Tetrakis(triphenylphosphin)palladium, polymergebunden extent of labeling: ~0.06 mmol/g loading | Sigma-Aldrich, <https://www.sigmaaldrich.com/DE/de/product/aldrich/10987>, (accessed 1 December 2023).
- 262Pd EnCat® 40 extent of labeling: 0.4 mmol/g Pd loading | Sigma-Aldrich, <https://www.sigmaaldrich.com/DE/de/product/aldrich/644722>, (accessed 1 December 2023).
- 263PhosphonicS L-PAPd1r Triphenylphosphine palladium(II) dichloride phosphadmantane ethyl Silica, <https://www.sigmaaldrich.com/DE/de/product/aldrich/744239>, (accessed 1 December 2023).
- 264Y. Segawa, S. Miyamoto, H. Omachi, S. Matsuura, P. Šenel, T. Sasamori, N. Tokitoh and K. Itami, *Angew. Chem.*, 2011, **50**, 3244–3248.
- 265Y. Segawa, P. Šenel, S. Matsuura, H. Omachi and K. Itami, *Chem. Lett.*, 2011, **40**, 423–425.
- 266L. Adamska, I. Nayyar, H. Chen, A. K. Swan, N. Oldani, S. Fernandez-Alberti, M. R. Golder, R. Jasti, S. K. Doorn and S. Tretiak, *Nano Lett.*, 2014, **14**, 6539–6546.
- 267P. Thordarson, *Chem. Soc. Rev.*, 2011, **40**, 1305–1323.
- 268D. Brynn Hibbert and P. Thordarson, *Chem. Commun.*, 2016, **52**, 12792–12805.
- 269T. Haino, M. Yanase and Y. Fukazawa, *Angew. Chem.*, 1997, **36**, 259–260.
- 270T. Kawase, K. Tanaka, N. Fujiwara, H. R. Darabi and M. Oda, *Angew. Chem.*, 2003, **115**, 1662–1666.
- 271A. Vörös, Z. Baán, P. Mizsey and Z. Finta, *Org. Process Res. Dev.*, 2012, **16**, 1717–1726.
- 272A. El-Faham and F. Albericio, *Chem. Rev.*, 2011, **111**, 6557–6602.
- 273A. Chartoire, C. Claver, M. Corpet, J. Krinsky, J. Mayen, D. Nelson, S. P. Nolan, I. Peñafiel, R. Woodward and R. E. Meadows, *Org. Process Res. Dev.*, 2016, **20**, 551–557.
- 274H. M. J. Wang and I. J. B. Lin, *Organometallics*, 1998, **17**, 972–975.
- 275R. Visbal, A. Laguna and M. C. Gimeno, *Chem. Commun.*, 2013, **49**, 5642–5644.
- 276D. A. Pantazis, X.-Y. Chen, C. R. Landis and F. Neese, *J. Chem. Theory Comput.*, 2008, **4**, 908–919.
- 277E. van Lenthe, A. Ehlers and E.-J. Baerends, *J. Chem. Phys.*, 1999, **110**, 8943–8953.
- 278F. Weigend and R. Ahlrichs, *Phys. Chem. Chem. Phys.*, 2005, **7**, 3297–3305.
- 279C. Adamo and V. Barone, *J. Chem. Phys.*, 1999, **110**, 6158–6170.
- 280J. P. Perdew, M. Ernzerhof and K. Burke, *J. Chem. Phys.*, 1996, **105**, 9982–9985.
- 281F. Neese, *WIREs Comput. Mol. Sci.*, 2012, **2**, 73–78.
- 282F. Neese, *WIREs Comput. Mol. Sci.*, 2022, **12**, e1606.
- 283M. Stradiotto and R. J. Lundgren, *Ligand design in metal chemistry. Reactivity and catalysis*, John Wiley & Sons, Chichester, UK, Hoboken, NJ, 2016.

- 284H. Clavier and S. P. Nolan, *Chem. Commun.*, 2010, **46**, 841–861.
- 285A. Poater, F. Ragone, S. Giudice, C. Costabile, R. Dorta, S. P. Nolan and L. Cavallo, *Organometallics*, 2008, **27**, 2679–2681.
- 286A. Poater, F. Ragone, R. Mariz, R. Dorta and L. Cavallo, *Chem. Eur. J.*, 2010, **16**, 14348–14353.
- 287A. Poater, B. Cosenza, A. Correa, S. Giudice, F. Ragone, V. Scarano and L. Cavallo, *Eur. J. Inorg. Chem.*, 2009, **2009**, 1759–1766.
- 288L. Falivene, R. Credendino, A. Poater, A. Petta, L. Serra, R. Oliva, V. Scarano and L. Cavallo, *Organometallics*, 2016, **35**, 2286–2293.
- 289A. Gómez-Suárez, D. J. Nelson and S. P. Nolan, *Chem. Commun.*, 2017, **53**, 2650–2660.
- 290L. W. Bieber and M. F. Da Silva, *Tetrahedron Lett.*, 2007, **48**, 7088–7090.
- 291C. E. Colwell, T. W. Price, T. Stauch and R. Jasti, *Chem. Sci.*, 2020, **11**, 3923–3930.
- 292S. Kancharla, K. Jørgensen and M. Fernández-Ibáñez, *Synthesis*, 2019, **51**, 643–663.
- 293A. Murtaza, Z. Ulhaq, B. Shirinfar, S. Rani, S. Aslam, G. M. Martins and N. Ahmed, *Chemical record (New York, N.Y.)*, 2023, **23**, e202300119.
- 294N. R. Judge, A. Logallo and E. Hevia, *Chem. Sci.*, 2023, **14**, 11617–11628.
- 295C. Miao and J. Yao, *Chin. J. Org. Chem.*, 2023, **43**, 1341.
- 296L. Krause, R. Herbst-Irmer, G. M. Sheldrick and D. Stalke, *J. Appl. Crystallogr.*, 2015, **48**, 3–10.
- 297G. M. Sheldrick, *Acta Crystallogr.*, 2015, **71**, 3–8.
- 298G. M. Sheldrick, *Acta Crystallogr.*, 2015, **71**, 3–8.
- 299C. Bannwarth, E. Caldeweyher, S. Ehlert, A. Hansen, P. Pracht, J. Seibert, S. Spicher and S. Grimme, *WIREs Comput. Mol. Sci.*, 2021, **11**, e1493.
- 300P. Pracht, F. Bohle and S. Grimme, *Phys. Chem. Chem. Phys.*, 2020, **22**, 7169–7192.
- 301S. Grimme, *J. Chem. Theory Comput.*, 2019, **15**, 2847–2862.
- 302S. Grimme, S. Ehrlich and L. Goerigk, *J. Comput. Chem.*, 2011, **32**, 1456–1465.
- 303S. Grimme, J. Antony, S. Ehrlich and H. Krieg, *J. Chem. Phys.*, 2010, **132**, 154104.
- 304V. Barone and M. Cossi, *J. Phys. Chem. A*, 1998, **102**, 1995–2001.
- 305F. Weigend, *Phys. Chem. Chem. Phys.*, 2006, **8**, 1057–1065.
- 306B. Helmich-Paris, B. de Souza, F. Neese and R. Izsák, *J. Chem. Phys.*, 2021, **155**, 104109.
- 307S. Hirata and M. Head-Gordon, *Chem. Phys. Lett.*, 1999, **314**, 291–299.
- 308L. Falivene, Z. Cao, A. Petta, L. Serra, A. Poater, R. Oliva, V. Scarano and L. Cavallo, *Nat. Chem.*, 2019, **11**, 872–879.
- 309Q. Huang, G. Zhuang, H. Jia, M. Qian, S. Cui, S. Yang and P. Du, *Angew. Chem.*, 2019, **58**, 6244–6249.
- 310D. Wassy, M. Hermann, J. S. Wössner, L. Frédéric, G. Pieters and B. Esser, *Chem. Sci.*, 2021, **12**, 10150–10158.
- 311M. Stender, R. J. Wright, B. E. Eichler, J. Prust, M. M. Olmstead, H. W. Roesky and P. P. Power, *J. Chem. Soc., Dalton Trans.*, 2001, 3465–3469.
- 312A. M. Mfuh, V. T. Nguyen, B. Chhetri, J. E. Burch, J. D. Doyle, V. N. Nesterov, H. D. Arman and O. V. Larionov, *J. Am. Chem. Soc.*, 2016, **138**, 8408–8411.
- 313A. W. Waltman and R. H. Grubbs, *Organometallics*, 2004, **23**, 3105–3107.